



The spin-ladder and spin-chain system $(\text{La}, \text{Y}, \text{Sr}, \text{Ca})_{14}\text{Cu}_{24}\text{O}_{41}$: Electronic phases, charge and spin dynamics

T. Vuletić^a, B. Korin-Hamzić^a, T. Ivek^a, S. Tomić^{a,*}, B. Gorshunov^{b,1},
M. Dressel^b, J. Akimitsu^c

^a*Institut za fiziku, P.O. Box 304, HR-10001 Zagreb, Croatia*

^b*Physikalisches Institut, Universität Stuttgart, D-70550 Stuttgart, Germany*

^c*Department of Physics, Aoyama-Gakuin University, Kanagawa, Japan*

Accepted 25 January 2006

editor: D.K. Campbell

Abstract

The quasi-one-dimensional cuprates $(\text{La}, \text{Y}, \text{Sr}, \text{Ca})_{14}\text{Cu}_{24}\text{O}_{41}$, consisting of spin-chains and spin-ladders, have attracted much attention, mainly because they represent the first superconducting copper oxide with a non-square lattice. Theoretically, in isolated hole-doped two-leg ladders, superconductivity is tightly associated with the spin gap, although in competition with a charge-density wave (CDW). Indeed, both the gapped spin-liquid and CDW states have been established in the doped spin-ladders of $\text{Sr}_{14-x}\text{Ca}_x\text{Cu}_{24}\text{O}_{41}$, however the relevance of these objects to electronic properties and superconductivity is still subject of intensive discussion. In this treatise, an appreciable set of experimental data is reviewed, which has been acquired in recent years, indicating a variety of magnetic and charge arrangements found in the chains and ladders of underdoped $(\text{La}, \text{Y})_y(\text{S}, \text{Ca})_{14-y}\text{Cu}_{24}\text{O}_{41}$ and fully doped $\text{Sr}_{14-x}\text{Ca}_x\text{Cu}_{24}\text{O}_{41}$. Based on these data, phase diagrams are constructed for the chains of underdoped systems (as a function of La, Y-substitution), as well as for the chains and ladders of the fully doped ones (as a function of Ca-substitution). We try to reconcile contradictory results concerning the charge dynamics in the ladders, like the hole redistribution between ladders and chains, collective modes and pseudogap, field-dependent transport and the temperature scales and doping levels at which the two-dimensional CDW develops in the ladder planes. The remaining open issues are clearly extracted. In the discussion the experimental results are contrasted with theoretical predictions, which allows us to conclude with two important remarks concerning the nature of the competing CDW and superconducting ground states. A density wave in ladders, characterized by a sinusoidal charge modulation, belongs to the class of broken symmetry patterns, which is theoretically predicted for strongly correlated low-dimensional electron systems; however its precise texture and nature is still an open issue. As for superconductivity, the presence of the spin gap in the normal state points towards *d*-wave symmetry and magnetic origin of the attractive interaction. However, there is a finite density of mobile quasi-particles that appears for high Ca contents and increases with pressure, concomitantly with increased two-dimensionality and metallicity. For this reason the superconductivity in the doped ladders of $\text{Sr}_{14-x}\text{Ca}_x\text{Cu}_{24}\text{O}_{41}$ which occurs under high pressure cannot simply be a stabilization of the *d*-wave superconductivity expected for a pure single ladder system.

© 2006 Published by Elsevier B.V.

PACS: 74.72.Jt; 75.10.Pq; 71.45.Lr; 71.27.+a; 74.20.Mn

Keywords: Hole-doped quasi-one-dimensional cuprates; Spin-ladders and gapped spin-liquid; Unconventional density waves and superconductivity; Antiferromagnetic dimer and charge order in chains; Spin and charge response in strongly correlated system

* Corresponding author. Tel.: +385 1 469 8820; fax: +385 1 469 8889.

E-mail addresses: stomic@ifs.hr (S. Tomić), dressel@pi1.physik.uni-stuttgart.de (M. Dressel).

¹ Permanent address: A.M. Prokhorov General Physics Institute, Russian Academy of Sciences, Moscow, Russia.

Contents

1. Introduction	2
2. Ladders and chains: strongly interacting one-dimensional electron systems	5
2.1. One-dimensional extended Hubbard model in strong coupling limit	5
2.1.1. On-site attraction, $U < 0$	5
2.1.2. On-site repulsion, $U > 0$	6
2.2. Strong coupling limit for cuprates	7
2.3. t – J model for two-leg ladders	9
3. Materials and structure	10
3.1. Crystallographic structure of quasi-one-dimensional cuprates $(\text{La}, \text{Y}, \text{Sr}, \text{Ca})_{14}\text{Cu}_{24}\text{O}_{41}$	10
3.2. Electronic structure of quasi-one-dimensional cuprates $(\text{La}, \text{Y}, \text{Sr}, \text{Ca})_{14}\text{Cu}_{24}\text{O}_{41}$	12
3.2.1. Copper–oxygen bonds	12
3.2.2. Magnetic structure	13
3.2.3. Band structure of $\text{Sr}_{14}\text{Cu}_{24}\text{O}_{41}$: theory and experiment	15
3.3. Hole distribution between chains and ladders in $(\text{La}, \text{Y}, \text{Sr}, \text{Ca})_{14}\text{Cu}_{24}\text{O}_{41}$	18
3.3.1. X-ray absorption spectroscopy	19
3.3.2. Far-infrared optical conductivity	21
3.3.3. Nuclear magnetic resonance	24
4. Physics of chains	25
4.1. Fully doped $\text{Sr}_{14-x}\text{Ca}_x\text{Cu}_{24}\text{O}_{41}$: antiferromagnetic dimer and charge order	25
4.1.1. Magnetic susceptibility	25
4.1.2. Inelastic neutron scattering and X-ray diffraction	27
4.1.3. Nuclear magnetic resonance and electron spin resonance	31
4.2. Underdoped $(\text{La}, \text{Y})_y(\text{Sr}, \text{Ca})_{14-y}\text{Cu}_{24}\text{O}_{41}$: one-dimensional disordered system	34
4.2.1. Spin response	34
4.2.2. Charge response	36
5. Physics of ladders	40
5.1. Gapped spin-liquid	40
5.1.1. Undoped ladders of $(\text{La}, \text{Y})_y(\text{Sr}, \text{Ca})_{14-y}\text{Cu}_{24}\text{O}_{41}$	40
5.1.2. Doped ladders of $\text{Sr}_{14-x}\text{Ca}_x\text{Cu}_{24}\text{O}_{41}$	43
5.2. Superconductivity in doped ladders of $\text{Sr}_{14-x}\text{Ca}_x\text{Cu}_{24}\text{O}_{41}$	47
5.2.1. dc electrical transport	47
5.2.2. Nuclear magnetic resonance under pressure	51
5.3. Charge-density wave in doped ladders of $\text{Sr}_{14-x}\text{Ca}_x\text{Cu}_{24}\text{O}_{41}$	54
5.3.1. dc electrical transport	54
5.3.2. Low-frequency dielectric spectroscopy	58
5.3.3. Microwave and millimeter wave spectroscopy	61
5.3.4. Quasi-optical microwave and far-infrared spectroscopy	63
5.3.5. Electric field dependent transport	68
5.3.6. Low-frequency electronic Raman scattering	71
5.3.7. Resonant X-ray diffraction	73
6. Discussion	75
6.1. Phase diagrams	75
6.1.1. Phase diagram of chains in underdoped $(\text{La}, \text{Y})_y(\text{Sr}, \text{Ca})_{14-y}\text{Cu}_{24}\text{O}_{41}$	75
6.1.2. Phase diagrams of chains and ladders in fully doped $\text{Sr}_{14-x}\text{Ca}_x\text{Cu}_{24}\text{O}_{41}$	77
6.2. Doped ladders of $\text{Sr}_{14-x}\text{Ca}_x\text{Cu}_{24}\text{O}_{41}$	80
6.2.1. Normal phase and nature of charge transport	80
6.2.2. Ground states: Charge-density wave and superconductivity	82
7. Summary	84
Acknowledgements	86
References	86

1. Introduction

The spin-ladder and spin-chain systems $(\text{La}, \text{Y}, \text{Sr}, \text{Ca})_{14}\text{Cu}_{24}\text{O}_{41}$ belong to a vast class of strongly correlated materials—transition metal oxides—which exhibit some of the most intriguing phenomena in condensed matter physics. These materials are with open d and f electron shells, where electrons are spatially confined to orbitals close to the nuclei.

The one-electron bandwidths are small due to these inner orbitals and hence the Coulomb repulsion experienced by the electrons is large compared with the bandwidth. Such strongly interacting electrons cannot be described as particles embedded in a static mean field created by the other electrons: the correlations are too pronounced to be treated independently of each other. These systems fall within two well understood theoretical limits: on the one side, there are metals with weakly correlated electrons which are suitably described by band theory, and on the other side are insulators which are better treated in the real space picture as a collection of localized charges. In other words, the charges in the strongly correlated systems are neither fully itinerant, nor fully localized at their atomic sites. Thus, new theoretical approaches have been developed to describe the electronic phases, and the charge and spin arrangements in these systems [1].

The building block common to most transition metal oxides are either tetrahedrons or octahedrons formed by a metal ion in the center surrounded by four or six oxygen atoms, respectively. Since polyhedrons have the tendency to align in chains and layers by sharing corners or edges, these materials are often highly anisotropic in their physical properties. Among them are quasi-one-dimensional conductors, spin-chains and ladders [2–4]. The clear theoretical concepts and analytical solutions in the field of one-dimensional physics makes investigations of these systems so rewarding. The coupling of chains, building of ladders and eventually layers calls for advanced theoretical descriptions. The crossover from one to two and finally three dimensions makes the understanding of real systems a challenge.

The family of $(\text{La}, \text{Y}, \text{Sr}, \text{Ca})_{14}\text{Cu}_{24}\text{O}_{41}$ is such a quasi-one-dimensional system which consists of a composite structure, in the sense that it contains layers of ladders and layers of chains, separated by strings of La, Y, Sr, Ca atoms. The layers are oriented in the crystallographic *ac* plane and stacked in alternating manner along the perpendicular *b*-axis. An incommensurability between the chains and ladders creates distortions, which lead to additional modulations of the crystallographic positions. These effects may be regarded as an intrinsic source of disorder. The influence of correlations on this material is profound; and the interplay of spin and charge degrees of freedom in both the chains and ladders exhibit a rich variety of exotic spin and charge arrangements. This interplay makes both the chains and ladders extremely sensitive to variations in external parameters, such as temperature, doping and pressure.

The vast literature on the topics of spin-chains and spin-ladders accumulated in the last ten years shows that this area of research has become one of the most exciting and fertile subjects in condensed matter physics. The reason, which has triggered this broad interest and intense research is certainly the discovery of superconductivity in the two-leg ladder compound $\text{Sr}_{14-x}\text{Ca}_x\text{Cu}_{24}\text{O}_{41}$ under pressure, in particular since this system is the first superconducting copper oxide material with a non-square-lattice [5]. Theoretically, in an undoped ladder spin singlets located on rungs produce a ground state which is usually referred to as a gapped spin-liquid [6]. The undoped ladders are half-filled cuprate system and the doping of ladders leads to deviations from half-filling. Added holes² tend to share the same rung on the ladder in order to minimize the energy paid to break the spin singlets. Hence the formation of hole pairs is expected to lead to superconductivity with *d*-wave symmetry. Upon doping, the spin gap remains constant or slightly decreases in size, but it is still finite when superconductivity sets in. Because of the quasi-one-dimensional nature of ladders, a competing charge density wave (CDW) phase may prevent the occurrence of superconductivity. Thus, the ladder systems provide a challenging possibility to study spin and charge dynamics and their interplay in a spin-gapped environment with clear significance for the phase diagram of high-temperature superconducting cuprates. Motivated by theoretical work and the possibility to get insight into some of the key issues of correlated electron systems, an enormous effort in the experimental research started in order to synthesize suitable materials and to search for the two other main predictions in addition to superconductivity: spin gap and CDW. As is shown in this review, clear evidence has finally been obtained that doped ladders in $\text{Sr}_{14-x}\text{Ca}_x\text{Cu}_{24}\text{O}_{41}$ have a finite gap in their spectrum of spin excitations, they develop a CDW at low Ca contents and also exhibit superconductivity when a sufficiently large number of holes is introduced and high enough pressure is applied. Naturally, it is tempting to associate this superconducting phase with the one predicted for a pure single ladder system. Recently accumulated experimental data, however, clarify that the superconducting phase is two-dimensional in nature and further indicate that the origin of superconductivity might not be the one previously predicted by theorists.

We also try to spell out the open issues and to reconcile contradictory results concerning the charge dynamics in the doped ladders of $\text{Sr}_{14-x}\text{Ca}_x\text{Cu}_{24}\text{O}_{41}$ in the normal phase and in the CDW ground state. In particular, we focus on

² Throughout this paper we consider the undoped ladder as the system with only spins (and no holes), while by holes we mean holes added by doping into the ladder.

highly disputed issues like the hole redistribution between ladders and chains, collective modes and the pseudogap, field-dependent transport, and the temperature scales and doping levels at which the CDW develops. We show, on the basis of acquired data, that the CDW develops in two dimensions in the ladder planes, that it is characterized by a sinusoidal charge (hole) modulation and that the collective excitations of this phase possess an anisotropic phason-like dispersion. Although this CDW phase bears some of the fingerprints well known to conventional CDW systems, triggered by electron–phonon coupling, it is quite evident by now that the origin of the CDW in the ladders of $\text{Sr}_{14-x}\text{Ca}_x\text{Cu}_{24}\text{O}_{41}$ cannot be explained by the current theories.

A strong emphasis in this review is also given to the spin-chains, equally important in the underdoped $(\text{La},\text{Y})_y(\text{Sr},\text{Ca})_{14-y}\text{Cu}_{24}\text{O}_{41}$ as well as in fully doped $\text{Sr}_{14-x}\text{Ca}_x\text{Cu}_{24}\text{O}_{41}$ systems. Although the former did not attract so much interest since they appear unrelated with the fully doped, superconducting partners, their phase diagram shows diverse electronic phases and interesting spin and charge arrangements. Hopefully our presentation will convincingly demonstrate that the knowledge of their phase diagram is beneficial for the understanding of physics of spin-ladders in the fully doped materials, as well.

The enormous amount of experiments carried out on spin-ladder and spin-chain $(\text{La},\text{Y},\text{Sr},\text{Ca})_{14}\text{Cu}_{24}\text{O}_{41}$ materials during the last decade and a fair number of apparently contradictory results called for a comprehensive review, which presents the acquired data systematically, contrasts them with current theoretical models and demonstrates the phase diagrams these data generate. With the exception of an excellent review by Dagotto [7] published in 1999, and devoted to spin-ladder materials in general, and two recent but specialized reviews dedicated to magnetic light scattering and to optical spectroscopy in low-dimensional quantum spin systems [8,9], no similar attempt was undertaken until now.³ This review is written in order to accomplish these needs with hope that it will stimulate further experimental and theoretical activities. Besides the comprehensive presentation of the findings, comments by the authors on experiments and some analysis are included in the text. With this goal in mind the outline of this review is as follows.

In Section 2 we present some models developed to describe strongly interacting one-dimensional electron systems. A theoretical description commonly starts with the Hubbard model for one dimension which is modified according to the particular case of interest. Due to the large number of reviews and monographs [11–14] a very brief outline of the specific properties relevant for our purpose suffices here. In Section 3 we present important features of the crystallographic and electronic structure of $(\text{La},\text{Y},\text{Sr},\text{Ca})_{14}\text{Cu}_{24}\text{O}_{41}$ materials and show how the configuration of copper–oxygen σ -bonds formed between $\text{Cu}3d$ and $\text{O}2p$ orbitals determines the cuprate structure. We also give a short comparative overview of variety of magnetic structures and ground states in undoped cuprate systems in order to demonstrate how the nature of the particular coupling between the Cu^{2+} spins decisively determines the magnetic structure in cuprates in general, and in spin-chains and spin-ladders of $(\text{La},\text{Y},\text{Sr},\text{Ca})_{14}\text{Cu}_{24}\text{O}_{41}$ in particular. Finally, we present experiments probing electronic structure and hole distribution between chains and ladders of these materials and compare the results with the theoretical calculations. In Section 4 we present those experiments performed in order to investigate spin and charge arrangements, as well as charge transport in the spin-chains of underdoped $(\text{La},\text{Y})_y(\text{Sr},\text{Ca})_{14-y}\text{Cu}_{24}\text{O}_{41}$ and fully doped $\text{Sr}_{14-x}\text{Ca}_x\text{Cu}_{24}\text{O}_{41}$ materials. Section 5 covers the physics of spin-ladders. There, we give an overview of experiments conducted to study gapped spin-liquid ground state of undoped and doped spin-ladders, as well as the normal phase and the ground states in the charge sector of doped ladders: CDW and superconductivity. The current theoretical understanding of the spin excitation spectrum for an isolated spin-ladder is also given and used to discuss the experimental results of the spin response. Section 6 is devoted to a presentation of the phase diagrams of the chains and ladders generated on the basis of the acquired data. Finally, the main features of the normal phase and the charge transport, as well as the CDW and superconducting phases established in the doped ladders of $\text{Sr}_{14-x}\text{Ca}_x\text{Cu}_{24}\text{O}_{41}$ are compared with predictions of current theoretical models for ladders. A comprehensive summary is provided in Section 7 pointing to future perspectives in the subject of spin-ladders and spin-chains of $(\text{La},\text{Y},\text{Sr},\text{Ca})_{14}\text{Cu}_{24}\text{O}_{41}$. Among them, further research aiming to unveil the mystery of CDW and superconductivity in the doped ladders of $\text{Sr}_{14-x}\text{Ca}_x\text{Cu}_{24}\text{O}_{41}$ presents certainly the most prominent task.

³ After the manuscript was finished, we became aware of the treatise by Gozar and Blumberg [10] devoted to collective spin and charge excitations in $(\text{Sr},\text{La})_{14-x}\text{Ca}_x\text{Cu}_{24}\text{O}_{41}$ spin-ladders.

2. Ladders and chains: strongly interacting one-dimensional electron systems

In this section we introduce the main concepts and models utilized to describe the physical phenomena observed in chain and ladder compounds. Of greater importance is the one-dimensional Hubbard model which can be extended by the inter-site repulsion. The discovery of high-temperature superconductivity triggered an enormous amount of literature dealing with the application to cuprates; here we can present only a small fraction relevant to the ladder compounds.

2.1. One-dimensional extended Hubbard model in strong coupling limit

The Coulomb repulsion between electrons has an important effect on the properties of the Fermi gas at low densities. Due to this repulsion, the electrons become localized and a Mott insulator is formed. While the free electron gas condenses into the Wigner lattice upon the introduction of Coulomb repulsion, in a real crystal one has to take the atomic potentials into account. It is natural to see how this problem is resolved in one dimension, although both Mott and Wigner crystals can be realized in two dimensions as well. A common description starts with the simple Hubbard model [15,16]:

$$H = -t \sum_{j,\sigma} (c_{j,\sigma}^\dagger c_{j+1,\sigma} + \text{h.c.}) + U \sum_j n_{j,\uparrow} n_{j,\downarrow}. \quad (1)$$

This is a model of tight-binding type with one atomic orbital per lattice site j with spin $\sigma = \uparrow$ or \downarrow (single-band model). The creation operator $c_{j,\sigma}^\dagger$ inserts an electron into the atomic orbital at site j and the annihilation operator $c_{j+1,\sigma}$ removes an electron from the nearest neighbor site $j + 1$. As usual, h.c. indicates the hermitian conjugate which has to be added. The first term of the Hamiltonian (1) thus represents the effect of orbital overlap between the neighboring sites, i.e. t is the overlap integral of the tight-binding theory; the bandwidth is $4t$. It describes the kinetic energy due to the electron hopping. The second term competes with the first one adding an extra energy (Coulomb repulsion, i.e. the on-site interaction U) whenever we have two electrons at the same site ($n_{j,\sigma} = c_{j,\sigma}^\dagger c_{j,\sigma}$ is the standard particle number operator). The Hubbard model is capable of spanning the range from the independent-electron band theory to the fully localized Mott insulator, with an increase in the ratio U/t (see Fig. 1) [11,12,17,18].

The extended Hubbard model adds the Coulomb interaction V between neighboring sites. It gives a particularly simple picture of the possible states of the system in the large- U limit, in which t and the inter-site interaction V related terms are treated as perturbations [19,20]:

$$H = -t \sum_{j,\sigma} (c_{j,\sigma}^\dagger c_{j+1,\sigma} + \text{h.c.}) + U \sum_j n_{j,\uparrow} n_{j,\downarrow} + V \sum_{j,\sigma,\sigma'} n_{j,\sigma} n_{j+1,\sigma'}. \quad (2)$$

It is not necessarily assumed that large U corresponds to any particular material, and for the present purpose it is merely a limit in which the theoretical properties of systems can easily be related to physically meaningful variables.

The properties of the system depend upon the sign of U . When this parameter is taken to be positive, it corresponds to repulsive on-site interaction between the electrons of the opposite spin, occupying the same orbital. Thus, the electrons avoid doubly occupied sites and in the ground state all sites are either singly occupied or empty. However, the direct Coulomb repulsion may be reduced, and the indirect interaction can lead to the attraction $U < 0$. It is instructive here to schematically present the possible orderings in the one-dimensional (1D) electron gas of a single chain [21].

2.1.1. On-site attraction, $U < 0$

The electrons of opposite spin form pairs, to take advantage of the on-site attraction. The molecular sites are either doubly occupied or empty (Fig. 2(a), (b)). The ground state is highly degenerate because the energy does not depend upon which of the sites are occupied, since there is no interaction between the sites for both t and V are equal to zero, Fig. 2(a). The CDW states occur in an extreme form when there is a finite inter-site repulsion $V > 0$ but still no hopping t , i.e. $t = 0$, as shown in Fig. 2(b) for the half-filled band. To minimize the energy, the pairs are then equally spaced. Along the chains the charge density varies periodically from 1 to 0 in the inter-site distance, so the wave vector is just $2k_F$. This is a possible ground state because the system is classical when $t = 0$. More realistically, when $t \neq 0$ (not shown), the picture is not so static and the modulation amplitude of the charge density is much smaller. Also, the density

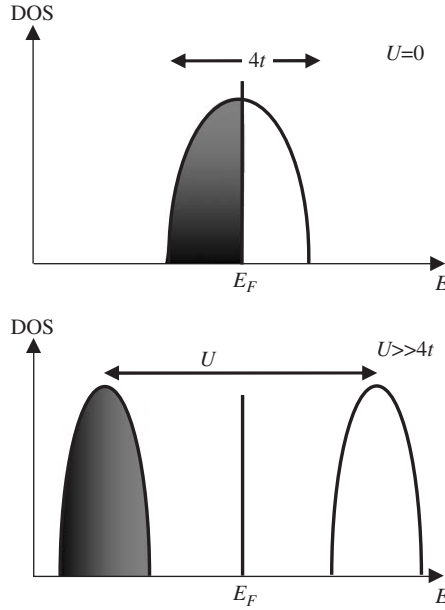


Fig. 1. The electronic density of states (DOS) in a material varies as a function of the on-site Coulomb interaction U . Upper panel: For the case of entirely independent electrons ($4t$: the bandwidth, $U = 0$) and half filling, the Fermi level E_F is located in the middle of the band. Lower panel: For the case $U \gg 4t$, the band is split into a lower and an upper Hubbard band, separated by the Mott–Hubbard gap, which can be measured by photoemission or optical spectroscopy, for instance. While in the former case the system is metallic, in the latter case it is insulating.

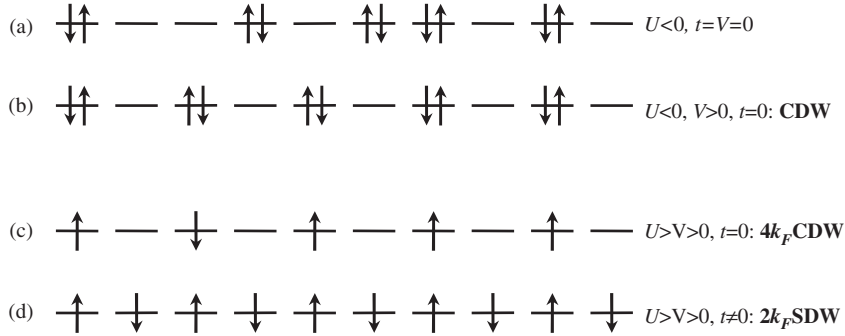


Fig. 2. Different configurations of electrons, spin up (\uparrow), or spin down (\downarrow) on a separated chain when a strong on-site interaction U is present, as suggested by Emery [21].

modulation may be incommensurate with the inter-site distance: in this case, the electrons cannot be distributed so neatly amongst the sites. Nevertheless, the wave vector $2k_F$ always characterizes the periodicity of the CDW. For the case of inter-site attraction, $V < 0$ (not shown), singlet superconductivity can arise when hopping, t , is included. The electron pairs are bosons, bound in a singlet state, and it is possible that they become superfluid (and hence superconducting since they are charged) at low enough temperatures. Triplet superconductivity with parallel spins will not occur because the electrons are bound into singlet pairs before long-range triplet correlations can build up.

2.1.2. On-site repulsion, $U > 0$

Anderson [22] first pointed out that in the strongly repulsive case, $U > 0$, and $U \gg t$, for the half-filled band, when all sites are singly occupied, the Hubbard model can be mapped onto a spin-1/2 Heisenberg chain, with charges (carrying spins) Mott-localized, one on each site. Virtual hopping produces an effective antiferromagnetic exchange interaction $J = (4t^2/U) > 0$, which acts between the neighboring spins. Such an antiferromagnetic insulator is described by a

simple t – J Hamiltonian:

$$H = -t \sum_{j,\sigma} (c_{j,\sigma}^\dagger c_{j+1,\sigma} + \text{h.c.}) + J \sum_j \mathbf{S}_j \cdot \mathbf{S}_{j+1}. \quad (3)$$

The first term describes the hopping as already known from Eq. (1). In the second, new term \mathbf{S}_j are spin-1/2 operators for fermions, where interaction characterized by J is restricted between the nearest neighbor spins. Emery [19] analyzed the Heisenberg chain with inter-site interaction included. The essential point of his work was the derivation of electronic correlation functions, which are used to discuss long range order in the ground state. The ground state here exhibits a modulation of the spin density, which is illustrated in Fig. 2(d). It may be understood as a $2k_F$ spin-density wave (SDW) instability, clearly visualized for this case where only the spin degrees of freedom have to be considered. For weaker coupling and a different number of electrons per site, the situation is more dynamic, but the wave vector is still $2k_F$. CDW states can occur again in an extreme form when there is an inter-site repulsion $V > 0$, but zero hopping. In contrast to the $U < 0$ case, however, single electrons rather than pairs are equally spaced so the period of the CDW is halved and its wave vector is $4k_F$. This is the so-called $4k_F$ CDW or Wigner crystal in 1D. Often it is called charge ordering to distinguish it from $2k_F$ CDW. The stabilization of $4k_F$ CDW can be surely taken as a signature of strong Coulomb interactions. This case is shown in Fig. 2(c) for a quarter-filled band.

For non-zero hopping, numerical calculations have shown that, different density waves are possible: in addition to both the $2k_F$ and $4k_F$ CDW, also $2k_F$ and $4k_F$ bond-density waves (BOW) can be stabilized. While the coexistence of some of these phases is possible for the quarter-filled band [23], only an excluding competition is found among $2k_F$ SDW, CDW and BOW for the half-filled band [24]. It is noteworthy that the $4k_F$ CDW may also be generated in the *g*-ology picture for a quarter-filled band by strong interactions [25,26].

Finally, we want to point out that in the quasi-one-dimensional materials structural instabilities are driven by $2k_F$ and $4k_F$ electronic instabilities [27,28]. Variations in t , U and V parameters produced by lattice distortions lead to modifications of phonon dispersion relation, which depend on electronic polarizabilities [29]. In particular, the electron–phonon induced modulation of the site energy yields the charge modulation on sites, i.e. CDW, whereas the modulation of the overlap integral between adjacent sites yields a BOW [24,30]. Notice that while the intra-site electron–phonon coupling plays the key role for CDW, it is the inter-site coupling which is pertinent for BOW. In this regard, the reported purely electronic $2k_F$ CDW [31,32] is probably also accompanied by intramolecular distortions; however, this assumption is still waiting to be confirmed experimentally.

The extended Hubbard model is widely utilized to describe the electronic structure and related physical properties of strongly correlated electron systems. The above considerations show that ordering effects of different nature occur in the strong coupling limit.

2.2. Strong coupling limit for cuprates

For the hole gas in the cuprates the Coulomb repulsion U has an important effect on the electronic properties. The strong correlation viewpoint was put forward by Anderson [33] who revived his original treatment of magnetic insulators [22]. He proposed a two-dimensional (2D) single-band Hubbard model as the simplest model to describe the high-temperature superconductivity pointing out that all the action takes place in the CuO_2 plane. Generally, the electron Hamiltonian of the layered cuprate systems could also incorporate terms related to the copper $\text{Cu}3d_{x^2-y^2}$ and to the oxygen $\text{O}2p_x$ and $\text{O}2p_y$ orbitals, oriented within the CuO_2 plane. Various extensions have been suggested [16,34], of which we choose the Zhang–Rice model as the most instructive for the quasi-one-dimensional cuprate ladders [35]. This approach seems appropriate since in the ladders, these orbitals also form the CuO_4 square (Fig. 3). Zhang and Rice (ZR) [35] used Anderson’s original methods and derived explicitly a single-band effective Hamiltonian. They assumed that doping creates holes primarily on oxygen sites, i.e. the Cu–O hybridization strongly binds a hole on each square of O atoms to the central Cu^{2+} ion to form a local singlet, which can then move through the lattice of Cu^{2+} ions in a way similar to a hole in the single-band effective Hamiltonian of the strongly interacting Hubbard model.

The initial assumption of ZR was that the oxygen orbitals $2p_x$ and $2p_y$ are equal in energy, thus they started from a model given by

$$H = \varepsilon_d \sum_{j,\sigma} d_{j,\sigma}^\dagger d_{j,\sigma} + \varepsilon_p \sum_{l,\sigma} p_{l,\sigma}^\dagger p_{l,\sigma} + U \sum_j n_{j,\uparrow} n_{j,\downarrow} + t_0 \sum_{j,\sigma} \sum_{l \in j} (d_{j,\sigma}^\dagger p_{l,\sigma} + \text{h.c.}). \quad (4)$$

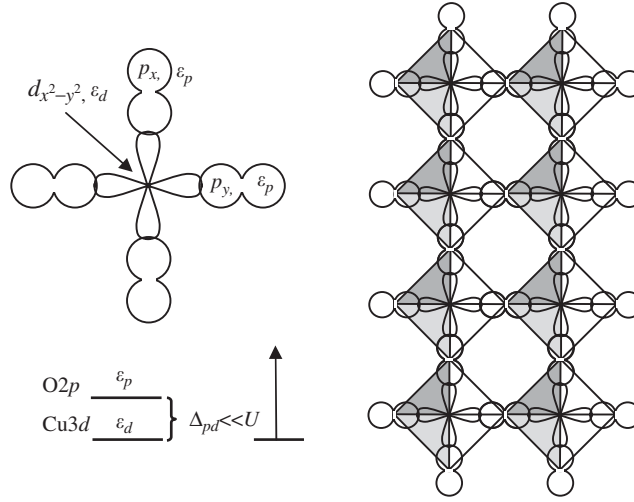


Fig. 3. Schematic diagram of the hybridization of the O hole ($2p^5$) and $\text{Cu}3d^9$ hole within the CuO_4 square. At the oxygen sites only one of the two orbitals (p_x or p_y) is shown. The splitting of the energy levels is denoted on the lower left side. On the right, the squares assembled into a ladder structure are shown.

In the first two terms ε_d and ε_p are the energy levels of holes at copper sites j and oxygen sites l , respectively. The filled $\text{Cu}3d^{10}$ and $\text{O}2p^6$ states define the vacuum energy. The operator $d_{j,\sigma}^\dagger$ creates a hole in the $\text{Cu}3d_{x^2-y^2}$ orbital and the operator $p_{l,\sigma}^\dagger$ one in the $\text{O}2p_x$ ($2p_y$) orbitals. The third term denotes the Coulomb repulsion at the copper sites. The hybridization is described by the last term. The amplitude t_0 of the wave-function overlap between Cu and O orbitals is independent of the specific cuprate lattice geometry. The sign of t_0 alternates depending on the phases of the p_x (p_y) and $d_{x^2-y^2}$ wave functions, and also on the specific lattice geometry (exact expressions can be found in Ref. [35]). At exactly half-filling and for $t_0 = 0$, each Cu site is occupied by a single $\text{Cu}3d^9$ hole due to the strong on-site Coulomb repulsion represented by the third term, and consequently all the O sites are empty ($2p^6$) in the hole representation.

If the hybridization t_0 is finite but small (as it is commonly the case in cuprates), the virtual hopping processes involving the doubly occupied Cu-hole states produce an antiferromagnetic (AF) superexchange interaction between the neighboring $\text{Cu}3d^9$ holes. The Hamiltonian given by Eq. (4) is reduced to the spin-1/2 Heisenberg model on the lattice of a single type, i.e. of Cu sites. (To some extent, this is analogous to a reduction of a single-band Hubbard model to a t - J model, mentioned in Section 2.1.)

$$H_S = J \sum_{i,j} \mathbf{S}_i \mathbf{S}_j, \quad J = \frac{4t_0^4}{\Delta_{pd}^2 U} + \frac{4t_0^4}{2\Delta_{pd}^3}. \quad (5)$$

In Eq. (5) $\mathbf{S}_{i,j}$ are spin-1/2 operators of $\text{Cu}3d^9$ holes, with the interaction between the nearest neighbor spins, U is the Coulomb repulsion at copper sites and $\Delta_{pd} = \varepsilon_p - \varepsilon_d$ denotes the energy difference between the $\text{O}2p$ and $\text{Cu}3d$ states (see Fig. 3). In fact, this model was developed following Anderson [22] and is consistent with the fact that the undoped La_2CuO_4 parent compound of the layered superconducting cuprates is an antiferromagnetic insulator [36,37].

If the system is doped, the physical situation strongly depends on the energy splitting Δ_{pd} and wave-function overlap t_0 between Cu and O orbitals. Also the ratio between the on-site (within the copper orbital) repulsive interaction U and Δ_{pd} determines the picture. In the typical cuprate systems, U and Δ_{pd} are much larger than t_0 . Upon doping holes into the crystal, the charge is transferred into the cuprate lattice and located either at the $\text{Cu}3d^9$ sites (rendering $3d^8$ configuration) if $U < \Delta_{pd}$, or at the oxygen orbitals if $U > \Delta_{pd}$. In the first case (Hubbard limit), the O sites are not relevant and can be eliminated from the picture: the effective Hamiltonian describes the hole motion on Cu sites alone [38]. In the opposite case $U > \Delta_{pd}$ (charge-transfer limit), which ZR have taken as a more relevant for the cuprate layer on the basis of the theoretical work by Zaanen et al. [39] and results by Kelly et al. [40] and Tokura et al. [41], it is energetically favorable to have the doped holes located in oxygen orbitals $2p^6$ surrounding the Cu site, and form a singlet state (ZR singlet) with the $\text{Cu}3d^9$ hole in the copper orbital.

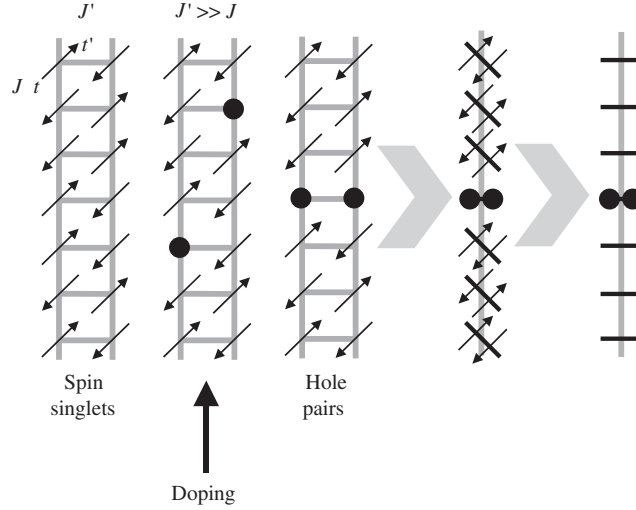


Fig. 4. Schematic description of the t - J - t' - J' model of a spin-ladder. Hopping and coupling along the legs, and along the rungs of the ladders are denoted by t and J , and by t' and J' , respectively. The arrows indicate sites occupied by spin $1/2$, while the full dots denote doped holes, which carry no spin due to formation of singlets with $\text{Cu}3d^9$ holes.

ZR have shown that in this case the Hamiltonian (H_{eff}) is just the effective t - J Hamiltonian of the single-band Hubbard model (as in Eq. (3)) in the large- U limit, but considering only the $\text{Cu}3d^9$ holes

$$H_{\text{eff}} = \sum_{i \neq j, \sigma} t_{ij} (1 - n_{i, -\sigma}) d_{i, \sigma}^{\dagger} d_{j, \sigma} (1 - n_{j, -\sigma}) + J \sum_{i, j} \mathbf{S}_i \cdot \mathbf{S}_j. \quad (6)$$

The operator $d_{i, \sigma}^{\dagger}$ creates a hole of spin σ on Cu-site i . The projection operator $(1 - n_{i, -\sigma})$ means that hopping is possible only between sites occupied by one and by two holes. There are no hoppings between a doubly occupied site and an empty site, or between two singly occupied sites, as would occur in the full Hubbard Hamiltonian. Note that the singly occupied site carries a spin $1/2$, while for the doubly occupied site (no spin) a ZR singlet is formed. The number of double occupancies, that is, the number of doped holes (taking the system away from the half-filling), is conserved. The second term describes the magnetic interaction between the singly occupied sites.

2.3. t - J model for two-leg ladders

There is a general consensus that the strong electronic correlations are the driving force behind the complex phase diagram of cuprates. As noted above, the simplest model which captures strong correlations is the Hubbard model in its strong coupling limit: the t - J model. The model of two-leg ladders by Dagotto et al. [6,7,42], schematically presented in Fig. 4, consists of two chains each described by the t - J model. In addition, the two adjacent chains are coupled by t' - J' interaction. This t - J - t' - J' model considers hopping/coupling along the legs, t/J , and along rungs of ladders t'/J' in the following way:

$$H = J \sum_{i, \lambda = -1, 1} \mathbf{S}_{i, \lambda} \cdot \mathbf{S}_{i+1, \lambda} + J' \sum_i \mathbf{S}_{i, 1} \cdot \mathbf{S}_{i, -1} - t \sum_{i, \sigma, \lambda = -1, 1} (c_{i, \lambda, \sigma}^{\dagger} c_{i+1, \lambda, \sigma} + \text{h.c.}) - t' \sum_{i, \sigma} (c_{i, 1, \sigma}^{\dagger} c_{i, -1, \sigma} + \text{h.c.}). \quad (7)$$

The $c_{i, \lambda, \sigma}^{\dagger}$ operator is defined as a creation operator for a hole with spin σ on a given site i along the chains, that is, the legs of ladders. Physically, this site refers to a CuO_4 square, as demonstrated for the cuprate layer in Section 2.2. The index $\lambda = -1, 1$ denotes sites on the same rung, at one or at the other leg of the ladder. It is noteworthy that an approximation has been made in going from Eqs. (6) to (7), in that the projection operators have been removed,

although the same hopping paths are allowed (and forbidden) in both models. In the large J' limit, at half filling, the ground state consists of a set of spin singlets in each rung of the ladder. To flip a spin costs energy, hence there is a spin gap in the excitation spectrum which is of the order of J' ; it corresponds to the creation of a spin triplet in one of the rungs. The prediction of a gapped spin-liquid ground state was experimentally confirmed for the quasi-1D cuprate ladder materials, as shown in Sections 3.3.2 and 5.1. If the ladder system is now doped by holes, we find that at low hole concentration and in the limit $J' \gg J$ the system prefers to combine two holes in the same rung, in order to lower the energy.⁴ Otherwise, the two holes have to break two singlets, which produces a substantial energy cost. Therefore, each added pair of holes forms a bound state in a given rung (Fig. 4).

The final important step is to recognize that a subspace of rung singlets may be mapped onto a linear chain, as shown in Fig. 4. This means that each rung corresponds to a single site of the resulting chain. The sites in this chain are either doubly occupied (mapped from the bound holes on the rung) or empty (mapped from the two spins which form a rung singlet). In this subspace the effective on-site interaction $|U_{\text{eff}}|$ is similar to J' , and $U_{\text{eff}} < 0$, which implies that U_{eff} is attractive. There is some important analogy of this model with the Hubbard model for a linear chain (see Section 2.1.1 and Fig. 2). The attractive Hubbard model exhibits superconducting or CDW correlations. Indeed, Dagotto et al. [6] have discussed the ladder model away from half-filling (i.e. hole-doped ladders) and argued that this model predicts superconducting or CDW ground states, but under the unrealistic condition $J' > t'$. In particular, their numerical calculations show that the spin gap and pairing correlations exist for $t'/t = 0.1$ and $J' \leq J$. It is not evident that the picture of pairing on the same rung should be valid for arbitrary J' and t' . Indeed, Noack et al. [44] examined the ground state properties of a Hubbard model on a hole-doped ladder (close to half-filling) for $t = 1$ and $U = 8$ (strong coupling limit). They have shown that while the spin gap exists at half-filling for a broad range of t' and U , in the doped system the spin-gap and pairing correlations develop only for a restricted range of parameters (t' values between 0.5 and 1.7). In addition, both the spin gap and pairing correlations become negligibly small for small t' . They have also shown that the pairing in the spin liquid is strongest across the rung, while it is weaker along the ladder legs. Finally, it has to be noted that since $J' \approx 0.07$ eV [45] and $t \approx 0.5$ eV [46] are found for $\text{Sr}_{41}\text{Cu}_{24}\text{O}_{41}$, a weak coupling *g*-ology model may also be considered to describe the ordering in the ladders. The balance between superconductivity and CDW, and the question which ground state actually dominates, depends on the parameters of the model and more generally on the residual interactions between hole pairs; all of which is hard to predict theoretically [6,21,47].

3. Materials and structure

The observed phenomena can only be described and eventually understood if the structure of the crystals is well known, including the relevant interactions. In the case of the spin-ladder and spin-chain compounds $(\text{La}, \text{Y}, \text{Sr}, \text{Ca})_{14}\text{Cu}_{24}\text{O}_{41}$ the crystal structure is extremely complicated and two interacting and incommensurate subsystems have to be taken into considerations. Thus a thorough knowledge of the crystallographic structure is required for any further considerations of the electronic structure. The interaction of chains and ladders, in particular the distribution of the electronic charge, turns out to be of crucial importance for the understanding of the rich phase diagram of these systems.

3.1. Crystallographic structure of quasi-one-dimensional cuprates $(\text{La}, \text{Y}, \text{Sr}, \text{Ca})_{14}\text{Cu}_{24}\text{O}_{41}$

Copper and oxygen form the functional units which are assembled in the particular structure of the quasi-one-dimensional cuprates. Since the Cu ions are coordinated to four oxygen ions, CuO_4 squares serve as the basic building block. It should be pointed out that the CuO_4 square is only an approximation, because in the real materials this unit is slightly distorted into tetragon or even in flattened tetrahedron. For simplicity, we will refer to this building block as a square throughout this article.

As depicted in Fig. 5, the composite material $\text{Sr}_{14}\text{Cu}_{24}\text{O}_{41}$ consists of two different substructures: CuO_2 chains and Cu_2O_3 two-leg ladders [48,49]. Chains may be regarded as strings of edge-sharing CuO_4 squares. The two-leg ladders are arranged from two zig-zag chains composed of edge-sharing CuO_4 squares which are rotated by 45° with respect to the squares in the CuO_2 chains; the zig-zag chains have mirror image symmetry and touch at the corners of

⁴ Creating a hole (by doping) on a given site effectively creates Cu^{3+} , spin $S = 0$ ion, which Dagotto et al. in Ref. [42] compared to a ZR singlet, although the latter is a free quasi-particle.

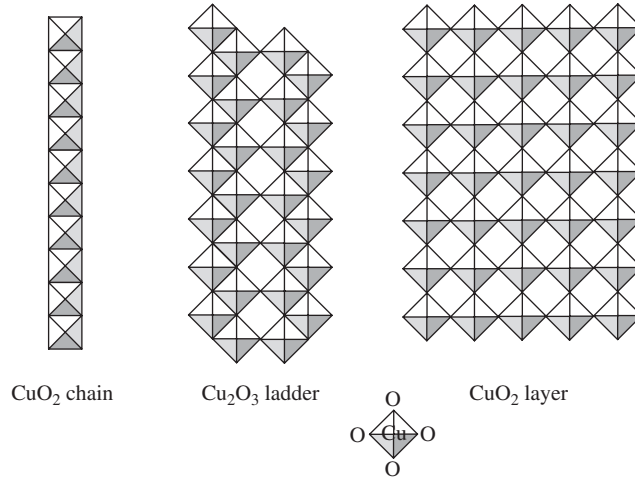


Fig. 5. Crystal structure of (La,Y,Sr,Ca)₁₄Cu₂₄O₄₁ cuprates (left and middle) and of high-temperature superconducting cuprates (right). The basic building block is a CuO₄ square. Corner- and/or edge-sharing arrangements of these squares produce substructures like chains, ladders and layers.

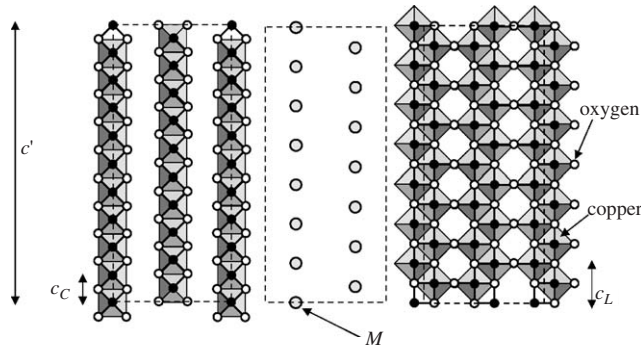


Fig. 6. CuO₂ chain layer (left), layer of strings of $M = \text{La, Y, Sr, Ca}$ atoms (middle) and Cu₂O₃ ladder layer (right). The periodicity of the chains and the ladders $\alpha = c_C/c_L = 1/\sqrt{2}$ is not commensurate, but close to 7/10.

CuO₄ squares. Neighboring ladders are offset by $c_L/2$ (see Fig. 6). Thus the so-formed ladders consist of both corner and edge-sharing squares. For comparison, the CuO₂ layer formed in high-temperature superconducting cuprates, also shown in Fig. 5, is formed by solely corner-sharing (oxygen sharing) CuO₄ squares.

Fig. 6 exhibits the arrangement of chain and ladder layers [49]. Strings of M atoms ($M = \text{Sr, Ca, La, Y}$) are intercalated between these layers. Strictly speaking, these atoms are coordinated to the ladder layer. They enter in the void opened between the zig-zag chains. Thus, M strings and the ladder layer constitute the ladder subsystem ($M_2\text{Cu}_2\text{O}_3$), while solely the CuO₂ chains arranged in a parallel layer form the chain subsystem (CuO₂). Both of these two sublattices have orthorhombic symmetry. For Sr₁₄Cu₂₄O₄₁, the lattice parameters are: $a = 11.469 \text{ \AA}$, $b = 13.368 \text{ \AA}$, along the c -direction the unit cell for the ladders is $c_L = 3.931 \text{ \AA}$ and for the chains $c_C = 2.749 \text{ \AA}$. If the CuO₄ squares were ideal, there would always be a $\alpha = c_C/c_L = 1 : \sqrt{2}$ incommensurability between the chain and ladder subsystems, that is simply the ratio of the side to the diagonal of a square. The distance between two copper atoms in the chains corresponds to the side of the CuO₄ square; its diagonal gives the distance between two Cu ions in the ladders. Therefore, the chemical formula taking this structural feature into account reads (Sr₂Cu₂O₃) _{α} (CuO₂). The first publications approximated $\alpha \approx 5/7$ [50] and $\alpha \approx 7/10$ [48,49], meaning Sr₁₀Cu₁₇O₂₉ and Sr₁₄Cu₂₄O₄₁, respectively. The subsequent literature uses $\alpha \approx 7/10$ as better choice. In the real quasi-one-dimensional cuprate materials the squares are more or less distorted, nevertheless chain and ladder subsystems are still incommensurate. The distortions, however, which are related to the

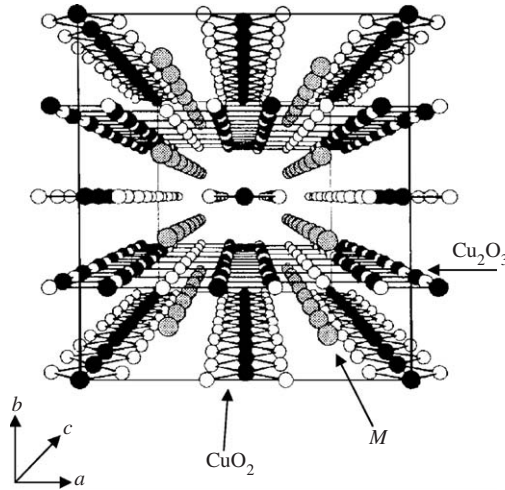


Fig. 7. A three-dimensional drawing of the $(\text{La,Y,Sr,Ca})_{14}\text{Cu}_{24}\text{O}_{41}$ approximate super-structure cell, consisting of four formula units, viewed along the c -axis. The CuO_2 layers, the strings of M (Sr, Ca, La, Y) atoms, and the Cu_2O_3 layers are placed in the crystallographic ac plane, aligned along the c -direction and stack in alternating manner along the b -axis. The composition of strings primarily dictates the superstructural cell parameter in b -direction. After Ref. [49].

incommensurability, lead to additional modulations of the crystallographic positions, i.e. each subsystem is weakly modulated to adjust to the other. These effects may be regarded as an intrinsic source of disorder [51,52].

The structure of the incommensurate composite determined by the conventional X-ray diffraction method is the average structure in which the two subsystems are very close to commensurability. Due to this fact and for practical reasons, an approximate super-structure cell (Fig. 7) with the parameter $c' = 10 \cdot c_C = 7 \cdot c_L \approx 27.5 \text{ \AA}$ is commonly used, as shown in Fig. 6 [48,49]. This super-structure cell with large volume of about 4000 \AA^3 has orthorhombic symmetry, but belongs to different space groups depending on the (La,Y,Sr,Ca) content. In (Sr,Ca) compounds with low Ca content, the ladder sublattice has F-centered orthorhombic symmetry (i.e. face centered symmetry on all faces), while the chain sublattice has A-centered (i.e. face centered symmetry centered only on one face and that is the bc plane), which changes to F-centered symmetry for high Ca concentration [49]. While the a and c lattice parameters remain almost the same, the b -axis parameter depends on the (La,Y,Sr,Ca) content; i.e. the distance between the chain and ladder layers changes.

On the other hand, the modulated structure of this composite system can be taken into account by a four-dimensional description, meaning that four integers (h, k, l, m) are required to index both main and satellite reflections systematically [53,54]. The reciprocal lattice vector is $\mathbf{q} = h\mathbf{a}^* + k\mathbf{b}^* + l\mathbf{c}_C^* + m\mathbf{c}_L^*$. Choosing the CuO_2 chain subsystem as the base structure, we can thus write $\mathbf{q} = h\mathbf{a}^* + k\mathbf{b}^* + (l + am)\mathbf{c}_C^*$. Each Bragg peak can then be classified as follows: $(h, k, l, 0)$ represents the main reflections of the CuO_2 chain subsystem, $(h, k, 0, m)$ stands for the main reflections of the $M_2\text{Cu}_2\text{O}_3$ ladder subsystem, $(h, k, 0, 0)$ indicates the common reflections to the two sublattices, and indices (h, k, l, m) represent pure satellite reflections in l th order of CuO_2 subsystem and m th order of $M_2\text{Cu}_2\text{O}_3$ subsystem. The latter arise from the mutual interaction of the two subsystems, as explained previously.

3.2. Electronic structure of quasi-one-dimensional cuprates $(\text{La,Y,Sr,Ca})_{14}\text{Cu}_{24}\text{O}_{41}$

It is amazing how diverse the electronic properties are which develop from the particular arrangement of CuO_4 squares. Since the quasi-one-dimensional cuprates $(\text{La,Y,Sr,Ca})_{14}\text{Cu}_{24}\text{O}_{41}$ are among the most complex systems, we try to develop their properties step by step, starting from the simple copper–oxygen bonds, going through the ordering phenomena and finally arriving at the band structure.

3.2.1. Copper–oxygen bonds

The configuration of $\text{Cu–O } \sigma$ -bonds formed between $\text{Cu}3d$ and $\text{O}2p$ orbitals determines the cuprate structure. The copper atoms are not directly connected. Between the two nearest neighbor copper atoms, there are essentially two

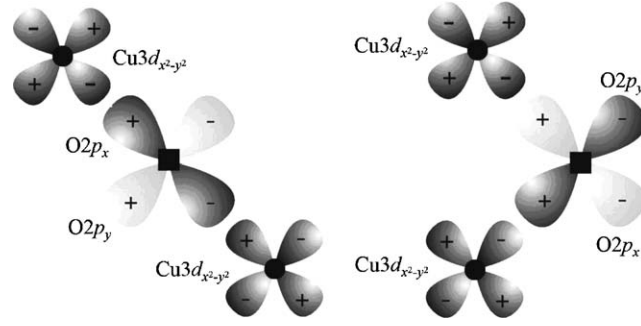


Fig. 8. Copper and oxygen orbitals relevant for Cu–O–Cu 180° (left) and 90° (right) bond configurations.

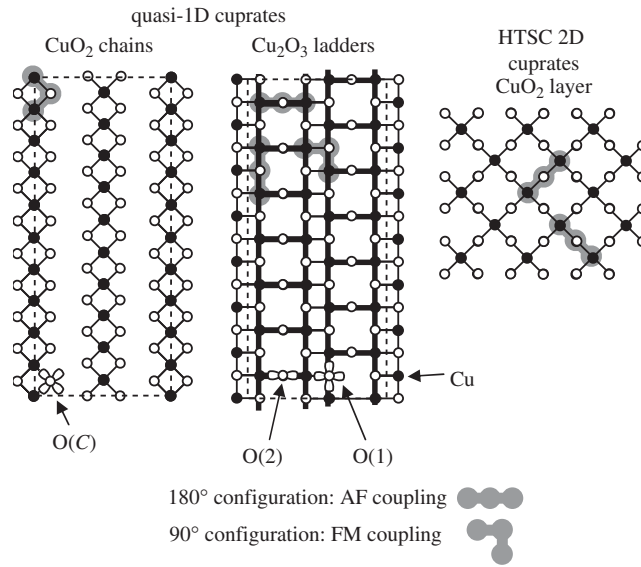


Fig. 9. Bond configurations (denoted by gray shapes) in the chains (left) and ladders (middle) of quasi-one-dimensional cuprates $(\text{La,Y,Sr,Ca})_{14}\text{Cu}_{24}\text{O}_{41}$ and in the layers (right) of two-dimensional high-temperature superconducting cuprates. In the former there are three non-equivalent oxygen sites O(C), O(1) and O(2) and five non-equivalent $\text{O}2p$ orbitals in the ac plane.

bond configurations possible, which differ in the angle between the two σ -bonds that copper atoms establish with the relevant p -orbital(s) of an oxygen: a 180° and a 90° configuration, as sketched in Fig. 8. These bond configurations are shown as solid lines which connect the atoms in Fig. 9. In high-temperature superconducting cuprates, for instance, the 180° Cu–O–Cu bond configurations are mutually orthogonal, thus forming the square lattice layer. For the chains, the $(\text{La,Y,Sr,Ca})_{14}\text{Cu}_{24}\text{O}_{41}$ compounds of interest here, on the one hand, exhibit a structure where two neighboring Cu atoms along the chain are connected via two 90° Cu–O–Cu bonds. Between the chains no Cu–O σ -bonds are present. On the other hand, in the ladders, 180° Cu–O–Cu bond configurations form legs and rungs of the ladder, while the copper atoms on the neighboring ladders are connected via 90° Cu–O–Cu bonds.

3.2.2. Magnetic structure

A copper site in the cuprate materials is characterized either by a spin $S = 1/2$ of the unpaired $3d^9$ hole of the Cu^{2+} ion or by an effective Cu^{3+} site ($3d^8$) with spin $S = 0$. The spin $S = 0$ is observed because a ZR singlet is formed as described in Section 2.2 [35]. The ZR singlet effectively decouples spin and charge degrees of freedom for a doped hole. Between the spins of the nearest neighbor Cu^{2+} ions, superexchange interaction occurs either along the σ -bond configurations (for intraladder, intrachain and interladder couplings), or through a quasi-linear Cu–O–O–Cu

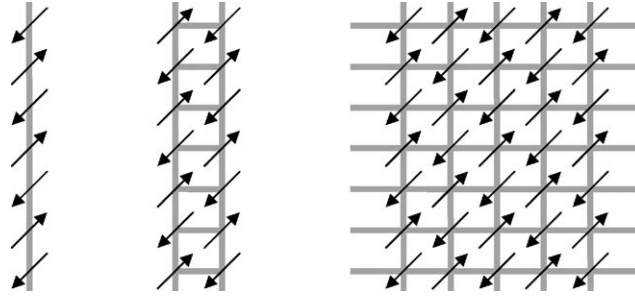


Fig. 10. The Heisenberg spin-1/2 antiferromagnetic model on chain (left), two-leg ladder (middle) and two-dimensional square lattice (right).

path (for interchain coupling). In the latter case, the coupling is weakly antiferromagnetic due to a slight overlap of the O orbitals [55]. On the other hand, the strength and the sign of the dominant coupling J , which occurs along the σ -bond configurations, considerably depends upon the angle between the Cu–O bonds [56–58]. In the case of a 180° configuration, the strong antiferromagnetic (AF) coupling between two nearest neighbor Cu^{2+} in $3d^9$ configuration with the single hole which occupies an antibonding orbital, is mediated via a single ligand (oxygen $2p$) orbital. In a 90° configuration, the character of the superexchange interaction transforms into a much weaker ferromagnetic (FM) coupling, due to the orthogonal orbitals coupled via Hund's rule [59].

The nature of the particular coupling between the Cu^{2+} spins decisively determines the magnetic structure in cuprates. In the following a short comparative overview of possible magnetic structures/ground states in undoped cuprate systems is given, in order to understand better the variety of magnetic structures found in the chains and ladders of underdoped and fully hole-doped quasi-one-dimensional cuprates $(\text{La}, \text{Y}, \text{Sr}, \text{Ca})_{14}\text{Cu}_{24}\text{O}_{41}$.

The copper oxides such as Sr_2CuO_3 and Ca_2CuO_3 contain chains of corner-sharing CuO_4 squares, in which Cu^{2+} spins are coupled by AF 180° Cu–O–Cu interaction [60,61]. They are considered as ideal examples of the spin-1/2 1D Heisenberg antiferromagnets with AF nearest neighbor coupling. In fact, a famous exact solution, found by Bethe many years ago [62], showed that the quantum fluctuations are strong enough to prevent the long-range order in such a chain and that spin–spin correlations decay slowly to zero as a power law of distance. Still, they remain dominant over finite length scales, and thus the spin-chain has a quasi-long-range order AF character (Fig. 10, left). On the other hand, the copper oxides with chains of edge-sharing CuO_4 squares, in which Cu^{2+} spins are coupled by weak FM 90° Cu–O–Cu interaction, exhibit various interesting phenomena. For example, in undoped Li_2CuO_2 an AF transition occurs at $T = 9.3$ K due to the interchain interaction which is AF, and comparable in magnitude to the FM interaction within the chains [63].

La_2CuO_4 , the insulating parent compound of high-temperature superconducting cuprates, whose characteristic structural element is a CuO_2 layer, is the best example of a planar spin-1/2 Heisenberg antiferromagnet with isotropic and predominantly nearest neighbor coupling via 180° Cu–O–Cu bond configurations [64]. In La_2CuO_4 the AF long-range order is established, in agreement with the Heisenberg spin-1/2 AF model (Fig. 10, right). This model predicts that spin–spin correlations decay to a constant but finite value as the mutual spin distance grows. This non-zero value indicates that there is a long-range order in the spin system [42].

To make the transition from the quasi-long-range order in the one-dimensional Heisenberg chain to the true long-range order that occurs in a two-dimensional layer, one can assemble chains to form ladders as depicted in the central part of Fig. 10. Apparently, the magnetic structure of ladders is somewhere between the one- and two-dimensional case. But the crossover between the one- and two-dimensional case is not smooth at all. Although in both limiting cases of one- and two-dimensional antiferromagnets there is no spin gap, theoretical investigations indicated that the Heisenberg model for two-leg ladders should show a spin gap [6]; similar arguments hold for other even-leg ladders. In general, a spin gap occurs when a finite energy is required to create a spin excitation with $S = 1$. This makes the ladder systems qualitatively different from the chains and layers. The presence of a spin gap is more or less obvious in the strong coupling limit which implies that the coupling along the rungs, J' , is stronger than the interaction along the legs of the ladder, $J' \gg J$. In this case, the ladder ground-state may be regarded as a product of spin singlets, one per rung (see Section 2.3, Fig. 4). The overall spin of the ladder in the ground-state is zero. It costs the energy J' to create a triplet on the rung by flipping one of the spins. If such excitations are created, they may propagate along the ladder,

but their correlations decay exponentially due to the finite spin gap. Since the correlations are purely short-range, this state is also referred to as a gapped spin-liquid [42].

In the simple ladder materials like SrCu_2O_3 [7,65], the intraladder couplings J and J' along legs and rungs, respectively, are produced by strong 180° Cu–O–Cu bonds, whereas the interladder coupling is arranged via a much weaker 90° Cu–O–Cu bond configuration. The value of $J = 0.16$ eV is obtained from fits to the temperature dependent spin susceptibility, when the important assumption for ladders is made: $J'/J \approx 0.5$ [66]. The absolute value of the exchange interaction J is also comparable to the value obtained for the similar 180° coupling in layers of high-temperature superconducting cuprates [64]. The ratio $J'/J \approx 0.5$ is directly confirmed by NMR measurement of spin polarization in the oxygen-ligand orbitals for the undoped ladders in $\text{La}_6\text{Ca}_8\text{Cu}_{24}\text{O}_{41}$ [67]. The FM 90° coupling between two ladders may be considered to be of the similar strength as the intrachain 90° coupling, which is two orders of magnitude smaller than the interactions J and J' within the ladder. In addition, the interladder coupling is frustrated due to a triangular arrangement of the Cu atoms (Fig. 6) between neighboring ladders, because they are offset by $c_L/2$. The theoretical considerations of Gopalan et al. [68] indicated that, due to the frustration, even if a much larger interladder coupling is assumed (only an order of magnitude smaller than J and J'), the ladder layer may be considered as a system composed of almost isolated ladders.

Finally, we mention briefly magnetic structures observed in the chains and in the ladders of quasi-one-dimensional cuprates $(\text{La}, \text{Y}, \text{Sr}, \text{Ca})_{14}\text{Cu}_{24}\text{O}_{41}$. This issue will be addressed in more detail in Sections 4 and 5. A large gap in the spin-excitation spectrum is observed in the ladders almost independently of the number of holes (see Section 3.3 for hole distribution). A finite number of holes in the ladders does not change the ratio $J'/J \approx 0.5$, at least not for $\text{Sr}_{14}\text{Cu}_{24}\text{O}_{41}$ [67]. In all cases, the intraladder couplings J , J' remain significantly larger (≈ 0.1 eV) than the interladder coupling.

In contrast to the behavior observed for the ladders, in the chains of $(\text{La}, \text{Y}, \text{Sr}, \text{Ca})_{14}\text{Cu}_{24}\text{O}_{41}$ consisting of edge-sharing CuO_4 squares the magnetic structure varies with the number of holes in the chains. For completely undoped $\text{La}_6\text{Ca}_8\text{Cu}_{24}\text{O}_{41}$ and for strongly underdoped, e.g. $\text{La}_5\text{Ca}_9\text{Cu}_{24}\text{O}_{41}$ (one hole per formula unit), the susceptibility of the chains can be described by a Curie–Weiss law. Weak intrachain ferromagnetic coupling (2 meV) and interchain antiferromagnetic coupling (3 meV) are found, together with a transition at $T \approx 10$ K, similarly as observed in the pure chain of undoped material Li_2CuO_2 [63,69,70]. For higher doping levels of $(\text{La}, \text{Y})_y(\text{Sr}, \text{Ca})_{14-y}\text{Cu}_{24}\text{O}_{41}$ (in the intermediate range of four and five holes per formula unit), the coupling strength remains weak, but AF dimers start to assemble (see Section 4.2.1). In the fully doped materials $\text{Sr}_{14-x}\text{Ca}_x\text{Cu}_{24}\text{O}_{41}$ (total number of holes 6, which mostly reside in chains; for details see Sections 3.3 and 4.1) a long-range AF dimer structure is eventually formed in the chains, with the intradimer coupling being an order of magnitude stronger ($J_D \approx 11$ meV) than the coupling within the chains of underdoped materials (which is the 90° Cu–O–Cu coupling). The FM coupling between these dimers is about an order of magnitude weaker (1 meV) and thus comparable with the AF interchain coupling [55,71]. Due to the formation of AF dimers, the chains in the fully doped materials exhibit a spin gap (but only at low temperatures, see Section 4.1), which is distinctively different from the one found in the chains of the underdoped material. Kato et al. [72] studied in detail the crossover of the magnetic structure when going from underdoped to fully doped systems.

3.2.3. Band structure of $\text{Sr}_{14}\text{Cu}_{24}\text{O}_{41}$: theory and experiment

The electronic structure of the parent compound $\text{Sr}_{14}\text{Cu}_{24}\text{O}_{41}$ was calculated within the local-density approximation [46,73]. Ab initio, linear muffin-tin-orbital calculations were performed on a small cell containing one formula unit of $\text{Sr}_{14}\text{Cu}_{24}\text{O}_{41}$; the structural modulation is ignored for simplicity. However, this calculation does not consider electronic correlations, which leads to a finite DOS at the Fermi level, indicating a metallic system. This result is obviously in contradiction to the experimentally observed insulating behavior. Around the Fermi energy there exist quasi-one-dimensional bands originating from the ladder and chain subsystems. The bands can be fitted by simple quasi-one-dimensional tight-binding dispersions with nearest neighbor and next-nearest neighbor hopping energies along and between the ladders (or chains). The nearest neighbor interladder hopping energies are approximately 5–20% of the intraladder ones, which indicates the small but considerable transverse coupling.

Nevertheless, the calculated DOS for the valence band is in fairly good agreement with the results of angle-resolved photoemission spectroscopic (ARPES) study performed at 130 K along the c -axis [74]. The two peaks predicted in the total DOS, the first one at 2–3 eV and the second one at 5 eV below the Fermi energy E_F (Fig. 11, left panel), are in fact observed by ARPES at binding energies of 3 and 5.5 eV, respectively (Fig. 11, middle panel). The corresponding dispersion spectra in the reciprocal space, i.e. as a function of wave vector, are displayed in the right panel of Fig. 11. A band situated around 3 eV binding energy shows a periodicity which does not match the underlying lattice, neither

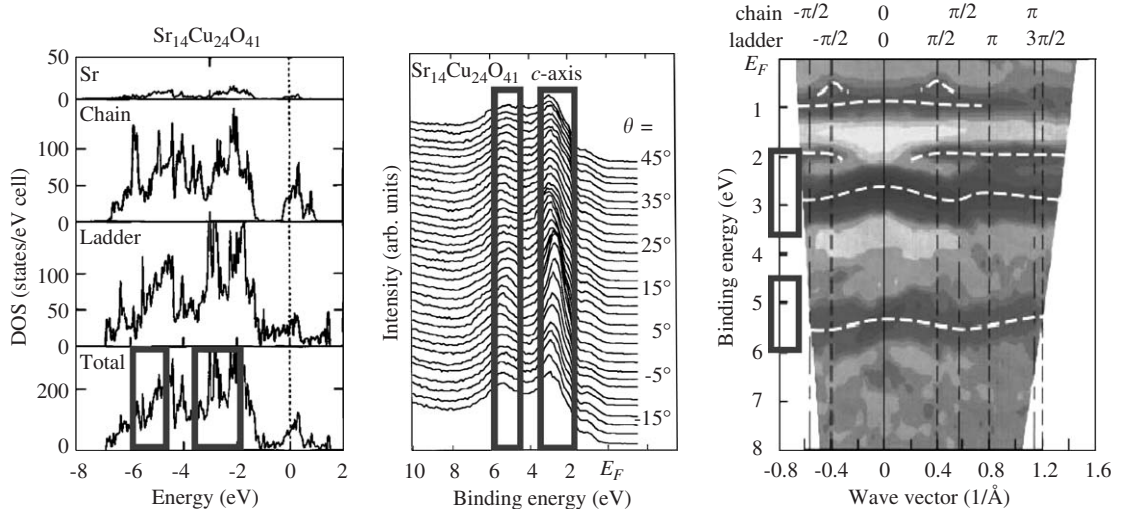


Fig. 11. Calculated (left panel) and measured (middle panel) valence band spectra for Sr₁₄Cu₂₄O₄₁ along the *c*-axis. The change of peak position with respect to the polar angle θ (middle panel) corresponds to the spectra in the reciprocal space (right panel). The dashed lines are guides to the eye, indicating energy dispersions. The boxes emphasize bands which appear both in the calculation and experiment. After Refs. [46,74].

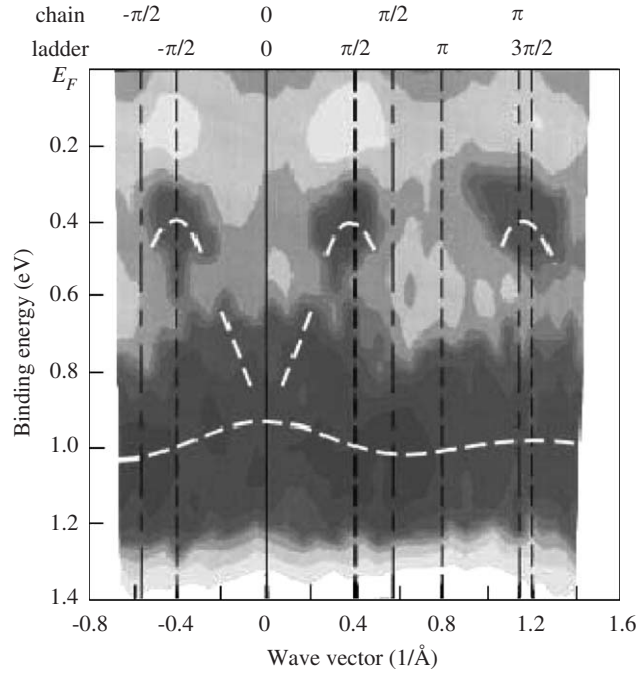


Fig. 12. Valence band structure near the Fermi level of Sr₁₄Cu₂₄O₄₁ measured by photoemission spectroscopy along the *c*-axis. The dashed lines are guides to the eye and indicate the energy dispersions. Two features are visible: a weakly dispersive band at 1 eV and a strongly dispersive band between 0.4 and 0.9 eV, which originates in ladders. After Ref. [74].

that of the ladders nor that of the chains. It might consist of more than two bands originating in both ladders and chains. In contrast, a band located at around 5.5 eV appears to match better the periodicity of the chain.

A detailed study by Takahashi et al. [74] reveals that in addition to these two bands, a band exists near the Fermi level with a remarkable dispersion of 0.5 eV, which matches well the periodicity of the ladders (Fig. 12). However, the band is folded at $q_c = (\pm\pi/2c_L)(2n + 1)$, with $n = 0, 1, 2, \dots$, without crossing E_F , indicating that a gap has opened.

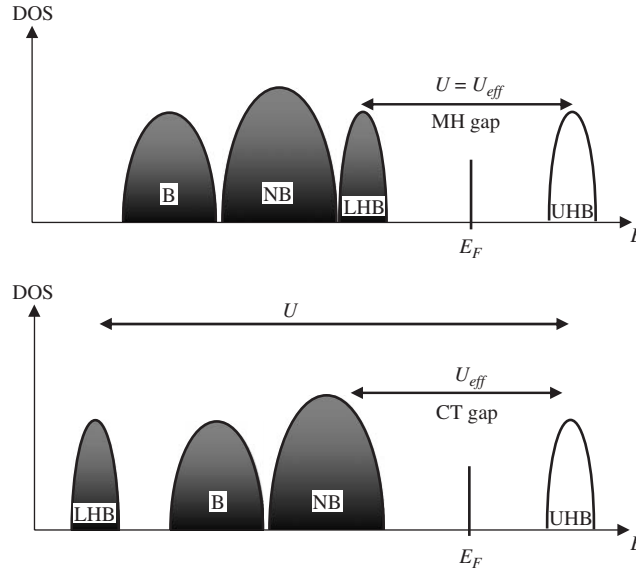


Fig. 13. Band structure for cuprates at half-filling (no doped holes) in the Mott–Hubbard limit (upper panel) and in the charge-transfer limit (lower panel). The lower Hubbard and upper Hubbard bands are indicated by LHB and UHB, the bonding and non-bonding bands by B and NB, respectively.

The authors ascribed this energy gap to a Mott–Hubbard gap associated with strong electron–electron correlations and the band at the vicinity of the Fermi level to the lower Hubbard band. However, this result can be understood equally well in the Mott–Hubbard and in the charge-transfer limit (see Section 2.2). The opening of the gap, either Mott–Hubbard or charge-transfer gap, is the effect of strong correlations (large U) on the half-filled hybridized band. This hybridized band originates from antibonding combination of Cu d - and O p -levels, although the contribution of the oxygen to the valence band is far more important in the charge-transfer case [75]. However, it is not the large Coulomb interaction U in the range of 8–10 eV that determines the gap size, as predicted in the simple Hubbard model (see Fig. 1), but an effective value U_{eff} of the order of only 2 eV [16,34,76]. In the Mott–Hubbard limit the bonding and the non-bonding bands locate below the lower Hubbard band, since U is smaller than the energy gap between copper and oxygen bands Δ_{pd} . In this case, the large U value is reduced because the Cu and O orbitals mix [33] and the lowest excitation is of Hubbard, spin-flip type, i.e. the closest band to the Fermi level (E_F) is the lower Hubbard band (Fig. 13, upper panel). In the charge-transfer limit, the fact that the energy splitting $\Delta_{pd} \approx 1$ –4 eV [76] is much smaller than U , makes the bonding and the non-bonding bands to be located right in between the lower and the upper Hubbard bands. Consequently, the gap size is also reduced to U_{eff} , but the lowest excitation is not of Hubbard type but of charge-transfer type, where no spins are involved (Fig. 13, lower panel).

Indeed, the theoretical estimate of the reduced gap size of approximately 2 eV is confirmed in the ladders of $\text{Sr}_{14-x}\text{Ca}_x\text{Cu}_{24}\text{O}_{41}$ compounds for which the optical gap of 2 eV is experimentally observed in the underdoped compound $\text{Y}_3\text{Sr}_{11}\text{Cu}_{24}\text{O}_{41}$ with no holes in the ladders (see Fig. 19) [77]. Photoemission experiments (Figs. 12, 14) detected that the top of the band which is closest to the Fermi level is situated at about 0.4 eV below E_F : an indication that holes are doped in the ladders. The existence of holes in the ladders already in the parent compound $\text{Sr}_{14}\text{Cu}_{24}\text{O}_{41}$ is therefore evident, and it implies a process of self-doping, i.e. the transfer of holes from the chains to the ladders. The issue of hole distribution will be addressed in detail in Section 3.3. Doped holes form ZR singlets and a corresponding resonance band forms at the Fermi level (Fig. 14) [78]. This band was not observed in the ladders of $\text{Sr}_{14}\text{Cu}_{24}\text{O}_{41}$ (see Fig. 12) [74]. However, in the high-temperature superconducting cuprates for doping levels of 0.05–0.07 holes per Cu site, which corresponds to the hole count in the ladders of $\text{Sr}_{14}\text{Cu}_{24}\text{O}_{41}$, a resonance band with only a weak spectral weight was identified [79]. In the case of optimal doping by 0.15 holes per Cu site, a fully developed resonance band is found.

Finally, we should note that an alternative explanation for the gap opening observed by ARPES experiments is based on charge order; however, no evidence for two-fold periodicity has been found up to now. In order to consider this

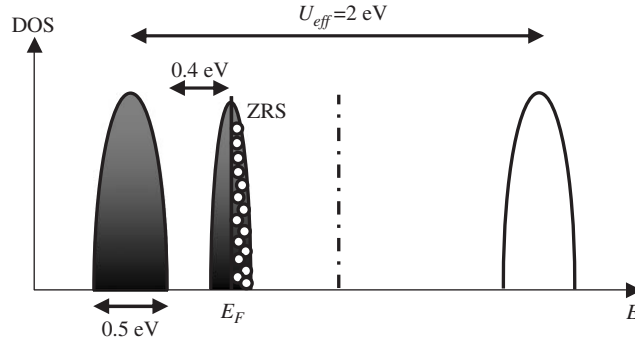


Fig. 14. Band structure for cuprates when holes (open circles) are doped into the system. The holes form ZR singlets (ZRS) and a resonance band forms at the Fermi level. In the ladders of $\text{Sr}_{14-x}\text{Ca}_x\text{Cu}_{24}\text{O}_{41}$ the gap size U_{eff} is identified by optical measurements to be 2 eV [77]. Other values are obtained by photoemission experiment. The resonance band was not observed [74].

Table 1

Different $(\text{La}, \text{Y}, \text{Sr}, \text{Ca})_{14}\text{Cu}_{24}\text{O}_{41}$ materials, which were synthesized and studied, and their nominal hole count n_h indicating the number of holes per formula unit

Nominal composition	Hole count n_h
$\text{La}_6\text{Ca}_8\text{Cu}_{24}\text{O}_{41}$	0
$\text{La}_{5.2}\text{Ca}_{8.8}\text{Cu}_{24}\text{O}_{41}$	0.8
$\text{La}_5\text{Ca}_9\text{Cu}_{24}\text{O}_{41}$	1
$\text{La}_3\text{Sr}_3\text{Ca}_8\text{Cu}_{24}\text{O}_{41}$	3
$\text{Y}_3\text{Sr}_{11}\text{Cu}_{24}\text{O}_{41}$	3
$\text{Y}_2\text{Sr}_{12}\text{Cu}_{24}\text{O}_{41}$	4
$\text{Y}_1\text{Sr}_{13}\text{Cu}_{24}\text{O}_{41}$	5
$\text{Sr}_{14}\text{Cu}_{24}\text{O}_{41}$	6
$\text{Sr}_9\text{Ca}_5\text{Cu}_{24}\text{O}_{41}$	6
$\text{Sr}_5\text{Ca}_9\text{Cu}_{24}\text{O}_{41}$	6
$\text{Sr}_{2.5}\text{Ca}_{11.5}\text{Cu}_{24}\text{O}_{41}$	6
$\text{Sr}_2\text{Ca}_{12}\text{Cu}_{24}\text{O}_{41}$	6

explanation on more serious grounds, ARPES studies of momentum-resolved gaps as a function of temperature and Ca-substitution are needed.

3.3. Hole distribution between chains and ladders in $(\text{La}, \text{Y}, \text{Sr}, \text{Ca})_{14}\text{Cu}_{24}\text{O}_{41}$

$\text{Sr}_{14-x}\text{Ca}_x\text{Cu}_{24}\text{O}_{41}$, independently of x , is intrinsically hole doped since the stoichiometry implies, for the system as a whole, an average copper valence of +2.25 : there is 1 hole per four Cu ions. These compounds (with either Sr^{2+} , or with certain isovalent substitutions of Sr^{2+} by Ca^{2+}) can be considered as fully doped and assigned $n_h = 6$ holes per formula unit. There are four formula units of $M_{14}\text{Cu}_{24}\text{O}_{41}$ per approximate super-structure cell (depicted in Fig. 7), implying a hole density of $6 \times 10^{21} \text{ cm}^{-3}$. On the other hand, $(\text{La}, \text{Y})_y(\text{Sr}, \text{Ca})_{14-y}\text{Cu}_{24}\text{O}_{41}$ materials for which the divalent Sr or Ca ions are partially substituted by trivalent La or Y ions have smaller number of holes varying in the range $0 \leq n_h \leq 5$; thus they can be considered as underdoped in comparison to the parent compound $\text{Sr}_{14}\text{Cu}_{24}\text{O}_{41}$. Various materials which were studied intensively are listed in Table 1, together with their nominal hole count.

The next important issue is the question, where exactly the holes are located in the underdoped, as well as in the fully doped materials. A fair number of investigations were dedicated to the distribution of holes in the parent system $\text{Sr}_{14}\text{Cu}_{24}\text{O}_{41}$ at room temperature and to the redistribution of holes between the chains and the ladders upon variation of temperature and Ca-substitution.

If we assume neutrality of the chains and ladders subsystems separately, the stoichiometric considerations for $\text{Sr}_{14-x}\text{Ca}_x\text{Cu}_{24}\text{O}_{41}$ indicate that all holes reside on the chains. The actual arrangement of these holes in a given subsystem is complementary to the spin arrangement as shown in Fig. 15. Calculations of the Madelung energy yield

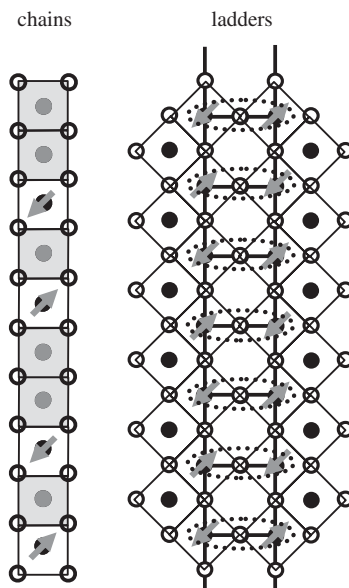


Fig. 15. The complementary arrangement of holes and spins in the chain and ladder subsystems of $\text{Sr}_{14-x}\text{Ca}_x\text{Cu}_{24}\text{O}_{41}$ based on stoichiometric considerations. Cu^{2+} ion of spin $S = 1/2$ is denoted with arrows, while the holes, which reside in the $2p$ orbitals of oxygens surrounding Cu^{2+} ions (whose spins form singlets with the spins of holes) are denoted by shaded squares.

the same conclusion for $\text{Sr}_{14}\text{Cu}_{24}\text{O}_{41}$, while the substitution of Sr by Ca leads to a hole transfer from the chains to the ladders [80]. One of the weak points of this approach is the arbitrary choice of the initial parameters for the calculation of the interaction and rearrangement in order to achieve the lowest energy state. Nevertheless, these calculations indicate the concept of self-doped holes. The distribution of holes between the chains and ladders induced by Ca-substitution is additionally supported by bond–valence sum calculations of Kato et al. [72] based on the crystallographic data for Cu–O bond lengths. Most important, the authors obtained a slight increase in the hole concentration in the ladders for $x = 6$ material in comparison to $x = 0$ material.

In the subsequent sections we will discuss experiments performed on $(\text{La}, \text{Y}, \text{Sr}, \text{Ca})_{14}\text{Cu}_{24}\text{O}_{41}$ with the aim to resolve this very important issue. As will be seen, the presented results clearly show that for the underdoped materials all holes reside in the chains [81], while for the fully doped materials, holes are distributed between chains and ladders [55,77,86,81,82,132]. In particular, in the parent compound $\text{Sr}_{14-x}\text{Ca}_x\text{Cu}_{24}\text{O}_{41}$, $x = 0$, there is already approximately one hole in the ladders (at room temperature); isovalent Ca-substitution does not change the total hole count, but causes additional transfer of holes from the chains into the ladders. However, as far as the amount of transferred holes is concerned, the experiments which have been performed up to now, give contradictory results; the reason for that has not been clarified.

3.3.1. X-ray absorption spectroscopy

The experimental technique, which can probe the hole distribution between chains and ladders most directly, is polarization-dependent near-edge X-ray absorption fine structure (NEXAFS). Measurements on single crystals of different underdoped and fully doped $(\text{La}, \text{Y}, \text{Sr}, \text{Ca})_{14}\text{Cu}_{24}\text{O}_{41}$ materials at room temperature were performed by Nücker et al. [81]. In these NEXAFS experiments, the excitation process involves highly localized $\text{O}1s$ core level. The spectral weight is related to the number of holes per unit cell. The measured absorption spectra depend on the polarization of incident radiation, because dipole selection rules reduce the coupling of the incident radiation to $\text{O}2p$ orbitals oriented likewise. In $(\text{La}, \text{Y}, \text{Sr}, \text{Ca})_{14}\text{Cu}_{24}\text{O}_{41}$ there are three non-equivalent oxygen sites associated with different Cu–O bond configurations (either 90° or 180°) and five non-equivalent $\text{O}2p$ orbitals in the ac plane (see Fig. 9), which can contribute to spectral weight in $\text{O}1s$ NEXAFS.

In Fig. 16 the room temperature NEXAFS spectra for different $(\text{La}, \text{Y}, \text{Sr}, \text{Ca})_{14}\text{Cu}_{24}\text{O}_{41}$ materials are displayed. First feature around 528 eV appears close to $\text{O}1s$ binding energy and represents therefore hole states. The spectral weight

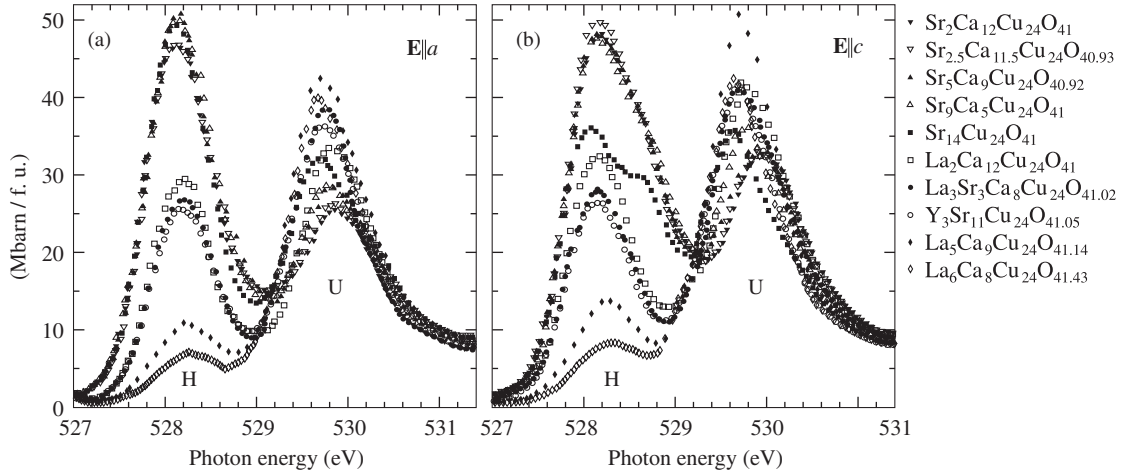


Fig. 16. Room-temperature O1s NEXAFS spectra with polarization of incident radiation oriented within the ladders and chains layers ($\mathbf{E}||a$ and $\mathbf{E}||c$ in (a) and (b), respectively) for different underdoped and fully doped $(\text{La}, \text{Y}, \text{Sr}, \text{Ca})_{14}\text{Cu}_{24}\text{O}_{41}$ materials. The features at lower energies (H) represent holes at oxygen sites, as discussed in the text. The feature at higher energies (U) is attributed to the upper Hubbard band and is not discussed here. After Ref. [81].

is the smallest for $\text{La}_6\text{Ca}_8\text{Cu}_{24}\text{O}_{41}$ and increases with Sr and Ca content indicating the increasing number of holes (see Table 1). For underdoped materials $\text{La}_3\text{Sr}_3\text{Ca}_8\text{Cu}_{24}\text{O}_{41}$ ($n_h = 3$), $\text{Y}_3\text{Sr}_{11}\text{Cu}_{24}\text{O}_{41}$ ($n_h = 3$) and $\text{La}_2\text{Ca}_{12}\text{Cu}_{24}\text{O}_{41}$ ($n_h = 4$) the hole feature has identical spectral weight for two different polarizations $\mathbf{E}||a$ and $\mathbf{E}||c$ and is almost symmetric in energy. This result evidences that in the underdoped materials all holes reside in the chains, since only in this case both polarizations measure equal projections of the same $\text{O}2p$ orbitals (associated with O(C) sites, see Fig. 9). On the other hand, for the fully doped materials $\text{Sr}_{14-x}\text{Ca}_x\text{Cu}_{24}\text{O}_{41}$ the “hole” feature is different for the $\mathbf{E}||a$ polarization compared to the $\mathbf{E}||c$ polarizations; there is a pronounced shoulder-like asymmetry at the high-energy wing for $\mathbf{E}||c$ indicating that the other $\text{O}2p$ orbitals (associated with all O sites, see Fig. 9) contribute to the absorption. This finding unambiguously shows the presence of holes in the ladders, as well.

In order to separate individual $\text{O}2p$ contributions, the authors performed least-squares fits to all measured spectra simultaneously, including both the hole feature and feature at higher energies attributed to the upper Hubbard band. In addition, two distributions (H1 and H2) were necessary to fit the hole feature properly for the fully doped systems (see Fig. 17). The basic assumption in this analysis was that for all the systems with different composition the individual (meaning O(C), O(1) and O(2)) spectral distributions are identical in shape, and that only their amplitudes and energy positions changes with composition. The appearance of the important H2 distribution in $\text{Sr}_{14}\text{Cu}_{24}\text{O}_{41}$ only for the $\mathbf{E}||c$ polarization (Fig. 17(a)) can be unambiguously attributed to holes on the O(1) ladder sites, since only $\text{O}2p$ orbitals on these sites oriented along the legs (see Fig. 9) contribute substantially to the $\mathbf{E}||c$ weight, and not to the weight in the orientation $\mathbf{E}||a$. However, for the compound $\text{Sr}_2\text{Ca}_{12}\text{Cu}_{24}\text{O}_{41}$ in addition to the hole contribution H2 for the polarization $\mathbf{E}||c$, there is a small but detectable H2 contribution for $\mathbf{E}||a$, as well, which indicates that holes contribute also to the ladder orbitals along the a -axis (see Fig. 17(b)). The number of holes and their distribution between chains and ladders as a function of Ca content is displayed in Fig. 18.

These results indicate that for the parent compound $\text{Sr}_{14}\text{Cu}_{24}\text{O}_{41}$ approximately one hole per formula unit is found in the ladders (i.e., 0.8 holes for $x = 0$), while the remaining five reside in the chains. Increasing the Ca content in $\text{Sr}_{14-x}\text{Ca}_x\text{Cu}_{24}\text{O}_{41}$ enhances only slightly the transfer of holes from the chains into the ladders (about 1.1 holes for $x = 12$). However, a notable effect happens in the distribution of holes in $\text{O}2p$ orbitals oriented along the c -axis and a -axis in both the ladders and chains. In particular, as far as the ladders are concerned, the number of holes strongly increases in $\text{O}2p$ orbitals oriented along the a -axis, while the number of holes in the orbitals oriented along the c -axis even slightly decreases.

Finally, we should mention a recent X-ray diffraction study performed on $\text{Sr}_{14}\text{Cu}_{24}\text{O}_{41}$ single crystal at room temperature by Gotoh et al. in which the structure analysis was done using centrosymmetric $(3 + 1)$ -dimensional

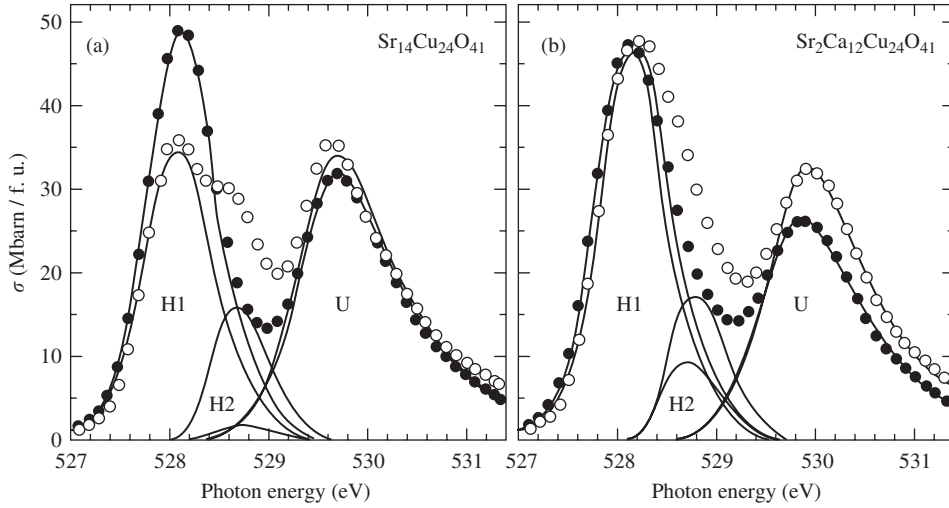


Fig. 17. NEXAFS spectra of (a) $\text{Sr}_{14}\text{Cu}_{24}\text{O}_{41}$ and (b) $\text{Sr}_2\text{Ca}_{12}\text{Cu}_{24}\text{O}_{41}$. Full and open points are for $\mathbf{E}\parallel a$ and $\mathbf{E}\parallel c$, respectively. Full lines are fits for distributions representing hole and upper Hubbard band features (see text). After Ref. [81].

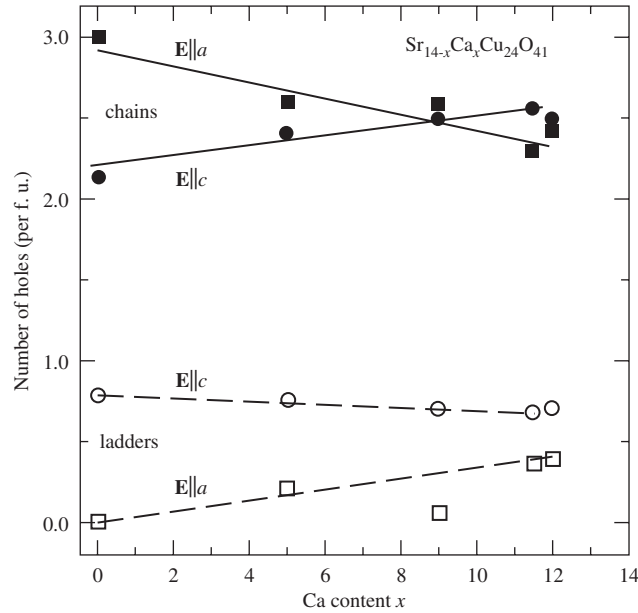


Fig. 18. Hole number per formula unit in the ladders and in the chains as a function of Ca content in $\text{Sr}_{14-x}\text{Ca}_x\text{Cu}_{24}\text{O}_{41}$ at room temperature, as obtained from NEXAFS. Contributions from $\text{O}2p$ orbitals oriented along the a - and c -axes (squares and circles, respectively) in the chain and ladder subsystems (solid and open symbols, respectively) are shown. After Ref. [81].

superspace group [82]. The bond-valence sum calculation has indicated that only 0.5 holes per formula unit reside in the ladders for the parent compound.

3.3.2. Far-infrared optical conductivity

Historically, the first evidence for a transfer of holes from the chains into the ladders with increasing Ca-substitution in the fully doped $\text{Sr}_{14-x}\text{Ca}_x\text{Cu}_{24}\text{O}_{41}$ compounds came from the optical study of Osafune et al. [77]. The room-temperature optical spectra for polarization $\mathbf{E}\parallel c$ of the fully doped $\text{Sr}_{14-x}\text{Ca}_x\text{Cu}_{24}\text{O}_{41}$ compounds ($n_h = 6$) for various

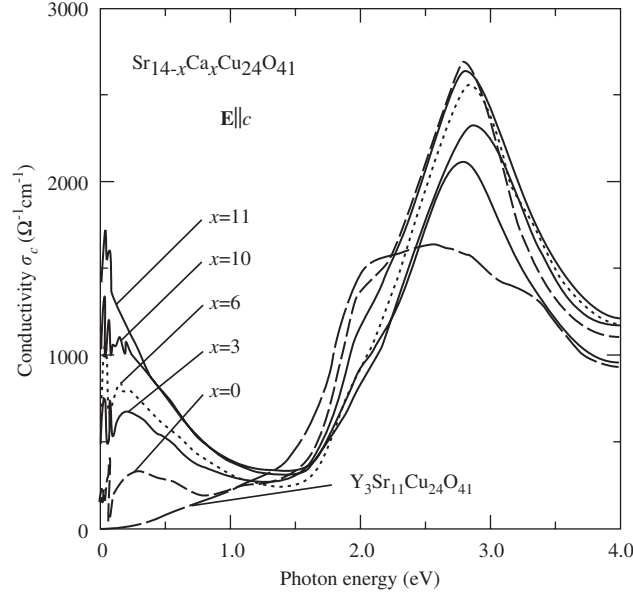


Fig. 19. Optical conductivity spectra of the fully doped $\text{Sr}_{14-x}\text{Ca}_x\text{Cu}_{24}\text{O}_{41}$ for different x recorded at room temperature for polarization $\mathbf{E} \parallel c$. In addition a spectrum of the underdoped $\text{Y}_3\text{Sr}_{11}\text{Cu}_{24}\text{O}_{41}$ is also shown. After Ref. [77].

degrees of Ca-substitution, together with a spectrum of an underdoped $\text{Y}_3\text{Sr}_{11}\text{Cu}_{24}\text{O}_{41}$ system ($n_h = 3$), are shown in Fig. 19. The spectrum of the latter compound, in which all 3 holes are located in the chains (as demonstrated by Nücker et al. [81], see previous Section 3.3.1), is characteristic for insulators with basically no spectral weight below an energy gap of 2 eV. As already discussed in Section 3.2.3, this gap can be assigned either to the Mott–Hubbard or to the charge-transfer gap. On the other hand, for the fully doped systems the conductivity at low energies (below 1 eV), is finite and increases with Ca-substitution, while the spectral weight of the peak centered at 3 eV decreases. This transfer of spectral weight is essentially the same as the transfer observed when the parent insulator of the high-temperature superconducting cuprates is doped with carriers [83]. As the substitution of isovalent Ca does not change the hole count in $\text{Sr}_{14-x}\text{Ca}_x\text{Cu}_{24}\text{O}_{41}$ materials, the observed spectral-weight transfer is attributed to a redistribution of holes between chains and ladders. The underlying assumption is the assignment of the peak centered at 3 eV to the charge excitations in the chains, while the low-energy spectral weight is attributed to excitations in the ladders. These assignments perfectly agree with the results of Nücker et al. [81] obtained by X-ray absorption spectroscopy, as well as with the calculated optical conductivity by Mizuno et al. [80].

In order to obtain the number of holes transferred to the ladder, Osafune et al. [77] calculated the effective charge density N_{eff} involved in the optical excitations by integrating the spectral weight up to energy $\hbar\omega$:

$$N_{\text{eff}}(\omega) = \frac{2m_0V}{\pi e^2} \int_0^\omega \sigma_c(\omega') d\omega'. \quad (8)$$

Here m_0 is the free electron mass and V is the volume containing one Cu atom. The resulting N_{eff} , i.e. the effective charge density per Cu site (with respect to the total number of Cu ions and the Cu ions in the ladders, respectively) for various Ca contents x , is shown in Fig. 20(a). It should be noted that two important assumptions are made to evaluate the total number of holes per Cu site. The first point concerns the cut-off energy of the integration at 1.2 eV, implying that only the spectral weight below 1.2 eV is associated with the holes in the ladders. This basically means that only the holes in the ladders are assumed to be mobile, while those in the chains are localized. Second, the charge density N_{eff} is proportional to the number δ of holes per Cu site in the ladder, that is $N_{\text{eff}} = A\delta$. The coefficient A can be determined from the known parameters for the parent compound $\text{Sr}_{14}\text{Cu}_{24}\text{O}_{41}$: $N_{\text{eff}}(1.2 \text{ eV}) = 0.1$ (see Fig. 20(a)) and $\delta = 0.07$ (since there is one hole per formula unit in which there are 14 ladder Cu sites as demonstrated by Nücker et al. [81], see previous Section 3.3.1). In this way, the number of holes δ for each Cu site on the ladder is obtained as a function of content x (Sr substituted by either Y or Ca) and plotted in Fig. 20(b).

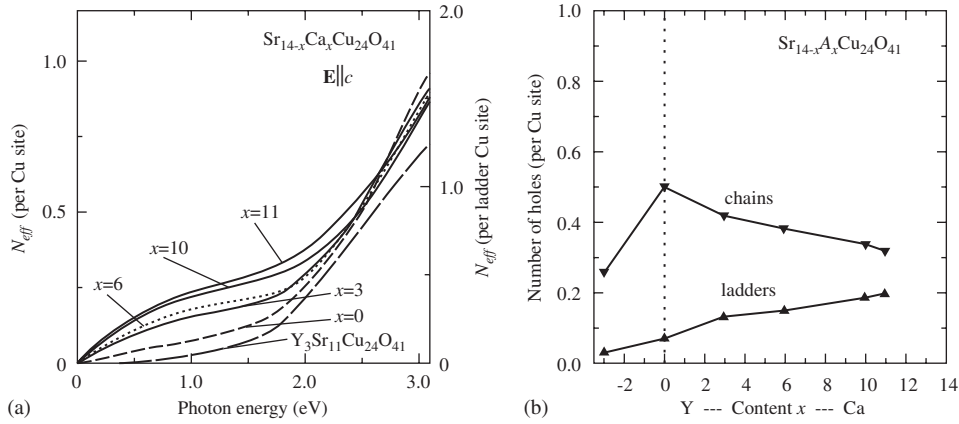


Fig. 20. (a) Effective charge density N_{eff} of $\text{Sr}_{14-x}\text{Ca}_x\text{Cu}_{24}\text{O}_{41}$ per Cu site (left-hand scale) and per Cu site in the ladders (right-hand scale) as a function of energy for various Ca contents. N_{eff} of $\text{Y}_3\text{Sr}_{11}\text{Cu}_{24}\text{O}_{41}$ is also shown. (b) The number of holes per ladder/chain Cu site, as a function of Y, Ca content. After Ref. [77].

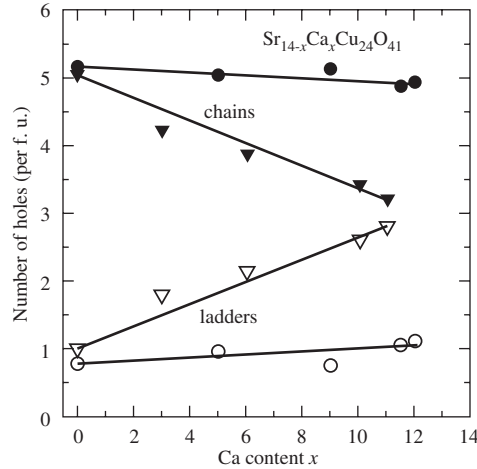


Fig. 21. Hole number per formula unit in the ladders and in the chains as a function of Ca content x in $\text{Sr}_{14-x}\text{Ca}_x\text{Cu}_{24}\text{O}_{41}$ obtained from NEXAFS (points) and optical (triangles) data.

The optical results imply a rather large hole transfer from the chains into the ladders induced by Ca-substitution, whereas NEXAFS results evidence only minor change. The results obtained using these two techniques are summarized in Fig. 21. For $x = 11$ the analysis of the optical data give 2.8 holes per formula unit in the ladders, i.e. almost half of the total hole count ($n_h = 6$), whereas NEXAFS results indicate only 1.1 holes. Therefore, while optical results indicate that Ca-substitution can be considered as doping of ladders, NEXAFS data contradict this conclusion revealing that hole redistribution between $\text{O}2p$ ladder orbitals oriented along the c - and a -axis is by far the most important effect.

The origin of this discrepancy has not been clarified yet. It might be due to the respective assumptions used in the data analysis, however as discussed by Nücker et al. [81], even then they can hardly be reconciled. Nevertheless, a few crucial points in the data analyses should be pointed out. NEXAFS reliability in determination of the absolute value of hole count suffers from changes in parameters (like hopping parameter) induced by Ca-substitution. Another, even more important problem is the uncertainty in determining the energy of the hole contribution on the rung $\text{O}(2)$ sites. There exists a possibility that it appears at the same energy as the contribution of holes on the $\text{O}(C)$ sites, and therefore that the ladder holes are counted as the chain ones. This possibility indicates that NEXAFS probably underestimates the number of holes transferred in the ladders. Nevertheless, this error cannot be so large as to account for the entire difference

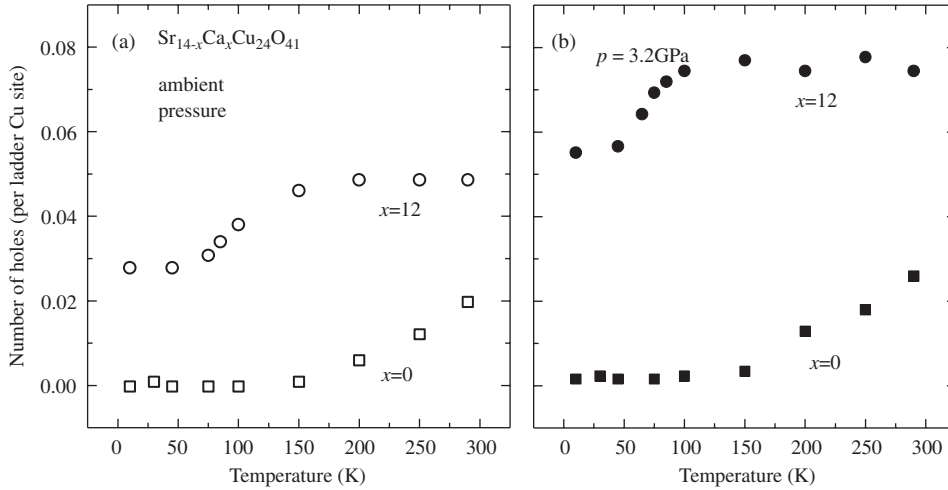


Fig. 22. The temperature dependence of the number of holes per ladder Cu site of $\text{Sr}_{14-x}\text{Ca}_x\text{Cu}_{24}\text{O}_{41}$, $x = 0$ and 12 at ambient pressure (a) and at pressure of $p = 3.2$ GPa (b). The number of holes in the ladders at low temperatures for $x = 0$ was assumed arbitrarily to be zero. After Ref. [86].

compared to the optical result. As for the analysis of the optical data, the starting assumption of a sharp cut-off energy between charge excitations in the chains and in the ladders certainly might lead to a largely overestimated number of transferred holes in the ladders. Such a possibility might become important in particular for larger Ca-concentration where the initial highly localized hole structure in the chains is destroyed (see Section 4.1). Indeed, this clearly happened in the case of the underdoped $\text{Y}_3\text{Sr}_{11}\text{Cu}_{24}\text{O}_{41}$ material, for which the applied analysis yields a small but finite number of holes in the ladders (see Fig. 20). No doubt, this result contradicts NEXAFS results for the underdoped materials, which reliably reveal that all holes reside in the chains.

3.3.3. Nuclear magnetic resonance

Nuclear magnetic resonance (NMR) and nuclear quadrupole resonance (NQR) spectroscopy measurements were also used to study the hole distribution between ladders and chains of $\text{Sr}_{14-x}\text{Ca}_x\text{Cu}_{24}\text{O}_{41}$ [86,123,132]. Magishi et al. [132] measured the ^{63}Cu nuclear spin-spin relaxation time probing the spin correlation length. The results showed that the number of holes for each Cu site on the ladder $\delta = 0.14, 0.22$ and 0.25 for $x = 6, 9$ and 11.5 , respectively, in agreement with estimates by Osafune et al. [77]. In contrast, Thurber et al. [123] who performed NMR measurements of the ^{17}O nuclear quadrupole interactions $^{17}\nu_Q$, have noticed only a minor increase of the hole number on going from $x = 0$ to $x = 8$: there is about 0.04 holes per ladder copper site (or 0.56 holes per formula unit) more in the $x = 8$ compound than in the $x = 0$ compound. Very recently, Piskunov et al. [86] reported results of a ^{63}Cu and ^{17}O NMR study of the nuclear quadrupole interaction tensor $^{17,63}\nu_{Q,\alpha}$ for different orientations of the single crystal of $\text{Sr}_{14-x}\text{Ca}_x\text{Cu}_{24}\text{O}_{41}$, $x = 0$ and 12 along $\alpha = a, b, c$ crystallographic axes. As in the work of Thurber et al., the changes of $^{17,63}\nu_{Q,\alpha}$ are related to a variation in effective hole number in the ladders. Generally, the quadrupole frequency consists of two terms: the lattice contribution and contributions coming from different ions like O(1), O(2) and Cu ladder sites (see Fig. 9). A rather large uncertainty in the determination of the lattice contribution leads to a uncertainty in the absolute determination of the hole density. On the other hand, the changes in the lattice contribution caused by a variation of the Ca-substitution, temperature and pressure are considered to be negligibly small. On this basis, Piskunov et al. for the first time provide the information on the hole distribution between the ladders and the chains not only as the function of Ca-substitution, but also as a function of temperature and pressure.⁵ As for the Ca-substitution, the obtained results are in accord with the conclusions of Nücker et al. [81]. First, these new findings demonstrate minor changes of the hole number $\delta(x = 12) - \delta(x = 0) \approx 0.03$ holes per ladder copper site (Fig. 22(a)). Second, they show

⁵ The authors pointed out that they have taken into account the small changes of the lattice contribution due to a variation of lattice parameters, using data from Ref. [150].

that for $x = 12$ the hole distribution is more two-dimensional, while for $x = 0$ the majority of holes reside on the O(1) sites [123].

Another important result concerns the temperature dependence of the hole distribution for $x = 0$, as well as for $x = 12$ (Fig. 22(a)). Already Isobe et al. [55] estimated, on the basis of bond-valence sum calculation from their neutron diffraction data, that for $x = 13.6$ almost all holes residing in the ladders at room temperature (about 0.07 holes per ladder Cu site) vanish at low temperatures. Piskunov et al. now obtain for $x = 0$ and 12 that the hole density in the ladders at low temperatures is reduced by only about 0.02 holes/ladder Cu site. Although the estimates of the amount of redistribution induced by decreasing temperature, differ, the overall tendency seems rather evident: the hole density in the ladders is reduced at low temperatures, independently of Ca content. Such a decrease can be due to a back-transfer of holes from the ladders into the chains with lowering the temperature. Previously Isobe et al. [55] suggested that the hole density in the ladders is governed by the minimum of the O(C)–Cu distance (see Fig. 9) of the modulated structure. This value expands at low temperatures in spite the fact that the average O(C)–Cu distance becomes shorter, which can in turn explain the back-transfer of holes from ladders to chains.

Also very important is the observation of an additional increase of the hole number δ for $x = 12$ under high pressure, whose amount is comparable with the effect of Ca-substitution on going from $x = 0$ to 12 (Fig. 22(b)). The number of transferred holes at room temperature mainly increases in the O(2) $2p$ orbitals oriented along the a -axis. This points to an additional increase of two-dimensionality of the hole distribution under pressure. On the other hand, the same amount of pressure applied on $x = 0$ does not change much the hole density in the ladders compared to ambient pressure, indicating that a different mechanism governs the transfer of holes from chains to ladders under pressure for low and high Ca contents. For the former case, Piskunov et al. suggested that the transfer might be related to a reduction of the b lattice parameter [150].

At the end, we would like to point out that the NEXAFS result, which evidences only a minor increase of the hole number in the ladders with Ca-substitution, is also supported by electron spin resonance [85] and by neutron diffraction data [55]. Therefore, we summarize this section by listing the most important conclusions drawn from the experiments: (a) in the underdoped materials (in which divalent Sr and/or Ca are partially substituted by trivalent La and/or Y, $n_h < 6$) all holes reside in the chains, (b) at room temperature in the fully doped material ($\text{Sr}_{14}\text{Cu}_{24}\text{O}_{41}$, $n_h = 6$) there is almost one hole per formula unit transferred in the ladders and about five in the chains, (c) Ca-substitution, that is, an increased Ca content in $\text{Sr}_{14-x}\text{Ca}_x\text{Cu}_{24}\text{O}_{41}$, induces an additional, but small, transfer of holes from the chains in the ladders, (d) decreasing temperature reduces the hole number in the ladders by transferring them partially to the chains, (e) pressure seems to induce an additional transfer of holes to the ladders, (f) Ca-substitution and pressure make the hole distribution more two-dimensional.

4. Physics of chains

The presentation of the experimental findings on the quasi-one-dimensional cuprates $(\text{La}, \text{Y}, \text{Sr}, \text{Ca})_{14}\text{Cu}_{24}\text{O}_{41}$ starts with phenomena related to the chain subsystem. In Section 5 we will proceed to the physics of the ladders. The chain subsystem is particularly important for the magnetic order. First, we consider the fully doped compounds, $\text{Sr}_{14}\text{Cu}_{24}\text{O}_{41}$ and the relatives for which Sr was partially substituted by the isovalent Ca. Section 4.2 deals with those chain compounds for which the holes were removed by La or Y doping.

4.1. Fully doped $\text{Sr}_{14-x}\text{Ca}_x\text{Cu}_{24}\text{O}_{41}$: antiferromagnetic dimer and charge order

For historical reasons, the starting point for the exploration of the spin-chain and spin-ladder systems is $\text{Sr}_{14}\text{Cu}_{24}\text{O}_{41}$ and its Ca derivatives, although by now it is known that these compounds are not the simplest to understand. We discuss in detail magnetic measurements like susceptibility, inelastic neutron diffraction, nuclear magnetic resonance and electron spin resonance; the latter ones are local probes which bear an enormous potential not fully utilized in the past. Scattering experiments give some insight into the ordering phenomena along and between the chains.

4.1.1. Magnetic susceptibility

The magnetic properties of quasi-one-dimensional (quasi-1D) cuprates were initially studied by the magnetic susceptibility measurements [43,70,87]. Although this method cannot directly distinguish between contributions of spins

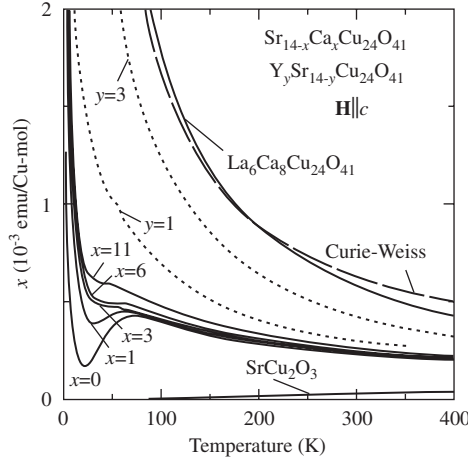


Fig. 23. Magnetic susceptibility, χ , versus temperature, of fully doped $\text{Sr}_{14-x}\text{Ca}_x\text{Cu}_{24}\text{O}_{41}$ (full lines), underdoped $\text{Y}_y\text{Sr}_{14-y}\text{Cu}_{24}\text{O}_{41}$ (dotted lines) and undoped $\text{La}_6\text{Ca}_8\text{Cu}_{24}\text{O}_{41}$ (full line). The magnetic field was oriented along the c -axis. The Curie–Weiss susceptibility of free spins occupying all chain Cu sites is denoted by the dashed line. After Ref. [43].

in the chains and those in the ladders, Carter et al. [70] argued that the susceptibility measurements primarily probe the magnetism of the chains. The conclusion is based on the assumption, that the ladder contribution should be negligibly small because it can be approximated by the susceptibility of the isostructural pure two-leg ladder compound SrCu_2O_3 that has a spin gap of about 36 meV (see Section 3.2.3) [65]. Indeed, a spin gap of similar size was detected in the ladders of quasi-1D cuprates (see Section 5).

In Fig. 23 the temperature dependence of the susceptibility $\chi(T)$, measured on single crystals of various compounds $(\text{La}, \text{Y}, \text{Sr}, \text{Ca})_{14}\text{Cu}_{24}\text{O}_{41}$ is plotted [43]. The studied materials range from undoped to fully doped systems (see Table 1, p. 29). A negligibly small susceptibility of the pure ladder compound SrCu_2O_3 is shown for comparison.

The most important result is that the susceptibility of all fully doped materials $\text{Sr}_{14-x}\text{Ca}_x\text{Cu}_{24}\text{O}_{41}$ is clearly distinct from the Curie–Weiss behavior, which describes a chain with spins occupying N_S Cu sites per formula unit

$$\chi_{\text{CW}}(T) = \frac{3}{4} N_S \frac{(g\mu_B)^2}{3k_B(T - \theta)}, \quad (9)$$

where g is g -factor, μ_B is Bohr magneton and θ is the Curie–Weiss temperature. We remind that there are 10 Cu sites in the chains per formula unit (confer Fig. 15). In contrast to fully doped, the susceptibility behavior of undoped $\text{La}_6\text{Ca}_8\text{Cu}_{24}\text{O}_{41}$ with no holes ($N_S = 10$) and of underdoped $\text{Y}_3\text{Sr}_{11}\text{Cu}_{24}\text{O}_{41}$ with three holes in the chains ($N_S = 7$) coincide perfectly well with the Curie–Weiss susceptibility given by Eq. (9) with a small Curie–Weiss temperature θ of about 10 K. The susceptibility of $\text{Y}_1\text{Sr}_{13}\text{Cu}_{24}\text{O}_{41}$ with five holes in the chains gradually deviates from the Curie–Weiss behavior below 200 K, while an additional effect arising for fully doped systems is the drop of $\chi(T)$ towards low temperatures, which is particularly pronounced for the parent compound $\text{Sr}_{14}\text{Cu}_{24}\text{O}_{41}$ below 80 K. Thus, the susceptibility data indicate that the ground state in the chains of the fully doped compounds is also characterized by a spin gap. The origin of this gap was identified by inelastic neutron scattering and nuclear magnetic resonance studies (see Sections 4.1.2 and 4.1.3).

Already prior to these investigations, a simple AF dimer model was established as a good description for the low temperature susceptibility behavior measured on both polycrystalline ceramic [70] and single crystals [87,88] of $\text{Sr}_{14}\text{Cu}_{24}\text{O}_{41}$. Once the Curie term due to paramagnetic impurities is subtracted from the measured susceptibility displayed in Fig. 23, a strong maximum at 80 K followed by an activated decrease is revealed (Fig. 24). Similar results are obtained with the magnetic field aligned along the c - and a -axes [43,87]. The AF dimer model is based on arranging the spins along the chain into isolated antiferromagnetically coupled pairs. The susceptibility is given by

$$\chi_D(T) = 2N_D \frac{(g\mu_B)^2}{k_B T [3 + \exp(J_D/k_B T)]}, \quad (10)$$

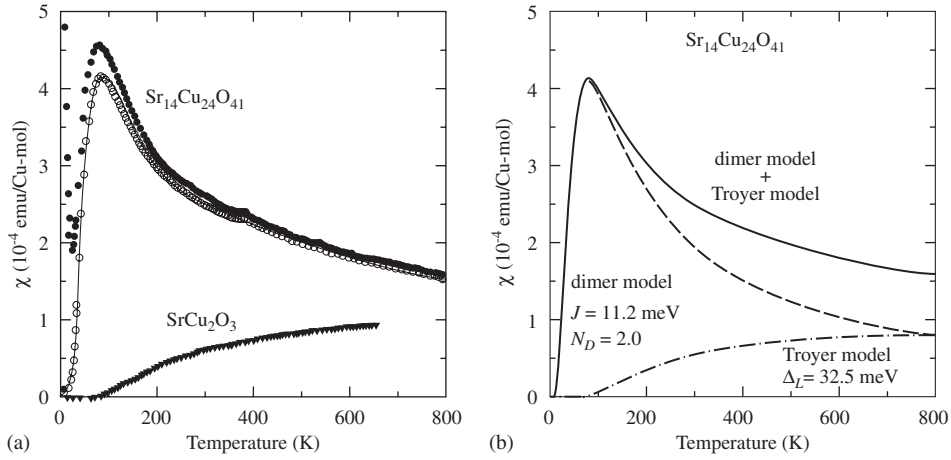


Fig. 24. (a) Experimental magnetic susceptibility of $\text{Sr}_{14}\text{Cu}_{24}\text{O}_{41}$ and the susceptibility with the Curie term due to paramagnetic impurities subtracted are shown by full and open circles, respectively. The susceptibility of the pure ladder compound SrCu_2O_3 is shown for comparison. The raw data are taken from [43,65]. (b) The susceptibility of $\text{Sr}_{14}\text{Cu}_{24}\text{O}_{41}$ (full line) is perfectly well described by two contributions: dimer term χ_D for the chains (dashed line) and Troyer term χ_T for the ladders (dash-dot line).

where N_D is the number of dimers per formula unit ($N_D \approx N_S/2$), g is g -factor and J_D is an intradimer exchange. As seen in Fig. 24, the results of the AF dimer model with $N_D = 2.0$, $g_c = g_a = 2.05$ [88] and $J_D = 11.2$ meV agree well with the measured susceptibility of $\text{Sr}_{14}\text{Cu}_{24}\text{O}_{41}$ at low temperatures after the Curie term due to paramagnetic impurities has been subtracted. On the other hand, at temperatures higher than 150 K the susceptibility behavior $\chi(T)$ gradually deviates from AF dimer behavior. This deviation is due to an increased ladder contribution to the susceptibility. A perfect agreement with the experimental data in the broad temperature range (20–800 K) is obtained if the susceptibility is described by the superposition of two contributions $\chi = \chi_D + \chi_T$: the dimer term χ_D for the chains (Eq. (10)) with $N_D = 2$ and $J_D = 11.2$ meV and a Troyer term χ_T [89] for the ladders (Eq. (11)) with a spin gap value $\Delta_L \approx 32.5$ meV as the one obtained from neutron scattering [45] (see Fig. 24(b))

$$\chi_T(T) = \frac{A}{\sqrt{T}} \exp\left(\frac{-\Delta_L}{k_B T}\right). \quad (11)$$

Δ_L is the spin gap in the ladders and A is a constant describing the dispersion of an isolated spin-1/2 ladder [66]. We will describe Troyer model for ladders in more details in Section 5.1.1.

4.1.2. Inelastic neutron scattering and X-ray diffraction

Inelastic neutron scattering (INS) experiments performed on the parent compound $\text{Sr}_{14}\text{Cu}_{24}\text{O}_{41}$ at low temperatures ($T \leq 20$ K) identified excitations at energies around 11 meV, which are ascribed to the dimer chains (see Fig. 25) [71,45,90,91]. The assignment is based on previous susceptibility data, which indicate the pertinent energy scale $J_D \approx 11$ meV. Additional scattering peaks at larger energies are ascribed to the ladders, as will be addressed in Section 5. Initially, Matsuda et al. described their data using a model with AF coupled dimers formed between spins, which are separated by 2 and 4 times the distance between the nearest neighbor copper ions in the chain [90]. Later, Eccleston et al. [45] used the expressions for the structure factor and dispersion of a dimer chain with essentially three free parameters, intradimer distance, interdimer distance and ratio of interdimer and intradimer exchange energies (J_c and J_D) to fit the observed data (see Fig. 26) [92]. Their analysis showed that the magnetic structure consists of dimers formed between next-nearest neighbor copper ions ($J_D \approx 11$ meV). The dimers are weakly ferromagnetically ($J_c \approx -1$ meV) coupled and separated by three times the Cu–Cu distance (Fig. 27, right panel). There are two dimers per formula unit and the super-structure periodicity of such a dimer chain is five chain c_C parameters. Note that this result confirms dimer model analysis of the susceptibility data exposed in Section 4.1.1.

The magnetic structure, suggested by Eccleston et al., was later confirmed by INS measurements and analysis by Regnault et al. and by Matsuda et al. [71,91]. Moreover, they showed that the AF dimer structure develops in two

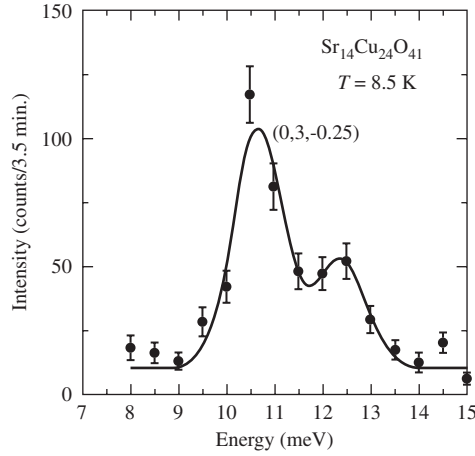


Fig. 25. Inelastic neutron scattering spectra of $\text{Sr}_{14}\text{Cu}_{24}\text{O}_{41}$ at 8.5 K at the reciprocal lattice point (0, 3, -0.25). The full line is a fit to two Gaussian forms. After Ref. [90].

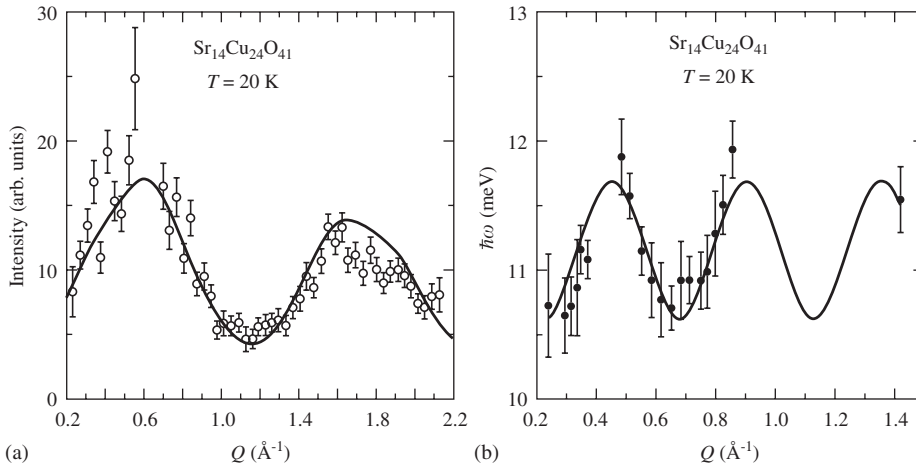


Fig. 26. (a) Inelastic neutron scattering data of $\text{Sr}_{14}\text{Cu}_{24}\text{O}_{41}$ at 20 K along the c direction in the reciprocal lattice space (c^*) integrated between 9 and 14 meV. The full line is a fit to the expression for structure factor of a dimer chain. (b) Scattering data along the c^* direction. The full line is a fit to the dispersion relation expected for a dimer chain. After Ref. [45].

dimensions in the chain ac plane with equally weak interdimer coupling along and between chains, but opposite in sign, i.e. $|J_c| \approx |J_a| \approx 1$ meV. As for the two excitation modes, observed first by Matsuda et al. [90] (Fig. 25), Regnault et al. suggested that these modes should be ascribed to a unique excitation associated with a $S = 1$ magnetic state whose degeneracy is lifted by magnetic coupling between chains. The relative shift η between neighboring chains (Fig. 27) is $c_C/2$ at low temperatures ($T < 10$ K). However, η can vary with temperature producing a change in the lattice structure with concomitant change in the magnetic structure. Indeed, as temperature increases, two excitation modes merge into a single line indicating that the interchain coupling becomes ineffective. This might be due to a deviation from a quasi-straight configuration of the Cu–O–O–Cu path through which the coupling between chains is realized.

Taking into account the complementary relation of spins and holes, the super-periodicity of $5c_C$ parameters implies that there is a charge order established in the chains. Moreover, this result indicates that all six holes (per formula unit) reside in the chains at low temperatures (Fig. 28, upper panel). The question arises whether the existence of this charge order is associated with the concomitant lattice distortion. Unfortunately, standard X-ray and electron diffraction techniques are, in this case, not the appropriate methods to clarify this point. Due to the low internal

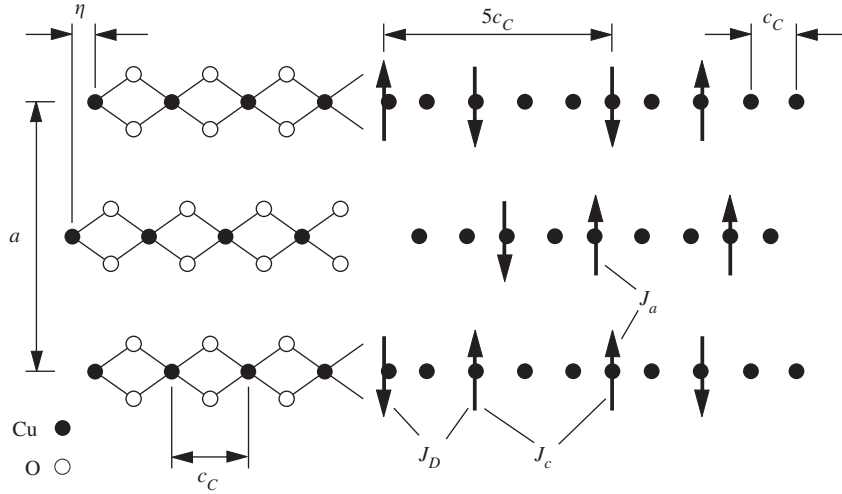


Fig. 27. Two-dimensional antiferromagnetic dimer structure in the chain layers of $\text{Sr}_{14}\text{Cu}_{24}\text{O}_{41}$ as determined by inelastic neutron scattering at $T < 10$ K.

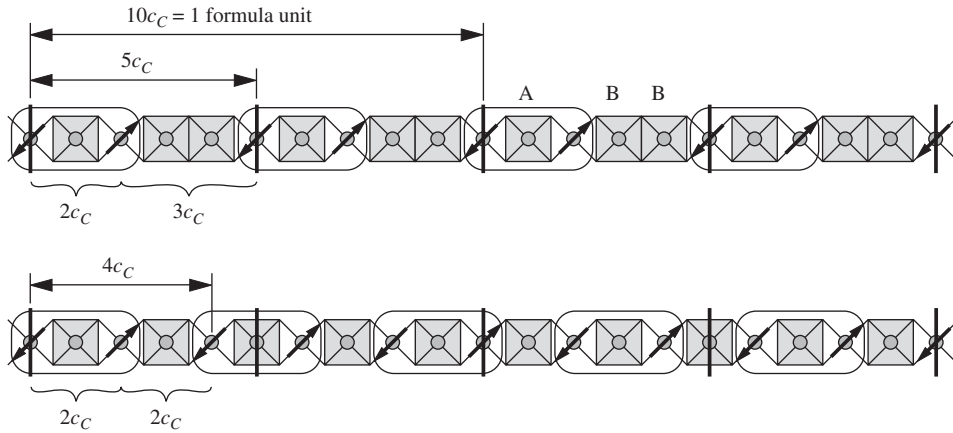


Fig. 28. Schematic illustration of the antiferromagnetic dimer structure and complementary charge order in the chains of $\text{Sr}_{14}\text{Cu}_{24}\text{O}_{41}$ along the c -axis as determined by inelastic neutron scattering at $T \leq 20$ K (upper panel) and by X-ray diffraction at $T = 50$ K (lower panel). Spins and holes (ZR singlets) are designated by arrows and shaded squares, respectively.

symmetry of the superstructural motif ($5c_C = 2c_C$ intradimer + $3c_C$ interdimer), the energy gained from creating the lattice super-structure is probably smaller than the modulation caused by interaction of the chain subsystem with the ladder subsystem [51,93]. Indeed, Hiroi et al. [52], who used an electron microscopy technique, pointed out that the long-range AF dimer order takes place either without the formation of additional super-structure or without a large change in the pre-existing super-structure as detected in electron diffraction. In the similar manner, the observation of additional lattice reflections at $(0, 0, 2n \pm 1/5)$ in X-ray diffraction experiment by Fukuda et al. [94] was not interpreted as being related to a charge order, rather to be a result of the mutual interaction between the chain and ladder subsystems of this composite crystal $\text{Sr}_{14}\text{Cu}_{24}\text{O}_{41}$ [95]. The latter interpretation is supported by a smooth temperature dependence of the satellite reflections and the fact that they were observed also at room temperature, where the long-range charge order is not established (see Section 4.1.3). The modulated structure was also investigated by Gotoh et al., who have used a centrosymmetric $(3 + 1)$ -dimensional superspace group to analyze their X-ray diffraction data collected at room temperature [82]. The authors applied the bond-valence sum method to study the role of atomic modulations, of the hole distribution and of hole-ordered structures. At variance to the arguments given by van Smaalen [95], they consider

that the modulated lattice super-structure due to the mutual interactions between the chains and ladders, necessarily induce the charge order in the chains with the same super-periodicity of $5c_C$ chain parameters.

Very recent elastic neutron diffraction measurements on single crystals of $\text{Sr}_{14}\text{Cu}_{24}\text{O}_{41}$ by Braden et al. [96] revealed additional reflections which appear upon cooling below 200 K. These satellite peaks at low temperatures differ from the normal satellites described previously due to their strong temperature dependence, due to their weak intensity, and due to their larger width in the reciprocal space. The authors interpreted the observed results as a lattice modulation associated with the charge ordering locking into the incommensurate composite structure.

Coming back to electron diffraction experiments, we would like to point out that the lattice reflection at $(0, 0, 2.2)$ was not detected neither in the work by Hiroi et al. [52], nor in previous work by Milat et al. [51]. Nevertheless, Hiroi et al. have shown that the pattern of AF dimer order and complementary charge order is determined by the misfit potential imposed on the chains by the more “rigid” ladders. Their evidence is based on the combined susceptibility and electron diffraction measurements on the samples $\text{Sr}_{14}\text{Cu}_{24}\text{O}_{41-\xi}$ with varying oxygen content ξ . A characteristic profile of the magnetic susceptibility (see Fig. 24) with $N_D = 2$ observed for $\xi = 0$, disappears with increasing or decreasing ξ , with concomitant significant change of the periodicity of the super-structure. The super-structure periodicity is uniquely related to the ratio $\alpha = c_L/c_C$ and for $\xi = 0$ it corresponds to $\alpha = 7/10$ (see Section 3.1 and Figs. 6 and 7).

For the sake of completeness, we should also mention the result of Cox et al. [97], who have reported the superlattice reflections with periodicity equal to four chain parameters (Fig. 28, lower panel). The intensity of these reflections is largest at $T = 20$ K and decreases with increasing temperature; the slope of this change becomes weaker above 200 K and disappears close to room temperature. This observation is difficult to reconcile with INS results exposed in this section. As a final remark concerning X-ray results, we point out that a resonant X-ray scattering technique used by Abbamonte et al. is well suited to clarify the issue, since it is directly sensitive to the hole ordering [98]. However, Abbamonte et al. claim that the charge order observed in their measurements on a single crystal of $\text{Sr}_{14}\text{Cu}_{24}\text{O}_{41}$ was established in the ladders, and not in the chains (see Section 5.3.7) [99].

Therefore, we have to state that there is no conclusive evidence in the standard meaning that the charge order in the chains is accompanied with a concomitant lattice distortion of the same periodicity. However, it does appear that the misfit potential determined by $\alpha = 7/10$ felt by charges residing in the chains plays a crucial role. Moreover, this modulation of the two subsystems additionally changes below 200 K, probably associated with the charge ordering in the chains. Nevertheless, notice that the relationship with the charge order in the ladders cannot be excluded.

Finally, we address the issue of hole count as a function of temperature in $\text{Sr}_{14}\text{Cu}_{24}\text{O}_{41}$. The INS result, that all six holes (per formula unit) reside in the chains at low temperatures, is apparently at variance with the findings of polarized near edge X-ray absorption spectroscopy obtained at room temperature, which show that only five holes reside in the chains, while almost one hole is transferred into the ladders (see Section 3.3.1) [81]. However, we remind that inelastic neutron scattering data by Regnault et al. and by Matsuda et al. [71,91] indicate that the two-dimensional AF dimer order, which is fully established at $T < 20$ K, becomes increasingly unstable with rising temperature and that changes of the internal magnetic structure (and therefore of the charge order) are highly probable. An interesting information comes from a comparison between the experimentally observed temperature dependence of the intensity of INS spectra and the theoretically expected behavior within the random phase approximation (Fig. 29) [91]. The fact that the observed intensity decreases faster indicates that in addition to thermal fluctuations other factors disturb the AF dimer order.

Since the prerequisite condition for the AF dimer and charge order, i.e. the misfit potential originating from the structural modulation of the chains and ladders [52] exists independently of temperature, these results can be consistently understood if a transfer of holes from the chains into the ladders, which occurs with increasing temperature, is assumed. The distribution at room temperature is slightly more than five holes per formula unit in the chains and almost one hole in the ladders, while at $T < 50$ K one would expect that almost all six holes per formula unit reside in the chains. A question arises what is an amount of transferred holes. As we have discussed in Section 3.3.3, a very recent nuclear magnetic resonance study by Piskunov et al. [86] indicates that about 0.02 holes per ladder Cu site is transferred by lowering temperature from 300 to 10 K. This would imply that at low temperatures 0.56 holes per formula unit remain in the ladders, while about 5.44 holes per formula unit reside in the chains. Gellé and Lepetit [100] attempted to theoretically solve the issue of hole number, as well as the misfit potential, and their importance on the AF dimer and charge order in the chains at low temperatures. They performed ab initio determination of on-site and nearest neighbor interactions for $\text{Sr}_{14-x}\text{Ca}_x\text{Cu}_{24}\text{O}_{41}$, $x = 0$ and 13.6. For the former, they obtained the result clearly showing that the number of holes per formula unit in the chains must be close to six, to make long-range AF dimer order

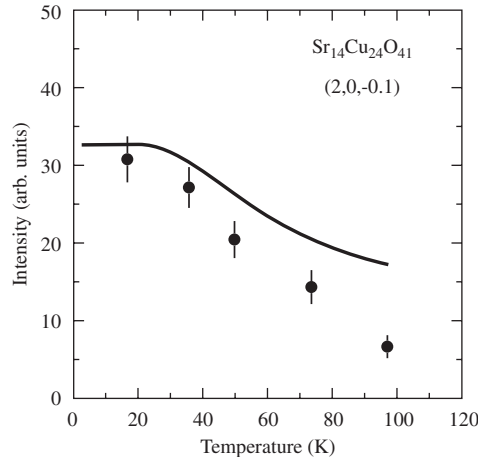


Fig. 29. Temperature dependence of the energy-integrated intensity at $(2, 0, -0.1)$ peak observed by neutron scattering in $\text{Sr}_{14}\text{Cu}_{24}\text{O}_{41}$. The full lines are fits to the random phase approximation expression for dynamic structure factor of the weakly coupled dimer system. After Ref. [91].

possible. For the latter, assuming that there are at maximum only five holes per formula unit in the chains, the structural modulation is so large that the low energy physics of this material is completely changed to antiferromagnetic order (see Section 4.1.3).

Unfortunately, no systematic study of chains as a function of Ca-substitution, neither inelastic neutron scattering nor X-ray diffraction, has been reported to date. However, we should briefly mention the inelastic neutron scattering investigations performed on $\text{Sr}_{11}\text{Ca}_3\text{Cu}_{24}\text{O}_{41}$ [91] and on materials with high Ca content: $\text{Sr}_{2.5}\text{Ca}_{11.5}\text{Cu}_{24}\text{O}_{41}$ [101] and $\text{Sr}_{0.4}\text{Ca}_{13.6}\text{Cu}_{24}\text{O}_{41}$ [55]. Low Ca content broadens the magnetic excitation peaks, but the coupling constants remain unchanged. On the other hand, no AF dimer order is found for high Ca contents. The main conclusion of these studies is that there is an antiferromagnetic order in the chains at very low temperatures (≈ 2.5 K) and that there is a back-flow of holes from the ladders into the chains with decreasing temperature, so that even at these high Ca contents almost all six holes (per formula unit) reside in the chains at very low temperatures. In the following section we will present nuclear magnetic resonance and electron spin resonance results, which, especially the latter, shed more light on the role of Ca-substitution in spin and charge orderings in the chains.

4.1.3. Nuclear magnetic resonance and electron spin resonance

NMR and NQR spectroscopies were used to study spin dynamics and spin arrangement in the chains [88,102,103]. The assignment of the observed ^{63}Cu (^{65}Cu) signals to chain sites was done on the basis of the observed two distinct quadrupole frequencies, 33 and 14 MHz, the latter one being close to the experimentally determined quadrupole frequency of the ladder ^{63}Cu (11 MHz) in SrCu_2O_3 . The most detailed study on single crystals of $\text{Sr}_{14}\text{Cu}_{24}\text{O}_{41}$ was performed by Takigawa et al. [88].

The first important result of Takigawa et al. is that the ^{63}Cu NMR spectrum center line splits below $T^* \approx 200$ K into two groups, A and B, indicating the appearance of non-equivalent Cu sites on the chain with different values of magnetic shift. Below 50 K the peaks become narrow and a sharp structure is well defined, so that the temperature variation of the shift is similar within each group but rather different between them. The closer inspection of the temperature variation reveals that the NMR shift for the A sites follows the behavior observed in the static susceptibility measurements (see Fig. 24), as expected. However, the shift of the B sites shows similar temperature dependence only below 50 K, while a quite distinct, weakly temperature dependent, above. NQR spectra (Fig. 30(b)) confirm that the clear site distinction with different charge distribution environment is well established at low temperatures and gradually smears out above 50 K. Takigawa et al. assigned both the A and B sites to the ZR singlet sites (hole sites), whereas the line, which only emerges below 30 K due to strong motional narrowing effects (detected at 88.6 MHz for 8.4 T), to the dimer chain sites (spin 1/2 sites). The satellite spectra of the latter also consist of distinct peaks indicating the existence of non-equivalent sites.

The second result concerns the spin-lattice relaxation rate $1/T_1$, measured at ZR and dimer sites, as a function of inverse temperature (Fig. 31). The relaxation is purely magnetic, meaning that no relaxation due to phonons and charge

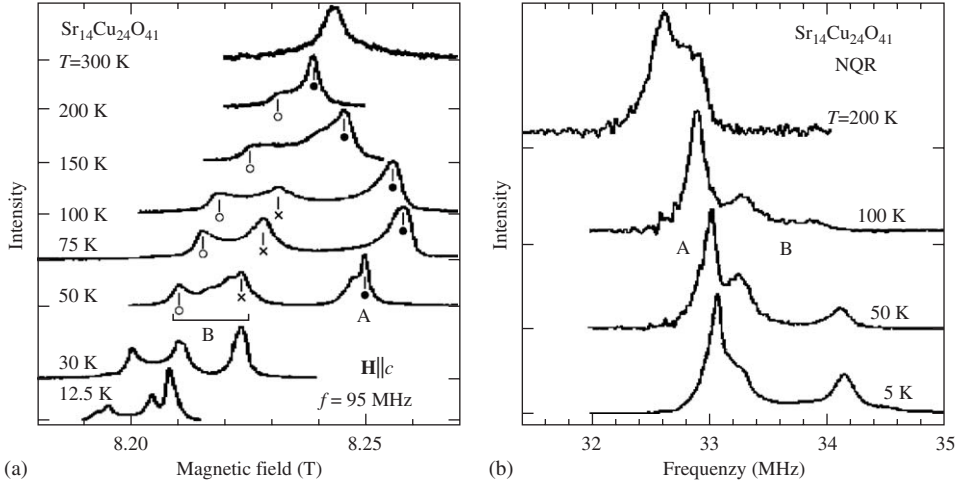


Fig. 30. Temperature variation of the NMR (a) and the NQR spectra (b) at the chain ^{63}Cu sites of $\text{Sr}_{14}\text{Cu}_{24}\text{O}_{41}$. After Ref. [88].

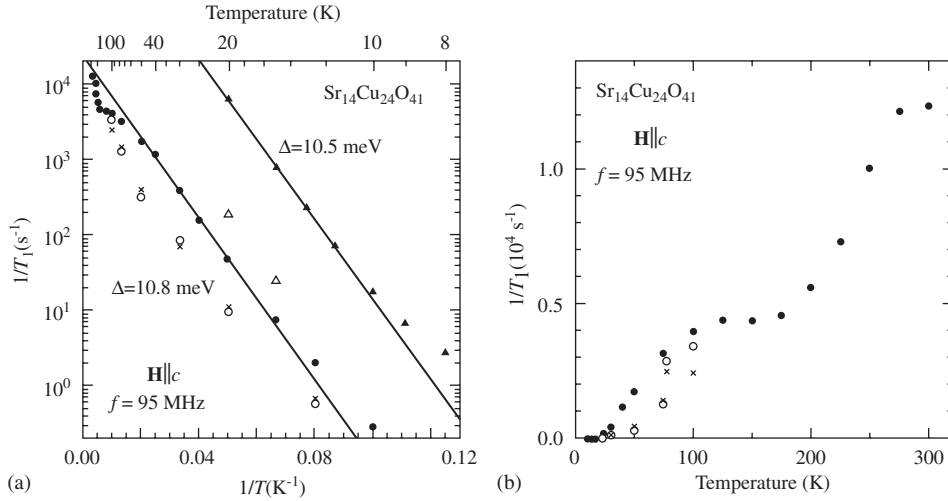


Fig. 31. Temperature dependence of the spin-lattice relaxation rate $1/T_1$ of $\text{Sr}_{14}\text{Cu}_{24}\text{O}_{41}$. The full circles are obtained for A ZR sites, while the open circles and crosses correspond to B ZR sites. Full and open triangles are for dimer sites. Full lines are fits to the activated behavior. After Ref. [88].

fluctuations was found. A clear activated behavior is observed below 50 K with the spin gap of 10.5–10.8 meV. This gap can be directly related to the intradimer exchange $J_D \approx 11$ meV determined from the static susceptibility behavior in the AF dimer model (see Section 4.1.1). Additionally, the linear scale plot (Fig. 31(b)) reveals an anomalous behavior of $1/T_1$ displaying a plateau between 100 and 200 K and a sharp increase above.

These results suggest that the AF dimer pattern starts to develop in the chains below $T^* \approx 200$ K, and that it is fully developed at long-range scale only at temperatures below 50 K. The remaining issue is how to identify the hole/spin arrangement. This might be done by considering the intensity ratio of lines, representing the population ratio, of three distinct groups of relaxation sites belonging to the A and B ZR sites, and to the dimer sites. At temperatures below 50 K data give $I_A/I_B = 0.65 \pm 0.1$ and $I_{\text{dimer}}/I_{\text{ZR}} = 0.39 \pm 0.1$, suggesting the AF dimer structure and complementary charge order in the chains as illustrated in the upper panel of Fig. 28. Therefore, both the INS and NMR data are consistent with the spin and charge pattern with the super-periodicity of five chain c_C parameters in which AF dimers are formed between next-nearest neighbor copper ions. We remind again that such a pattern implies that almost all six holes per

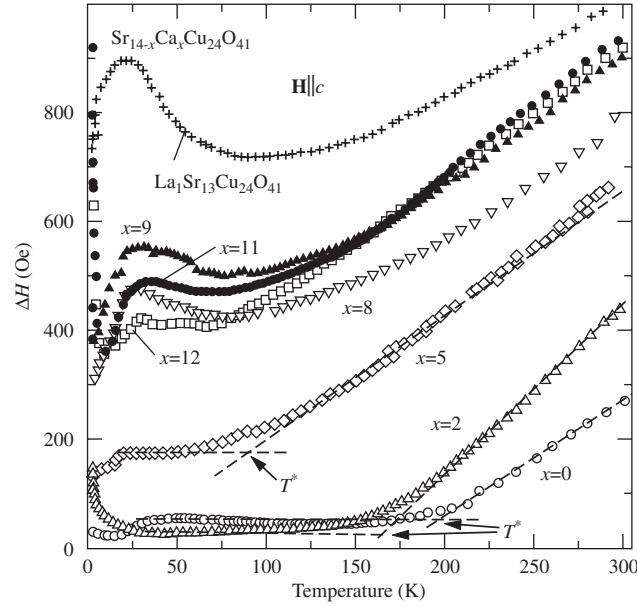


Fig. 32. Temperature dependence of the electron spin resonance linewidth $\Delta H(T)$ of $\text{Sr}_{14-x}\text{Ca}_x\text{Cu}_{24}\text{O}_{41}$. $\Delta H(T)$ of $\text{La}_1\text{Sr}_{13}\text{Cu}_{24}\text{O}_{41}$ is shown for comparison. After Ref. [85].

formula unit reside in the chains at $T < 50$ K. Therefore, NMR data are in nice agreement with neutron scattering data. Clearly, a long-ranged spin and charge order with the super-periodicity of $5c_C$ parameters at low temperatures changes with increasing temperature, gradually losing long-range formation and finally vanishes above $T^* \approx 200$ K. In addition to increased thermal fluctuations (see Fig. 29), the gradual destruction might be attributed to the transfer of holes from the chains to the ladders with increasing temperature, so that at room temperature a distribution of holes with five per formula unit in the chains and one in the ladders is established [81].

At the end we would like to point out that NMR and NQR investigation of $1/T_1$ in $\text{Sr}_{14-x}\text{Ca}_x\text{Cu}_{24}\text{O}_{41}$ polycrystalline samples ($x = 0, 3, 6, 9$) by Kumagai et al. has shown that the size of spin gap in the chains does not change with Ca content and remains well defined below about $T = 30$ K [103].

Electron spin resonance (ESR) investigation on the single crystals of $\text{Sr}_{14-x}\text{Ca}_x\text{Cu}_{24}\text{O}_{41}$ was performed by Kataev et al. [85]. On the basis of the same argument, invoking a large spin gap in the ladders used to interpret static susceptibility data, the dominant contribution to the ESR signal below $T^* \approx 200$ K can be attributed to the Cu^{2+} ions spin-1/2 in the chains.

The most important result is that the Cu^{2+} spin relaxation is remarkably influenced by the hole dynamics in the chains, resulting in a strong temperature dependence of the ESR linewidth ΔH above a crossover temperature T^* (Fig. 32). In $\text{Sr}_{14}\text{Cu}_{24}\text{O}_{41}$ ΔH is almost constant between 30 K and 180 K, while it increases rapidly above $T^* \approx 200$ K. Kataev et al. suggested that the temperature-independent behavior at $T < T^*$ is due to the hole localization, whereas the origin of the ESR line broadening is in the melting of the charge order at T^* and consequently an increased hole mobility at temperatures above T^* . Ca-substitution shifts the crossover temperature T^* from about 200 K in $\text{Sr}_{14}\text{Cu}_{24}\text{O}_{41}$ to 80 K in $\text{Sr}_9\text{Ca}_5\text{Cu}_{24}\text{O}_{41}$ ($x = 5$), indicating a rapid destruction of the charge order and complementary AF dimer pattern. The identification of $T^* \approx 200$ K as the charge order phase transition temperature (for $\text{Sr}_{14}\text{Cu}_{24}\text{O}_{41}$) might also explain the change in the NMR spin-lattice relaxation rate $1/T_1$: a plateau between 100 and 200 K and a sharp increase above (see Fig. 31(b)). For the $x = 8$ compound the short-range order remains, and it persists shortly until for $x > 12$ it is replaced by an AF long-range order at $T_N \approx 2.5$ K (Fig. 33). This result agrees with the inelastic neutron scattering studies (see Section 4.1.2) [55,101]. A critical broadening of the ESR line and the positive shift of the resonance field are clear signatures of the antiferromagnetic ordering. These data reveal that the increase of the Ca content from $x = 8$ to $x = 12$ continuously drives the system towards an AF instability. The negative shift of the resonance field found for all Ca contents x except for $x = 12$ indicates the presence of competing ferromagnetic correlations. The AF order has been also characterized by static susceptibility measurements, specific heat, nuclear magnetic resonance and neutron scattering

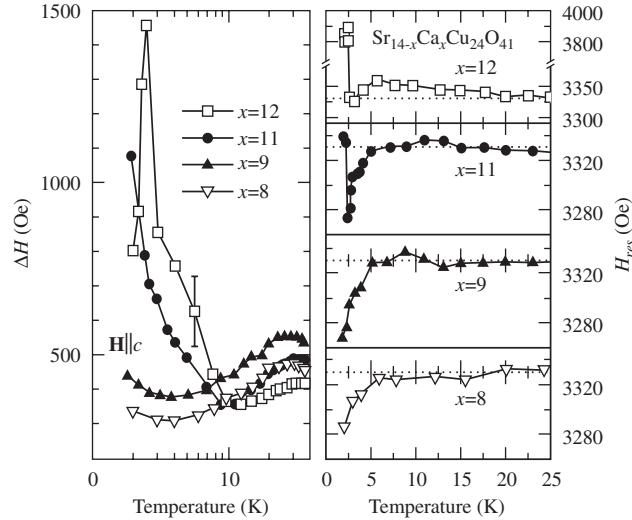


Fig. 33. Low-temperature behavior of the electron spin resonance linewidth ΔH (left panel) and resonance field H_{res} (right panel) of $\text{Sr}_{14-x}\text{Ca}_x\text{Cu}_{24}\text{O}_{41}$, $8 \leq x \leq 12$. After Ref. [85].

[101,104,105]. Ab initio calculations [100] have shown that the suppression of AF dimer order and establishment of antiferromagnetic order can be understood as to be due to structural modulation in $x = 13.6$ compound, independently of the hole transfer induced by Ca-substitution (1, 2 and 3 transferred holes per formula unit were assumed).

At the end, it is worth of noting that the ΔH vs. T slope for $\text{Sr}_{14-x}\text{Ca}_x\text{Cu}_{24}\text{O}_{41}$ is similar to the slope for the underdoped compound $\text{La}_1\text{Sr}_{13}\text{Cu}_{24}\text{O}_{41}$ containing five holes that all reside in the chains. Since the compound $\text{La}_2\text{Sr}_{12}\text{Cu}_{24}\text{O}_{41}$, which contains only four holes, is characterized by much broader linewidth with very weak temperature dependence of $\Delta H(T)$ (see Fig. 36), Kataev et al. put an upper limit of one hole being transferred from the chains to the ladders with maximum Ca-substitution (see Section 3.3).

4.2. Underdoped $(\text{La},\text{Y})_y(\text{Sr},\text{Ca})_{14-y}\text{Cu}_{24}\text{O}_{41}$: one-dimensional disordered system

Some of the phenomena become clearer if the holes are removed by substitution of Sr by the trivalent La or Y. We first discuss the magnetic properties, followed by the charge response.

4.2.1. Spin response

The magnetism of the underdoped quasi-1D cuprates was studied by magnetic susceptibility, ESR, NMR and INS measurements [43,69,84,103,106,107]. The hole count n_h and therefore the number of Cu^{2+} ions spin-1/2 residing in the chains can be varied by changing the La and/or Y content: from $n_h = 0$ and ten Cu^{2+} spins in $\text{La}_6\text{Ca}_8\text{Cu}_{24}\text{O}_{41}$ ($y = 6$) to $n_h = 5$ and five Cu^{2+} spins in $\text{Y}_1\text{Sr}_{13}\text{Cu}_{24}\text{O}_{41}$ ($y = 1$) (see Table 1, p. 29). High temperature susceptibility behavior for $1 \leq y \leq 6$ was already addressed in Section 4.1.1 and showed to follow the Curie–Weiss behavior of free spins (Fig. 23 and Fig. 34) [43,106]. However, at low temperatures, ferromagnetic correlations within the chains develop, and eventually for $y = 6$ (zero holes, ten spins) and $y = 5$ (one hole, nine spins) they result in the magnetic long-range order of ferromagnetic chains below 12.2 and 10.5 K, respectively [69,107]. The ferromagnetic order of spins within the chains (Fig. 35) reflects the nature of the Cu–O–Cu 90° bond configurations (see Section 3).

While for the $y = 5$ compound the long-range antiferromagnetic order is established (the easy-axis was determined to be the b -axis), this is not the case for the $y = 6$ compound with no holes. In the latter, the structure is incommensurate, revealing that the coupling between the chains is disturbed by some kind of disorder.⁶ On the other hand, the fact that

⁶ Volometry studies on samples from one batch of $\text{La}_6\text{Ca}_8\text{Cu}_{24}\text{O}_{41}$ [81] showed the existence of 0.86 extra holes. Scanning electron microscopy and microspot Auger analysis [108] revealed that a few percent of La in these samples is segregated as La-rich precipitates. This finding indicates that a high La content might lead to a phase instability in these compounds.

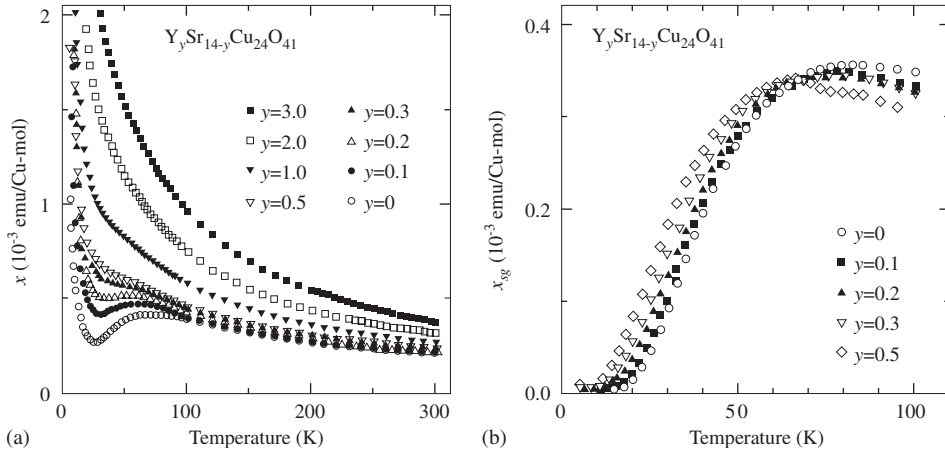


Fig. 34. (a) Temperature dependence of the magnetic susceptibility measured on polycrystalline samples of $Y_ySr_{14-y}Cu_{24}O_{41}$ for various y . (b) Susceptibility vs. temperature after subtracting the Curie term, due to paramagnetic impurities, for $0.5 \leq y \leq 0$. After Ref. [106].

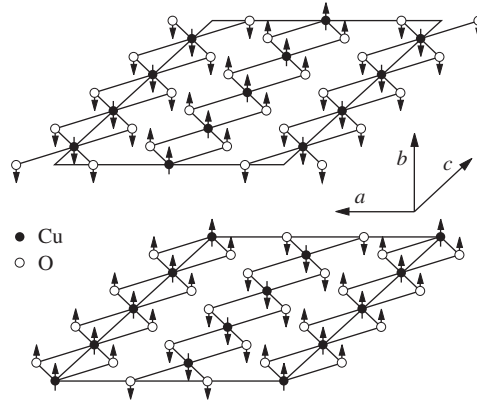


Fig. 35. Proposed model [69] for the antiferromagnetic order in the chains of $La_5Ca_9Cu_{24}O_{41}$ below $T = 10.5$ K.

the magnetic phase transition temperature for $y = 5$ is lower than for $y = 6$ can be understood to be due to increased number of holes (ZR singlets), which are expected to act as non-magnetic impurities.

Indeed, this conjecture is confirmed by ESR measurements [84], which show that by decreasing the La content from $y = 5$ to 2 the critical behavior of the ESR response (i.e. the critical broadening of the ESR signal and the positive shift of the resonance field) becomes less pronounced indicating a rapid suppression of AF correlations (Fig. 36).

Further, we address the crossover regime $1 \leq y \leq 0$ in which the total hole count n_h varies from five to six, while the number of holes and the spins in the chains remains approximately fixed [106]. The temperature dependence of the susceptibility (with the Curie term due to paramagnetic impurities subtracted) for compounds with $0.5 \leq y \leq 0$ is shown in Fig. 34 (b). It is evident that the susceptibility behavior for all y below 100 K corresponds to the AF dimers, as established for the parent compound $Sr_{14}Cu_{24}O_{41}$ (see Section 4.1.1). However, the position of the susceptibility peak shifts to lower temperatures with increasing y which indicates that the AF interaction becomes weaker between Cu^{2+} spins in the chains. The latter conclusion is also confirmed by the decreasing value of the Curie–Weiss temperature θ (see Eq. (9)) with increasing y , obtained from fits to the high-temperature susceptibility (Fig. 34(a)). INS experiment on $y = 0.1, 0.25$ and 1 compound clearly show a drastic suppression of the AF dimer structure: a broadening of a narrow line centered around 11 meV for $Sr_{14}Cu_{24}O_{41}$ (Fig. 25) is replaced by a broad feature between 6 and 13 meV [90,109]. However, a weak short-range AF dimer order persists until $y = 2$, as evidenced by NMR measurements that indicate a spin gap of similar size as for $Sr_{14}Cu_{24}O_{41}$ but in the narrow temperature range between 20 and 30 K [103].

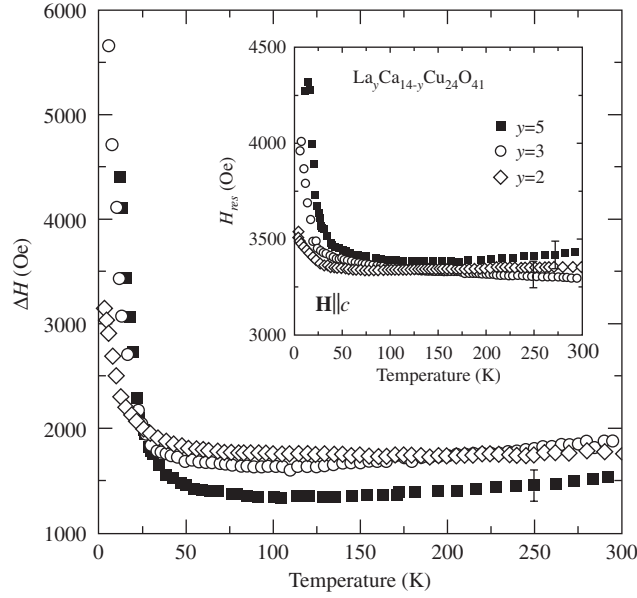


Fig. 36. Temperature dependence of the electron spin resonance linewidth $\Delta H(T)$ (main panel) and the resonance field (inset) for $\text{La}_y\text{Ca}_{14-y}\text{Cu}_{24}\text{O}_{41}$ for various La contents y . After Ref. [84].

Finally, two important remarks are in order. First, the extremely broad electron spin resonance line [84] indicates an unusually strong anisotropy of the Heisenberg superexchange. In this way it limits the applicability of the isotropic Heisenberg model to the quasi-1D cuprates (see Section 3.3.2). Kataev et al. suggested that the strong anisotropy can be explained by the geometry of two symmetrical 90° Cu–O–Cu bonds, which amplify the role of spin–orbit coupling. The second remark concerns the charge order. The complementary relationship of spin and charge arrangements leads to the conclusion that no charge ordering can be established in the underdoped quasi-1D cuprates. Indeed, the temperature-independent behavior of the electron spin resonance linewidth at low temperatures, associated with the charge order, was not at all found for $\text{La}_1\text{Sr}_{13}\text{Cu}_{24}\text{O}_{41}$ for which an order at very short scales probably exists. Therefore, a question arises about the charge dynamics in the chain subsystem of these compounds. This issue is addressed in the following section.

4.2.2. Charge response

The temperature dependence of the dc resistivity obtained on polycrystalline samples of $\text{Y}_y\text{Sr}_{14-y}\text{Cu}_{24}\text{O}_{41}$ for $0 \leq y \leq 3$ is displayed in Fig. 37 [106]. Note that for $y = 1, 2$ and 3 the hole count is $n_h = 5, 4$ and 3 , respectively, and that all holes reside in the chains. The room-temperature resistivity increases approximately by an order of magnitude each time one hole is removed which indicates the strongly insulating nature of these compounds. Indeed, while the plasma edge observed by optical measurements of $\text{Sr}_{14}\text{Cu}_{24}\text{O}_{41}$ is situated at about 0.5 eV, no plasma edge is found for $y = 3$ [77].

A detailed study of the temperature behavior of the dc transport on single crystals of $\text{La}_{5.2}\text{Ca}_{8.8}\text{Cu}_{24}\text{O}_{41}$ ($n_h = 0.8$) and $\text{La}_3\text{Sr}_3\text{Ca}_8\text{Cu}_{24}\text{O}_{41}$ ($n_h = 3$) along the c -axis, i.e. along the chains, revealed that the dc conductivity follows a simple activation behavior $\sigma_{\text{dc}}(T) \propto \exp(-\Delta/T)$ only at high temperatures, while at the crossover temperature T_{co} it enters into a variable-range hopping regime at lower temperatures (Fig. 38) [110]. The crossover temperature and activation energy diminish only slightly from $T_{\text{co}} = 330$ to 300 K, and from $\Delta = 370$ to 280 meV with increasing hole count: from $n_h = 0.8$ – 3 . Conversely, the room-temperature value of the resistivity decreases substantially from $\rho_{\text{dc}} = 1400 \Omega\text{cm}$ for $\text{La}_{5.2}\text{Ca}_{8.8}\text{Cu}_{24}\text{O}_{41}$ to $13 \Omega\text{cm}$ for $\text{La}_3\text{Sr}_3\text{Ca}_8\text{Cu}_{24}\text{O}_{41}$. It should be noted that it is not possible to account for this decrease in resistivity merely by an increase in the hole count. Below T_{co} the conductivity perfectly follows Mott's variable-range hopping behavior of a one-dimensional system ($d = 1$) system

$$\sigma_{\text{dc}}(T) = \sigma_0 \exp \left[- \left(\frac{T_0}{T} \right)^{1/(1+d)} \right], \quad (12)$$

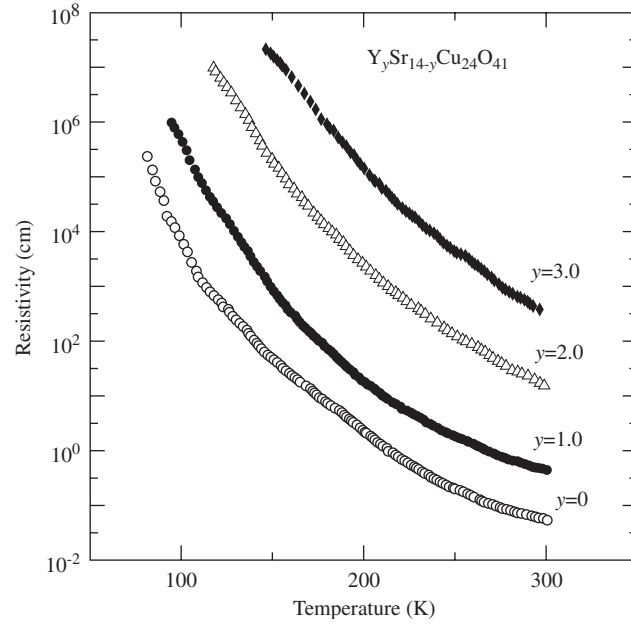


Fig. 37. Temperature dependence of the resistivity of $Y_ySr_{14-y}Cu_{24}O_{41}$ for various y . After Ref. [106].

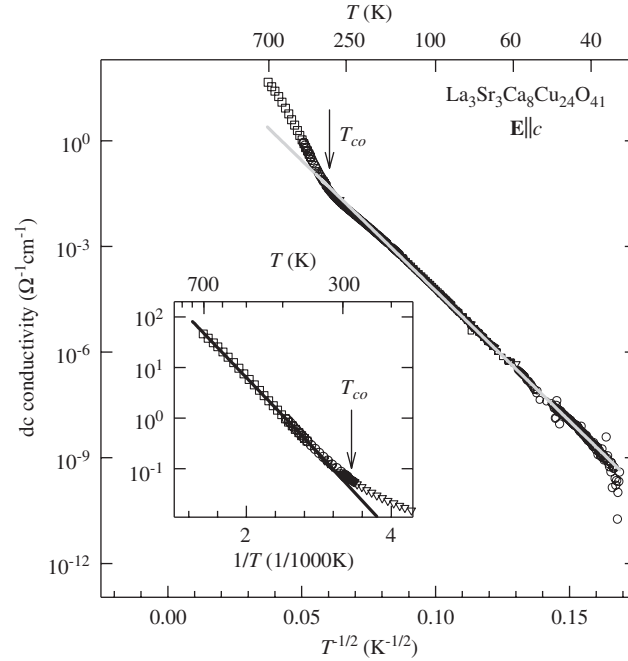


Fig. 38. The dc conductivity of $La_3Sr_3Ca_8Cu_{24}O_{41}$ along the c -axis as a function of $T^{-1/2}$ (main panel) and inverse temperature (inset). The full lines are fits to variable range hopping (main panel) and simple activation (inset) behavior. From Ref. [110].

where σ_0 is the infinite-temperature conductivity and $k_B T_0$ is the variable-range-hopping activation energy. These results clearly demonstrate that the charge transport along the chains of the underdoped quasi-1D cuprates is due to hopping in one dimension and that the chains should be modeled as a strongly disordered system where states are localized. For one-dimensional variable range hopping, the dc hopping length is given by $R_0 = [\Delta c_C / (2\alpha T)]^{1/2}$. It is

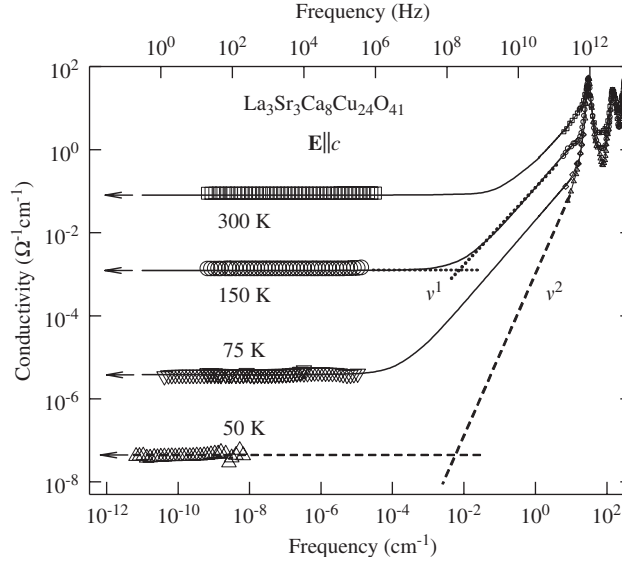


Fig. 39. Broadband conductivity spectra for $\text{La}_3\text{Sr}_3\text{Ca}_8\text{Cu}_{24}\text{O}_{41}$ along the c -axis at selected temperatures obtained by low-frequency dielectric spectroscopy and optical spectroscopy measurements. The arrows denote the dc values at the corresponding temperatures. The full lines are extrapolations and fits to Eq. (13) in the range 6–20 cm^{-1} . A pure power-law contribution is shown for 150 K by a dotted line. A ν^2 term due to the low-energy phonon tail is shown by the dash-dot line. From Ref. [110].

assumed that the energy of the sites near the Fermi energy which are available for hops, has a distribution in the range $-\Delta$ to $+\Delta$; the distance between the nearest Cu chain sites is $c_C = 2.77 \text{ \AA}$, and α^{-1} denotes the localization length. The temperature T_{co} at which the nearest neighbor hopping at higher temperatures crosses over to the variable-range hopping at lower temperatures is given by criterion that $R_0 = c_C$. It follows that $T_{co} = \Delta / (2\alpha c_C)$ [111,112]. Going from $y = 5.2$ to 3, i.e. increasing the number of holes from $n_h = 0.8$ to 3, the localization length increases slightly from $\alpha^{-1} = 0.43$ to 0.51 \AA . The variable-range-hopping activation energy $k_B T_0$ is obtained from fits of the data to Eq. (12). With changing the hole number n_h , $k_B T_0$ varies in the same manner as the energy Δ does, decreasing from 4.3 to 2.55 eV. These values are very close to the ones expected theoretically for the two compounds: $k_B T_0^{\text{th}} = 2\Delta c_C \alpha \approx 4.8$ and 3.0 eV, respectively [113,114].⁷

A further evidence that the underdoped quasi-1D cuprates can be considered as 1D disorder-driven insulators comes from the temperature-dependent behavior of the conductivity measured in the broad frequency range (Fig. 39) [110].

If we first consider the 50 K data, obviously only a ν^2 term is observed which is due to the low-energy phonon tail as shown by the dash-dot line in Fig. 39. Excluding the phonon component, the electronic conductivity can be expressed as the sum of two contributions

$$\sigma(\nu, T) = \sigma_{dc}(T) + A(T)\nu^s, \quad s \approx 1, \quad (13)$$

where $\sigma_{dc}(T)$ is given by Eq. (12). The crossover frequency ν_{co} from the frequency independent to the frequency dependent conductivity can be estimated from the condition that the ac hopping length R_ν must be smaller than the dc hopping length R_0 in order that $\sigma_{ac}(\nu, T)$ overcomes $\sigma_{dc}(T)$ [111]. The ac hopping length is $R_\nu = \alpha^{-1} \ln(\nu_{ph}/\nu_{co})$ [114], where the attempt frequency ν_{ph} depends on the electron–phonon interaction and may be considered equal to the lowest phonon frequency ($\nu_{ph} \approx 28 \text{ cm}^{-1}$). The crossover frequency ν_{co} calculated in this manner decreases with lowering the temperature (from 0.15 to 0.0006 cm^{-1} when T is changed from 300 to 75 K) and these values coincide well with those obtained by extrapolating the ν^s fits ($s \approx 1$ in the 6–20 cm^{-1} range) to lower frequencies.

Fig. 40 shows the optical conductivity and dielectric function of $\text{La}_3\text{Sr}_3\text{Ca}_8\text{Cu}_{24}\text{O}_{41}$ in the frequency range up to 60 cm^{-1} where the crossover from hopping to phonon-related response is observed [110]. The shaded contribution

⁷ We note that in the literature one can also find another formula $k_B T_0^{\text{th}} = 8\Delta c_C \alpha$ [112], which was used in Ref. [110]. An apparent agreement with the experimental data, found in the latter work, was due to a wrong assignment of the simple activation energy Δ .

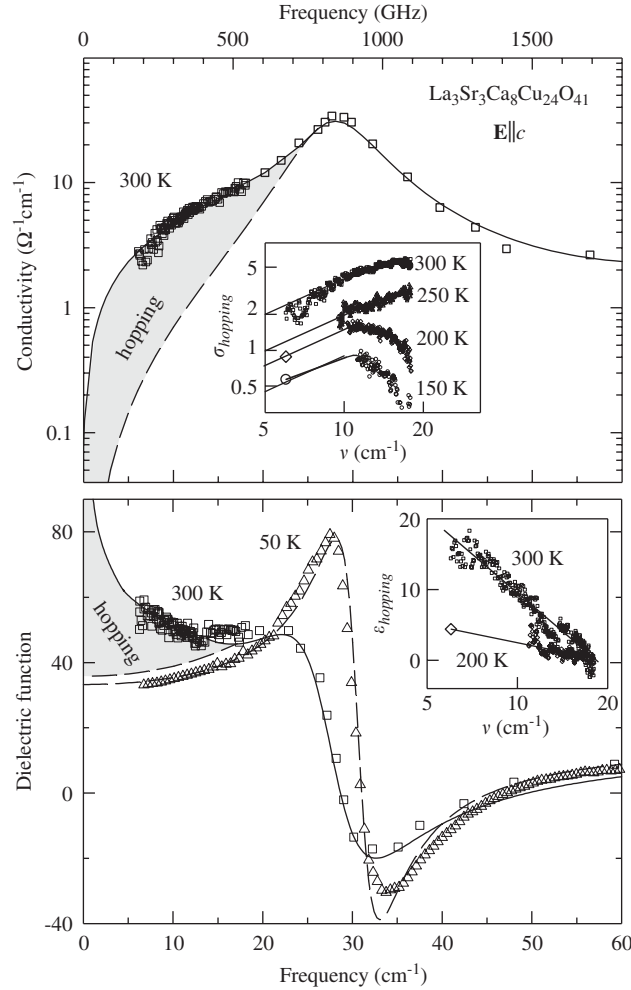


Fig. 40. Optical conductivity (upper panel) and dielectric function (lower panel) of $\text{La}_3\text{Sr}_3\text{Ca}_8\text{Cu}_{24}\text{O}_{41}$ measured with $\mathbf{E} \parallel c$. The dashed lines are fits which include only the contributions associated to the phonon at 28 cm^{-1} . The full lines correspond to the fit which in addition includes an electronic hopping conduction $A(T)v^5$. The insets show, for a few selected temperatures, the conductivity and the dielectric function due to hopping (the phonons contribution subtracted). From Ref. [110].

can clearly be identified as due to hopping. Most important, with lowering the temperature the electronic hopping contribution vanishes more drastically (see insets).

It was suggested [110] that the hopping transport in the underdoped compounds $(\text{La}, \text{Y})_y(\text{Sr}, \text{Ca})_{14-y}\text{Cu}_{24}\text{O}_{41}$ originates in the non-periodic potential in which holes reside and which is induced by strong local distortions of the chains due to the irregular coordination of La^{3+} , Y^{3+} , Sr^{2+} and Ca^{2+} ions [48,49,82]. The variable range hopping conductivity can then be explained as a result of the distorted distribution of microscopic conductivities, as predicted in Anderson's localization theory. Therefore, the copper–oxygen chains in the underdoped quasi-1D cuprates can be considered like a one-dimensional system in which disorder, associated with random distribution of holes, causes the Anderson localization. It is evident that the chain subsystem behaves as a one-dimensional disorder-driven insulator for the whole range of hole counts $0 \leq n_h \leq 5$, i.e. as long as there are no holes in the ladders. An intriguing question arises concerning the crossover to the charge-ordered phase established in the chains of the fully doped ($n_h = 6$) system. It should be noted that the crossover from $n_h = 5$ to 6 does not imply a change of the hole number in the chains, rather the appearance of one hole in the ladders. Measurements of the charge transport on single crystals with $0 < y < 1$ are needed to clarify this issue.

5. Physics of ladders

After we have discussed the chain subsystem of these composite compounds, we now focus on the ladders, which turn out to show a large diversity of different physical phenomena, reaching from magnetic order to density wave formation and even superconductivity. In the charge sector, the chains are one-dimensional entities, while the ladders are more two-dimensional, in particular since the hopping between the ladders is much larger. Magnetically, the chains and ladders are slightly coupled and thus behave more as two-dimensional systems.

5.1. Gapped spin-liquid

We have seen in Section 3.2.2 that a two-leg ladder of $S = 1/2$ spins has a finite spin gap in its spectrum of spin excitations, since in the strong-coupling limit the Heisenberg coupling along the rungs J' is much larger than along the legs J . The spin gap is of the order of J' implying that it is finite for the smallest non-zero J' . Spin excitations can only be produced by promoting a rung singlet to a triplet at the energy cost J' . These local excitations can propagate along the ladder. This implies that the spins show no long-range order; most of the time they form singlets on the rungs and the spin correlation decays with distance exponentially along the ladders. Such a state is called a spin-liquid.

5.1.1. Undoped ladders of $(\text{La}, \text{Y})_y(\text{Sr}, \text{Ca})_{14-y}\text{Cu}_{24}\text{O}_{41}$

Underdoped quasi-one-dimensional cuprates $(\text{La}, \text{Y})_y(\text{Sr}, \text{Ca})_{14-y}\text{Cu}_{24}\text{O}_{41}$ (with $y \geq 1$) are clearly distinct from the fully doped $(\text{Sr}, \text{Ca})_{14}\text{Cu}_{24}\text{O}_{41}$, since in the former no holes reside in the ladders—the ladders are undoped (Section 3.3) [81]. The physics of undoped ladders should be well described by the spin-ladder model [6], meaning that the ground state is the gapped spin-liquid.

Indeed, the results obtained by INS measurements and NMR experiments confirm this expectation. The INS measurements performed on single crystals of $\text{La}_6\text{Ca}_8\text{Cu}_{24}\text{O}_{41}$ (with no holes, $n_h = 0$, see Sections 3.3 and 4.2) [115] yield the spin gap of $\Delta_L \approx 31$ meV, confirming that the result $\Delta_L \approx 36$ meV for pure ladder compound SrCu_2O_3 [65] applies also for the ladders in the quasi-1D cuprates $(\text{La}, \text{Y})_y(\text{Sr}, \text{Ca})_{14-y}\text{Cu}_{24}\text{O}_{41}$. INS experiments were performed with the incident beam parallel to the a -axis (i.e. parallel to the rung direction). The data were collected in the detectors, which probe the magnetic scattering from the ladders in the ac plane. The summation of collected data for each incident energy corresponds to the integration over one Brillouin (AF) zone in the momentum transfer Q_c . Matsuda et al. [115] used the expressions for the scattering function and dispersion relation of the ladder with essentially two free parameters, spin gap (Δ_L) and the band maximum (C), to fit the observed data (see Fig. 41). Details of the fitting procedure are described in Ref. [45]. Dispersion relation displayed in the inset of Fig. 41 and in Fig. 43 reads

$$E^2(Q_c) = \Delta_L^2 + C^2 \sin^2(Q_c c_L). \quad (14)$$

Here $Q_c = \pi/c_L - q_c$ and q_c is the momentum. The antiferromagnetic zone center is located at $q_c = \pi/c_L = 0.8 \text{ \AA}^{-1}$. The data analysis shows that the band minimum corresponding to the spin gap of the ladders is $\Delta_L = (30.5 \pm 5) \text{ meV}$, while the band maximum amounts to $C = (191 \pm 5) \text{ meV}$. Using the theoretical relationship which connects Δ_L and the intraladder couplings J and J' along legs and rungs [66,116]

$$\frac{\Delta_L}{C} = 0.08 + 0.16\alpha, \quad (15)$$

$$\frac{\Delta_L}{J} = 0.4\alpha + 0.1\alpha^2, \quad (16)$$

where $\alpha = J'/J$, one gets $J'/J \approx 0.5$ with $J' = 53 \text{ meV}$ and $J = 106 \text{ meV}$. Matsuda et al. [115] argue that their data can be also consistently described with $J' = J = 110 \text{ meV}$ if a four-spin exchange interaction $J_{\text{ring}} = 16.5 \text{ meV}$ is included.

The local spin susceptibility of $\text{La}_6\text{Ca}_8\text{Cu}_{24}\text{O}_{41}$ was measured as the spin contribution to the ^{17}O NMR Knight shift at rung O(2) sites in the ladders.⁸ The observed behavior fits nicely with the Troyer model given by equation (11)

⁸ NMR as a local probe can selectively detect ^{17}O NMR signals from different oxygen sites in the ladder, O(1) and O(2), and in the chain, O(c), as well as ^{63}Cu NMR signals from the ladder and chain copper sites (see Fig. 9 in Sections 3 and 4.1.3).

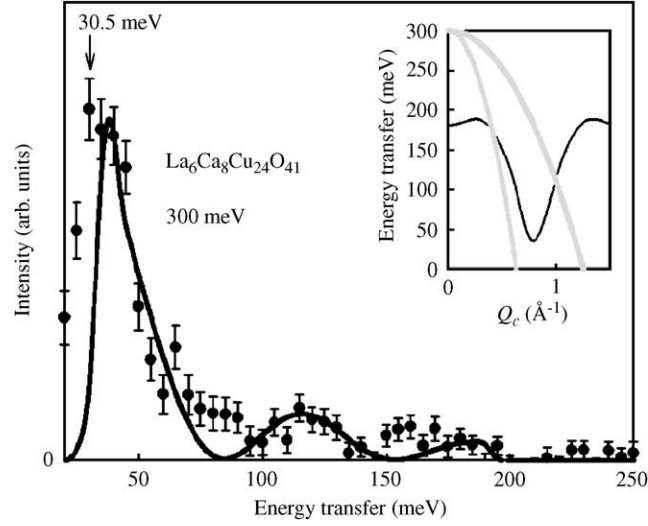


Fig. 41. Inelastic neutron scattering data of $\text{La}_6\text{Ca}_8\text{Cu}_{24}\text{O}_{41}$ with incident energy of 300 meV integrated over angles in the ac plane. The full line is a fit described in Ref. [45]. The inset shows the position of the dispersion relation and the portion of (Q, E) space, delimited by thick gray lines, over which the scattering is integrated. After Ref. [115].

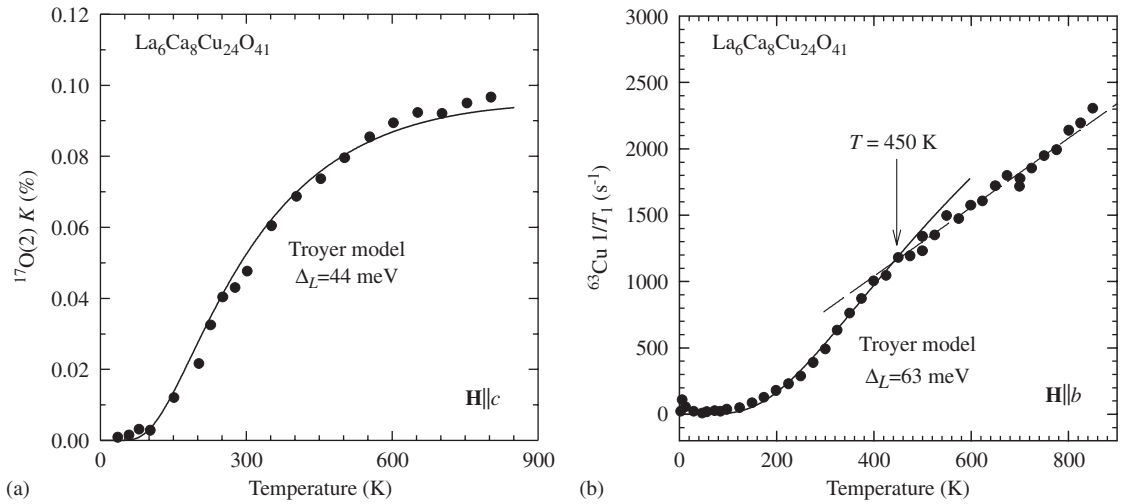


Fig. 42. (a) Local spin susceptibility of $\text{La}_6\text{Ca}_8\text{Cu}_{24}\text{O}_{41}$, proportional to the ^{17}O NMR Knight shift at O(2) sites in the ladders (full dots). The full line represents the fit to Troyer model. (b) Spin-lattice relaxation rate at ladder ^{63}Cu sites. The full line represents the fit to Troyer model. The dashed line represents Korringa-like behavior observed above $T \approx 450$ K. After Ref. [67].

(in Section 4), as shown in Fig. 42(a) [67]. However, the size of spin gap $\Delta_L = 44$ meV is somewhat larger than expected if compared with INS result, as well as with Δ_L extracted from both the static (bulk) and local susceptibility for the pure ladder material SrCu_2O_3 [65,117]. Moreover, the gap size for the ladders of $\text{La}_6\text{Ca}_8\text{Cu}_{24}\text{O}_{41}$ deduced from the activated behavior of the spin-lattice relaxation rate ($1/T_1$) [89]

$$1/T_1 = A \exp\left(-\frac{\Delta_L}{k_B T}\right) \quad (17)$$

is too large and amounts to $\Delta_L \approx 63$ meV (Fig. 42(b)) [67]. A similar discrepancy between Δ_L determined from the susceptibility ($\Delta_L \approx 36$ meV) and the spin-lattice relaxation rate ($\Delta_L \approx 59$ meV) was also found for the pure ladder

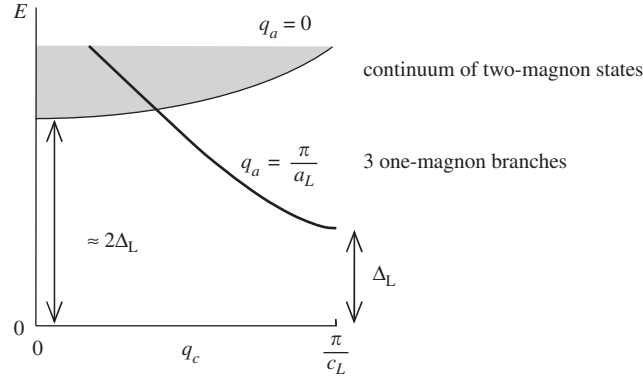


Fig. 43. Schematic illustration of the spin excitation spectrum for an isolated spin-1/2 ladder in the limit $J' \approx J$. After Ref. [89].

compound SrCu_2O_3 [65]. The question arises what might be the cause of the observed discrepancies. Another intriguing point concerns the temperature behavior of the spin-lattice relaxation rate measured at copper and oxygen sites: while both $1/T_1$ at ^{63}Cu and $1/T_1$ at ^{17}O exhibit similar activated behavior at low temperatures, only $1/T_1$ at the copper sites shows a change to a linear T dependence above $T \approx 450$ K.

Troyer et al. [89] calculated the whole excitation spectrum of an isolated spin-1/2 ladder described by the Hamiltonian

$$H = J \sum_{i,\lambda=-1,1} \mathbf{S}_{i,\lambda} \cdot \mathbf{S}_{i+1,\lambda} + J' \sum_i \mathbf{S}_{i,1} \cdot \mathbf{S}_{i,-1}, \quad (18)$$

where $\mathbf{S}_{i,\lambda}$ denotes spin-1/2 operators at ladder sites described by two indices: $\lambda = -1, 1$, which stands for two sites of the rung connecting ladder legs and i ($i = 1, \dots, N$), which denotes rungs along the leg direction. Note that the t - J - t' - J' Hamiltonian given by Eq. (7) reduces to (18) for zero doping. Using an improved quantum transfer-matrix method, Troyer et al. showed that the spectrum consists of two excitation bands as displayed in Fig. 43. The one-triplet excitations form a threefold degenerate band of collective excitations, magnons⁹ with the dispersion given by Eq. (14). The minimum of this band is at momentum $q_c = \pi/c_L$ along the ladder. The momentum along the rung is $q_a = \pi/a_L$, so that the antiferromagnetic zone center is located at $(\pi/a_L, \pi/c_L)$. The higher excited states form a continuum of two-magnon states with $q_a = 0$ and a minimum at $q_c = 0$. The minimum of the latter band is located at energies slightly larger than twice the gap $2\Delta_L$. At low temperatures the thermodynamics of the ladder is obtained by populating the modes with $q_c \approx \pi/c_L$ and $q_a \approx \pi/a_L$, since the smallest gap Δ_L is at these wave vectors. Therefore, only excitations with zero momentum transfer ($Q_a \approx 0$, $Q_c \approx 0$) contribute to susceptibility, as well as to the spin-lattice relaxation rate. Expressions (11) and (17) (in Section 4) are derived taking only these processes into account [89]. However, at high enough temperatures processes with momentum transfer different from zero, $Q_a \approx \pi/a_L$, $Q_c \approx \pi/c_L$ between one-magnon branch and continuum are particularly important since ladder has strong short range antiferromagnetic correlations. Using numerical quantum Monte Carlo methods, Sandvik et al. [118] were first to argue that the behavior of the spin-lattice relaxation rate is dominated by these processes in the upper range of temperatures covered in the experiments. Ivanov and Lee [119] calculated in the weakly coupled chain limit the contribution to $1/T_1$ at ^{63}Cu from processes with momentum transfer $(\pi/a_L, \pi/c_L)$. This contribution is of activation type with gap $2\Delta_L$ at lower temperatures:

$$1/T_1 \approx \frac{T}{\Delta_L} \exp\left(-\frac{2\Delta_L}{k_B T}\right), \quad (19)$$

but crosses over to a slowly decaying temperature dependence at $T \approx 450$ K. On the other hand, $(\pi/a_L, \pi/c_L)$ processes are considered to have minor, if any, influence on the relaxation at the oxygen sites: the hyperfine coupling constants

⁹ These collective excitations are not truly magnons, since there is no magnetic long-range order (see Section 3.2.2).

associated with the relaxation at the oxygen O(2) sites vanish for $\mathbf{Q} = (\pi/a_L, \pi/c_L)$, since the O(2) nuclear spin is coupled to the two nearest neighbor Cu spins (see Fig. 9 in Section 3). Also, this contribution is minor for the relaxation probed at O(1) sites [67]. Finally, Naef and Wang [120], by using transfer-matrix density-matrix renormalization group approach, calculated the temperature behavior of the spin-lattice relaxation rate at both the copper and oxygen sites for the experimentally relevant ratio of couplings: $J'/J \approx 0.6$ and 1. The relaxations at copper and oxygen sites are fully determined by appropriate combinations of dynamical structure factors with $Q_a = 0$ or π/a_L and $Q_c \approx 0$ or π/c_L : in addition to processes with $(0, 0)$ and $(\pi/a_L, \pi/c_L)$, they have also taken into account processes with $(\pi/a_L, 0)$ and $(0, \pi/c_L)$. In spite of the larger gap ($2\Delta_L$), they find that the contributions to the relaxation rate $1/T_1$ due to processes at $Q_a = \pi/a_L$ (i.e. scatterings between single magnon branch and continuum) dominate over those processes with $Q_a = 0$ in a wide intermediate temperature regime above about $0.35\Delta_L \approx 130$ K. This contribution accounts for the discrepancy between Δ_L extracted from INS and susceptibility measurements at one side and NMR measurements at the other. It is also crucial for the appearance of the crossover to linear T dependence in $1/T_1$ at ^{63}Cu experiments. However, a good quantitative agreement is missing concerning precise temperature dependence, which indicates the need to improve the determination of hyperfine coupling constants for the ladders. In addition, the results of Naef and Wang can reproduce the experimentally observed behavior of $1/T_1$ rather well only with $J'/J \approx 1$, indicating the inconsistency with J'/J estimates from inelastic neutron scattering and susceptibility measurements. Finally, the existence of two-magnon singlet bound states and the two-magnon continuum was verified by the optical conductivity experiments on $\text{La}_y\text{Ca}_{14-y}\text{Cu}_{24}\text{O}_{41}$ [121]. The observed data were described well using different theoretical approaches (Jordan–Wigner fermions and perturbation theory) for $J \approx 136$ meV and $J'/J \approx 0.8 - 1$.

The size of the spin gap for the undoped ladders in underdoped $(\text{La}, \text{Y})_y(\text{Sr}, \text{Ca})_{14-y}\text{Cu}_{24}\text{O}_{41}$, $y = 1$ and 2, (with five and four holes in the chains, respectively) [103], extracted from the activated behavior of NMR measured spin-lattice relaxation rate, is similarly enhanced as in the undoped $\text{La}_6\text{Ca}_8\text{Cu}_{24}\text{O}_{41}$ (with no holes in the chains) [67]. We conclude that the true spin gap size in undoped ladders of the undoped and underdoped $(\text{La}, \text{Y})_y(\text{Sr}, \text{Ca})_{14-y}\text{Cu}_{24}\text{O}_{41}$, as determined by inelastic neutron scattering and susceptibility measurements, is very close to the spin gap of undoped ladders in the pure-ladder compound SrCu_2O_3 and amounts to $\Delta_L \approx 33$ meV.

It is interesting also to mention that the magnon excitations in the undoped ladders contribute significantly to the thermal conductivity above 40 K due to their steep dispersion and related high velocity [122].

Finally we want to note that the charge environment of spins at Cu^{2+} ions in undoped ladders of $\text{La}_6\text{Ca}_8\text{Cu}_{24}\text{O}_{41}$ was probed by NMR measurements of ^{17}O nuclear quadrupole interactions [123]. As expected, only a minor change in the temperature dependence due to thermal expansion was found.

5.1.2. Doped ladders of $\text{Sr}_{14-x}\text{Ca}_x\text{Cu}_{24}\text{O}_{41}$

The gapped spin-liquid ground state is also established in doped ladders of the fully doped $\text{Sr}_{14-x}\text{Ca}_x\text{Cu}_{24}\text{O}_{41}$ (total hole count $n_h = 6$, for the distribution of holes between ladders and chains see Section 3.3). Inelastic neutron scattering measurements were performed on doped ladders of $\text{Sr}_{14}\text{Cu}_{24}\text{O}_{41}$ (approximately 0.8 holes per formula unit) [45], $\text{Sr}_{11.2}\text{Ca}_{2.8}\text{Cu}_{24}\text{O}_{41}$ [124] and on $\text{Sr}_{2.5}\text{Ca}_{11.5}\text{Cu}_{24}\text{O}_{41}$ (approximately 1.1–2.8 holes per formula unit) [125]. The results show that main features of the gapped spin-liquid state: the size of the spin gap Δ_L , the magnon band maximum C and the intraladder couplings J and J' along legs and rungs do not change substantially from that of the undoped ladders (see Table 2). A detailed inspection of Table 2 reveals that while Δ_L and J' remain unchanged upon doping ($\Delta_L \approx 32.5$ meV and $J' \approx 69.5$ meV), the ratio J'/J and the coupling constant along the legs J change slightly (for the relationship among Δ_L , C , J'/J and J see Eqs. (15) and (16)). The value $\Delta_L \approx 0.5J'$ follows from Eq. (16) for $J'/J \leq 1$ [66,116]. A remark should be also given concerning the anisotropy of the coupling constants J'/J . While $J'/J \approx 0.5$ for $\text{Sr}_{14}\text{Cu}_{24}\text{O}_{41}$ is suggested by INS measurements, almost isotropic values $J'/J \approx 1$ and 0.8 are derived by Raman spectroscopy [126,127].

Most important is the fact that the size of spin gap is robust for the Ca-substitution. This finding contrasts most of the existing theoretical models, which expect that the spin gap will reduce its size as the hole doping increases. At this point we remind that the presence of a finite spin gap is important for superconducting pairing of holes intrinsically doped into the ladders from the chains reservoir (see Section 5.2.2) [6,128–130]. The size of spin gap for the doped ladders in $\text{Sr}_{14-x}\text{Ca}_x\text{Cu}_{24}\text{O}_{41}$ was also extracted from either the activated behavior of ^{63}Cu nuclear spin-lattice relaxation rate $1/T_1$ using Eq. (17) (Fig. 44) or from Knight shift (local susceptibility) using Eq. (11) (in Section 4) [88,102,103,131–134]. All these measurements indicate that the size of the spin gap depends on the Ca content x (Fig. 45) at variance with the results obtained by inelastic neutron scattering (displayed in inset

Table 2

Spin gap Δ_L , magnon band maximum C , ratio of the intraladder couplings J' and J along rungs and legs J'/J

	Undoped ladders	Doped ladders $\text{Sr}_{14-x}\text{Ca}_x\text{Cu}_{24}\text{O}_{41}$		
	$\text{La}_6\text{Ca}_8\text{Cu}_{24}\text{O}_{41}$	$x = 0$	$x = 2.8$	$x = 11.5$
Δ_L (meV)	30.5 ± 5	32.5 ± 0.1	35	32.1 ± 0.3
C (meV)	191 ± 5	193.5 ± 2.4	145.8	157.8 ± 17.1
J'/J	0.50 ± 0.17	0.55 ± 0.01	1	0.77 ± 0.14
J (meV)	106 ± 28 (136 ± 28)	130 ± 3	70	90 ± 15
J' (meV)	53 ± 9 (67 ± 9)	71.4 ± 0.3	70	65 ± 10

J and J' extracted from inelastic neutron scattering experiments quoted in the text. The numbers in the brackets we obtained using Eqs. (15) and (16).

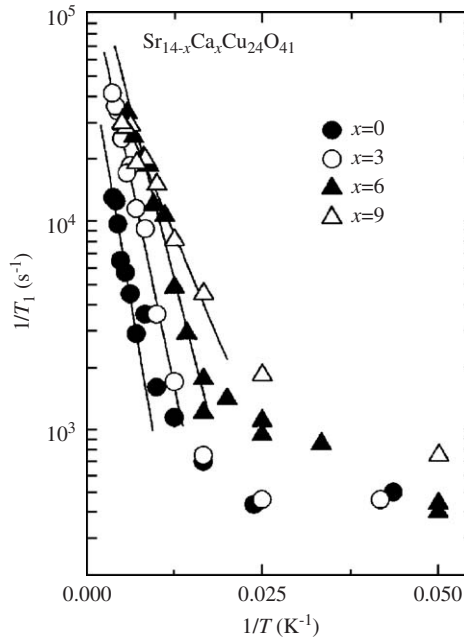


Fig. 44. Logarithm of the spin-lattice relaxation rate $1/T_1$ of ^{63}Cu NMR vs. inverse temperature of $\text{Sr}_{14-x}\text{Ca}_x\text{Cu}_{24}\text{O}_{41}$, $x = 0, 3, 6, 9$. Full lines are fits to the activated behavior given by Eq. (17). After Ref. [103].

of Fig. 45 and in Table 2). The thermal conductivity data as well indicate no change in the spin gap size for doped ladders [135,136]. It should be noted that only for $x < 5$ NMR results differ substantially from INS data and exhibit some dependence on Ca content. Similarly enhanced values of the spin gap, if compared to the INS results, were obtained in the case of undoped ladders (see Section 5.1.1). Indeed, the enhanced values of the gap for $x < 5$ result from fits of the NMR data by Eq. (11) (in Section 4) and (17) in the temperature range up to 300 K, while the almost x -independent values $\Delta_L \approx 32.5$ meV are always obtained from the INS data taken at low temperatures (20 K). Moreover, in the case the gap values are extracted from NMR data fitted mostly at temperatures lower than 100 K, they coincide nicely with INS results. Interestingly, for $T < 100$ K only excitations with zero momentum transfer ($Q_a \approx 0$, $Q_c \approx 0$) contribute to the susceptibility, as well as to the spin-lattice relaxation rate, so that Eqs. (11) and (17) are fully valid (see Section 5.1.1). In contrast to that, processes with momentum transfer (π/a_L , π/c_L) become dominant above the temperature of the order $\Delta_L/4$ independent of pressure and Ca-substitution [134]. Piskunov et al. [134] showed that the theory of undoped ladder is rather satisfactory to understand the spin excitation spectrum of doped ladder. Therefore, we conclude that the true spin gap size of doped ladders in $\text{Sr}_{14-x}\text{Ca}_x\text{Cu}_{24}\text{O}_{41}$, as well as of undoped ladders in $(\text{La},\text{Y})_y(\text{Sr},\text{Ca})_{14-y}\text{Cu}_{24}\text{O}_{41}$ amounts to $\Delta_L \approx 32.5$ meV and is essentially unchanged from the one in the

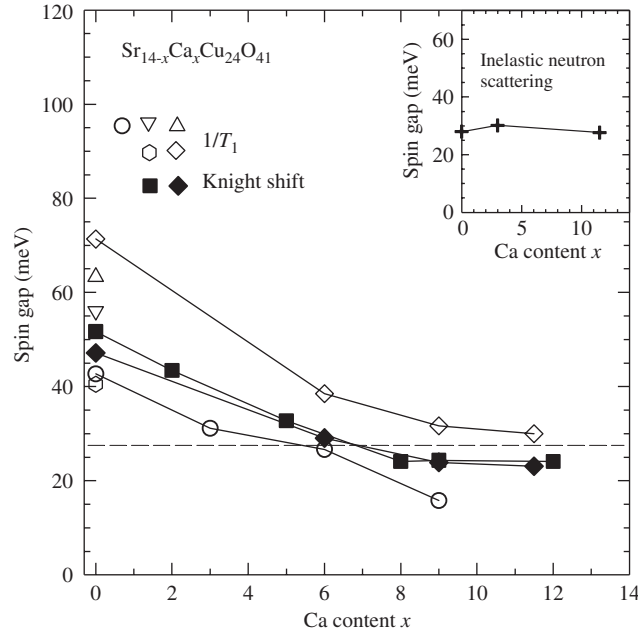


Fig. 45. Size of the spin gap in $\text{Sr}_{14-x}\text{Ca}_x\text{Cu}_{24}\text{O}_{41}$ for various Ca contents x . The plot summarizes the results obtained by different groups, as quoted in the text, using nuclear magnetic resonance measurements of relaxation rate $1/T_1$ and Knight shift (main panel) or inelastic neutron scattering (inset) techniques. The dashed line in the main panel indicates the spin gap size determined by inelastic neutron scattering.

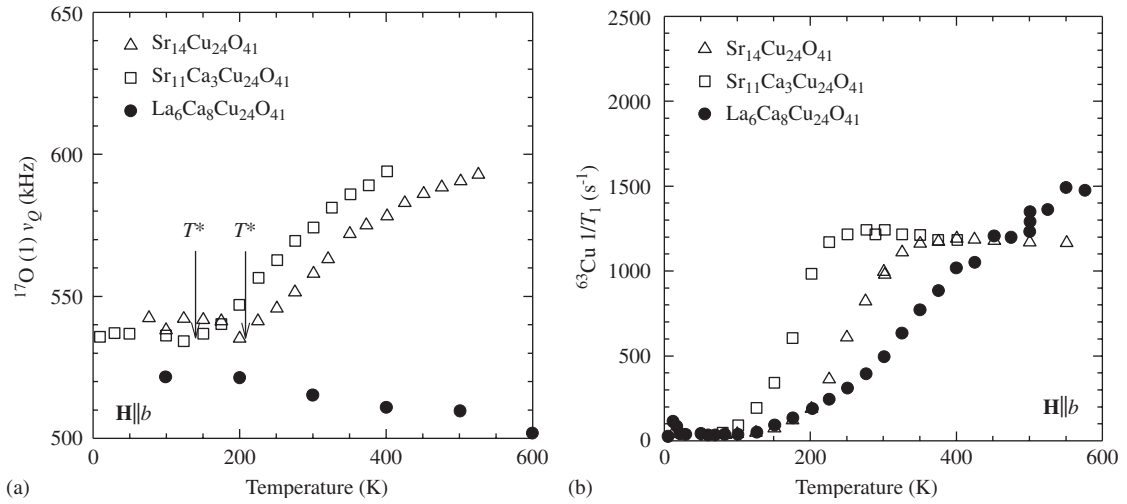


Fig. 46. (a) Quadrupole moment ν_Q at ladder leg oxygen site ($^{17}\text{O}(1)$) for doped ladders of $\text{Sr}_{14-x}\text{Ca}_x\text{Cu}_{24}\text{O}_{41}$ ($x=0, 11$). The behavior for undoped ladders of $\text{La}_6\text{Ca}_8\text{Cu}_{24}\text{O}_{41}$ is shown for comparison. T^* is the crossover temperature as explained in the text. (b) ^{63}Cu spin-lattice relaxation rate $1/T_1$ for doped ladders of $\text{Sr}_{14-x}\text{Ca}_x\text{Cu}_{24}\text{O}_{41}$ ($x=0, 11$). The behavior for undoped ladders of $\text{La}_6\text{Ca}_8\text{Cu}_{24}\text{O}_{41}$ is shown for comparison. After Ref. [67].

pure-ladder compound SrCu_2O_3 . Going one step further, the question arises whether the spin gap remains so robust when pressure is applied to $\text{Sr}_{14-x}\text{Ca}_x\text{Cu}_{24}\text{O}_{41}$ and doped ladders are driven to superconductivity. We will address this issue in Section 5.2.2.

The next interesting issue concerns the charge environment of copper spins in the doped ladders of $\text{Sr}_{14-x}\text{Ca}_x\text{Cu}_{24}\text{O}_{41}$, probed by NMR measurements of ^{17}O nuclear quadrupole interaction ν_Q (Fig. 46(a)) [67]. While an almost temperature-independent behavior is found at lower temperatures, as for the undoped ladders which are true insulators, for doped

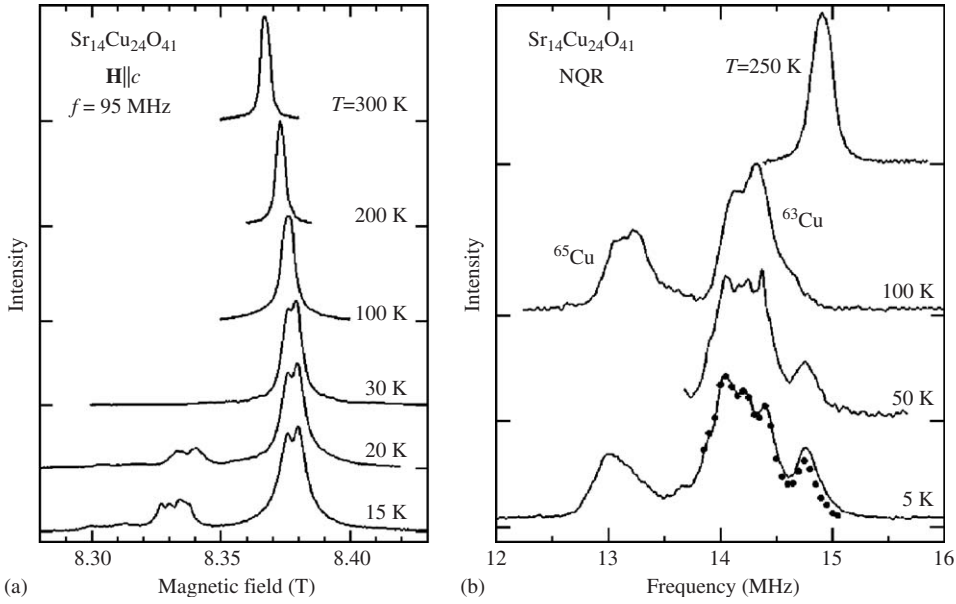


Fig. 47. Temperature variation of the NMR and the NQR spectra at the ladder ^{63}Cu sites of $\text{Sr}_{14}\text{Cu}_{24}\text{O}_{41}$ is shown in (a) and (b), respectively. The NQR feature at the ladder ^{65}Cu sites is also shown centered at 13 Hz. After Ref. [88].

ladders ν_Q starts to increase above crossover temperature $T^*(x=0) \approx 210$ K and $T^*(x=3) \approx 140$ K. In order to better understand this result, it is instructive to check the temperature dependence of ^{63}Cu spin-lattice relaxation rate $1/T_1$ plotted in Fig. 46(b). The displayed data reveal that a linear temperature dependence at high temperatures found for undoped ladders is replaced by a nearly T -independent behavior for doped ladders. Moreover, the overall crossover behavior shifts to lower temperatures for higher Ca contents, similarly to the change of T^* as extracted from ν_Q . Close inspection of the data reveals that T^* (Fig. 46(a)) corresponds to the onset of the crossover from the spin gap to the paramagnetic regime (Fig. 46(b)). Since the spin-lattice relaxation rate, which locally probes at ladder oxygen sites does not change compared to the undoped case, this result suggests that doped holes completely alter the low-energy spin excitation spectrum of the undoped ladder in the vicinity of momentum transfer $(\pi/a_L, \pi/c_L)$ (see Section 5.1.1). This is in contrast with the case of the CuO_2 square lattice, where no change was observed between undoped and hole-doped superconducting systems [137]. On the basis of all these results, Imai et al. [67] proposed that there are no freely mobile holes below T^* in the gapped spin-liquid ground state of doped ladders, while the presence of mobile holes above T^* frustrates the gapped spin-liquid ground state and transforms it into a basically paramagnetic state. Piskunov et al. [134] showed that as the temperature increases, the legs in the ladder become gradually decoupled in their magnetic properties and the magnitude of the wave vector dependent dynamical structure factor describing $(\pi/a_L, \pi/c_L)$ processes (and determining the temperature dependence of the nuclear spin lattice relaxation rate) becomes temperature-independent. In this way, the crossover to the paramagnetic regime is identified.

The behavior of the nuclear quadrupole interaction ν_Q at ^{17}O as a function of Ca content and temperature was studied in depth by Thurber et al. [123]. They argue that the changes in the quadrupole moment ν_Q are consistent with an increase of the effective hole concentration in the doped ladders above T^* . Taking into account that the hole concentration below T^* can appear small if holes are localized within NMR time scale ($\approx \mu\text{s}$), this observation confirms T^* as a crossover temperature above which holes in the ladders become delocalized. However, this assignment is at odds with the fact that no broadening or splitting of the NMR line is observed below T^* (Fig. 47(a)) as expected in the case of localized holes [88]. The NMR line splitting and broadening is clearly found for charge order in the chains (see Section 4.1.3). Further, at the first sight, NQR spectra displayed in Fig. 47(b) indicate the site distinction with different charge distribution environment established at low temperatures and only a single, well defined peak at 250 K. Interestingly, the splitting of the line is temperature-independent for $T < 100$ K in contrast to what is observed for the chains (see Fig. 30). The latter feature might be taken as an indication that the long-range hole localization is well established already (at least) below 100 K, but a missing splitting of the NMR line at the ladder ^{63}Cu sites prevents

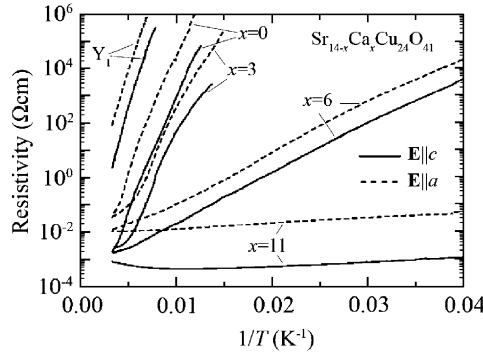


Fig. 48. Arrhenius plot of dc resistivity along the c -axis (full lines) and the a -axis (dashed lines) of $\text{Sr}_{14-x}\text{Ca}_x\text{Cu}_{24}\text{O}_{41}$ for various x at ambient pressure. The resistivity of underdoped $\text{Y}_1\text{Sr}_{13}\text{Cu}_{24}\text{O}_{41}$ (labeled as Y_1) is plotted for comparison. After Ref. [43].

any firm conclusion. Due to that, Thurber et al. [123] suggested an alternative assignment of T^* as the temperature below which the back-transfer of holes from ladders to chains takes place (see Section 3.3.3). Nevertheless this scenario cannot be simply accepted, because the strong quadrupole relaxation below 200 K clearly indicates the presence of holes in the ladders [88]. As Takigawa et al. pointed out, the relaxation is almost entirely magnetic above 200 K, while quadrupole contributions appear below $T^* \approx 200$ K and they become dominant below 100 K. The interesting point is that the magnetic relaxation prevails again at temperatures ≤ 20 K.

We conclude this section with a few remarks. First, since no quadrupole relaxation was observed in the chains, the hole mobility in the chains and ladders can be clearly distinguished: holes are fully localized in the chains, while they are rather mobile in the ladders (even below T^*). This immediately implies that if there is charge order in the ladders below some temperature, it must be certainly of different type than in the chains. The second remark concerns the temperature behavior of the quadrupole relaxation. It shows the existence of fluctuations in the electric field gradient, which are too slow to account for the single-particle conductivity. The microscopic origin of this motion is still an open question.

Finally, the magnon contribution to thermal conductivity being enormous in the undoped ladders (above 40 K), becomes smaller in the doped ladders. This reveals that the doped holes represent the main source of scattering of magnetic excitations [122,135]. We will address more of these issues in Sections 5.3.1 and 5.3.2.

5.2. Superconductivity in doped ladders of $\text{Sr}_{14-x}\text{Ca}_x\text{Cu}_{24}\text{O}_{41}$

A crucial breakthrough in the field of chains and ladders occurred in 1996, when Uehara et al. [5] discovered superconductivity in $\text{Sr}_{14-x}\text{Ca}_x\text{Cu}_{24}\text{O}_{41}$, $x = 13.6$ at a high pressure of 3 GPa. This discovery triggered an enormous effort devoted to the understanding of ladder compounds which has barely diminished after ten years.

5.2.1. dc electrical transport

For $\text{Sr}_{14-x}\text{Ca}_x\text{Cu}_{24}\text{O}_{41}$ materials the total hole count yields $n_h = 6$. At high temperatures, almost one hole out of six is transferred from the chains to the ladders. These holes are relatively mobile and are responsible for electrical transport observed in single crystals or in polycrystalline samples of $\text{Sr}_{14-x}\text{Ca}_x\text{Cu}_{24}\text{O}_{41}$ compounds [43,70,138–145]. A first comprehensive study of the anisotropic electrical resistivity on the single crystals of $\text{Sr}_{14-x}\text{Ca}_x\text{Cu}_{24}\text{O}_{41}$, $x = 0, 3, 6, 11$ at ambient pressure was performed by Motoyama et al. [43]. In Fig. 48 $\ln \rho$ vs. $1/T$ plots are shown for the resistivity along the c - (parallel to the legs of ladders) and a -axis (parallel to the rungs of ladders). Even the parent compound $\text{Sr}_{14}\text{Cu}_{24}\text{O}_{41}$ is not highly insulating if compared to the underdoped $\text{Y}_1\text{Sr}_{13}\text{Cu}_{24}\text{O}_{41}$ with five holes in the chains and none in the ladders (see Section 4.2.2). This is consistent with the optical results showing the plasma edge at about 0.5 eV in $\text{Sr}_{14}\text{Cu}_{24}\text{O}_{41}$ (see Section 5.3.4), while no plasma edge is found for $y = 3$ [77]. Room temperature c -axis conductivity value of $\text{Sr}_{14}\text{Cu}_{24}\text{O}_{41}$ is about $500 \Omega^{-1} \text{cm}^{-1}$ and increases slightly with Ca-substitution. All the compounds except $x = 11$, which behaves metallic along the c -axis but only down to about 100 K, exhibit a rapid increase in the resistivity upon cooling following the activated behavior of insulators. The value of a -axis resistivity

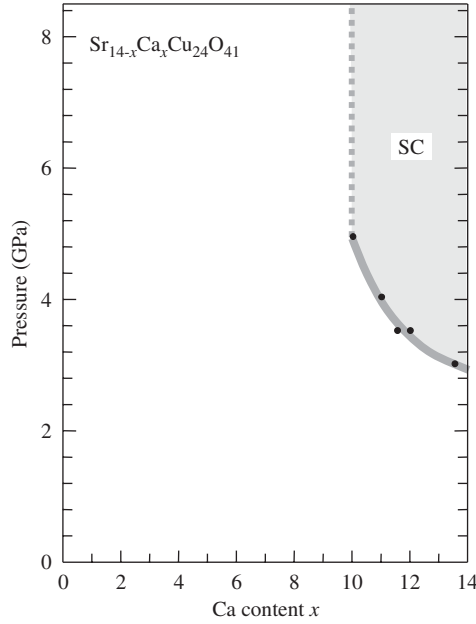


Fig. 49. The phase diagram illustrating how SC evolves in $\text{Sr}_{14-x}\text{Ca}_x\text{Cu}_{24}\text{O}_{41}$ as a function of Ca content x and pressure. After Ref. [143].

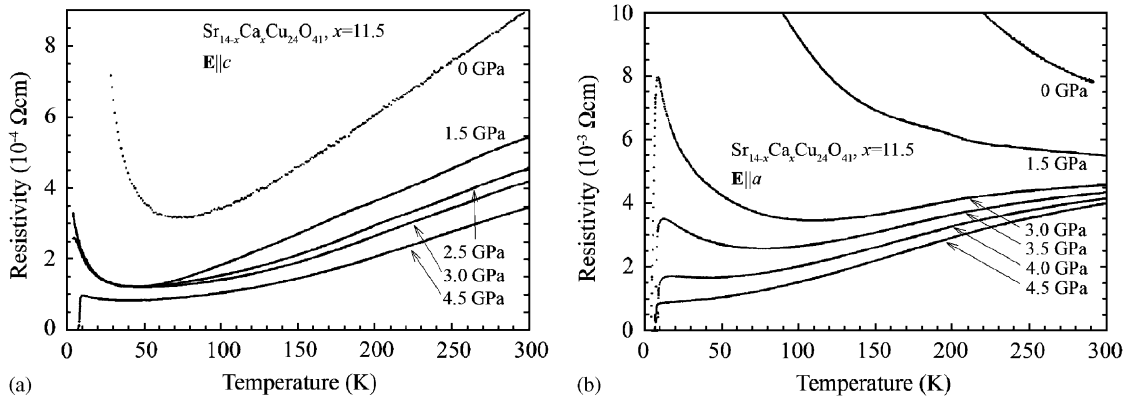


Fig. 50. Temperature dependence of dc resistivity along the c -axis (a) and along the a -axis (b) under various pressures in $\text{Sr}_{14-x}\text{Ca}_x\text{Cu}_{24}\text{O}_{41}$ with $x = 11.5$. After Ref. [146].

(ρ_a) is larger than the c -axis resistivity (ρ_c) by one to two orders of magnitude. The anisotropy ratio, ρ_a/ρ_c , does not strongly depend on x at high temperatures. The issue of the anisotropy as a function of temperature and Ca-substitution will be addressed in more detail in Section 5.3.1.

The remarkable theoretical prediction of superconductivity (SC) for the isolated ladder [6] was realized experimentally by application of high pressure on $\text{Sr}_{14-x}\text{Ca}_x\text{Cu}_{24}\text{O}_{41}$ compounds with Ca content x in the range $10 \leq x \leq 13.6$ (Fig. 49) [143,146]. The initial discovery has been reported by Uehara et al. [5] and Nagata et al. [147]. The former work was done on the $x = 13.6$ compound and the superconductivity was established below $T_c = 12$ K under pressure $P_c = 3$ GPa, while the latter was done on the $x = 11.5$ compound and SC was found at $T_c = 6.5$ K under $P_c = 4.5$ GPa. In Fig. 50 the results of transport measurements under various hydrostatic pressures are displayed. It is nicely seen how the application of pressure on the compound with high Ca content $x = 11.5$ suppresses the remaining insulating behavior and how superconductivity sets in. The observation of a metallic transport not only along ladders, but also along the ladder rungs, in the normal phase, below which superconductivity is established, suggests that pressure triggers the

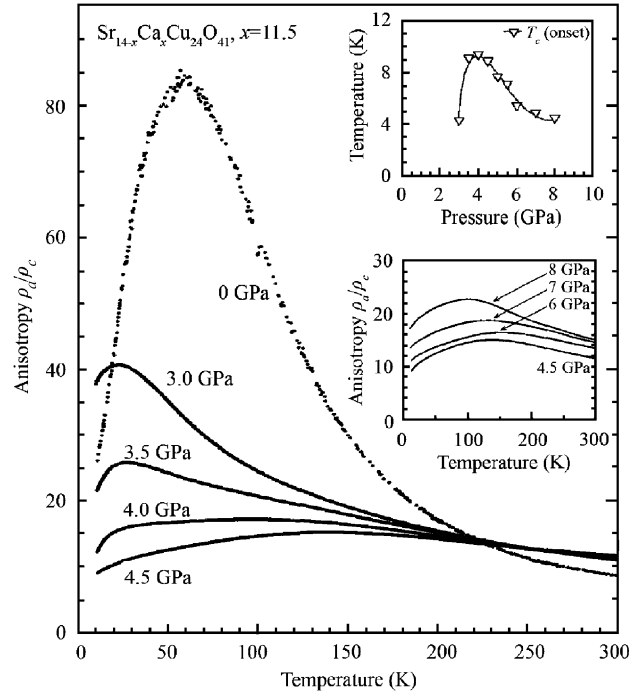


Fig. 51. The temperature variation of the resistivity anisotropy of $\text{Sr}_{14-x}\text{Ca}_x\text{Cu}_{24}\text{O}_{41}$, $x = 11.5$ at various pressures is displayed in the main panel and the lower inset. The upper inset shows the pressure dependence of the superconducting transition temperature. After Ref. [146].

crossover from one to two dimensions, and that SC might be a phenomenon in a two-dimensional anisotropic electronic system. Indeed, the temperature dependent anisotropy ratio ρ_a/ρ_c at varying pressures seems to confirm this conjecture (Fig. 51). The room temperature anisotropy is about 10 and does not change much with pressure. However, at ambient pressure, the ratio increases substantially with decreasing temperature, indicating incoherent transverse (interladder, along the a -axis) transport. The temperature behavior of the resistivity anisotropy in the compounds with high Ca content is consistent with the results obtained by X-ray diffraction for the $x = 13.6$ compound [148]. The lattice in the ladder plane shrinks anisotropically with decreasing temperature: from room temperature down to $T = 10$ K, the c -axis lattice parameter decreases 2.5 times more than the a -axis. At high pressure, the thermal compressibility of the a -axis lattice parameter becomes larger than the compressibility of the c -axis at low temperatures. Concomitantly, with increasing pressure the enhancement of the resistivity anisotropy gets less pronounced, and the occurrence of superconductivity basically correlates with the suppression of the temperature variation of the resistivity anisotropy and a crossover to the coherent interladder transport. More importantly, the highest T_c is achieved (inset of Fig. 51) at a pressure value for which the anisotropy is the smallest at low temperatures (implying an almost temperature-independent ratio). Another evidence for the two-dimensional charge transport, initiated by high pressure, is given by the value of the geometrical average resistivity $\rho_{av} = (\rho_a\rho_c)^{1/2}$ per one ladder plane, which becomes close to the universal value $h/4e^2$ at pressures when superconductivity is established [149]. Hence, the effect of pressure is distinct from that of Ca-substitution as far as the conductivity anisotropy is concerned, although the latter might be considered as a chemical pressure due to smaller ionic radius of Ca leading to lattice contraction [48].

The next important issue is the degradation of the SC transition temperature T_c when a certain pressure value is exceeded, eventually leading to disappearance of superconductivity. The suggestion put forward by Nagata et al. [146] is that too high pressure induces strong interladder coupling and transforms the electronic system of the ladders into a three-dimensional Fermi liquid not favorable for superconductivity. This proposal is supported by the temperature dependent resistivity

$$\rho(T) = \rho_0 + AT^n, \quad (20)$$

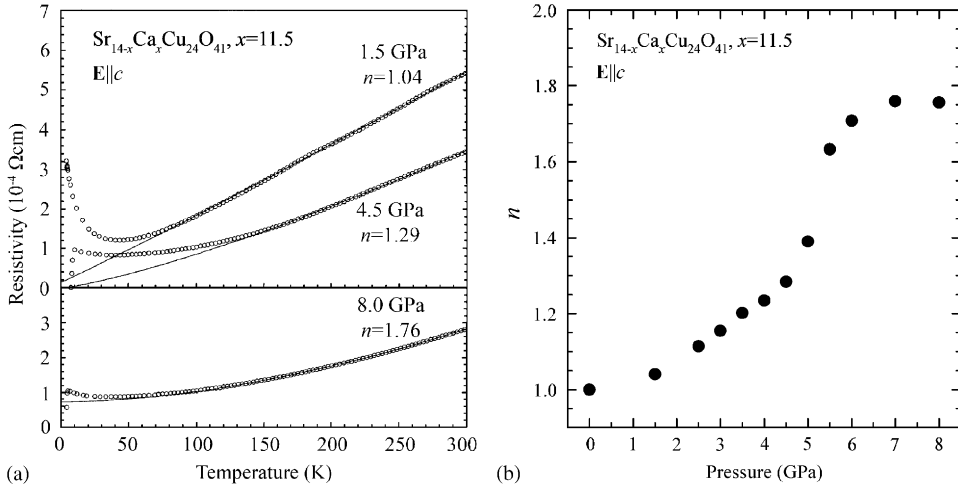


Fig. 52. (a) Temperature dependence of the resistivity along the c -axis (along the ladder legs) of $\text{Sr}_{14-x}\text{Ca}_x\text{Cu}_{24}\text{O}_{41}$, $x = 11.5$ at various pressure values in the range where superconductivity is established. The full lines are fits to power-law behavior $\rho = \rho_0 + AT^n$. (b) The exponent n as a function of pressure. After Ref. [146].

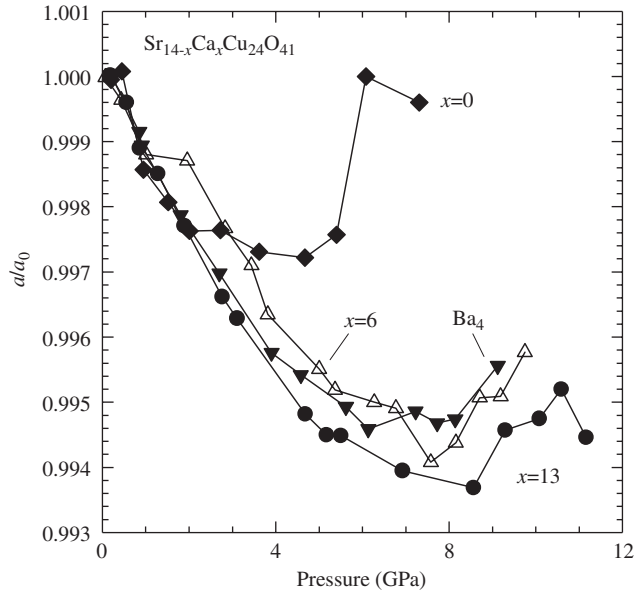


Fig. 53. The effect of pressure on the a -axis cell parameter of $\text{Sr}_{14-x}\text{Ca}_x\text{Cu}_{24}\text{O}_{41}$ for three representative Ca content x . Data for $\text{Sr}_{10}\text{Ba}_4\text{Ca}_{24}\text{O}_{41}$ are also shown. After Ref. [150].

which changes its power-law n as pressure is applied (see Fig. 52(a)). With increasing pressure $\rho(T)$ varies from T linear (at 1.5 GPa) to an approximate T^2 (at 8 GPa) dependence. Further, an anomalous increase of the exponent n between 5 and 7 GPa is striking and indicates that some abrupt change happens there (see Fig. 52(b)). It is interesting that in the same pressure range (5–8 GPa) a lattice anomaly is detected by synchrotron X-ray diffraction studies of $\text{Sr}_{14-x}\text{Ca}_x\text{Cu}_{24}\text{O}_{41}$ [150]. As seen in Fig. 53, the cell parameter a strongly increases at higher pressure values. This anomaly happens at $p_a \approx 5$ GPa for the parent compound ($x = 0$) and shifts to higher pressure with increasing Ca content in a nonlinear manner: at $p_a \approx 7.5$ GPa for $x = 6$ and at $p_a \approx 8.5$ GPa for $x = 13$. It might be that these two events in the transport and crystallographic properties are correlated. An additional signature that the suppression of the superconductivity might be related to this lattice anomaly, comes from the observation that superconductivity does not

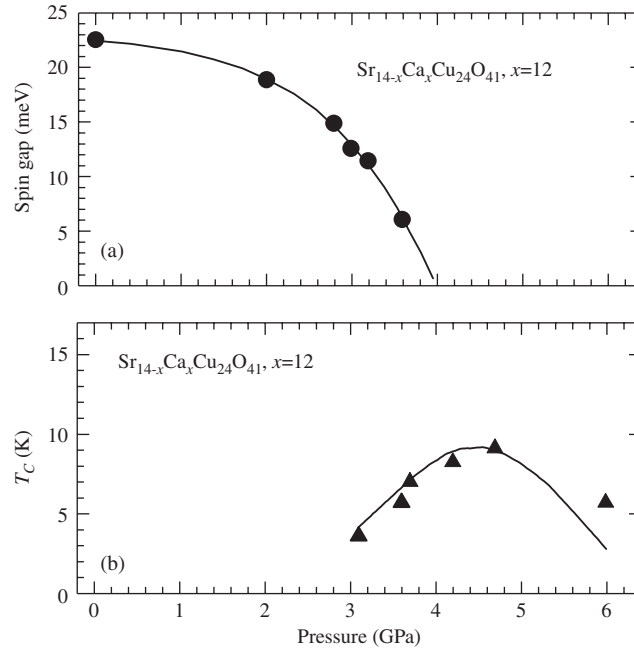


Fig. 54. The effect of pressure (a) on the size of the spin gap in $\text{Sr}_{14-x}\text{Ca}_x\text{Cu}_{24}\text{O}_{41}$, $x = 12$ obtained from the fits to the Knight shift data using Eq. (11), and (b) on the superconducting transition temperature T_c . The full lines are guides for the eye. After Ref. [133].

occur at least up to 8 GPa [143], although a metallic behavior for $\text{Sr}_{14-x}\text{Ca}_x\text{Cu}_{24}\text{O}_{41}$, $x = 0$ is achieved under pressure of 6.5 GPa. Indeed, note that the pressure of 6.5 GPa is higher than the value ($p_a \approx 5$ GPa) where the lattice anomaly happens. Pachot et al. suggested that the anomaly could originate in the abrupt vanishing of the ladder and chain layer buckling induced by the applied pressure. A sudden increase of the a cell parameter, while c - and b -axis parameters decrease monotonously with pressure, might either imply a smaller interladder coupling, or a smaller intraladder rung coupling.

The following final remark on this topic is in order. At room temperature, the only important changes by Ca-substitution and by applying pressure concern the b lattice parameter (it decreases for 6–8%, either by Ca-substitution from $x = 0$ to 13, or under 8 GPa for each x), while the changes of the a and c lattice parameters are small and comparable in size ($\approx 1\%$). The decrease of b lattice parameter gradually increases the coupling between ladders and chains; on the other hand, the (much smaller, but still detectable) decrease of the lattice parameters within the ladder plane does not change the charge transport anisotropy in this plane. It is important to realize that this conclusion is valid only at high temperatures, while changes of lattice parameters at low temperatures at ambient pressure and under high pressure are such that they allow to understand how the ladder plane charge transport anisotropy depends on Ca-substitution and pressure [148]. This issue is certainly of the foremost importance and will be addressed again in the following section, as well as in Sections 5.3.1 and 6.

5.2.2. Nuclear magnetic resonance under pressure

The relationship and the interplay between superconductivity and spin gap in the doped ladders of $\text{Sr}_{14-x}\text{Ca}_x\text{Cu}_{24}\text{O}_{41}$ are of central importance. Superconductivity is established under pressure at Ca-substitution levels where a finite spin gap is observed in the studies without pressure (see Sections 5.1.2 and 5.2.1). The important question is how the spin gap, which remains robust under Ca-substitution, evolves under pressure and whether it remains finite when superconductivity sets in.

NMR studies at ^{63}Cu or ^{17}O ladder sites under pressure were performed by Piskunov et al. [133,134] and by Fujiwara et al. [151]. The first important result is that the increasing pressure reduces the spin gap size for the superconducting $\text{Sr}_{14-x}\text{Ca}_x\text{Cu}_{24}\text{O}_{41}$ and that the spin gap remains finite when SC is established as depicted in Fig. 54. The latter would imply that the superconductivity in ladders is intimately connected with the existence of the spin-liquid state,

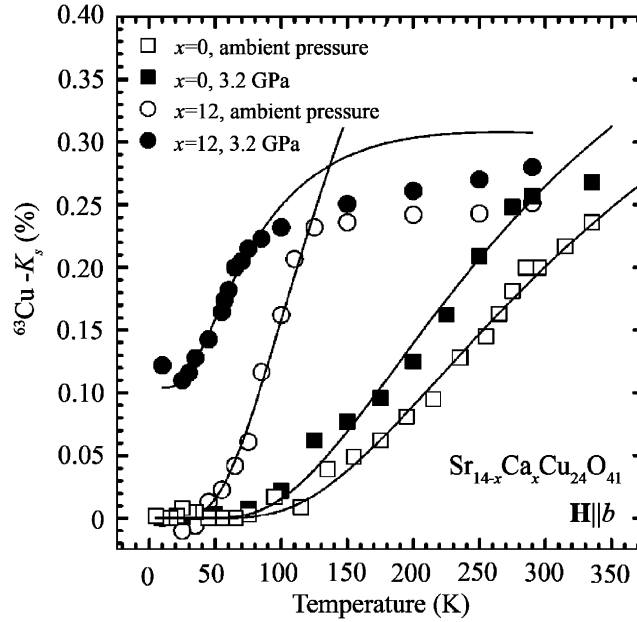


Fig. 55. Temperature dependence of the ^{63}Cu Knight shift (spin part) for $\text{Sr}_{14-x}\text{Ca}_x\text{Cu}_{24}\text{O}_{41}$, $x = 0$ and $x = 12$ at two representative pressures. The full lines are the fits to the data using Troyer model, Eq. (11). After Ref. [134].

as originally predicted by Dagotto et al. [6]. However, a more complex picture has to be considered, since the pressure introduces low-lying spin excitations giving rise to a residual spin susceptibility at low temperatures (see Fig. 55). It should be noted that there is no residual susceptibility at low temperatures for non-superconducting $\text{Sr}_{14}\text{Cu}_{24}\text{O}_{41}$ under equally high pressure. Concomitantly with the appearance of a finite residual susceptibility detected by Knight shift measurements, a Korringa-like contribution emerges in the behavior of the nuclear spin-lattice relaxation rate $1/T_1$ ($T_1 \cdot T = \text{const.}$). The third important result is the presence of a spin-lattice relaxation rate enhancement in the superconducting state. Fujiwara et al. [151] interpreted this peak as a Hebel–Slichter coherence peak, while they excluded the possibility that the observed peak is due to the field fluctuations generated by the vortex dynamics. The overall behavior is displayed in Fig. 56. The coherence peak would indicate that no nodes appear in the superconductivity gap, meaning that SC has an s -wave-like character. The first two results are a necessary condition for the observation of superconductivity: the existence of zero-frequency spin fluctuations within the magnon gap. This condition is met only at high pressure (≥ 3.2 GPa, as displayed in Fig. 49) in the compounds with high Ca content ($10 \leq x \leq 13.6$).

Therefore, the role of applied pressure, stemming out from the NMR results, is to dissociate bound holes in the ladder rungs (see Section 2.3) and to increase the number of mobile quasi-particles at low temperatures. These quasi-particles have a finite DOS at the Fermi level and contribute to the superconducting instability. In a single ladder approach, this scenario is schematically illustrated in Fig. 57 [151]. The ground state of doped ladders in $\text{Sr}_{14-x}\text{Ca}_x\text{Cu}_{24}\text{O}_{41}$ at ambient pressure is depicted in Fig. 57(a): spins are coupled in the rungs giving rise to the gapped spin-liquid ground state and doped holes are paired on the same rung in order to minimize their energy (see Section 2.3). The applied pressure on $\text{Sr}_{14-x}\text{Ca}_x\text{Cu}_{24}\text{O}_{41}$ with high Ca content dissociates bound holes in the rungs and creates quasi-particles with spin-1/2 and charge $|e|$ (denoted by a rectangle in Fig. 57). In the normal state at high temperatures, singlet-triplet excitations dominate, which causes the activated behavior of the nuclear spin-lattice relaxation rate $1/T_1$ (Fig. 57(b)). At lower temperatures (< 40 K), the majority of copper spins form singlet state, while the spins-1/2 of the quasi-particles move rather freely and contribute to the Korringa-like relaxation of $1/T_1$ (Fig. 57(c)). These quasi-particles contribute to a finite density of states at the Fermi level as detected by non-zero Knight shift. Finally, below the superconducting transition temperature T_c , SC can be realized by pairing of two quasi-particles Fig. 57(d). If this scenario applies, the spin gap does not contribute to the pairing mechanism of the SC. Note, however, that a single ladder model cannot be used to describe the superconductivity in the ladders of $\text{Sr}_{14-x}\text{Ca}_x\text{Cu}_{24}\text{O}_{41}$. A realistic description should also take into account the pressure induced crossover from one to twodimensions, as explained in Section 5.2.1.

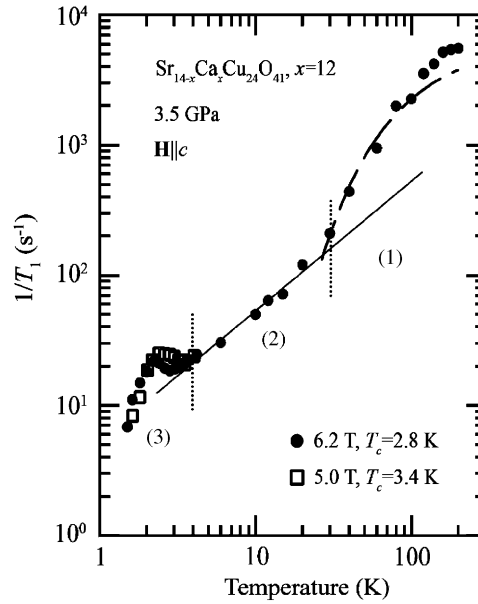


Fig. 56. Nuclear spin-lattice relaxation rate $1/T_1$ at ^{63}Cu ladder sites for $\text{Sr}_{14-x}\text{Ca}_x\text{Cu}_{24}\text{O}_{41}$, $x = 12$ under pressure of 3.5 GPa. Three temperature ranges can be distinguished: (1) spin gap (the dashed line is the fit to data using Eq. (17)); and (2) Korringa-like behavior (the full line is the fit to the data using equation $T_1 \cdot T = \text{const.}$) in the normal state. In the superconducting state (3) an enhancement of spin-lattice relaxation rate, which might be interpreted as a Hebel–Slichter coherence peak is visible. After Ref. [151].

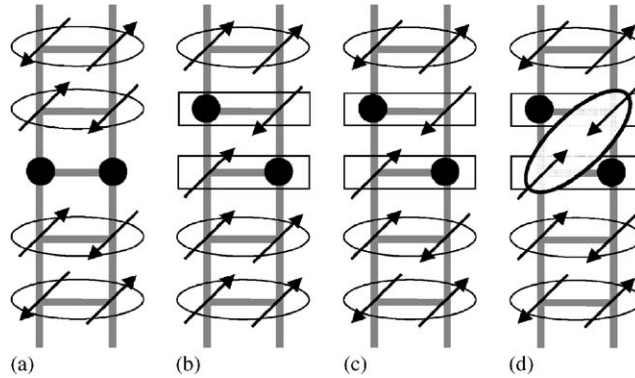


Fig. 57. Schematic illustration of the scenario in a single ladder approach leading to superconductivity in the ladders of $\text{Sr}_{14-x}\text{Ca}_x\text{Cu}_{24}\text{O}_{41}$ is shown [151]. Pressure-induced crossover from one to two dimensions is here entirely neglected. (a) ground state of doped ladders at ambient pressure, (b) normal state at high temperatures under pressure, (c) normal state at low temperatures above superconducting transition temperature T_c , (d) superconducting state. Note that in a two-dimensional system the superconducting state can be realized by pairing of two quasi-particles originating at two different ladders.

Finally, we should point out that these quasi-particles appear as being similar to quasi-particles in conventional Fermi liquid. A theoretical model, which seems to be appropriate for the case of doped ladders in $\text{Sr}_{14-x}\text{Ca}_x\text{Cu}_{24}\text{O}_{41}$ under pressure has been developed by Tsunetsugu et al. [152]. They show that the excitation spectrum of the ladders sufficiently away from half-filling consists of excitations due to a limited number of holon–spinon quasi-particles, which carry charge $+|e|$ and spin-1/2 in addition to a well known triplet collective mode (magnon-like, see Fig. 43). The holon–spinon quasi-particles are generated when the bound hole pair in the rung dissociates into two separate holons, each bound to a spinon on the same rung (Fig. 57(c)). As for the triplet mode, it is due to a singlet pair of spins to form a spin-triplet in the rung, spatially separated from the doped hole pair. Therefore the excitation spectrum of undoped

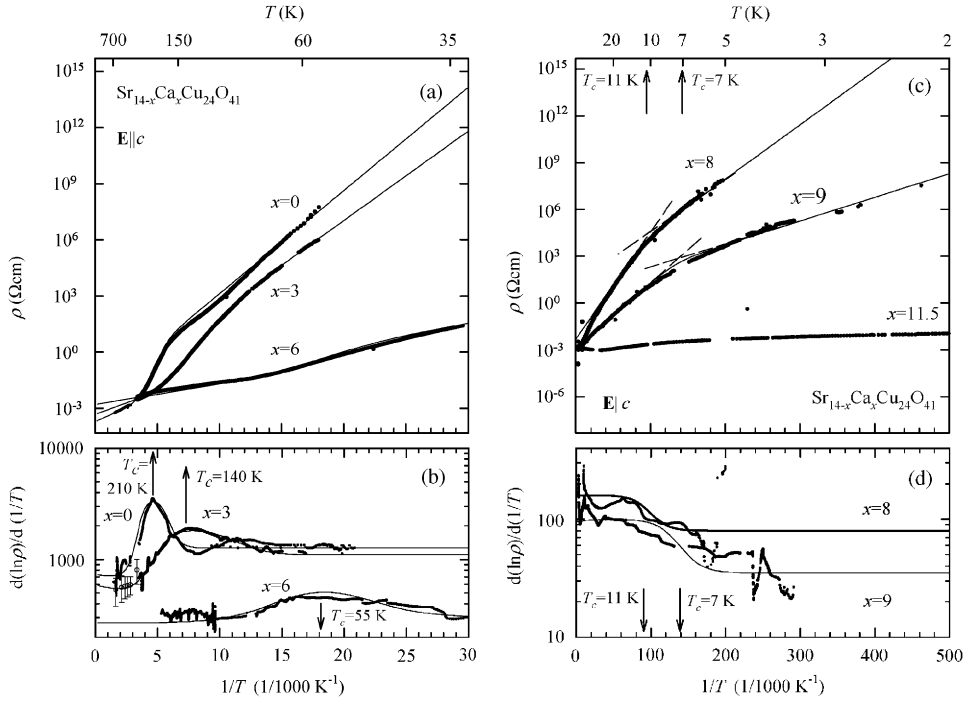


Fig. 58. dc resistivity along c -axis ((a), (c)) and logarithmic derivatives ((b), (d)) as a function of inverse temperature of $\text{Sr}_{14-x}\text{Ca}_x\text{Cu}_{24}\text{O}_{41}$ for various x . Phase transition temperatures T_c are indicated by arrows. The full lines are guides for the eye in the transition region, while above and below they are based on the fits to $\ln\rho$ vs. T^{-1} . After Ref. [145].

ladders, as illustrated in Fig. 43 and described in Section 5.1.1, remains valid for doped ladders in $\text{Sr}_{14-x}\text{Ca}_x\text{Cu}_{24}\text{O}_{41}$ at ambient pressure, but requires reconsideration when pressure is applied (and Ca content is high) and quasi-particles play an important role [134].

At the end, a remark is in order which concerns the gradual suppression of the resistivity rise along the a -axis (ladder rungs) under pressure (see Fig. 50 (b)). Piskunov et al. [134] suggested that it might be attributed to an increasing number of single quasi-particles. This interpretation is based on the assumption (in analogy to underdoped high-temperature superconducting cuprates [153]) that the insulating behavior of the resistivity along the a -axis is due to the reduction of the interladder hopping probability for bound hole pairs as compared to that of quasi-particles. A very recent NMR study by the same authors [86] suggests that a finite residual spin susceptibility at low temperatures which grows with pressure might be, at least partially, related to a pressure-induced increased number of holes transferred from the chains to the ladders.

At this point, the nature of insulating phase and the related charge dynamics in the ladder layers (i.e. along the c - and a -axis), as well as the mechanism which governs its suppression by Ca-substitution (and by pressure) deserve to be addressed in detail. We focus on this issue in the remaining part of this section.

5.3. Charge-density wave in doped ladders of $\text{Sr}_{14-x}\text{Ca}_x\text{Cu}_{24}\text{O}_{41}$

Although the existence of a CDW ground state was proven rather late, by now it is well established by a number of experiments. Related to the more quasi-two-dimensional structure of the ladders, the nature of this CDW state is more complicated compared to the standard one-dimensional model compounds.

5.3.1. dc electrical transport

The electrical transport observed in single crystals or in polycrystalline samples of $\text{Sr}_{14-x}\text{Ca}_x\text{Cu}_{24}\text{O}_{41}$ compounds was studied by a number of groups over the years [43,70,138–143]. The most detailed dc electrical transport investigation on single crystals of $\text{Sr}_{14-x}\text{Ca}_x\text{Cu}_{24}\text{O}_{41}$, $x = 0, 3, 6, 8, 9$ and 11.5 was performed by Vuletić et al. [144,145] covering

Table 3
dc transport parameters of $\text{Sr}_{14-x}\text{Ca}_x\text{Cu}_{24}\text{O}_{41}$ for various x along all three crystallographic directions

	$\sigma_{\text{RT}} (\Omega^{-1} \text{ cm}^{-1})$			$T_c (\text{K})$	σ_c/σ_a		σ_c/σ_b	
	<i>c</i> -axis	<i>a</i> -axis	<i>b</i> -axis		RT	CDW	RT	CDW
$x = 0$	500 ± 100	17 ± 4	0.030 ± 0.006	210	30	15	10^4	300
$x = 3$	400 ± 100	28 ± 6	0.07 ± 0.2	140	13	3	10^4	15
$x = 6$	300 ± 100	70 ± 20		55	4	5		
$x = 8$	600 ± 100	54 ± 10		11	10	12		
$x = 9$	1200 ± 200	40 ± 8	0.15 ± 0.03	7	30	150	10^4	$3 \cdot 10^4$
$x = 11.5$	1000 ± 200	100 ± 20		–	10	50		
					$T < 10 \text{ K}$			

Room temperature (RT) conductivity, CDW transition temperature T_c , *c*-axis to *a*-axis conductivity anisotropy (σ_c/σ_a) at RT and in CDW phase, *c*- to *b*-axes anisotropy (σ_c/σ_b) at RT and in CDW phase. Since no CDW transition occurs for $x = 11.5$, anisotropy below 10 K is given.

a large range of temperature and all three crystallographic directions. Fig. 58 shows the dc resistivity ρ along the *c*-axis (along the ladders legs), as a function of inverse temperature $1/T$. The temperature range covered by the measurements is from 750 K down to 2 K. All the single crystals show small room temperature resistivities or, correspondingly, large conductivities $\sigma = 1/\rho$ in the range $300\text{--}1200 \Omega^{-1} \text{ cm}^{-1}$ (Table 3), confirming the existence of mobile holes in the ladders. The observed results in most parts comply with findings of other authors, as briefly presented in Section 5.2.1.

As first pointed out in [144], the resistivity data show the existence of an insulator-to-insulator phase transition, which can be inferred from the peak in the logarithmic derivative of resistivity (Fig. 58(b)).¹⁰ For $x = 0$ the peak in the derivative is centered at $T_c = 210 \text{ K}$, characterized by the full width at half maximum $2\delta T_c \approx 40 \text{ K}$. The transition is quite broad: $2\delta T_c/T_c$ is 20% indicating a certain level of intrinsic disorder in the nominally pure single crystals in accord with the results of crystallographic studies [51]. Both insulator phases, above and below the phase transition, are primarily characterized by well defined, but different, activation energies: $\rho(T) \propto \exp(\Delta/k_B T)$. The activation energy $\Delta_{\text{HT}} = 80 \text{ meV}$ in the high temperature (HT) phase, is smaller than $\Delta_{\text{LT}} = 112 \text{ meV}$ in the low temperature (LT) phase. The low temperature phase of the ladders in $\text{Sr}_{14-x}\text{Ca}_x\text{Cu}_{24}\text{O}_{41}$ with $0 \leq x < 11.5$ is supposed to be a CDW ground state, as will be argued in the following sections. Therefore, we assign $\Delta_{\text{LT}} = \Delta_{\text{CDW}}$ (for $0 \leq x \leq 9$).

Calcium substitution suppresses the CDW phase with the transition temperature T_c decreasing from 210 K for $x = 0$ to 7 K for $x = 9$, and the CDW gap (Δ_{CDW}) from 112 meV down to 2.5 meV, respectively (Table 4). The transition also broadens substantially with increasing x , as reflected by an increase of the transition width and a decrease of the peak height of $d(\ln \rho)/d(T^{-1})$ (Fig. 58(b)). The broadening might be attributed to an additional disorder introduced by Ca-substitution; a well known effect in quasi-1D compounds [154]. For $x = 8$ and 9, T_c was determined as a crossing point in which the fits to activated behavior in the high and low temperature regions meet (Fig. 58(c)). This is also applied to the logarithmic derivatives in which only a step-like feature appears (Fig. 58(d)), i.e. the transition temperature is defined as the center of the transition region between the low and high activation regions. The energy gaps become larger (Table 4) when going from high temperatures into the CDW phase, indicating that an additional gap opens for $0 \leq x \leq 6$ (Fig. 58(a), (b)). Conversely, for $x = 8, 9$, Δ_{CDW} is strongly suppressed: it becomes 2–3 times smaller than Δ_{HT} (Fig. 58(c), (d)).

While for the standard CDW, a phase transition from the metallic into the insulating state is observed due to the opening of an energy gap [155], in the present case the transport in the high temperature phase is already non-metallic. This might be explained by strong electron–electron interactions within the ladders, leading towards a Mott–Hubbard or charge-transfer insulator (Section 3.2.3) [145]. As far as the CDW ground state observed in the ladders of $\text{Sr}_{14-x}\text{Ca}_x\text{Cu}_{24}\text{O}_{41}$ is concerned, it might fall between the two well defined limits of charge order: the charge-density wave of itinerant charges and the charge order of localized charges. These issues will be addressed in more detail in Section 6.2.

For $x = 11.5$ the dc resistivity is metallic from room temperature down to about 100 K, where it changes over into a semiconducting behavior. The activation energy of only 2 meV is well defined below 50 K and gradually becomes even smaller below about 6.5 K ($\approx 0.5 \text{ meV}$). This crossover cannot be associated with the phase transition since the ratio $2\Delta_{\text{LT}}/(k_B T_c) \approx 1$ is much smaller than 3.5, the value predicted within mean-field theory. In practice the value of

¹⁰ Very first measurements, indicating the existence of the phase transition, were done on polycrystalline samples by Adachi et al. [140].

Table 4

dc transport parameters of $\text{Sr}_{14-x}\text{Ca}_x\text{Cu}_{24}\text{O}_{41}$ along all three crystallographic directions

$\text{Sr}_{14-x}\text{Ca}_x\text{Cu}_{24}\text{O}_{41}$	Δ_{HT} (meV)	Δ_{CDW} (meV)	T_c (K)	$2\delta T_c/T_c$
$x = 0$				
c -, a -axis	80 ± 20	112 ± 4	210	0.2
b -axis, $T > 170$ K		160 ± 10	–	–
b -axis, $T < 170$ K		95 ± 5	–	–
$x = 3$				
c -, a -axis	70 ± 15	95 ± 7	140	0.6
b -axis, $T < 300$ K		80 ± 5	–	–
$x = 6$				
c -, a -axis	28 ± 8	26 ± 4	55	0.8
$x = 8$				
c -, a -axis	14 ± 2	7 ± 1	11	0.7
$x = 9$				
c -, a -axis	8.5 ± 2.0	2.5 ± 0.5	7	0.8
b -axis, $T < 300$ K		6 ± 1	–	–
$x = 11.5$				
c -, a -axis, 6.5 K $< T < 50$ K		2.0 ± 0.5	–	–
c -, a -axis, $T < 6.5$ K		0.5 ± 0.1	–	–

High temperature insulating phase activation energy Δ_{HT} , CDW gap Δ_{CDW} , CDW transition temperature T_c and width of the CDW transition normalized to the transition temperature $2\delta T_c/T_c$. Long dash denotes that no transition to CDW phase occurs.

$2\Delta_{\text{LT}}/(k_B T_c)$ is much larger than 3.5 for CDW transitions. According to standard explanations the values larger than 3.5 can be due to the suppression of the mean field transition temperature by fluctuations which are more pronounced in low dimensional systems, or to the strong coupling interactions [156] or to the imperfect nesting [157]. The large ratio $2\Delta_{\text{LT}}/(k_B T_c) \geq 9$ observed in $\text{Sr}_{14-x}\text{Ca}_x\text{Cu}_{24}\text{O}_{41}$ materials with $x = 0, 3, 6, 8, 9$, where the CDW transition was identified, is most probably due to strong coupling interactions in the ladders.

Further, we compare dc transport properties of $\text{Sr}_{14-x}\text{Ca}_x\text{Cu}_{24}\text{O}_{41}$ with $x = 0, 3, 6, 8, 9, 11.5$ along all three crystallographic directions. Fig. 59 reveals that the phase transition temperatures T_c , when measured along the c - and a -axes i.e. in the ladders plane, are equal in value and have the same dependence on Ca-substitution. The same holds for the energy gaps in the high temperature phase above T_c and in the CDW ground state, which both are isotropic. The energy gaps become larger when going from high temperatures into the CDW phase, indicating that an additional gap opens for $x \leq 6$, as already discussed. The substantial transition broadening with increasing x , observed along the ladder legs is also found along the ladder rungs, with similar transition widths. The results obtained for all $0 \leq x \leq 11.5$ are summarized in Table 4. For $x = 11.5$ (where no CDW transition occurs) dc transport properties along the a -axis are also similar to the ones along the c -direction.

The conductivity anisotropy in the ladders plane at room temperature is of the order of 10 (the values vary between 10 and 30, confer Table 3) and does basically not vary with Ca content [43,146]. Apart from a variation in the region of the CDW phase transition temperature, the anisotropy seems to be temperature-independent for $0 \leq x \leq 8$, while it becomes enhanced at low temperatures for $x = 9$ and 11.5, as depicted in Fig. 60 [158]. It might be correlated with the results of X-ray diffraction for $x = 13.6$ compound [148]. The lattice in the ladder plane shrinks anisotropically with decreasing temperature: from room temperature to 10 K, c lattice parameter decreases 2.5 times more than a lattice parameter. This finding indicates that standard nesting arguments [155,159] cannot explain the suppression of the CDW by Ca-substitution. This issue is addressed in detail in Section 6.2. Fig. 60 reveals further that for low Ca-substitution, $x = 0$ and 3, in contrast to $x = 6$ and 8, the anisotropy drops significantly with lowering the temperature when approaching the CDW phase transition and levels off below about 150 K. As for the anisotropy rise for $x = 9$ and 11.5, it becomes comparable for both x at the lowest temperatures. The non-monotonic variation of the anisotropy found for $x = 0$ and 3, as well as for $x = 6$ and 8, in the vicinity of CDW transition, remain unclear at the present moment.

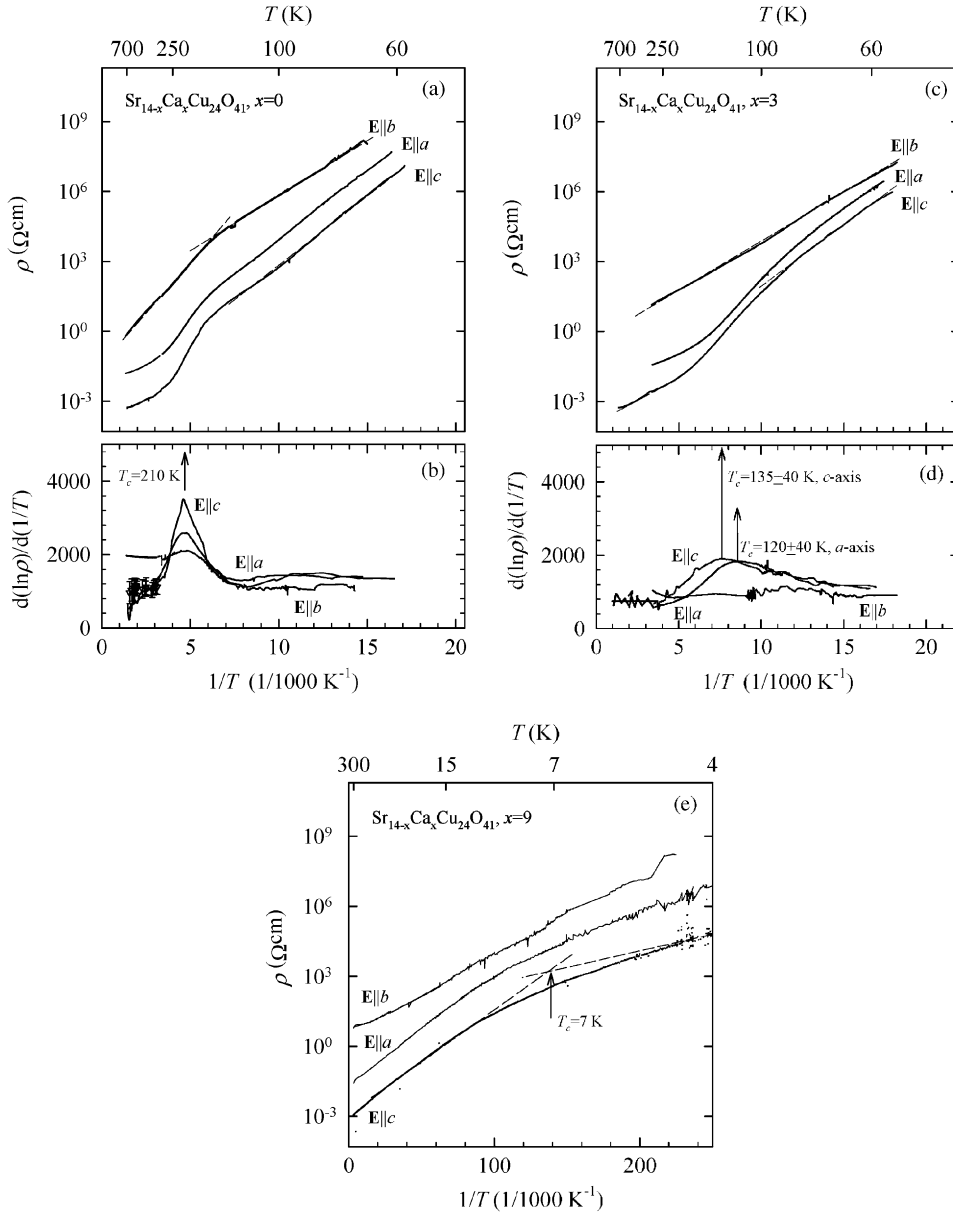


Fig. 59. dc resistivity along three crystallographic directions and logarithmic derivatives of $\text{Sr}_{14-x}\text{Ca}_x\text{Cu}_{24}\text{O}_{41}$ for representative Ca contents $x=0$ ((a) and (b)), $x=3$ ((c) and (d)) and $x=9$ (e). Phase transition temperatures T_c are indicated by arrows. After Ref. [145].

While dc transport within the ladder ac plane of $\text{Sr}_{14-x}\text{Ca}_x\text{Cu}_{24}\text{O}_{41}$ shows a number of properties similar for both directions, the dc resistivity along the third, b -direction, perpendicular to the ladder planes exhibits a distinct behavior (see Tables 3 and 4, Fig. 59). Different activation energies are observed when compared to the other directions, and no phase transition is registered. For the pure compound $x=0$ the activation energy is much larger at high temperatures (160 meV) than the one in the ac plane and becomes smaller below about 170 K. For $x=3$ and 9, there is a single activation in the whole temperature range. The simple activation process indicates that the charge transport perpendicular to the ladder planes happens via nearest neighbor hopping, as expected between disordered chains. This different transport mechanism together with the fact that no peak in $d(\ln \rho)/d(T^{-1})$ is found in the b -direction, indicates that the CDW does not develop a long-range order in 3D. Rather, CDW develops only in the ac ladders plane with a 2D order.

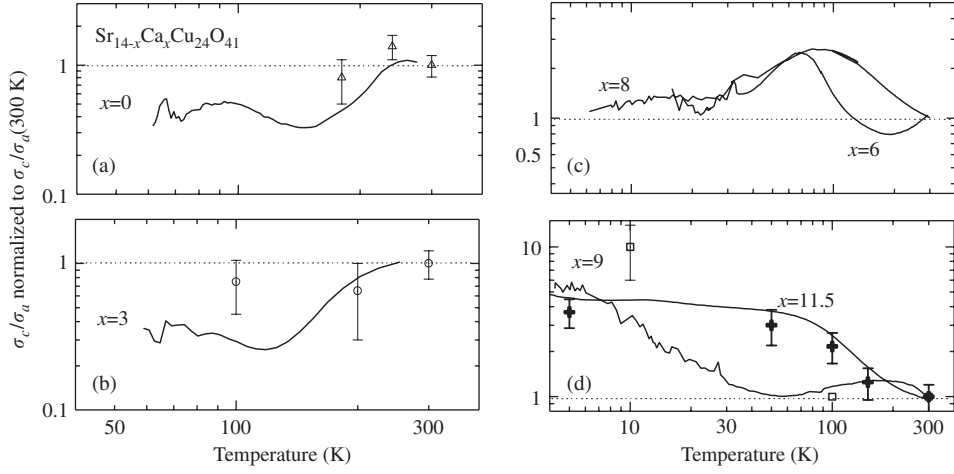


Fig. 60. Temperature dependence of the conductivity anisotropy of $\text{Sr}_{14-x}\text{Ca}_x\text{Cu}_{24}\text{O}_{41}$ for various Ca content x normalized to the corresponding room temperature value. Lines and symbols stand for dc and ac (at optical frequency 50 cm^{-1}) conductivity, respectively.

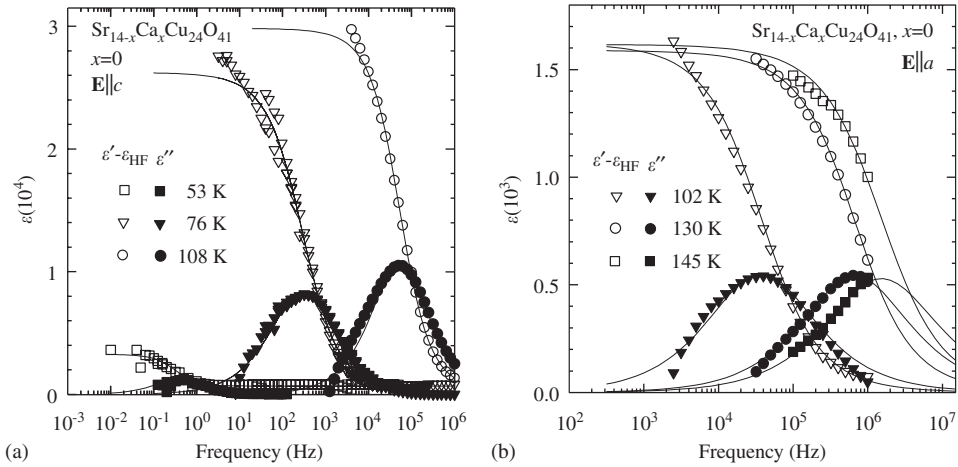


Fig. 61. Real and imaginary part of the dielectric function of $\text{Sr}_{14-x}\text{Ca}_x\text{Cu}_{24}\text{O}_{41}$, $x = 0$ at three representative temperatures as a function of frequency with the ac electric field applied along the c -axis (a) and along a -axis (b). The full lines are the fits to the data using Eq. (21). After Refs. [144,145].

Finally, we would like to mention that the charge transport in the ladders of $\text{Sr}_{14-x}\text{Ca}_x\text{Cu}_{24}\text{O}_{41}$ was also studied via the hole–magnon interaction by measuring the heat transport carried by magnetic excitations [160]. Clear evidence was obtained that the charge ordering happens below T_c as determined from dc resistivity measurements, leading to a freezing out of magnon–hole scattering. The latter is attributed to a drastic change of the hole mobility below the phase transition temperature.

5.3.2. Low-frequency dielectric spectroscopy

Detailed low-frequency dielectric spectroscopy measurements on single crystals of $\text{Sr}_{14-x}\text{Ca}_x\text{Cu}_{24}\text{O}_{41}$ with $x = 0, 3, 6, 8, 9, 11.5$ were performed by Vuletić et al. [144,145] along all three crystallographic directions. Gorshunov et al. [161] and Blumberg et al. [162] independently identified the insulating ground state in the ladders of the parent compound $\text{Sr}_{14}\text{Cu}_{24}\text{O}_{41}$ as a CDW.

A significant temperature-dependent relaxation of the dielectric function $\varepsilon(\omega) = \varepsilon' + i\varepsilon''$ for $\mathbf{E}||c$ -axis (parallel to the legs of ladders) and for $\mathbf{E}||a$ -axis (parallel to the rungs of ladders) detected for $\text{Sr}_{14}\text{Cu}_{24}\text{O}_{41}$ are shown in Fig. 61.

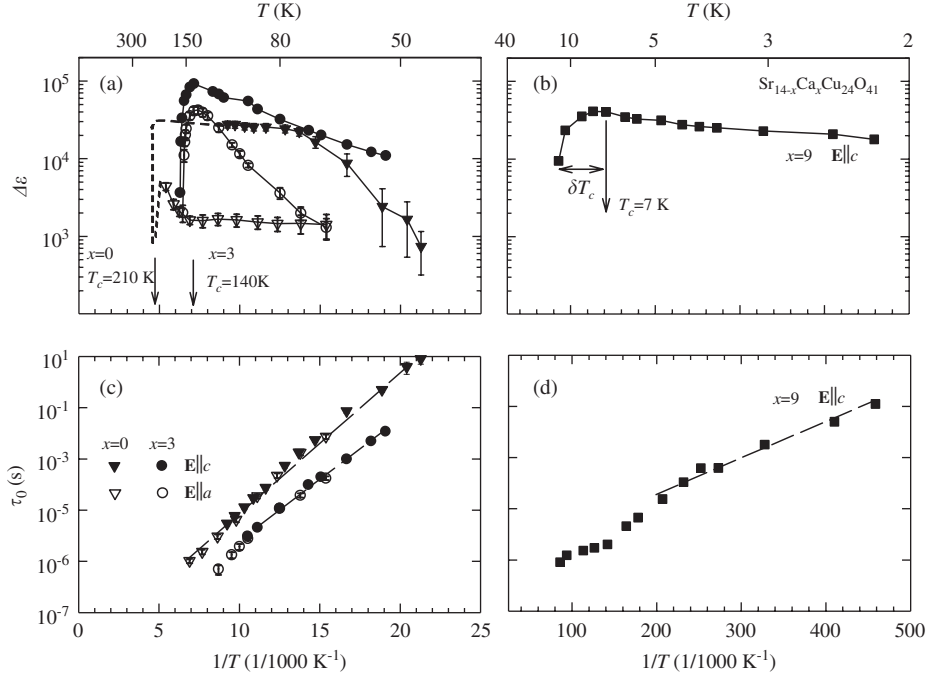


Fig. 62. Parameters of the anisotropic dielectric relaxation in the ladders of $\text{Sr}_{14-x}\text{Ca}_x\text{Cu}_{24}\text{O}_{41}$ with $x = 0, 3$ and 9 as a function of the inverse temperature. The dielectric strength $\Delta\epsilon$ and the mean relaxation time τ_0 are shown in panels (a), (b) and (c), (d), respectively. CDW phase transition temperatures T_c are indicated by arrows. The full lines (upper panels) are guides for the eye, while the dashed lines (lower panels) are fits to the Arrhenius behavior $\tau_0(T) \propto \exp(\Delta_{\text{CDW}}/k_B T)$. The half-width δT_c of the transition is marked for $x = 9$. An assumed behavior of $\Delta\epsilon$ for $x = 0$ based on the observed behavior for $x = 3$ and 9 , is represented by dotted line. After Refs. [144,145].

A pronounced absorption peak in $\epsilon''(\omega)$ corresponds to a large step in ϵ' . The screened loss peak (ϵ'') centered at τ_0^{-1} moves toward lower frequencies and smaller amplitudes with decreasing temperature. Experimental data are fitted by the generalized Debye expression

$$\epsilon(\omega) - \epsilon_{\text{HF}} = \frac{\Delta\epsilon}{1 + (i\omega\tau_0)^{1-\alpha}}, \quad (21)$$

where $\Delta\epsilon = \epsilon_0 - \epsilon_{\text{HF}}$ (ϵ_0 and ϵ_{HF} are static and high-frequency dielectric constants, respectively) is the dielectric strength of the relaxation, $1 - \alpha$ is the symmetric broadening of the relaxation-time distribution and τ_0 is the mean relaxation time. The fits to the data yield the main parameters of this relaxation: the dielectric strength $\Delta\epsilon \approx 10^3 - 10^4$ (for $\mathbf{E} \parallel a$ and for $\mathbf{E} \parallel c$, respectively), $1 - \alpha \approx 0.8$, and $\tau_0 \propto \rho(T)$, i.e. τ_0 closely follows a thermally activated behavior similar to that of the dc resistivity. These main features of the relaxation provide a clear evidence for the CDW formation, since they resemble the relaxation well known to characterize the collective CDW response. This so-called phason mode is pinned in the random impurity potential with the crucial influence of the free carrier screening [155]. In addition to this screened CDW collective response, there is a narrow, unscreened pinned resonance, which can be detected in the microwave conductivity measurements (see following Section 5.3.3). Since in the third b -direction no signature of a CDW-related dielectric response is detected (at any Ca content),¹¹ the observed dispersion indicates that a CDW develops in the ac plane with a two-dimensional long-range order. Although all features are similar to the relaxation along the highest conductivity c -axis, the observation of the CDW-related relaxation also along the perpendicular direction (i.e. along the rungs) was not expected. A theoretical model developed previously to explain the phason response to applied ac electric field is based on the assumption that CDW is a purely one-dimensional phenomenon [163]. However, in a two-dimensional system of coupled chains, the CDW develops according to the ordering vector \mathbf{Q} . Therefore, an ac

¹¹ In the third direction, i.e. with the $\mathbf{E} \parallel b$, a completely featureless radio-frequency conductivity is observed, similarly as for underdoped $(\text{La}, \text{Y})_y(\text{Sr}, \text{Ca})_{14-y}\text{Cu}_{24}\text{O}_{41}$ compounds (for similarity of dc transport see Section 5.3.1).

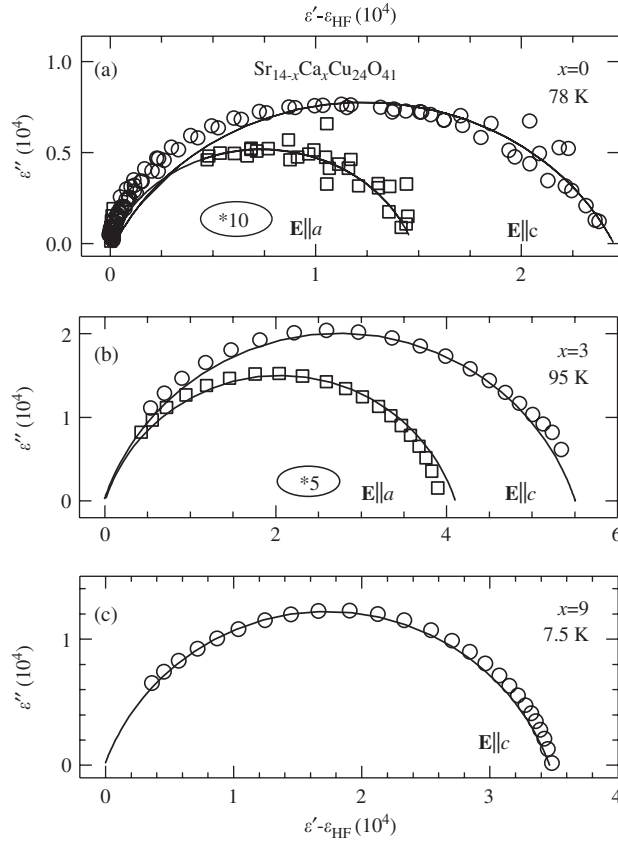


Fig. 63. Representative Cole–Cole plots of the real (ϵ') and imaginary (ϵ'') parts of the dielectric function of $\text{Sr}_{14-x}\text{Ca}_x\text{Cu}_{24}\text{O}_{41}$ for $x = 0$ (a), $x = 3$ (b) and $x = 9$ (c) with the $E \parallel c$ (along legs) and $E \parallel a$ (along rungs). The plots for the response along the a -axis are blown-up by a factor of 10 ($x = 0$) and 5 ($x = 3$). The full lines are the fits to the data using Eq. (21). The intersections of the arcs with $\epsilon' - \epsilon_{HF}$ axis indicate the values of dielectric strength $\Delta\epsilon$. After Refs. [145].

electric field applied either parallel or perpendicular to the chains couples to the CDW developed along Q^{-1} resulting in an anisotropic dispersion. Indeed, the loss peak centered at τ_0^{-1} decays Arrhenius-like ($\tau_0(T) \propto \exp(\Delta_{\text{CDW}}/k_B T)$) for both directions $E \parallel c$ and $E \parallel a$ (Fig. 62, lower left panel). The dielectric strength of the loss peak along the a -axis is about 10 times smaller than the one along c -axis, which corresponds to the single-particle conductivity anisotropy (see Table 3 and Fig. 63).

A distinct phase transition to the CDW ground state, corresponding to the insulator-to-insulator phase transition, and the suppression of this transition by Ca-substitution (Fig. 59) is also clearly revealed by dielectric spectroscopy measurements (Fig. 62): on decreasing temperature a sharp growth of the dielectric strength $\Delta\epsilon$ starts in the close vicinity of T_c (at $T_c + \delta T_c$) and reaches the huge value of the order of 10^4 – 10^5 at T_c .¹² The T_c values, as well as the width of the transition (Fig. 62), correspond well to the temperatures and width of the phase transition as determined in the dc resistivity measurements (Table 4). For higher Ca contents $x = 8$ and 9 there is no CDW dispersion with the $E \parallel a$ (Fig. 63), while for $x = 11.5$ no dispersion exists neither with the $E \parallel c$, nor with $E \parallel a$.

On the basis of these results, as well as the results obtained by dc resistivity measurements, we can conclude on the robustness of the two-dimensional CDW in the ladders as a function of temperature and of Ca-substitution. The temperature dependence can be tracked from the overall decrease of $\Delta\epsilon$ below T_c : Since the dielectric strength is directly associated with the CDW condensate density, this result indicates a back-transfer of holes from the ladders to

¹² For $x=0$, there are no data in the close vicinity of T_c since the dielectric mode leaves the upper bound (1 MHz) of the experimental frequency window already at $T > 110$ K with the $E \parallel c$, and at $T > 185$ K with $E \parallel a$.

the chains, which occurs with decreasing temperature. We remind that the back-transfer is necessary to understand the full formation of the AF dimer and charge order in the chains of the parent compound $\text{Sr}_{14}\text{Cu}_{24}\text{O}_{41}$ at low temperatures, as well as its development with changing temperature (see Sections 4.1.2 and 4.1.3). It should be noted that the decrease of $\Delta\epsilon$ appears to be substantial for $x = 0$ and 3, and not for $x = 9$, implying only minor, if any, back-transfer of holes for higher Ca contents. The latter stands a variance with larger estimates of transferred holes obtained by nuclear magnetic resonance [86] and neutron diffraction measurements [55].

As for the in-plane extent of the CDW order, the peak in $d(\ln \rho)/d(T^{-1})$ is a clear sign of the phase transition indicating that the long-range order should be established below T_c in the ac ladder plane for $x \leq 6$. However, rather broad transition found for even the pure compound $x = 0$ might imply that the correlation lengths are rather restricted and that the full long-range order cannot be established in the whole crystal. Indeed, recent resonant X-ray scattering results [99] seem to confirm this assumption (see Section 5.3.7). In any case, Ca-substitution quickly suppresses the length scale at which the 2D CDW develops in the ladder plane, as the broadening of the CDW phase transition indicates (Table 4). For $x = 8$ and 9, the absence of the peak in dc resistivity logarithmic derivative suggests that the long-range order is destroyed in the ladder planes. Consequently, in this range of Ca-substitution the CDW is able to respond only along the legs of the ladders as demonstrated by the Cole–Cole diagram in Fig. 63, before CDW disappears completely from the phase diagram for even higher doping $x > 9$. However, although neither CDW phase transition, nor CDW dielectric response is observed for high Ca contents, there are indications extracted from low-frequency Raman scattering that some CDW fluctuations might persist independently of Ca-substitution and at temperatures higher than 300 K as discussed in Section 5.3.6 [162,165].

In Section 6.2, we will address in more detail the nature of this CDW phase, as well as the mechanism which governs its suppression by Ca-substitution.

5.3.3. Microwave and millimeter wave spectroscopy

In addition to the screened phason loss peak centered at τ_0^{-1} , discussed in the previous Section 5.3.2, the standard theoretical model for the CDW collective mode dispersion in one-dimension developed by Littlewood [163] predicts an unscreened phason pinned mode at Ω_0 . While the former relaxation happens in the radio-frequency range, usually below 1 MHz, the latter resonance should be detected in the microwave and far-infrared range of frequency [155]. The pinned mode is due to the coupling of the CDW transverse mode to applied ac field, while the broad low-frequency loss peak is attributed to the coupling of longitudinal screened mode mixing in the transverse response due to the non-uniform pinning.¹³

Kitano et al. [166,167] reported some evidence for the CDW pinned mode at $\Omega_{0(c)} \approx 1.8 \text{ cm}^{-1}$ (60 GHz) with the $\mathbf{E} \parallel c$ (Fig. 64). As demonstrated in Fig. 65 this mode emerges from the frequency dependence of the conductivity, measured in the microwave and millimeter-wave range, below about 170 K. While this effect is clearly evident with the $\mathbf{E} \parallel c$, it is much smaller with the $\mathbf{E} \parallel a$. The mode was detected for $\text{Sr}_{14-x}\text{Ca}_x\text{Cu}_{24}\text{O}_{41}$, $x = 0$ and 3 with the $\mathbf{E} \parallel c$, but not for $x = 9$, which may be due to the increased screening by a larger number of free carriers and smaller energy gaps at this high Ca content (confer Table 4). Later on, Vuletić et al. [145] suggested that a thorough analysis of the data with $\mathbf{E} \parallel a$ published in Ref. [166] also leads to evidence for the pinned mode along rungs at the nearby frequency $\Omega_{0(a)} \approx 1.5 \text{ cm}^{-1}$ (see Fig. 64). Very recently, a microwave conductivity study of collective SDW response in the organic quasi-one-dimensional compound $(\text{TMTSF})_2\text{PF}_6$ by Petukhov et al. [164] revealed that the phason response in the microwave range of frequencies is present not only along the best conductivity axis as thought previously, but also along the intermediate conductivity axis.

In one dimension, the effective mass of the CDW condensate can be estimated by using an expression, which connects the microwave unscreened pinned mode at $\Omega_{0(c)}$ with the screened loss peak in the radio-frequency range at $\tau_{0(c)}^{-1}$ [163]

$$m_c^* = \frac{e^2 n}{\sigma_c} \tau_{0(c)} \Omega_{0(c)}^2. \quad (22)$$

In Eq. (22) $\sigma_c = 1/\rho_c$ is the dc conductivity along c -axis, and n is the carrier concentration condensed in the CDW. Using values for σ_c and $\tau_{0(c)}$ obtained from dc resistivity and low-frequency dielectric measurements, $\Omega_{0(c)} \approx 1.8 \text{ cm}^{-1}$ and assuming the fact that approximately one out of six holes per formula unit is condensed in the CDW in the ladders

¹³ In the single crystals of different compounds for which CDW is established, defects and impurities are randomly distributed. They create a non-uniform background potential in which CDW is pinned at low electric dc fields.

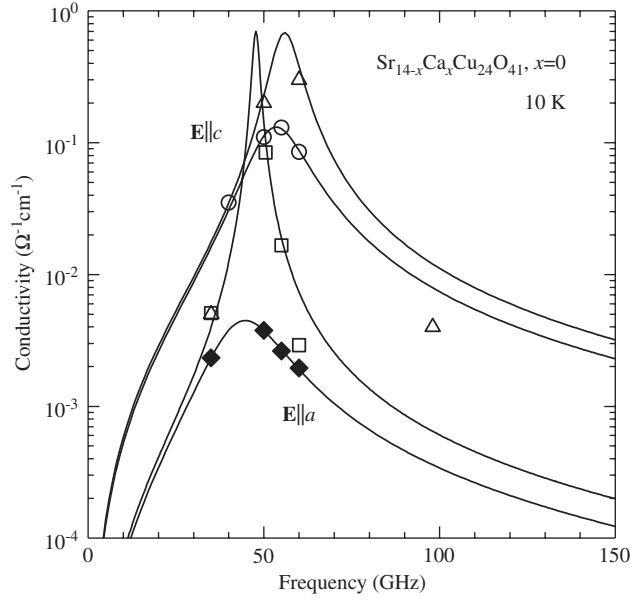


Fig. 64. Low temperature ($T = 10$ K) conductivity spectra of the single crystals from different batches of $\text{Sr}_{14-x}\text{Ca}_x\text{Cu}_{24}\text{O}_{41}$ with the $\mathbf{E}||a$ and $\mathbf{E}||c$. The full lines are based on the fits to a Lorentzian lineshape. Data taken from Ref. [166].

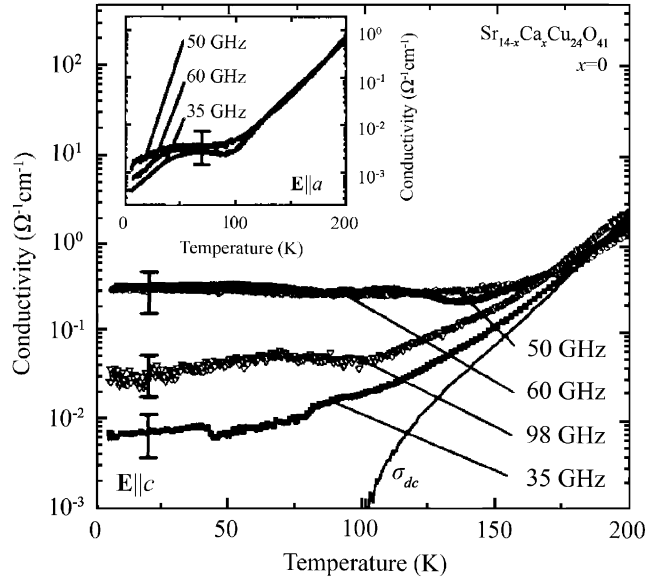


Fig. 65. Temperature dependence of the conductivity of $\text{Sr}_{14-x}\text{Ca}_x\text{Cu}_{24}\text{O}_{41}$, $x = 0$ at various frequencies with the $\mathbf{E}||c$ (main panel) and $\mathbf{E}||a$ (inset). After Ref. [166].

(see Section 3.3.1), the CDW effective mass is estimated to be about $m^* \approx 100m_0$, where m_0 is free electron mass.¹⁴ This value basically does not depend on temperature and Ca content for x between 0 and 9 (assuming the same $\Omega_{0(c)}$ for $x=9$, as for $x=0$ and 3). The small value of m^* ¹⁵ clearly indicates that electron–electron interaction is

¹⁴ The value previously given in Ref. [144] is underestimated by a factor of 4 due to an erroneous calculation of the carrier density.

¹⁵ For the standard CDW with $\Delta_{\text{CDW}} \approx 110$ meV, it is expected that $m^* \approx 1000m_0$ [155].

dominant in formation of this CDW, but that the electron–phonon interaction still plays some role. On the other hand, Abbamonte et al. [99] claim that the two-dimensional charge order in the ladders, which they observed using resonant soft X-ray scattering, exists without a detectable lattice distortion; see Section 5.3.7 for details.

Based on the anisotropic dispersion in both the radio-frequency and microwave range, we can extrapolate from Eq. (22), which was developed for one dimension, to the 2D case [145]. Assuming that the CDW effective mass anisotropy is given by the band mass anisotropy [168], we derive

$$\Omega_{0(a)}^2 = \Omega_{0(c)}^2 \frac{\sigma_c}{\sigma_a} \frac{m_{\text{band}(c)}}{m_{\text{band}(a)}}. \quad (23)$$

The band mass anisotropy $m_{\text{band}(c)}/m_{\text{band}(a)} \approx 0.1$ follows from the transfer integral anisotropy, which is estimated to be $t_a/t_c \approx 0.1$; the latter value was calculated by Arai et al. [46]. It can be alternatively obtained from the measured conductivity anisotropy assuming the coherent and hopping transport along the c -axis and a -axis, respectively [169]

$$\frac{\sigma_c}{\sigma_a} = \left(\frac{t_c}{t_a} \right)^2 \frac{c_L}{a}. \quad (24)$$

$\sigma_c/\sigma_a \approx 10$ – 30 is the conductivity anisotropy given in Table 3, while $c_L = 3.931 \text{ \AA}$ and $a = 11.469 \text{ \AA}$ are the ladders unit cell parameters (Section 3.1). Therefore, inserting $m_{\text{band}(c)}/m_{\text{band}(a)} \approx 0.1$, the pinned mode $\Omega_{0(c)} \approx 1.5 - 1.8 \text{ cm}^{-1}$ (Fig. 64) [166] and $\sigma_c/\sigma_a \approx 10 - 30$ in Eq. (23), one finds $\Omega_{0(a)} \approx 1.5 - 3.5 \text{ cm}^{-1}$. The latter values correspond well to the result obtained by fit to the experimental data, as shown in Fig. 64.

At the end, few important remarks are in order. The first concerns the magnitude and temperature dependence of the spectral weight of the conductivity peak at $\Omega_{0(c)} \approx 1.8 \text{ cm}^{-1}$. The experimentally obtained spectral weight $I_{\text{coll}(c)}$ is temperature-independent below 100 K and extremely small [166]: its magnitude is five orders of magnitude smaller than a theoretically expected one [155]

$$I_{\text{coll}} = \frac{ne^2}{m^*} \quad (25)$$

for the pinned mode of the CDW with the effective mass $m_{(c)}^* \approx 100 \cdot m_0$ and $n \approx 10^{21} \text{ cm}^{-3}$ (corresponding to one hole per formula unit in the ladders). Extrapolation to the 2D case gives 10 times smaller weight of the pinned mode with the $E_{||a}$ if $m_{(a)}^*/m_{(c)}^* \approx 10$ is taken into account. This is in a rather good agreement with the experiment ($I_{\text{coll}(c)}(\text{exp})/I_{\text{coll}(a)}(\text{exp}) \approx 10 - 40$). The missing spectral weight is difficult to understand if the pinned mode belongs to the CDW [155]. For a standard one-dimensional CDW established in $(\text{TaSe}_4)_2\text{I}$, for instance, the pinned mode in the microwave region contains most of the theoretically expected spectral weight [170]. Further, an unchanged magnitude of the observed spectral weight is at variance with the decreasing dielectric strength of the loss peak in the radio frequency range, shown in Fig. 62. The latter indicates that the CDW condensate density n decreases below 100 K, while the former implies no change. Therefore, one might be tempted to conclude that either the resonance mode at microwave frequencies and the loss peak in the radio-frequency range are not manifestations of the same phenomenon (a collective CDW mode), or a more elaborated theory should be applied to analyze the experimental data. We suggest that this apparent contradiction might be reconciled if we assume that a decrease of the spectral weight with temperature, expected due to the back-transfer of holes from the ladders into the chains (see Section 3.3.3), is hidden in the missing part of the spectral weight. This issue needs to be clarified in order to construct a self-consistent phase diagram of the ladders and chains in $\text{Sr}_{14-x}\text{Ca}_x\text{Cu}_{24}\text{O}_{41}$. In particular, the clarification is necessary, since the microwave spectroscopy data indicating constant spectral weight even at the lowest temperature stand at variance not only with the low-frequency spectroscopy results for the CDW in the ladders, but also with the inelastic neutron scattering and NMR data for the charge order in the chains. All of these results indicate the back-transfer of holes from the ladders to chains (see Sections 4.1.2 and 4.1.3), as very recently confirmed by NMR study of the nuclear quadrupole interaction tensor [86].

5.3.4. Quasi-optical microwave and far-infrared spectroscopy

A number of different research groups studied the optical response in $\text{Sr}_{14-x}\text{Ca}_x\text{Cu}_{24}\text{O}_{41}$ over the last decade [77,144,145,158,161,171]. For any deeper analysis of the optical properties, contributions from the chain and ladder subsystems should be separated. Choosing an upper bound of the frequency window of 10^4 cm^{-1} assures that the observed spectra (excluding phonons) can be attributed only to the charge excitations in the ladders, and not in the

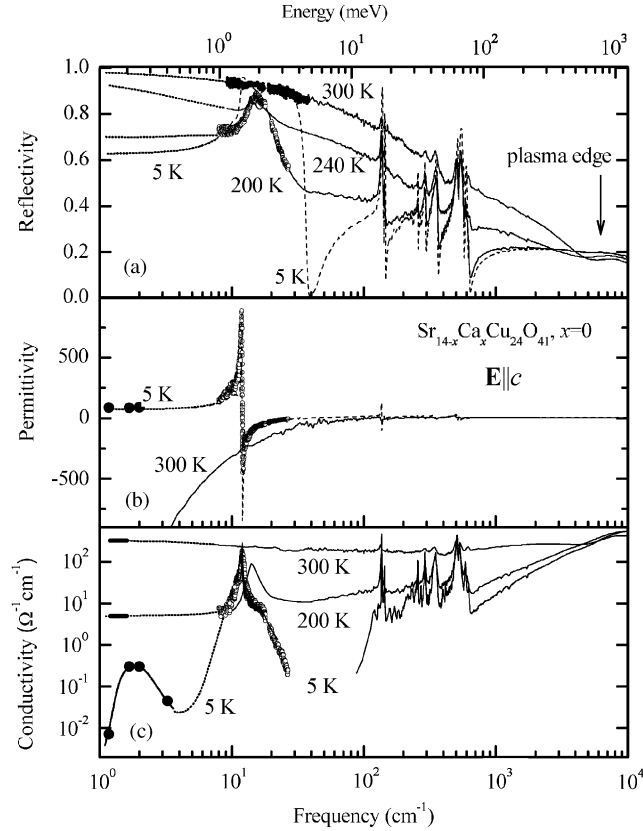


Fig. 66. Optical reflectivity (a), permittivity (b) and conductivity (c) of the pure compound $\text{Sr}_{14}\text{Cu}_{24}\text{O}_{41}$ along the c -axis at several representative temperatures. The dotted lines in the (a) and (b) panels show extrapolations used for the Kramers-Kronig analysis and between the infrared and the microwave data, respectively. The plasma edge is indicated by the arrow. Thick horizontal bars in panel (c) indicate dc conductivities at 300 and 200 K. The solid dots in the microwave range are due to the pinned CDW mode. After Refs. [144,161,166].

chains (see Section 3.3.2). A pronounced anisotropy of the electronic structure (see Section 3.2) is revealed in the optical response of the c -, a - and b -axes, in a similar manner as in the other physical properties, already described in the previous sections.

Fig. 66 shows an example of the permittivity and conductivity spectra in the infrared (IR) range along the legs of the ladder ($\mathbf{E} \parallel c$) of the pure compound $\text{Sr}_{14}\text{Cu}_{24}\text{O}_{41}$ [144,161,166]. At room temperature, the reflectivity increases with decreasing frequency and approaches 100% as frequency tends to zero. It also reveals the typical plasma edge at around $6000\text{--}7000\text{ cm}^{-1}$. This behavior translates into an almost dispersionless conductivity spectrum and into a permittivity which decreases towards low frequencies. Similar properties are also detected at 300 K for the $\mathbf{E} \parallel a$ polarization revealing the existence of a metallic Drude response in the optical conductivity along both c -axis and a -axis in the ladders at room temperature (Fig. 67). This is consistent with the fact that the ladder sub-system is not a genuine insulator, but has a certain amount of free charges [77,171].

On lowering the temperature below about 200 K, the reflectivity saturates at frequencies smaller than 10 cm^{-1} indicating that an insulating behavior develops. An associated suppression of the Drude weight below 200 K is clearly visible in the conductivity spectra along the c -axis and a -axis (Fig. 67). Since the screening by free carriers is weakened, the phonon lines are getting more pronounced at low temperatures. These results support the existence of a phase transition, which, in agreement with dc conductivity data ($T_c = 210\text{ K}$), can be attributed to the phase transition into the CDW ground state (Sections 5.3.1 and 5.3.2). The values of the CDW gap determined from the activated dc resistivity for both the $\mathbf{E} \parallel c$ and $\mathbf{E} \parallel a$ are equal ($\Delta_{\text{CDW}} \approx 112\text{ meV}$ corresponding to $\approx 900\text{ cm}^{-1}$) and are indicated in Fig. 67 by arrows. No clear threshold, which would correspond to the CDW gap, is observed in the optical spectra; this can be explained by phononic and electronic absorptions at these frequencies. The mid-infrared conductivity in the range

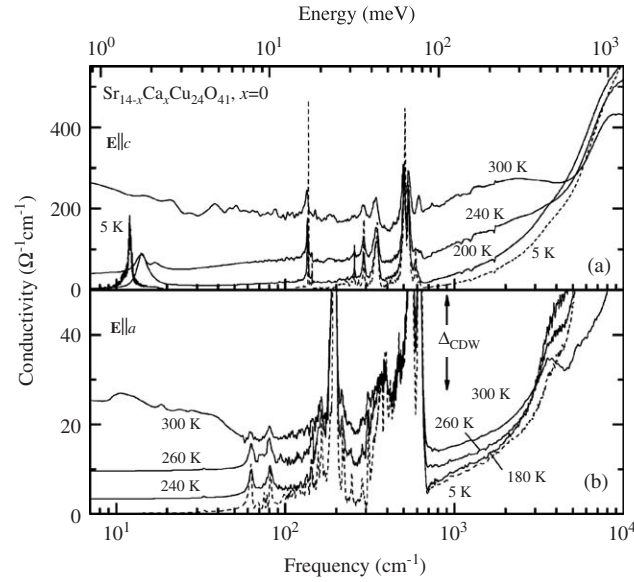


Fig. 67. Optical conductivity of the pure compound $\text{Sr}_{14-x}\text{Ca}_x\text{Cu}_{24}\text{O}_{41}$, $x=0$ along the c -axis (a) and along the a -axis (b) at several representative temperatures. Vertical arrows show the CDW gap obtained from the activated dc resistivity. After Refs. [144,145,161].

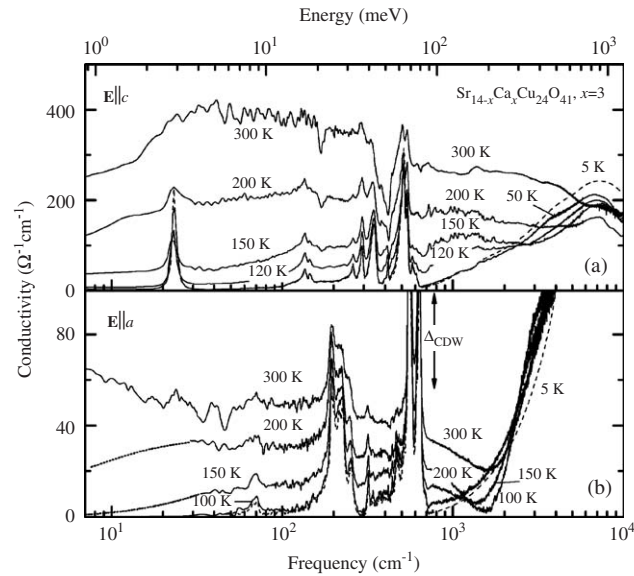


Fig. 68. Optical conductivity of $\text{Sr}_{14-x}\text{Ca}_x\text{Cu}_{24}\text{O}_{41}$, $x=3$ along the c -axis (a) and along the a -axis (b) at several representative temperatures. Dotted lines in the lower panel show the extrapolations of the infra-red conductivity to the corresponding dc values. Vertical arrows indicate the CDW gap obtained from the activated dc resistivity. After Refs. [144,145].

from 1000 to 10000 cm^{-1} is strongly influenced by the peaks associated with electronic interband transitions situated above 10000 cm^{-1} (see Section 3.3.2). Upon lowering the temperature, these tails become more visible.

Ca-substitution for $x \leq 5$ does not change the response much, except that from the temperature dependence it becomes obvious that the transition temperature T_c is lower and the CDW gap smaller, again in full accord with dc and dielectric data (Fig. 68). In contrast to that, for larger Ca contents, $x \geq 8$, the temperature dependence of the conductivity is qualitatively different between two polarization directions (confer Fig. 69 and Fig. 70). Along the c -axis,

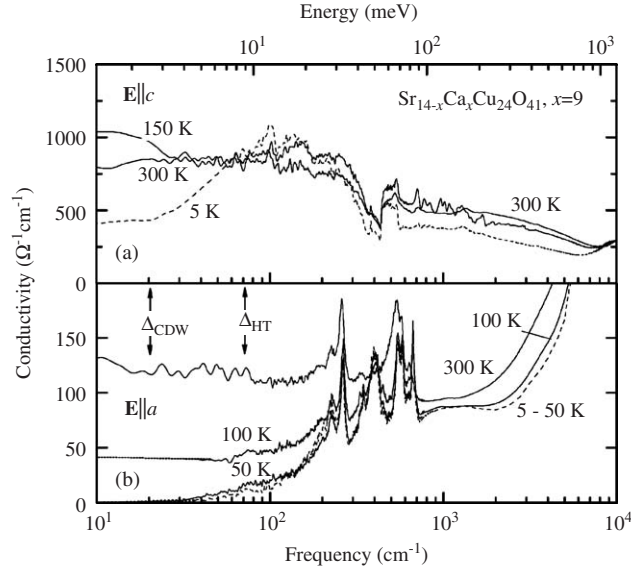


Fig. 69. Optical conductivity of $\text{Sr}_{14-x}\text{Ca}_x\text{Cu}_{24}\text{O}_{41}$, $x = 9$ along the c -axis (a) and along the a -axis (b) at several representative temperatures. The vertical arrows show the CDW gap and the energy gap in the high temperature phase obtained from the activated dc resistivity. After Refs. [144,145].

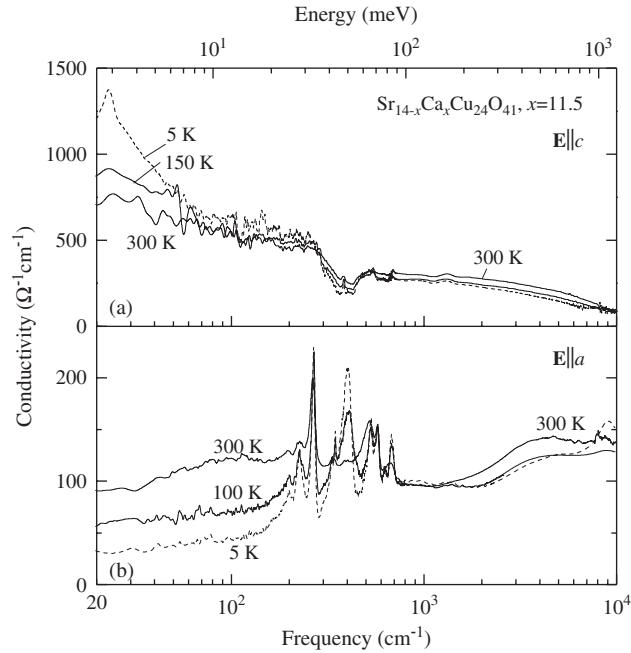


Fig. 70. Optical conductivity of $\text{Sr}_{14-x}\text{Ca}_x\text{Cu}_{24}\text{O}_{41}$, $x = 11.5$ along the c -axis (a) and along the a -axis (b) at several representative temperatures.

the far-infrared conductivity increases with decreasing temperature (metallic behavior), while the conductivity is continuously suppressed along the a -axis (as in a semiconductor).

In addition, for $x = 8$ and 9 the conductivity clearly decreases below about 100 cm^{-1} , a behavior not found for $x = 11$ and 11.5 . Further, for $x = 8$ and 9 the conductivity along a -axis drops much stronger than for $x = 11$ and 11.5 . Two different interpretations of these conductivity spectra are suggested. First, the peak below 100 cm^{-1} found in the c -axis spectrum may be assigned to a CDW pinned collective mode, while the conductivity decrease in the a -axis spectrum

corresponds to the opening of the pseudogap associated with the formation of hole pairs [158]. This interpretation is difficult to reconcile with recent results of microwave conductivity and dielectric spectroscopy (Sections 5.3.3 and 5.3.2). These investigations have shown the CDW unscreened pinned mode centered at 1.8 cm^{-1} [166] and that this pinning frequency corresponds rather well to the characteristic frequency of the CDW screened loss peak observed in the radio-frequency range [144], as expected in the framework of the theoretical model for CDW phason response [163].

The second approach is based on the dc data which for $x = 9$ show a transition temperature $T_c = 7 \text{ K}$ and a CDW gap $\Delta_{\text{CDW}} \approx 2.5 \text{ meV}$ (corresponding to 20 cm^{-1}). Here, the broad feature around 100 cm^{-1} seen for the $\mathbf{E} \parallel c$ is attributed to the opening of the CDW gap [144]. However, for $x = 9$ this energy gap Δ_{CDW} is smaller than the gap in the high temperature phase Δ_{HT} ($8.5 \text{ meV} \approx 70 \text{ cm}^{-1}$), which implies that the latter dominates the transport down to $T = 7 \text{ K}$ (Section 5.3.1). Indeed, this scenario explains much better the conductivity drop at 5 K along c -axis. For $x = 11.5$, a very small gap of about 2 meV (16 cm^{-1}) found in the activated dc resistivity lies below the optical frequency window. Since both dc resistivity along c - and a -axis are thermally activated with the same activation energies in the high temperature phase (Section 5.3.1), one would expect similar value of the gap from the optical conductivity data for the $\mathbf{E} \parallel a$, as observed for the polarization $\mathbf{E} \parallel c$; in contrast the conductivity drop along a -axis starts apparently at higher frequencies. This is probably due to long tails of peaks associated with electronic interband transitions situated above 10000 cm^{-1} , so that the onset of the high temperature phase gap at 70 cm^{-1} for $x = 9$ and at 16 cm^{-1} for $x = 11.5$ is hindered. In addition, the spectra for the $\mathbf{E} \parallel a$ between 100 and 200 cm^{-1} are dominated by tails of strong phonon features.

The qualitatively different spectra for two directions of $\text{Sr}_{14-x}\text{Ca}_x\text{Cu}_{24}\text{O}_{41}$, $x = 9$ and 11.5 might be understood as a mere reflection of a strong rise of the conductivity anisotropy on lowering the temperature, which starts below 50 K and 300 K , respectively (see Fig. 60). Conversely, similar spectra for both directions observed for $x = 0$ and 3 reflect a rather small anisotropy, so that the values of optical conductivity along c -axis and a -axis differ only for one order of magnitude or less.

Finally, the conductivity spectra along the b -axis, i.e. the direction perpendicular to the ladder planes, indicate a dielectric-like behavior in accordance with the much lower dc conductivity (Fig. 71). For $x = 0$ the gap might be identified around 160 meV (although smeared by phonons), as observed in the activated dc conductivity. The appearance of additional phonon lines in the low temperature phase of $\text{Sr}_{14}\text{Cu}_{24}\text{O}_{41}$ (see inset of Fig. 71) should be pointed out, as well as a certain anomaly of the low-frequency phonon along the c -axis (Fig. 66 and Fig. 67), whose eigen-frequency is shifted from 14 cm^{-1} down to 11 cm^{-1} at the phase transition. These observations might be connected with structural changes of the crystal lattice accompanying either a CDW phase transition in the ladders, or a charge order transition in the chains (see Section 4.1.3); in any case corresponding to a Brillouin-zone folding. This issue is open and would deserve to be studied in depth, especially in the light of the CDW effective mass of about $100m_0$, signaling a role of phonons in interactions responsible for CDW creation (see Section 5.3.3).

It is instructive to compare the conductivity spectra of $\text{Sr}_{14-x}\text{Ca}_x\text{Cu}_{24}\text{O}_{41}$ as a function of temperature in the wide frequency range: from dc limit up to 10000 cm^{-1} (see Fig. 72). The optical conductivity, along both the c - and a -axes, is Drude-like at room temperature, as well as at all temperatures above the CDW phase transition temperature T_c (210 , 140 and 7 K for $x = 0$, 3 and 9 , respectively), and agrees fairly well with the values obtained in dc limit. As soon as the CDW phase is entered, the conductivity exhibits a step-like increase in the radio-frequency range, corresponding to the broad and strongly temperature-dependent CDW relaxation mode, which can be clearly seen in the spectra of imaginary part of dielectric function (Fig. 61). It is followed by a power-law dispersion attributed to hopping conduction (for more details on hopping transport see Section 4.2.2), which leads to relatively high ac conductivity in the microwave and far-infrared region, as compared to the conductivity in dc limit. In the microwave region, the most prominent feature is the narrow temperature-independent CDW pinned mode [166], while the far-infrared and infrared regions are mainly characterized by the suppression of the Drude weight, below either the CDW gap ($x = 0$ and 3) or the high temperature phase gap ($x = 9$) and strong phonon features. The conductivity anisotropy in the ac plane is of the order of 10 at room temperature which is in nice agreement with the one found in dc limit. The increase of the anisotropy at lower temperatures, which was observed for $x = 9$ and 11.5 in the dc limit, is also found in the optical data (see Fig. 60). Due to strong phonon features and the low conductivity base-line, a drop of the conductivity anisotropy below T_c cannot be detected in the optical data for $x = 0$ and 3 . Finally, both dc transport and optical data along the b -axis indicate an only slightly temperature-dependent insulator-like behavior, which is distinct from the transport within the ladder planes, showing that the charge dynamics is very anisotropic.

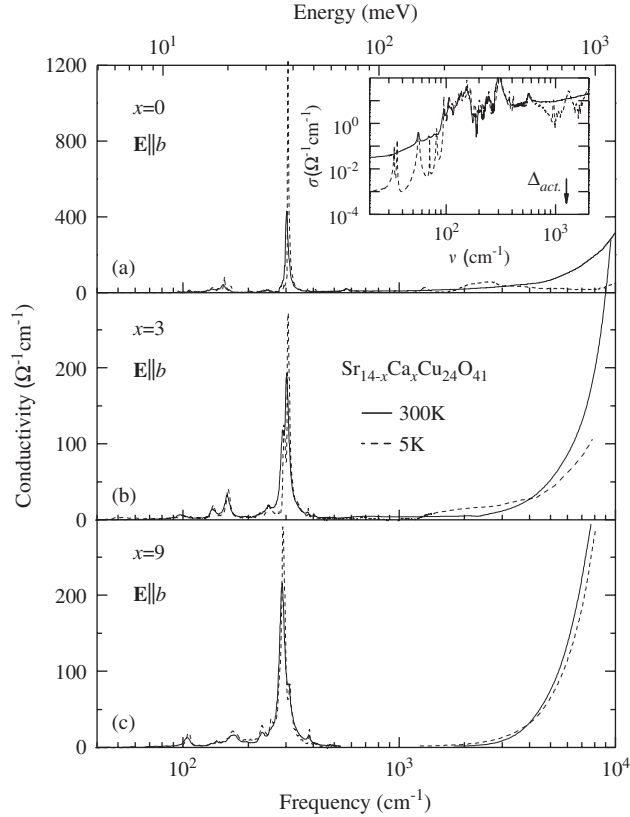


Fig. 71. Optical conductivity of $\text{Sr}_{14-x}\text{Ca}_x\text{Cu}_{24}\text{O}_{41}$, $x = 0$ (a), $x = 3$ (b) and $x = 9$ (c) along the b -axis at 300 K (full line) and 5 K (dashed line). Vertical arrow in the inset show the gap obtained from the activated dc resistivity.

We conclude this section by demonstrating how the optical conductivity spectra of $\text{Sr}_{14}\text{Cu}_{24}\text{O}_{41}$ for the polarization $\mathbf{E} \parallel c$ develop in the broad energy range with decreasing temperature. These data offer additional experimental evidence for the back-transfer of holes from the ladders into the chains with decreasing temperature (Fig. 73) [141]. The decrease of the low energy spectral weight with lowering temperature is accompanied with the increase of the spectral weight around 3 eV. The latter weight is assigned to the charge excitations in the chains, while the low-energy spectral weight is attributed to excitations in the ladders (see Section 3.3.2). Therefore, the suppression of the weight at low energies cannot be solely attributed to the phase transition at $T_c = 210$ K, but at least partially it is due to the back-transfer of holes from the ladders to the chains.

5.3.5. Electric field dependent transport

In standard one-dimensional CDW compounds, the collective mode (phason) couples to an applied dc electric field and gives a novel contribution to the electrical conductivity. In a perfect material, such a motion of the collective mode could in principle lead to superconductivity as originally proposed by Fröhlich [172]. However, in real materials this motion is hindered by various pinning mechanisms such as lattice defects, impurities and commensurability potentials and only sets in above a finite threshold field E_T . Hence, nonlinear current–voltage characteristics, accompanied by broad and narrow band noise, with sharp threshold fields of the order of 10–1000 mV/cm are a well known signature of CDW motion [155,156,173]. A similar behavior might be expected for the CDW established in the ladders of $\text{Sr}_{14-x}\text{Ca}_x\text{Cu}_{24}\text{O}_{41}$.

Electric field dependent transport measurements on $\text{Sr}_{14-x}\text{Ca}_x\text{Cu}_{24}\text{O}_{41}$ were performed by several groups [144,161, 162,174,175]. For $x = 0$ contradictory results were reported ranging from the one that nonlinear effect arises only above a finite threshold field (Fig. 74 main panels) to the other that nonlinearity emerges from the noisy background, and finally that no threshold field can be defined (Fig. 75, main panel). The latter result was also reported for $x = 3$ and 9

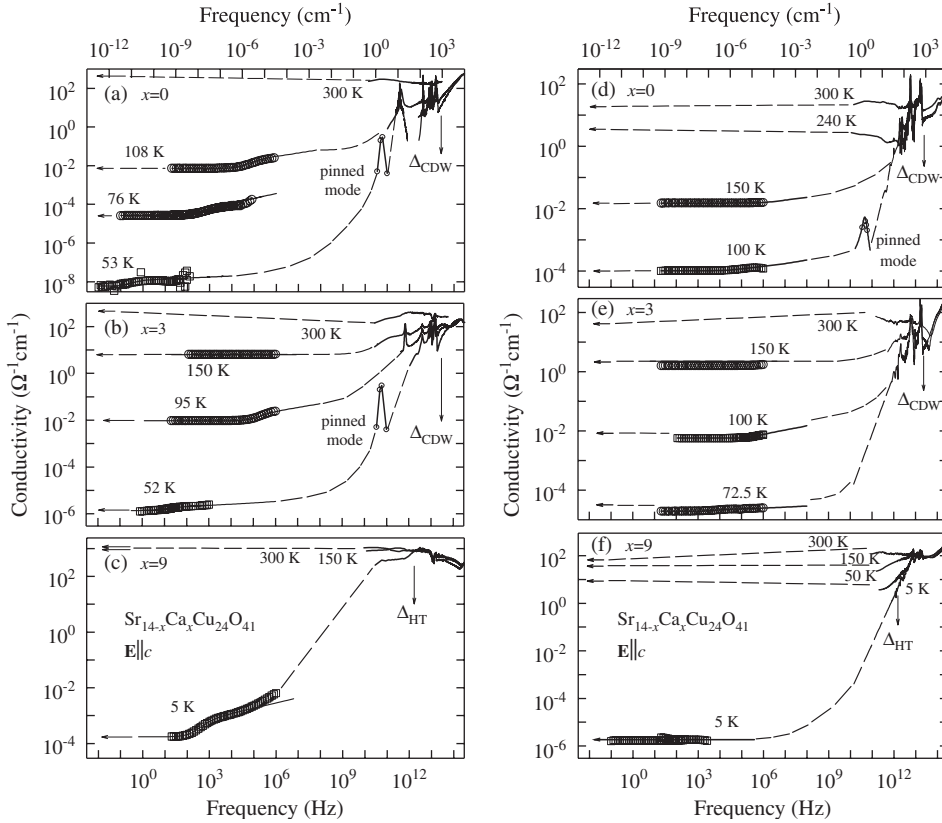


Fig. 72. Broad-band conductivity spectra of $\text{Sr}_{14-x}\text{Ca}_x\text{Cu}_{24}\text{O}_{41}$ for $x = 0, 3$ and 9 along the c -axis (left panels: (a), (b), (c)) and along a -axis (right panels: (d), (e), (f)) at a few selected temperatures. Vertical arrows show the CDW gap Δ_{CDW} and the high temperature phase gap Δ_{HT} obtained from the activated dc resistivity. The dashed lines are guides for the eye. After Refs. [144,145,161,166].

[144]. Similarly, very different nonlinear effects were reported. Blumberg et al. [162] found a strong rise of conductivity $\sigma_c(E)$, which reaches 50% of the low-field value $\sigma_c(0)$ for electric field equal to twice the threshold (Fig. 74(a)), while Maeda et al. [174] and Gorshunov et al. [161] observed a rise of only few percent at the highest applied fields of few V/cm (Fig. 74(b) and Fig. 75).

In an attempt to reconcile these reports, it is instructive to present the conductivity data of Blumberg et al. and Maeda et al. as a function of electric field using the linear E scale. Such a plot is usually considered to be the most relevant for extracting the threshold field for sliding CDW [156,173]. It is evident that E_T cannot be clearly determined for the data of Blumberg et al. and Maeda et al. (insets of Fig. 74), similarly as for the data of Gorshunov et al. (Fig. 75, main panel). This problem was pointed out by Maeda et al. and by Gorshunov et al. It is well known that the nonlinearity due to the CDW sliding is highly sample-dependent and influenced by a number of side-effects; nevertheless the large discrepancy between the observed magnitude of the nonlinear conductivity in reported measurements is striking. Vuletić [176] found a large nonlinearity either for the high quality sample with improper contact preparation method applied, or for the sample with large unnested voltage. In the former case, the same sample with the properly prepared contacts showed only negligible nonlinearity as displayed in Fig. 75. In either of the cases, it was not possible to identify a threshold field.

A CDW in disordered one-dimensional compounds is characterized by a smaller dielectric strength $\Delta\epsilon$ of the loss peak in the radio-frequency range (see Section 5.3.2) and correspondingly enhanced and broad sliding threshold field [155]. Therefore, for an intrinsically disordered compound as the composite $\text{Sr}_{14-x}\text{Ca}_x\text{Cu}_{24}\text{O}_{41}$ (disordered even for $x = 0$, see Section 3.1), it is not surprising that the observed $\Delta\epsilon$ are smaller than 10^7 – 10^8 , the magnitude typically encountered for one-dimensional CDW. A comparison of the dielectric strength $\Delta\epsilon \approx 4 \times 10^6$ and $\Delta\epsilon \approx 4 \times 10^4$

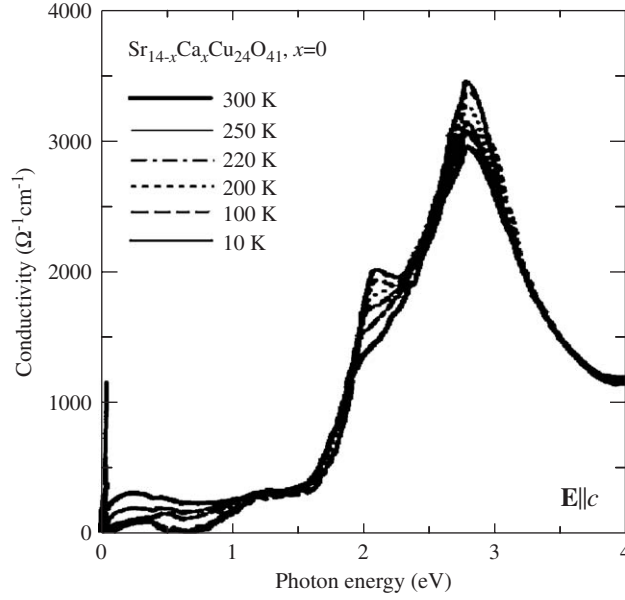


Fig. 73. Optical conductivity of $\text{Sr}_{14-x}\text{Ca}_x\text{Cu}_{24}\text{O}_{41}$, $x = 0$ along the c -axis at various temperatures. After Ref. [141].

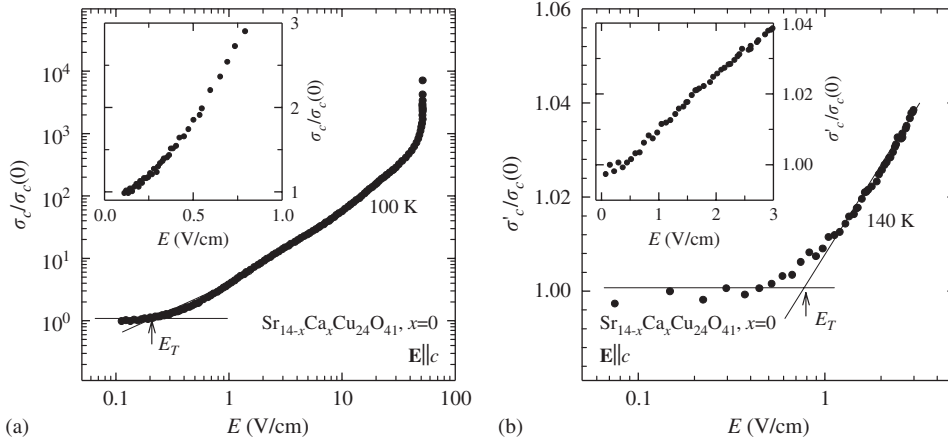


Fig. 74. Conductivity σ_c (a) and differential conductivity $\sigma'_c = d\sigma_c/dE$ (b) normalized to the low-field value $\sigma_c(0)$ of $\text{Sr}_{14-x}\text{Ca}_x\text{Cu}_{24}\text{O}_{41}$, $x = 0$ along the c -axis in the CDW phase as a function of electric field E plotted in the logarithmic E scale. A possible threshold field E_T is denoted by arrow. After Refs. [162,174]. In the insets the same data are displayed using a linear E scale. Obviously, no threshold field can be defined.

observed by Blumberg et al. and Gorshunov et al., respectively, indicates that single crystals with larger disorder were used in the latter work. This would imply a smoother field dependence of the conductivity and a smaller nonlinear effect for a particular electric field, which is qualitatively in accord with the observations.

We can estimate the threshold field for CDW in the ladders of $\text{Sr}_{14}\text{Cu}_{24}\text{O}_{41}$ using the simple relation $E_T \cdot \Delta\varepsilon = \text{constant}$, which holds for the standard CDW [155]. As a reference we take CDW established below 200 K in TaS_3 , which is characterized with $\Delta\varepsilon \approx 4 \times 10^7$ and $E_T = 0.4 \text{ V/cm}$ [177]. We get $E_T \approx 4 \text{ V/cm}$ and $E_T \approx 400 \text{ V/cm}$ for CDW in single crystals used in Ref. [162] and in Ref. [161], respectively. The estimate of 400 V/cm is far above the highest field applied, implying that E_T might have not been reached at all in the experiment by Gorshunov et al. (see Fig. 75). Conversely, the value of 4 V/cm lies in the range of fields applied by Blumberg et al. Since the threshold field cannot be defined using the criteria applied for standard CDW, we suggest that another mechanism, different than sliding, might be responsible for the observed nonlinearity.

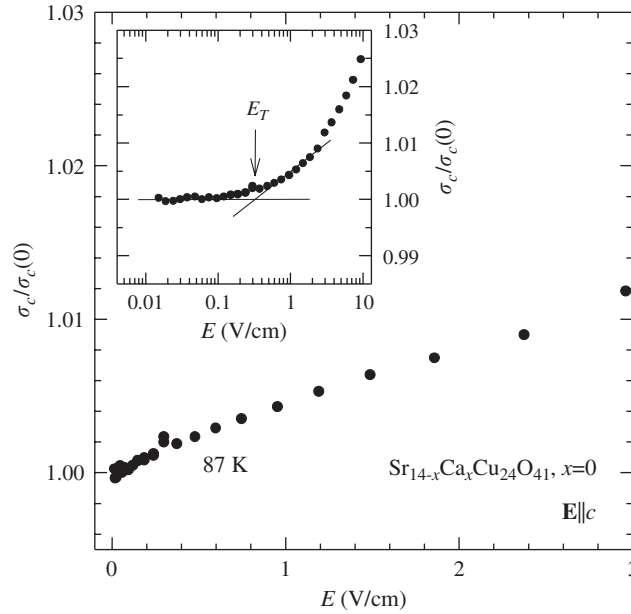


Fig. 75. Conductivity (σ_c) of $\text{Sr}_{14-x}\text{Ca}_x\text{Cu}_{24}\text{O}_{41}$, $x = 0$ along the c -axis normalized to the low-field value $\sigma_c(0)$ as a function of electric field E plotted in the linear E scale in the CDW phase at $T = 87$ K. Threshold field E_T , denoted by arrow, can be found only if data are plotted in the logarithmic E scale (inset). After Refs. [161,176].

Finally, two experimental observations regarding the field dependent transport should be mentioned. The first point concerns a second threshold of ≈ 50 V/cm with an extremely sharp rise of the conductivity observed for $\text{Sr}_{14-x}\text{Ca}_x\text{Cu}_{24}\text{O}_{41}$, $x = 0$ at 100 K (see Fig. 74(a)) [162]. The authors attributed this phenomenon to the crossover to a regime of free CDW sliding, which is found in the standard CDW when single particles cannot screen the CDW response [178]. However, this interpretation meets difficulties since in the relevant temperature range the screening due to single particle excitations above the CDW gap is clearly identified in thermally activated mean relaxation time of the CDW loss peak in the radio frequency range (see Section 5.3.2 and Fig. 62(c)) [161,162]. The second observation concerns the features of field-dependent transport along the c - and a -axis in the ladders of $x = 0$ compound [174,175]. The authors pointed out that the nonlinear transport is distinct along the c - and a -axis, since they found that the scaling relation between nonlinear and low-field conductivity holds independently of temperature only for the transport along the c -axis. However, this distinction fails already for $x = 1$ compound (also concerning threshold field, which was not identified for $x = 1$), indicating that this nonlinear transport is extremely sensitive on Ca-substitution. The latter feature, as well as a distinct response to dc electric field along c - and a -axis for $x = 0$, are difficult to reconcile with the CDW response to ac fields, which is basically similar and only different in magnitude within the ladder plane (see Sections 5.3.2 and 5.3.3).

At the end, we are led to conclude that a more systematic investigation is needed to be done on single crystals of $\text{Sr}_{14-x}\text{Ca}_x\text{Cu}_{24}\text{O}_{41}$ from different syntheses to clarify the origin and mechanism behind the observed nonlinear effects.

5.3.6. Low-frequency electronic Raman scattering

Electronic Raman scattering is considered to probe directly the longitudinal electronic channel, since the Raman response function $\chi''(\omega)$ is proportional to $\text{Im}(1/\varepsilon(\omega))$ [179]. Low-frequency electronic Raman scattering measurements on single crystals of $\text{Sr}_{14-x}\text{Ca}_x\text{Cu}_{24}\text{O}_{41}$, $x = 0, 8$ and 12, as well as on single crystals of undoped $\text{La}_6\text{Ca}_8\text{Cu}_{24}\text{O}_{41}$, were performed by Blumberg and collaborators [162,165].

The temperature dependence of the low-frequency Raman response function $\chi''(\omega)$ of $\text{Sr}_{14-x}\text{Ca}_x\text{Cu}_{24}\text{O}_{41}$, $x = 0$ and 12 with the electric field applied along the legs of the ladder ($\mathbf{E} \parallel c$) is shown in Fig. 76. A quasi-elastic scattering peak, observed in the $1.5\text{--}5\text{ cm}^{-1}$ range at high temperatures 300–700 K, moves towards lower frequencies and shows a larger amplitude with decreasing temperature. It should be noted that Raman spectra look qualitatively similar for

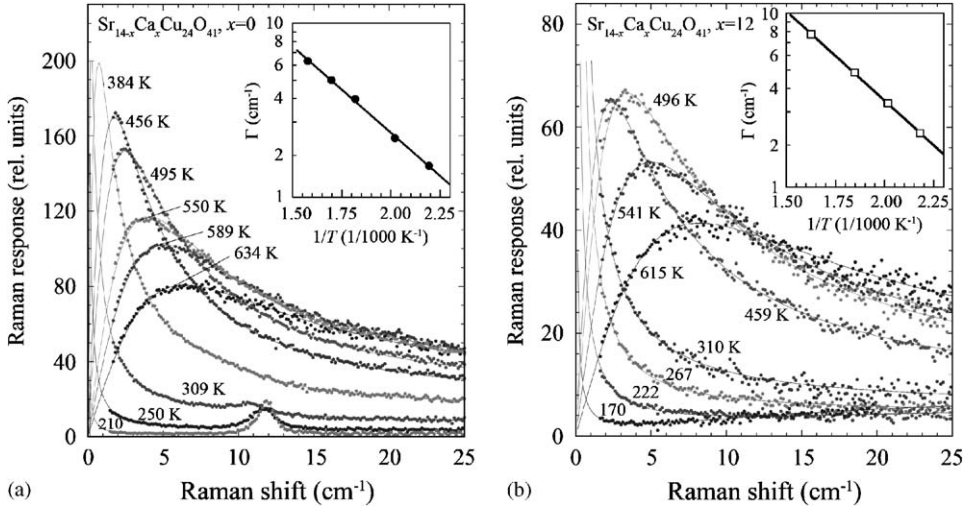


Fig. 76. Temperature dependent electronic Raman response with the $\mathbf{E}||c$ of $\text{Sr}_{14-x}\text{Ca}_x\text{Cu}_{24}\text{O}_{41}$, $x=0$ (a) and $x=12$ (b). Insets show the damping of the quasi-elastic peak as a function of the inverse temperature. The full lines are fits to the Arrhenius behavior. After Ref. [165].

both the parent compound, $x=0$ and for the compound with high Ca content ($x=12$). In contrast, no quasi-elastic peak was observed for $\text{La}_6\text{Ca}_8\text{Cu}_{24}\text{O}_{41}$ with no holes. The observed data can be described by a relaxational form of Raman response function

$$\chi''(\omega) = A(T) \frac{\omega \Gamma}{\omega^2 + \Gamma^2}, \quad (26)$$

where Γ is the damping parameter. The damping of the quasi-elastic peak is thermally activated $\Gamma(T) \propto \exp(-\Delta_\Gamma/k_B T)$. The activation energy of about $\Delta_\Gamma \approx 185 \text{ meV}$ for the $x=0$ compound remains similar for $x=12$ (see insets of Fig. 76). Blumberg and collaborators suggested that the observed quasi-elastic scattering peak is a manifestation of CDW fluctuations, which persist to remarkably high temperatures and are almost insensitive to Ca-substitution. The assignment is based on the observation that the frequency of the peak ($1.5\text{--}5 \text{ cm}^{-1}$ corresponding to $\approx 2.2\text{--}7 \text{ K}$ and to $\approx 0.2\text{--}0.6 \text{ meV}$) is much lower than the thermal energy and dc activation gap ($\Delta_{\text{HT}} = 80 \text{ meV}$, see Table 4); it should therefore be attributed to a collective rather than to a single particle excitation. In this interpretation, the Raman quasi-elastic peak traces the dielectric relaxational peak (see Section 5.3.2) to high temperatures, which suggests their common origin. It is also expected that the damping of the Raman peak is governed by single particle screening $\Gamma(T) \propto \sigma_c$, in analogy with the peak in the dielectric response. It should be noted, however, that Δ_Γ (the activation energy of the scattering peak damping) is more than 2 times larger than the activation energy of the c -axis dc conductivity for $x=0$ compound in 300–700 K range. Δ_Γ is also almost 2 times larger than the CDW gap $\Delta_{\text{CDW}} = 112 \text{ meV}$. Moreover, it remains the same for compounds with high Ca-substitution ($x=12$) although the c -axis dc conductivity presents metallic behavior (see Figs. 48 and 50(a)). Gozar et al. suggested that a mid-infrared feature at 0.14 eV observed for all $\text{Sr}_{14-x}\text{Ca}_x\text{Cu}_{24}\text{O}_{41}$, $0 \leq x \leq 11.5$ (see Fig. 19) [77] might be responsible for the similar activated behavior of the damping of the quasi-elastic scattering peak for both the $x=0$ and 12 compounds.¹⁶ Nevertheless, the difficulty remains to interpret the damping for $x=12$ compound as to be due to single particle screening, that is as the damping of the loss peak observed in the low-frequency dielectric spectroscopy measurements.

Finally, it is important to note that no quasi-elastic peak in the electronic Raman response is found with the electric field applied along the a -axis (along the ladder rungs). This would imply that while the CDW collective response can be detected along both the legs and rungs of the ladder below the phase transition temperature (for $x=0$, $T_c = 210 \text{ K}$, see Sections 5.3.1 and 5.3.2), the response at high temperatures, where only short-range fluctuations persist, exhibits a purely one-dimensional character. A second note concerns the temperature range of CDW fluctuations above T_c .

¹⁶ The energy scale of the mid-infrared peak may be set by the exchange energy of the ladder $J \approx 100 \text{ meV}$ (see Table 2).

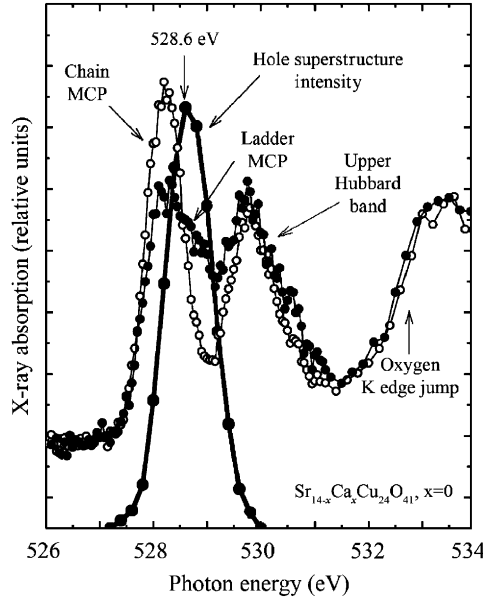


Fig. 77. Integrated intensity of the hole super-structure reflection centered at 528.6 eV in $\text{Sr}_{14-x}\text{Ca}_x\text{Cu}_{24}\text{O}_{41}$, $x=0$ as a function of incident photon energy. X-ray absorption spectra below oxygen K edge jump are shown for comparison. Hole features belonging to the chains (chain MCP, mobile carrier prepeak) and to the ladders (ladder MCP) are indicated by arrows. Full and open points for $\mathbf{E}\parallel c$ and $\mathbf{E}\parallel a$, respectively. After Ref. [99].

It is surprising that while the low-frequency dielectric spectroscopy data identify a CDW fluctuation region only 20 K above T_c for $x=0$ (see Section 5.3.2),¹⁷ the Raman data suggest their existence up to at least 700 K.

We have to conclude that the picture in which CDW fluctuations and the activated damping of 185 meV persist for all Ca contents (including metallic $x=12$, which becomes superconducting under high pressure) is difficult to reconcile with dc resistivity and low-frequency dielectric spectroscopy data indicating a full suppression of CDW for $x>9$.

5.3.7. Resonant X-ray diffraction

Abbamonte et al. used a resonant soft X-ray scattering technique to search for charge ordering in ladders of $\text{Sr}_{14-x}\text{Ca}_x\text{Cu}_{24}\text{O}_{41}$, $x=0$ [99]. The experiment was carried out at X-ray energy close to an absorption peak of the K shell of oxygen. Since doped holes reside in the oxygen orbitals (see Sections 2.2 and 3.3.1), the X-rays scattered from the resonant oxygen atom sample the local environment and can distinguish between the different structures that might occur. In particular the scattered X-rays should be sensitive to the ordering of doped holes. We remind that in $x=0$ compound holes reside in both the ladders and chains, and the oxygen peak near 528 eV is split into resolvable chain and ladder features for $\mathbf{E}\parallel c$ polarization: a pronounced shoulder-like feature at the high-energy wing is due to holes in the ladders (see Section 3.3.1, Fig. 17) [81]. Abbamonte et al. tuned the X-ray energy to this high-energy wing of the oxygen peak (528.6 eV) at which scattering from the holes is selectively enhanced more than 1000 times. In this case, a pronounced super-lattice reflection appears (Fig. 77) centered at $(0, 0, 0.200 \pm 0.009)$ in terms of the ladder reciprocal unit cell, indicating the existence of the modulation along the ladder with period $(5.00 \pm 0.24)c_L$, where c_L is the ladder unit cell parameter (see Fig. 78(a)). It is argued that the observed reflection represents the true superlattice peak, because it occurs at $l=0.14$ in terms of the chain unit cell¹⁸ and does not have a periodicity of the super-structure cell (27.3 Å, see Section 3.1). The peak width gives longitudinal (along c -axis) and transverse (along a -axis) coherence

¹⁷ Low-frequency dielectric spectroscopy can detect CDW response in the fluctuation region above the phase transition temperature. The fluctuation region determined by these measurements corresponds well to the one defined by X-ray diffuse scattering or electron diffraction for the standard CDWs [180–183].

¹⁸ We use the notation we introduced in Section 3.1: $(h, k, l, 0)$ and $(h, k, 0, m)$ represent Miller indices in terms of the chain and ladder unit cell, respectively.

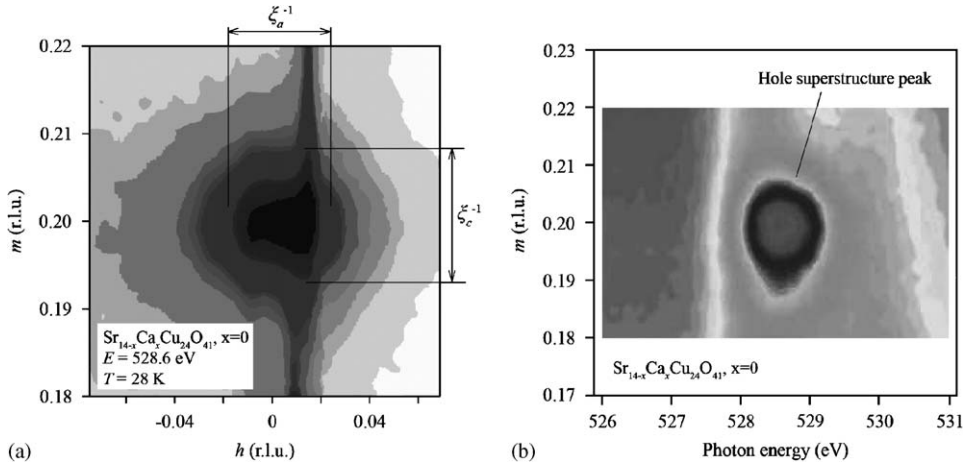


Fig. 78. (a) Reciprocal ladder space map around $(h, k, m) = (0, 0, 0.2)$ with the X-ray energy tuned to the ladder hole absorption feature (MCP at 528.6 eV) taken at $T = 28$ K in $\text{Sr}_{14-x}\text{Ca}_x\text{Cu}_{24}\text{O}_{41}$, $x = 0$. Inverse coherence length ξ_c^{-1} and ξ_a^{-1} are denoted. (b) Hole super-structure peak intensity across the oxygen K edge. After Ref. [99].

lengths of $\xi_c = 255 \text{ \AA} = 64.9c_L$ and $\xi_a = 274 \text{ \AA} = 23.89a$ (c_L and a are ladder unit cell parameters given in Section 3.1, [49]). The latter implies the transverse ordering scale of almost 50 ladders, confirming an important interladder coupling. It is significant that the reflection is undetectable at all other energies, including the oxygen K edge jump (see Fig. 78(b)). The latter means that oxygen atoms are not involved in the observed reflection, implying that no lattice distortion takes place.

From the peak energy dependence and commensurate $5c_L$ periodicity, Abbamonte et al. inferred that this two-dimensional hole modulation originates in the ladders. Two-dimensional hole ordering is in accord with the results obtained by low-frequency dielectric spectroscopy and microwave spectroscopy. The authors also argued that the modulation has no magnetic character. That is, the resonance near the L edge of copper was not observed at the absorption peak maximum, rather at the L shoulder, which arises from holes on the neighboring ligands.

An additional important observation is that no harmonic at $m = 0.4$ was found, implying that the hole order is not a fully localized Wigner crystal, i.e. $4k_F$ CDW (see Section 2.1). The authors propose that it can be described as a sinusoidal, delocalized modulation as suggested by White et al. [184]. We remind that a standard $(2k_F)$ CDW is also a sinusoidal modulation. The authors also argue that if lattice distortion exists, associated with the hole order, it would be very weak and impossible to detect. The conclusion is that the electron–electron interaction, rather than the electron–phonon, drives the ordering. Nevertheless, the latter should play some role as indicated from the effective mass of the collective mode $m^* \approx 100m_0$ (see Section 5.3.3). We will address the nature of the CDW observed in the ladders more in detail in Section 6.2.

The experiment with the X-rays tuned at 528.6 eV (ladder holes feature, MCP, see Fig. 78(a)) was carried out at varying temperature and the result is shown in Fig. 79. The intensity starts to grow gradually below ≈ 250 K, and the onset of the hole order is at about $T_c \approx 210$ K, as extracted from the dc resistivity and low-frequency dielectric spectroscopy data (see Sections 5.3.1 and 5.3.2). The integrated intensity of the peak gradually increases with decreasing temperature and attains a maximum value at the lowest temperature of 28 K. The super-structure peak width is temperature-independent, implying that the coherence length is limited by some mechanism other than thermodynamics.

The CDW order observed at 28 K indicates that the back-transfer of holes from the ladders into the chains, which occurs with decreasing temperature, is not complete: there is a small, but finite hole density in the ladders at low temperatures. The unifying conclusion concerning the distribution of holes in the ladders and in the chains of $\text{Sr}_{14}\text{Cu}_{24}\text{O}_{41}$ might be now drawn on the basis of the results presented in this section and in Sections 3.3.3, 4.1.2 and 4.1.3. The distribution at room temperature is almost one hole per formula unit in the ladders and five holes in the chains. As the temperature is decreasing below $T_c = 210$ K, the back-transfer of holes from the ladders into the chains gradually takes place and at $T < 50$ K a very little, but still finite amount of holes remain in the ladders, while almost six holes per formula unit reside in the chains.

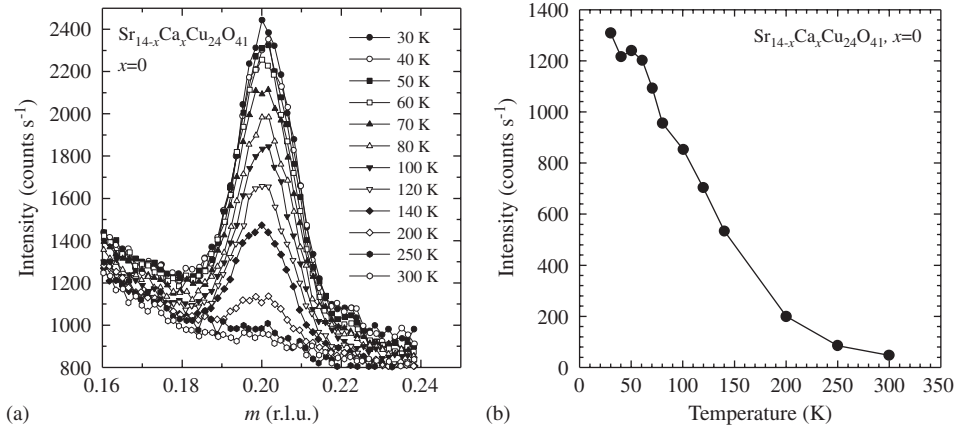


Fig. 79. (a) Resonant X-ray scattering intensity in the vicinity of $(h, k, m) = (0, 0, 0.2)$ in the reciprocal ladder space of $\text{Sr}_{14-x}\text{Ca}_x\text{Cu}_{24}\text{O}_{41}$, $x = 0$ at various temperatures. (b) Temperature dependence of the energy-integrated intensity of the superlattice reflection peak. After Ref. [99].

A final remark concerns the statement of Abbamonte et al. that no reflection is visible when the X-ray energy is tuned at the energies away from 528.6 eV (ladders hole prepeak). It would be important to know if this also implies that no reflection is visible when the X-ray energy is tuned at 528.0 eV i.e. at the oxygen peak associated with the holes in the chains (see Fig. 77 and Section 3.3.1). Inelastic neutron scattering results indicate the charge order with the super-periodicity of $5c_C$ chain parameters (see Section 4.1.2). Therefore, we would expect that a hole super-structure reflection peak should be visible at $(h, k, l) = (0, 0, 0.2)$ in terms of the chain reciprocal unit cell, or at $(h, k, m) = (0, 0, 0.285)$ in terms of the ladder reciprocal unit cell. We suppose that a concomitant probing of the charge order in the chains and in the ladders, using the same technique sensitive to the holes, would be of primary importance.

6. Discussion

In this section we try to organize the experimental findings in such a way that some phase diagrams can be suggested, which summarize the important aspects observed in these compounds. The rough sketches certainly simplify specific details; nevertheless they might help to get some overview. Theory will never be able to describe all details, but it might catch the essentials.

6.1. Phase diagrams

The systematic studies of the spin-ladder and spin-chain compounds $(\text{La}, \text{Y}, \text{Sr}, \text{Ca})_{14}\text{Cu}_{24}\text{O}_{41}$ allows us to summarize the doping dependence of the various ground states in phase diagrams. Preliminary suggestions have been made previously [133,143,144], but it turns out that more detailed considerations are required in order to draw a complete picture of the complex system.

6.1.1. Phase diagram of chains in underdoped $(\text{La}, \text{Y})_y(\text{Sr}, \text{Ca})_{14-y}\text{Cu}_{24}\text{O}_{41}$

The ladders in $(\text{La}, \text{Y})_y(\text{Sr}, \text{Ca})_{14-y}\text{Cu}_{24}\text{O}_{41}$ are undoped (no holes) and the ground state is a gapped spin-liquid. Therefore, the phase diagram of $(\text{La}, \text{Y})_y(\text{Sr}, \text{Ca})_{14-y}\text{Cu}_{24}\text{O}_{41}$ reduces to the phase diagram of chains. The total hole count $n_h = 6 - y$ is determined by the substituted ions y . The number of holes per formula unit in the chains equals n_h for $1 \leq y \leq 6$. For y between 1 and 0 when n_h increases from 5 to 6, it seems that the number of holes in the chains remains fixed at five [106], while ladders start to be doped gradually to accommodate one hole per formula unit for $y = 0$ ($n_h = 6$). The qualitative phase diagram of the chains in $(\text{La}, \text{Y})_y(\text{Sr}, \text{Ca})_{14-y}\text{Cu}_{24}\text{O}_{41}$ is displayed in Fig. 80. The high temperature phase is best described as a paramagnetic one-dimensional (1D) disorder-driven insulator. The charge transport happens via hopping of holes between localized states along the chain. The room temperature

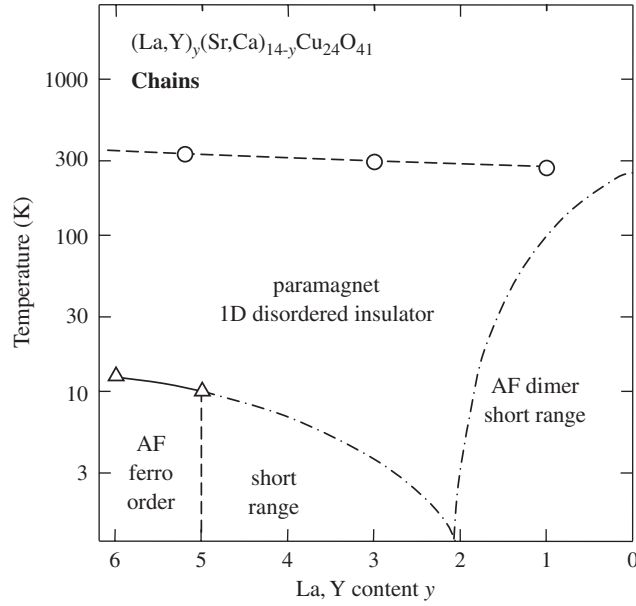


Fig. 80. Qualitative phase diagram of the chains in $(\text{La},\text{Y})_y(\text{Sr},\text{Ca})_{14-y}\text{Cu}_{24}\text{O}_{41}$. The high temperature phase is a paramagnetic one-dimensional (1D) disordered insulator. The dashed line in the insulating phase denotes the smooth crossover T_{co} (circles) in the conduction mechanism from nearest neighbor hopping to variable-range hopping [43,110]. The AF order of FM chains (AF ferro) is established for $6 \geq y \geq 5$ below the phase transition denoted by triangles [69,107]. Short-range AF correlations persist up to $y \lesssim 2$ [84]. Also sketched is the AF dimer phase, which exists at short scales for $0.1 \leq y \lesssim 2$ [90,106,109].

Table 5

Total hole count n_h and dc conductivity along the c -axis at room temperature in $(\text{La},\text{Y},\text{Sr},\text{Ca})_{14}\text{Cu}_{24}\text{O}_{41}$ [43,110]

n_h	Chains		Ladders	
	Number of holes per f.u.	σ_c ($\Omega^{-1} \text{cm}^{-1}$)	Number of holes per f.u.	σ_c ($\Omega^{-1} \text{cm}^{-1}$)
0.8	0.8	0.0007	0	—
3	3	0.07	0	—
5	5	0.5	0	—
6	5	—	1	500

The number of holes per formula unit in the chains and in the ladders correspond to the hole distribution in the underdoped $(\text{La},\text{Y})_y(\text{Sr},\text{Ca})_{14-y}\text{Cu}_{24}\text{O}_{41}$, $y = 5.2, 3, 1$, and in the fully doped $\text{Sr}_{14-x}\text{Ca}_x\text{Cu}_{24}\text{O}_{41}$, $x = 0$, respectively [81].

conductivity increases substantially with the total hole count (Table 5); a result that has not been understood yet. It is evident that the increased number of holes per formula unit in the chains cannot account completely for this, orders of magnitude, rise in conductivity. For $y = 6$ and no holes in the chains, the dominant magnetic interaction within the chains is the nearest neighbor interaction between the Cu^{2+} spins (J_{nn}), which is FM (Table 6). These FM chains order in a bulk AF state at low temperatures. Decreasing y (increasing number of holes in the chains) destroys long-range order quickly so that only AF short-range correlations survive up to $y \approx 2$. The AF interaction between the spins of the next-nearest neighbor Cu^{2+} ions, separated by a hole, prevails for $y \approx 2$ and smaller [70]. Nevertheless, the AF dimer order develops only at short scales as long as $y > 0$. This might be due to deviations from almost six holes per formula unit in the chains [106], which is necessary to establish the long-range AF dimer order. This deviation appears to be critical for the suppression of the complementary charge-ordered gapped phase (established in the chains for $y = 0$) in favor of disorder-driven insulating phase in the chains of $(\text{La},\text{Y})_y(\text{Sr},\text{Ca})_{14-y}\text{Cu}_{24}\text{O}_{41}$. Disorder is associated with random distribution of holes and causes the Anderson localization.

An intriguing issue is how the charge transport switches from the chains to the ladders when y decreases from 1 to 0 and holes are doped into the ladders. Is there a phase transition from underdoped $(\text{La},\text{Y})_y(\text{Sr},\text{Ca})_{14-y}\text{Cu}_{24}\text{O}_{41}$ to

Table 6

Exchange couplings between Cu^{2+} spins in the chains and ladders of $(\text{La,Y,Sr,Ca})_{14}\text{Cu}_{24}\text{O}_{41}$

Chains		Ladders	
Nearest neighbor	Next-nearest neighbor	Along legs	Along rungs
$J_{nn} \approx -1 \text{ meV}$	$J_D \approx 11 \text{ meV}$ $J_D \sim \Delta_C$	$J \approx 130 \text{ meV}$	$J' \approx 70 \text{ meV}$ $J' \sim 2\Delta_L$
Interchain $J_a \approx 1 \text{ meV}$		Interladder $J_a \approx -1 \text{ meV}$	

The coupling values do not change substantially with doping. Nearest neighbor intrachain interaction J_{nn} and interladder interaction J_a are FM, while the other intrachain J_D , interchain J_a and intraladder interactions J and J' are AF. J_D also denotes the intradimer coupling relevant for the AF dimer order. Δ_C and Δ_L stand for the spin gap of the AF dimer order in the chains and for the spin gap of the gapped spin-liquid in the ladders, respectively [71,87,88,45,91].

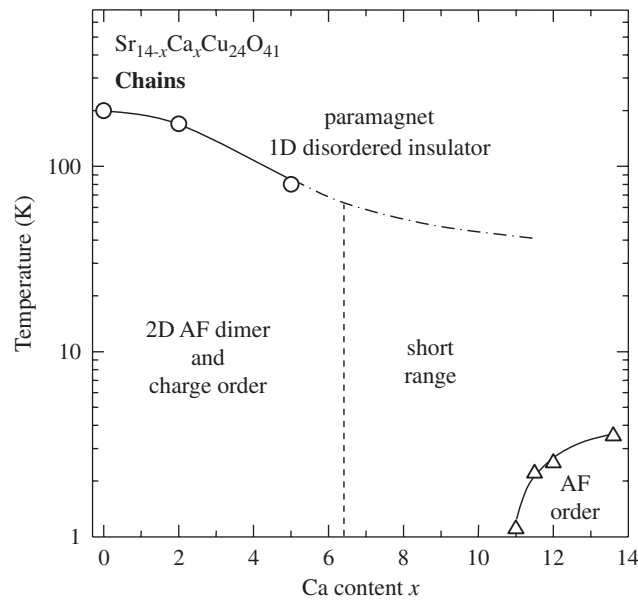


Fig. 81. Qualitative phase diagram of the chain subsystem in $\text{Sr}_{14-x}\text{Ca}_x\text{Cu}_{24}\text{O}_{41}$. The high temperature phase is a paramagnetic disordered insulator. Two-dimensional (2D) AF dimer and complementary charge order set in for $0 \leq x \lesssim 6$ below the crossover temperature denoted by circles [85,88]. Short-range AF dimer correlations persist up to $x \approx 11.5$ [105]. For $x \geq 11$ the AF Néel order is established below the phase transition denoted by triangles [85,101,104,105].

fully doped $\text{Sr}_{14-x}\text{Ca}_x\text{Cu}_{24}\text{O}_{41}$? How does the ladders phase diagram of the former series merge with the one of the latter compounds in the charge sector? These are the questions worth to be addressed in the future.

6.1.2. Phase diagrams of chains and ladders in fully doped $\text{Sr}_{14-x}\text{Ca}_x\text{Cu}_{24}\text{O}_{41}$

The qualitative phase diagrams of chains and ladders in $\text{Sr}_{14-x}\text{Ca}_x\text{Cu}_{24}\text{O}_{41}$ are displayed in Figs. 81 and 82. Doped holes are distributed between the chains and the ladders, so that at room temperature there are approximately five holes per formula unit in the chains and approximately one hole in the ladders for $x = 0$. With decreasing temperature, this distribution changes due to a partial back transfer of holes from the ladders to the chains (Sections 3.3.3, 4.1 and 5.3). Upon Ca-substitution, holes are transferred from the chains to the ladders. A number of suggestions have been made of how many holes are actually redistributed. They can be classified in the two groups. A first estimate yields a substantial transfer of about 1.8 holes per formula unit (or 0.13 holes per ladder Cu site) when the Ca-substitution increases from $x = 0$ to $x = 12$, while another one suggests only a minor change of about 0.4 holes per formula unit (or 0.03 holes per ladder Cu site). However, further experiments are needed to resolve this issue.

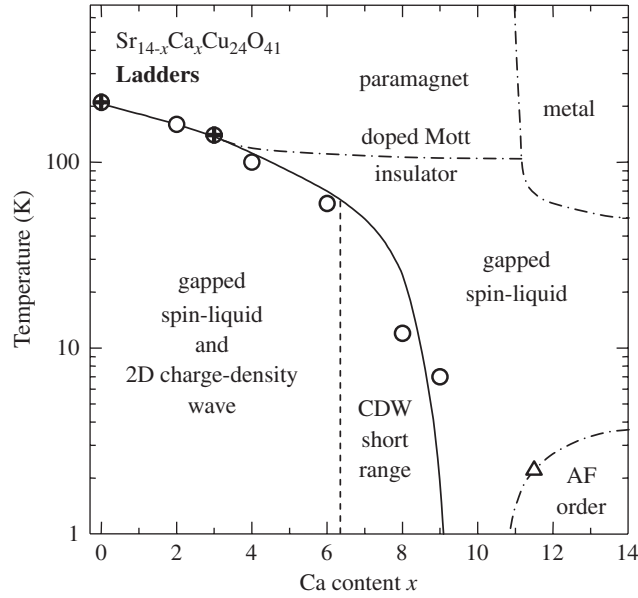


Fig. 82. Qualitative phase diagram of the doped ladders in $\text{Sr}_{14-x}\text{Ca}_x\text{Cu}_{24}\text{O}_{41}$. The high temperature phase is a doped Mott insulator. Gapped spin-liquid and two-dimensional (2D) CDW order set in below the crossover and phase transition temperature (crosses and circles), respectively. [67,122,123,132,134,144,145]. CDW order persists only at short length scales for $6 < x \leq 9$ and is fully suppressed for $x \geq 11.5$ [144,145]. The horizontal dash-dot line denotes an onset of the crossover from gapped spin-liquid to paramagnetic regime for $x > 4$ [132–134]. Sketched are also metallic and AF phases [43,105] for large Ca-substitution.

The high temperature phase of the chains in the fully doped materials $\text{Sr}_{14-x}\text{Ca}_x\text{Cu}_{24}\text{O}_{41}$ is a paramagnetic one-dimensional (1D) disorder-driven insulator, similar to the phase established for the chains in $(\text{La},\text{Y})_y(\text{Sr},\text{Ca})_{14-y}\text{Cu}_{24}\text{O}_{41}$. Upon decreasing temperature an AF dimer order with concomitant charge order is established in two dimensions in the ac planes. While in the chains of $(\text{La},\text{Y})_y(\text{Sr},\text{Ca})_{14-y}\text{Cu}_{24}\text{O}_{41}$, $y \lesssim 2$ this order can develop only at short length scales, in the chains of $\text{Sr}_{14-x}\text{Ca}_x\text{Cu}_{24}\text{O}_{41}$ the number of holes is close to six per formula unit at low temperatures (due to the back transfer of holes), and therefore permits the AF dimer order to develop fully.

Increasing Ca content destroys the long-range order quickly (for x between 5 and 8) so that only the AF dimer short-range order persists at least up to $x = 11.5$. For $x \geq 11$ an AF order is established at low temperatures, characterized by a large magnetic moment of about $0.56\mu_B$ which is typical for localized spins.

A comparison of the phase diagrams displayed in Fig. 80 and Fig. 81 reveals a similar effect of La, Y and of Ca-substitution, which destabilize the AF dimers in favor of an AF order. However, an increase of La, Y content weakens the AF interaction within the chains in favor of an FM one, while this is not the case for Ca-substitution. The reason is the substantial decrease of the hole number when La or Y is doped, while even for the largest Ca content the number of holes in the chains of $\text{Sr}_{14-x}\text{Ca}_x\text{Cu}_{24}\text{O}_{41}$ remains rather high. In this way the next-nearest neighbor AF interaction prevails over the nearest neighbor FM interaction for all x of $\text{Sr}_{14-x}\text{Ca}_x\text{Cu}_{24}\text{O}_{41}$ (Table 6). Note that, on the other hand, the interaction between the chains is always AF, independently of either La, Y or Ca content (i.e. independently of the number of doped holes); the interaction is furthermore responsible for the stabilization of either AF dimer order or AF Néel order (Fig. 81).

The high temperature (normal) phase of the ladders is different compared to the one in the chains. It might be considered as close to a doped Mott insulator in the paramagnetic regime. Holes in the ladders appear as being mobile when compared with the holes in the chains. The room temperature conductivity of the ladders along the c -axis in $\text{Sr}_{14}\text{Cu}_{24}\text{O}_{41}$ is 1000 times larger than the conductivity of the chains in $(\text{La},\text{Y})_y(\text{Sr},\text{Ca})_{14-y}\text{Cu}_{24}\text{O}_{41}$, $y = 1$ (see Table 5). We remind that in these two compounds the number of holes in the chains is the same (five holes per formula unit), while only the number of holes in the ladders differ (one hole per formula unit in $\text{Sr}_{14}\text{Cu}_{24}\text{O}_{41}$ and none in the latter compounds). This implies that the enormous difference in the conductivity is probably also valid between the ladders and chains of $\text{Sr}_{14}\text{Cu}_{24}\text{O}_{41}$. Charge transport basically takes place in the ladder subsystem; an issue addressed again in Section 6.2.

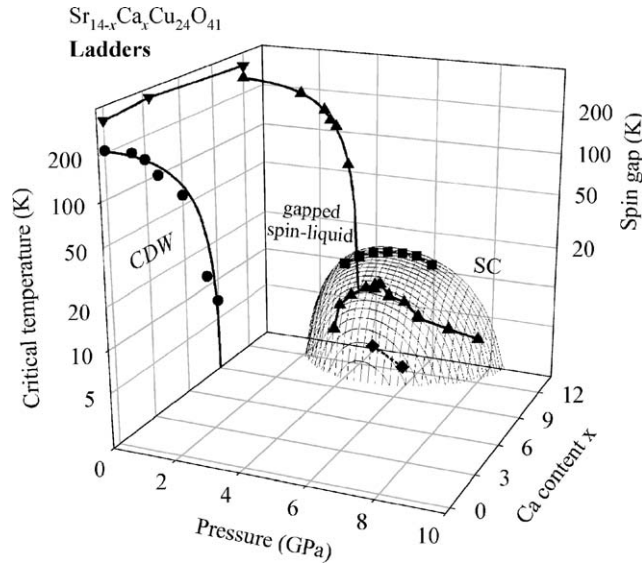


Fig. 83. Dependence of the critical temperatures on Ca content x and on pressure for the doped ladder subsystem in $\text{Sr}_{14-x}\text{Ca}_x\text{Cu}_{24}\text{O}_{41}$. The points indicate the transition temperature of the CDW phase [122,144,145]. The superconducting (SC) phase is determined by the critical temperature denoted by diamonds, triangles and squares for $x = 10, 12$ and 13.6 , respectively [5,143,146,148]. The gapped spin-liquid phase is described by the spin gap (inverted triangles [124,125] and triangles for $x = 12$ [133]). The lines are guides for the eye.

The ground state in the spin sector is a gapped spin-liquid. The exchange coupling parameters are given in Table 6. It is possible to define the crossover from the gapped spin-liquid to the paramagnetic regime (Section 5.1.2) that coincides well with the CDW phase transition in the charge sector. This order, with periodicity of five ladder unit-cell parameters, develops in two dimensions in the ac planes at length scales, which suggest the influence of intrinsic disorder in these compounds related with their composite structure. Both dc resistivity and low frequency dielectric spectroscopy show that increasing the Ca content destroys the long-range order rapidly (for $x \gtrsim 6$) so that only CDW short-range order survives, before it vanishes completely for $x > 9$.¹⁹ Conversely, the gapped spin-liquid phase persists to the largest Ca contents for which the ladders become superconducting under high pressure. For $x = 11.5$ and 12 a tiny amount of small magnetic moments ($\approx 0.02\mu_B$), associated with mobile quasi-particles, emerges and develops magnetic order at low temperatures. The metallic phase appears for $x \geq 11$, but the insulating phase prevails at lower temperatures even for the largest Ca content.

A close inspection of the phase diagrams for the chains and ladders (Figs. 81 and 82) reveals the interdependence between the chains and ladders. It is striking that the charge order (associated with the AF dimer pattern) in the chains, and CDW in the ladders are suppressed by the similar rate. Note, however, that both the AF dimer phase, as well as the gapped spin-liquid state, persist up to the highest Ca contents at shorter length scales producing the spin gaps of a size which does not change with x . For $x \geq 11$, an AF Néel order is established below these phases at very low temperatures [104,105].

In order to incorporate pressure as an additional important parameter besides Ca content x , a three-dimensional phase diagram of the doped ladders in $\text{Sr}_{14-x}\text{Ca}_x\text{Cu}_{24}\text{O}_{41}$ was constructed as displayed in Fig. 83. While the CDW phase is fully suppressed for high Ca content already at ambient pressure, the spin gap remains unchanged. Upon application of pressure, the spin gap decreases but remains finite when superconductivity sets in within the pressure range of 3–8 GPa. The role of the spin gap in superconducting pairing is not clear yet, since there is some evidence for the presence of quasi-particles with a finite density of states at the Fermi level, which contribute to superconductivity. We will address more the issue of the superconductivity in Section 6.2. Nothing is known about the pressure dependence of the CDW

¹⁹ In an alternative scenario, based on the low-frequency electronic Raman scattering, CDW correlations persist up to $x = 12$ at least at high temperatures.

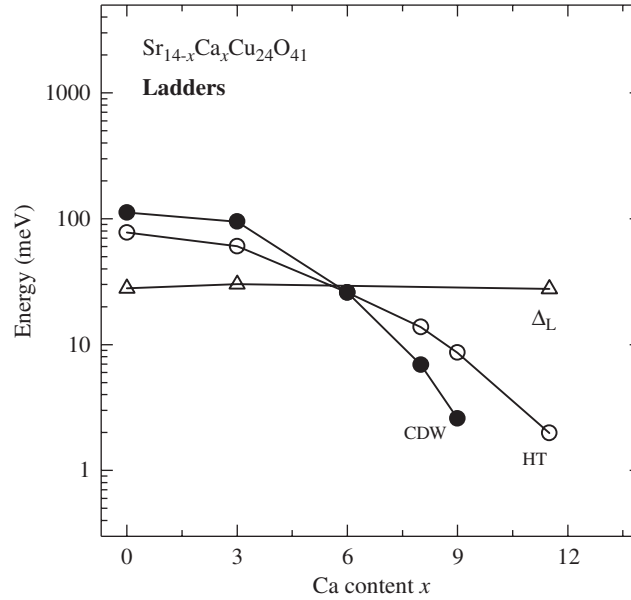


Fig. 84. Relevant parameters for the charge and spin response of the ladders in $\text{Sr}_{14-x}\text{Ca}_x\text{Cu}_{24}\text{O}_{41}$ as a function of Ca content x . Δ_{CDW} , Δ_{HT} and Δ_L stand for the CDW gap, the high temperature insulator activation energy and the spin gap, respectively [124,125,144,145].

state, but it is known that pressure as high as 8 GPa cannot bring back the metallic state for $1 \leq x \leq 8$, except for $x = 0$ compound [143].

Fig. 84 demonstrates how the CDW gap and the activation energy of the high temperature insulating phase change upon Ca-substitution. For comparison the spin gap dependence is also displayed. While the CDW gap completely vanishes for high Ca content, the insulating phase is more robust. High pressure is required to fully suppress the insulating phase in favor of a metallic one. This is achieved only for $x \geq 11.5$ under pressures larger than 4.5 GPa.

6.2. Doped ladders of $\text{Sr}_{14-x}\text{Ca}_x\text{Cu}_{24}\text{O}_{41}$

6.2.1. Normal phase and nature of charge transport

The undoped ladders in $(\text{La}, \text{Y})_y(\text{Sr}, \text{Ca})_{14-y}\text{Cu}_{24}\text{O}_{41}$ can be described as a system with one electron carrying a spin $1/2$ per Cu^{2+} site. Due to strong electron–electron on-site repulsion this half-filled system is a Mott–Hubbard or a charge-transfer insulator. The gap in the charge excitation spectrum is about $U_{\text{eff}} \approx 2 \text{ eV}$ and no spectral weight is found below this gap. The comparably large spectral weight found around 3 eV is attributed to the chains and the associated excitations contribute to the conductivity (Table 5) [80]. On the other hand, the conductivity of the doped ladders in $\text{Sr}_{14-x}\text{Ca}_x\text{Cu}_{24}\text{O}_{41}$ is related to a finite spectral weight at low energies (below 1 eV). This spectral weight increases with Ca-substitution at the expense of the weight above the charge-transfer gap.

The room temperature conductivity of lightly doped ladders in $\text{Sr}_{14-x}\text{Ca}_x\text{Cu}_{24}\text{O}_{41}$ with $x = 0$ (one hole per formula unit, which is equivalent to $\delta = 0.07$ holes per ladder copper site) along the c - and a -axis is $\sigma_c \approx 500 \Omega^{-1} \text{ cm}^{-1}$ and $\sigma_a \approx 20 \Omega^{-1} \text{ cm}^{-1}$. Although σ_c is rather high, it decreases with lowering the temperature similar to $\sigma_a(T)$ showing insulating behavior. The small value of σ_a and its temperature dependence indicate non-coherent transport along the a -axis (i.e. along the rungs of the ladders), which might be related with the presence of the spin gap. The spin gap implies the formation of hole pairs in the rungs; compared to quasi-particles, these pairs presumably have a much smaller interladder hopping probability. On the other hand, the insulating behavior of σ_c (along the legs of the ladders) is not in accord with the assumption that doped holes form a resonance band at the Fermi level. Serious questions arise about the origin of the insulating charge transport along the c -axis. For a conventional metal the smallest value of the conductivity σ^{min} consistent with the standard Boltzmann transport theory is reached when the mean-free path ℓ becomes comparable to the Fermi wavelength $\lambda_F = 2\pi/k_F$ [185]. For a quasi-one-dimensional system, such as the

doped ladders can be pictured, the conductivity along the best conducting c -axis is given by

$$\sigma_c = 4 \frac{e^2}{h} \frac{z}{ab} \ell, \quad (27)$$

where (z/ab) is the areal density of the ladders. There are $z = 4$ ladders per unit cell cross-section perpendicular to the legs of the ladders (the c -axis), and the unit cell parameters are $a \approx 11.5 \text{ \AA}$ and $b \approx 13.5 \text{ \AA}$. The doped ladders in $x = 0$ material can be described as a system close to half-filling, so that $k_F \approx \pi/2c_L$. Using $c_L \approx 3.9 \text{ \AA}$, we get that the mean-free path $\ell_m = 2\pi/k_F \approx 15.6 \text{ \AA}$. Inserting ℓ_m in Eq. (27) gives the Ioffe–Regel limit: $\sigma_c^{\min} \approx 6000 \Omega^{-1} \text{ cm}^{-1}$. In the entire doping regime the room temperature conductivity is smaller than the calculated σ_c^{\min} , implying that the conductivity of the doped ladders even for $x = 11.5$ ($\sigma_c \approx 1100 \Omega^{-1} \text{ cm}^{-1}$ at ambient pressure, $\sigma_c \approx 3000 \Omega^{-1} \text{ cm}^{-1}$ at 4.5 GPa) cannot be considered as metallic in the standard sense. This also holds for the conductivity at low temperatures at ambient pressure, as well as under pressure, except for the case of very high pressure when the ladders become superconducting.

Similar conclusions can be also reached if only a band formed by doped holes is considered, meaning that we introduce the density of holes measured from half-filling. We assume that there are 1.4 holes per formula unit in the ladder, which is close to the result obtained by the near-edge X-ray absorption. This means $\delta = 0.1$ hole per ladder copper site, implying $k_F \approx \pi/20c_L$. This band filling yields $\sigma_c^{\min} \approx 6 \times 10^4 \Omega^{-1} \text{ cm}^{-1}$, which is again larger than the measured conductivity. Qualitatively the same result ($\sigma_c^{\min} \gg \sigma_c$) is obtained if $\delta = 0.2$ holes per copper site of the ladders is assumed; this value of δ corresponds to the optical conductivity result for $x = 11.5$.

The conductivity of doped two-leg ladders was studied by Orignac and Giamarchi [186] and by Kim [187] using renormalization group methods. At half-filling the presence of strong on-site Coulomb repulsion puts one electron per site, so that the electrons are equally spaced with period c_L . In other words, the electron density is maximum at the lattice site and minimum in between: this can be viewed as $4k_F$ CDW [13]. Orignac and Giamarchi showed that doping i.e. moving away from half-filling does not change the picture considerably since both spin gap and $4k_F$ CDW persist,²⁰ while $2k_F$ CDW fluctuations remain absent. The transport is governed by $4k_F$ CDW fluctuations, which become pinned due to the coupling to disorder. This localization is an inherent feature of one-dimensional ladder physics. Indeed, this scenario is confirmed by Kim, who calculated σ_c for $x = 8$ and 11 compounds using a model of hole pairs which form a strongly correlated liquid. These results reproduce well the low temperature insulating behavior, while they fail to recover the metallic conductivity above 80 K for $x = 11$ [187]. The crossover to a metallic behavior might be due to pairing fluctuations, whose contribution to the conductivity is not taken into account. Following Orignac and Giamarchi, we suggest that the appearance of a metallic behavior for $x \geq 11$ under pressure, indicates that the interladder coupling starts to prevail over one-dimensional effects, which dominate the charge transport at ambient pressure.

For a better understanding of the charge transport in the normal phase of the doped ladders in $\text{Sr}_{14-x}\text{Ca}_x\text{Cu}_{24}\text{O}_{41}$, two additional experimental facts must be taken into account. The first concerns a clear interdependence of the conduction anisotropy and the anisotropy of the thermal compressibility of the lattice parameters, which both decrease with increasing pressure. Second, for $x \geq 11.5$ quasi-particles appear with a finite density of states at the Fermi level, whose amount grows upon increasing pressure, concomitantly as the spin gap size decreases. The origin of quasi-particles might be twofold. Increased pressure dissociates bound holes in the ladder rungs, but it also induces an additional transfer of holes from the chains in the ladders. These mobile quasi-particles have a larger interladder hopping probability than bound hole pairs and can contribute more substantially to the a -axis conductivity compared to the c -axis [188]. The complete suppression of the insulating behavior coincides with the appearance of a two-dimensional metallic transport along the ladders and in between them. The dimensional crossover from one to two dimensions induced by external pressure seems to be a clue, which eliminates localization and restores a metallic transport in the doped ladders of $\text{Sr}_{14-x}\text{Ca}_x\text{Cu}_{24}\text{O}_{41}$.

Finally, the influence of the chain layers on the physics of the ladders should not be neglected. A decrease of the b -axis lattice parameter induced by Ca-substitution, as well as by applying pressure, indicates a gradual strengthening of the coupling between ladders and chains. This change is substantial if compared to variations of the in-plane ladder lattice parameters. A question, which also remains open, concerns the $4k_F$ CDW fluctuations: do they persist under pressure when the dimensional crossover takes place, when the ladders become metallic and eventually superconductivity sets in?

²⁰ Note that moving away from half-filling means that the system becomes incommensurate so that $4k_F$ CDW fluctuations can develop.

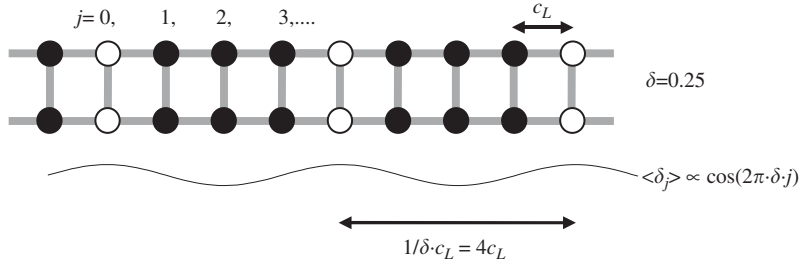


Fig. 85. Sketch of the charge arrangement in a ladder with a period $4c_L$ for the hole density $\delta = 0.25$ corresponding to a gapped CDW $\langle \delta_j \rangle$ according to Eq. (28). The full dots represent electrons and the open circles holes. Rungs are indexed by $j = 0, 1, 2$, etc.

6.2.2. Ground states: Charge-density wave and superconductivity

It is of particular interest to understand the nature of the CDW and superconducting (SC) order in the doped ladders of $\text{Sr}_{14-x}\text{Ca}_x\text{Cu}_{24}\text{O}_{41}$, which present a nice experimental system of strongly interacting electrons.

There is a vast class of broken symmetry patterns, predicted theoretically for strongly correlated electronic systems. In particular, an important amount of work was dedicated to study competing orders in doped two-leg ladders, including CDW and SDW and superconductivity, both of different symmetries. In the following, we will briefly present some of them trying to see to which extent these models can describe the CDW phase and the superconducting phase in the doped ladders of the real system $\text{Sr}_{14-x}\text{Ca}_x\text{Cu}_{24}\text{O}_{41}$.

A theoretical prediction for the existence of a gapped CDW, established at long-range scale, in a two-leg t – J ladder was worked out by White et al. [184]. The starting Hamiltonian is given by Eq. (7) (in Section 2), but with the approximation made $t \approx t'$ and $J \approx J'$, where t and J , and t' and J' are hopping integrals and exchange couplings along the legs, and along the rungs of the ladders, respectively. They have applied the density–matrix renormalization group method to study the binding of holes into pairs when weakly doped into a half-filled two-leg ladder. In this approach, the spin degrees of freedom are gapped and the low energy sector of hole pairs can be described by a model of bosons on a chain with each boson representing a pair of holes. In addition to the $4k_F$ CDW phase with a gapless charge mode, which is considered a generic phase in two-leg t – J ladder, a completely gapped CDW can occur at special commensurate fillings, depending on the value of J/t . This $4k_F$ phase corresponds to a broken translational symmetry and is characterized by a sinusoidal charge-density modulation

$$\langle \delta_j \rangle \propto \cos(2\pi \cdot \delta \cdot j + \alpha) + \text{const.}, \quad (28)$$

where δ is the density of holes (number of doped holes per ladder copper site), j is an integer denoting the rungs and α is a phase constant. Such a sinusoidal charge modulation is similar as for the conventional (Peierls) $2k_F$ CDW, which arises due to electron–phonon coupling. For example, a hole density $\delta = 0.25$ leads to the periodicity of this charge modulation $1/\delta = 4$ unit cell parameters (Fig. 85). The stabilization of the gapped $4k_F$ CDW critically depends on the ratio J/t , meaning that the CDW is present for $J/t \approx 0.25$, while it is absent for larger values of the exchange coupling J .

The ratio of $J/t \approx 0.25$ is rather close to the value expected for the ladders of $\text{Sr}_{14}\text{Cu}_{24}\text{O}_{41}$, where $J \approx 130$ meV and $t \approx 0.5$ eV. On the other hand, resonant X-ray diffraction experiments observe a periodicity of the charge-density modulation in the doped ladders of $\text{Sr}_{14}\text{Cu}_{24}\text{O}_{41}$, of 5 times the ladder unit-cell parameter c_L , which according to the model by White et al. implies a density $\delta = 0.2$. This is rather unrealistic since it is more than twice the hole density detected by near-edge X-ray absorption ($\delta = 0.07$ holes per ladder copper site). The model also faces difficulties to explain the suppression of the CDW by Ca-substitution. For large $x \approx 11.5$ the exchange coupling J slightly decreases, while the transfer integral t is expected to increase to some extent due to the shorter c_L parameter. This implies a smaller ratio J/t , while White et al. find that the $4k_F$ gapped CDW is absent for larger values of J/t . Finally, it is noteworthy that the question, concerning the relationship between the observed CDW periodicity [99] and the hole density [81], remains also open in the theoretical models predicting $2k_F$ CDW [188–190]. In this case the CDW periodicity is $2/\delta$ unit cell parameters, implying the hole density $\delta = 0.4$, if the observed periodicity of $5c_L$ is taken into account. This hole density estimate is again far from the one observed experimentally.

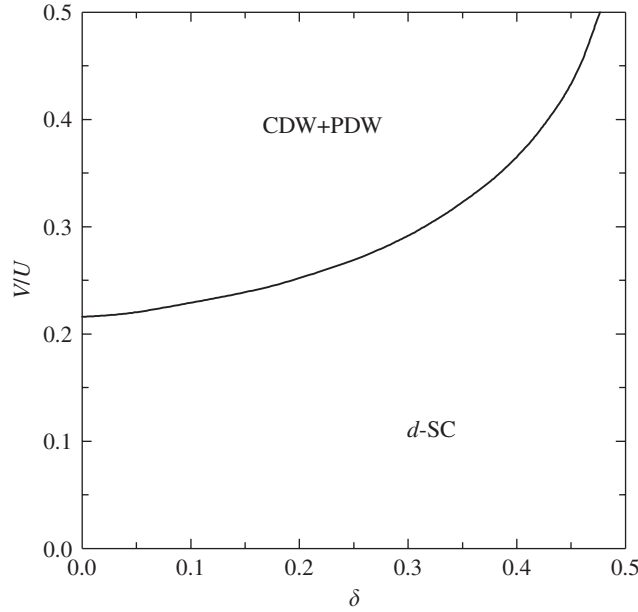


Fig. 86. Phase diagram of doped two-leg ladder in the weak-coupling limit. CDW+PDW is the coexisting CDW and PDW state, while d -SC denotes d -wave superconductivity. V/U is the ratio of inter-site V and on-site U couplings and δ is the hole number per ladder Cu site. The choice of parameters is $V_{\parallel} = V_{\perp} = V$, $t_{\parallel} = t_{\perp} = t$ and $U/t = 3$. After Ref. [190].

At this point, angle-resolved photoemission studies of momentum-resolved gaps and self-energies as a function of temperature and Ca-substitution could help in understanding the mechanism responsible for producing the CDW phase in the doped ladders of $\text{Sr}_{14-x}\text{Ca}_x\text{Cu}_{24}\text{O}_{41}$.

Further, the extended Hubbard model was also applied to study doped two-leg ladders [186,189,190,192,193]. Tsuchiizu and Suzumura, for instance, used a weak-coupling renormalization group method in order to study how the dominant fluctuations change from the d -wave superconducting phase into the $2k_F$ CDW and p -density wave (PDW) phases²¹ [189,190]. Their approach does not consider the $4k_F$ CDW, which also develops quasi-long-range order in the phase diagram of two coupled chains (i.e. a ladder) [194], since they argue that the $4k_F$ CDW remains a subdominant fluctuation if compared to CDW and PDW.

The influence of doping on the mutual stability of SC and CDW phases is demonstrated in Fig. 86: doping reduces the effect of the inter-site repulsion V . Note that for a realistic choice of parameters $U = U_{\text{eff}} \approx 2 \text{ eV}$, $V \approx 0.5 \text{ eV}$, $t \approx 0.5 \text{ eV}$, an increase of the hole density from $\delta = 0.1$ to 0.2 is sufficient to drive the ladder system from the CDW+PDW phase into d -wave superconductivity.

The phase diagram is summarized in Fig. 87. It resembles the phase diagram of the doped ladders in $\text{Sr}_{14-x}\text{Ca}_x\text{Cu}_{24}\text{O}_{41}$ displayed in Fig. 83. However, the expected quantum critical point at which the magnon spin gap collapses is not observed experimentally. In the experimental phase diagram the CDW phase and the superconducting phase do not have a common boundary. While the theory predicts only one external parameter, which is the number of doped holes δ per ladder Cu site, in the real system there is another parameter—pressure, which is necessary for superconductivity to be established. Pressure seems to act similarly as Ca-substitution, in the way that it increases the number of doped holes in the ladder. On the other hand, it is rather clear that pressure increases the interladder coupling and that superconductivity is two-dimensional. The latter fact and the critical temperature of about 10 K bears similarities to the high-temperature superconducting cuprate $\text{La}_{2-x}\text{Sr}_x\text{CuO}_4$ in which superconductivity with similar T_c is established for doping levels $\delta = 0.07 - 0.25$ (maximum T_c is for $\delta = 0.16$) [195]. These values of δ correspond to those found

²¹ The p -density wave is the bond charge-density wave in the limit $\delta \approx 0$, i.e. at half-filling. For the bond CDW, the charges polarize on bonds, while they polarize on sites for the CDW. The CDW (conventional CDW) is the s -density wave, while PDW has a finite angular momentum $l = 1$ [191].

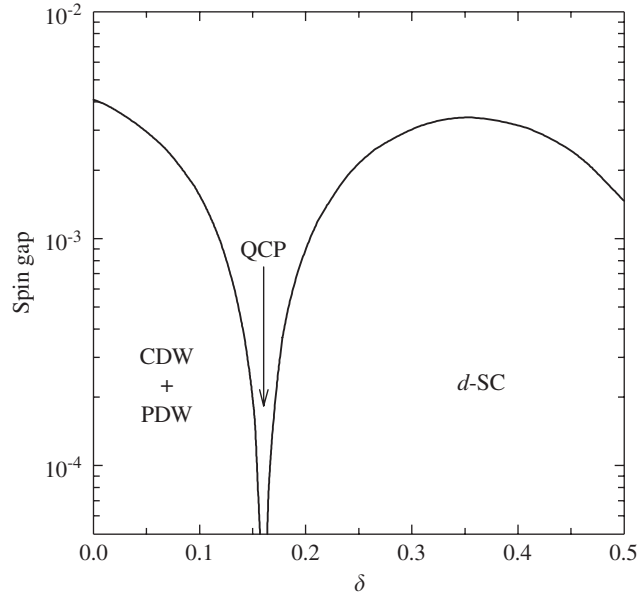


Fig. 87. Magnon spin gap as a function of the number of doped holes per ladder Cu site δ . CDW+PDW is the coexisting CDW and PDW state, while d -SC is d -wave superconductivity. The quantum critical point (QCP) is at $\delta = \delta_c \approx 0.18$. The choice of parameters is $V_{\parallel}/t = V_{\perp}/t = 0.7$, $t_{\parallel} = t_{\perp} = t = 1$ and $U/t = 3$. After Ref. [190].

in the ladders of $\text{Sr}_{14-x}\text{Ca}_x\text{Cu}_{24}\text{O}_{41}$ at ambient pressure. It should be also noted that these δ values estimated at room temperature are similar to δ values found at high pressure but at low temperatures where SC sets in. Thus, the partial failure of the theoretical model, which is purely one-dimensional (i.e. developed for a single ladder), is not surprising.

Another, but still related, problem concerns the origin of the insulating phase at high temperatures, and the nature of the CDW phase and the superconducting phase. The model of Tsuchiizu and Suzumura assumes that $2k_F$ CDW is dominant and that it prevails over $4k_F$ CDW. It also neglects disorder, which is certainly a relevant parameter in the ladders of the composite $\text{Sr}_{14-x}\text{Ca}_x\text{Cu}_{24}\text{O}_{41}$. Based on these assumptions the model falls short to explain the increase in resistivity with decreasing temperature in the normal phase. As far as the d -wave symmetry of the superconducting phase is concerned, a few reasons call against this option. First, the role of the spin gap in the pairing mechanism is not clear because of the presence of mobile quasi-particles, which might instead contribute to superconductivity. Second is the observation of an enhancement of the spin-lattice relaxation rate in the superconducting state, which might be interpreted as a Hebel–Slichter coherence peak. Finally, the d -wave SC is shown to be extremely sensitive to disorder [186]. Taking all these facts into account, it seems clear that the superconductivity observed in the doped ladders of $\text{Sr}_{14-x}\text{Ca}_x\text{Cu}_{24}\text{O}_{41}$ under high pressure cannot be a simple stabilization of the d -wave SC expected for a pure single ladder.

7. Summary

In this review, the experimental aspects of the study of spin-chains and spin-ladders in quasi-one-dimensional cuprates $(\text{La}, \text{Y}, \text{Sr}, \text{Ca})_{14}\text{Cu}_{24}\text{O}_{41}$ have been discussed and contrasted with predictions of theoretical models. In spite of the enormous amount of work allocated to these compounds, it is by far not a closed chapter in the fields of quantum spin systems, low-dimensional magnetism and low-dimensional conductors.

By now it is well understood that the amount of doped holes and their distribution between chains and ladders determines electronic phases and the spin and charge dynamics. In the underdoped materials $(\text{La}, \text{Y})_y(\text{Sr}, \text{Ca})_{14-y}\text{Cu}_{24}\text{O}_{41}$ all holes reside in the chains. The number of holes per formula unit in the chains equals $n_h = 6 - y$ for $1 \leq y \leq 6$. For y between 1 and 0, i.e. when the total number of holes increases from 5 to 6, the number of holes in the chains remains fixed at five.

In the fully doped materials $\text{Sr}_{14-x}\text{Ca}_x\text{Cu}_{24}\text{O}_{41}$ the total number of holes is six, independently of x . For $x = 0$ (zero Ca content) at room temperatures there is close to one hole per formula unit transferred in the ladders and about five remain in the chains. The increased Ca content induces an additional transfer of holes from the chains into the ladders. Although there is still some dispute on the amount of this transfer, it looks likely that the change is minor, rather than substantial. The hole distribution is also temperature dependent. The back-transfer of holes from the ladders into the chains takes place gradually with decreasing temperature. Most of the experiments indicate that at low temperatures a very small, but still finite amount of holes remains in the ladders, while almost six holes per formula unit reside in the chains. Pressure seems to induce an additional transfer of holes from the chains into the ladders, however this number again becomes smaller at low temperatures. Thus, although the estimates of the amount of redistribution induced by either Ca-substitution, or by decreasing temperature, differ, our overall knowledge is sufficient to permit a rather consistent analysis of the experimental data and the construction of the phase diagrams for the chains and ladders.

We first summarize the basic understanding of the physics of spin-chains, starting with the arrangement of the spins. The chains consist of edge-sharing CuO_4 squares, in which nearest neighbor Cu^{2+} spins are coupled by weak ferromagnetic interactions, while the next-nearest neighbor and interchain interactions are AF. The amount of doped holes determines the dominant magnetic interaction and the ground state in the spin sector. In the underdoped compounds $(\text{La}, \text{Y})_y(\text{Sr}, \text{Ca})_{14-y}\text{Cu}_{24}\text{O}_{41}$ the FM with no holes ($y = 6$) order in a bulk AF state. Replacing La, Y by Sr, Ca increases number of holes in the chains, which destroys AF long-range order quickly, while short-range correlations survive up to $y \approx 2$ (four holes per formula unit). For $y \approx 2$ and smaller (4 and 5 holes per formula unit) AF interaction between the spins of the next-nearest neighbor Cu^{2+} ions, separated by a hole, prevails. This interaction yields the AF dimer pattern with tightly associated charge order (AF dimer + CO). The AF dimer + CO pattern develops only at short scales in the underdoped $(\text{La}, \text{Y})_y(\text{Sr}, \text{Ca})_{14-y}\text{Cu}_{24}\text{O}_{41}$, $0.1 \leq y \lesssim 2$. The main condition to establish AF dimer + CO at long length scales is that the number of holes in the chains per formula unit is close to six. This requirement is satisfied in the chains of the fully doped $\text{Sr}_{14-x}\text{Ca}_x\text{Cu}_{24}\text{O}_{41}$, $0 \leq x \lesssim 6$ at low temperatures, while at room temperature this number is five or less. In other words, the long-range AF dimer + CO order is conditioned on the back-transfer of holes from the ladders to the chains with decreasing temperature. For this reason the pattern of AF dimer + CO, which starts to develop in the chains at high temperatures, is fully established in two dimensions within the ac planes only at low temperatures. Below about 50 K a spin gap is observed; the super-periodicity of this spin and charge arrangement is determined to be five chain unit-cell parameters along the c -axis. While there exists no conclusive evidence that the charge order in the chains is accompanied by a concomitant lattice distortion of the same period, it is clear that the misfit potential determined by the incommensurability ($\alpha = 1/\sqrt{2} \approx 7/10$) between the chain and ladder subsystems, felt by the charges residing in the chains, plays a crucial role. Raising the Ca content reduces the number of holes in the chains and induces changes in the misfit potential, which destroys the AF dimer + CO long-range order quickly, so that only the short-range correlations persists at least up to $x = 11.5$. Concomitantly, for $x \geq 11$ an AF order is established at low temperatures, which is characterized by a large magnetic moment typical for localized spins.

As far as the charge degree of freedom is concerned, the chains in the normal phase can be described as one-dimensional disorder-driven insulators in which the charge transport happens via hopping of holes between localized states. Disorder is attributed to a random distribution of holes which causes Anderson localization. In the chains the localized holes arrange in a charge order (CO) ground state tightly bound to AF dimer pattern (AF dimer + CO) only in the well-defined window of doping, just described.

Now we turn to the spin-ladders, which consist of both corner and edge sharing CuO_4 squares. The ground state in the spin sector is the gapped spin-liquid state. As far as the undoped ladders in $(\text{La}, \text{Y})_y(\text{Sr}, \text{Ca})_{14-y}\text{Cu}_{24}\text{O}_{41}$ are concerned, the physics seems to be rather well understood; however, the doped ladders in $\text{Sr}_{14-x}\text{Ca}_x\text{Cu}_{24}\text{O}_{41}$ still present a fruitful area of research. At ambient pressure the charge and spin dynamics of the ladder system can be well described by one-dimensional physics. The anisotropy of the conductivity data indicates that the movement of the holes is confined to the legs of the ladders. It is surprising that for all Ca contents, except for $x \geq 11.5$ at high temperatures, the behavior along the legs is non-metallic (decreasing conductivity with decreasing temperature) in the normal phase, since doped holes are thought to form a resonance band at the Fermi level. This discrepancy might be explained by disorder, which certainly is important in real systems. $4k_F$ CDW fluctuations which are responsible for the charge transport can be localized by pinning to disorder. In the normal state the conductivity along the rungs of the ladder is small and insulator-like for all Ca contents, because the spin gap remains robust upon Ca-substitution. This spin gap implies the formation of hole pairs in the rungs, which presumably have a much smaller interladder hopping probability than the quasi-particles.

A variety of experiments have clearly confirmed the existence of a CDW phase at ambient pressure. The CDW sets in below the insulator-to-insulator phase transition temperature. The sinusoidal charge modulation develops in two dimensions in the *ac* ladder planes at relatively limited length scales due to strong intrinsic disorder of the real system. The collective excitations of this phase possess an anisotropic phason-like dispersion. It is an open question whether such a dispersion is a unique feature of the CDW in ladder structures or whether it is common to quasi-two-dimensional systems in general. Increasing the Ca content destroys the order quickly, so that the CDW seems to vanish for $x > 9$. Based on the extended Hubbard model and on the $t - J$ model, $2k_F$ and $4k_F$ CDW phases are theoretically predicted for the doped two-leg ladder. Increasing the number of doped holes reduces the inter-site repulsion, which promotes the stability of the CDW order. On the other hand, the observed periodicity of the CDW is difficult to reconcile with the number of doped holes; a fact which indicates that the CDW in the ladder system of $\text{Sr}_{14-x}\text{Ca}_x\text{Cu}_{24}\text{O}_{41}$ cannot be merely a stabilization of the CDW phase which is expected for a single ladder.

When for compounds with high Ca content external pressure is applied, the interladder hopping becomes strong enough so that the ladder system does not retain its one-dimensional features, but is more accurately described by two-dimensional physics. The spin gap decreases in size, but remains finite even when SC sets in. The increasing interladder coupling, due to a pressure-induced strong rise of compressibility along the ladder rungs, and the decreasing spin gap eventually lead to metallic transport along both the legs and rungs of the ladders. In addition, applying pressure increases the number of mobile quasi-particles at low temperature. They have a finite density of states at the Fermi level and might contribute to the superconducting instability. These results, together with an indication for the existence of a Hebel–Slichter coherence peak in the SC state and the significant level of disorder in the doped ladders of $\text{Sr}_{14-x}\text{Ca}_x\text{Cu}_{24}\text{O}_{41}$, pose severe questions on the superconducting pairing mechanism and symmetry, which might turn out to be different compared to pure single ladders.

Future research, experimental as well as theoretical, should focus on providing new information to reveal the nature of the CDW and superconducting ground state in the ladders of $\text{Sr}_{14-x}\text{Ca}_x\text{Cu}_{24}\text{O}_{41}$. This issue is likely to be important for understanding the mystery of superconductivity in cuprates and the electronic phases in strongly correlated systems in general.

Acknowledgements

In the course of conducting research on spin-chain and spin-ladder materials, the authors have benefited from numerous discussions with K. Biljaković, A. Bishop, A. Bjeliš, G. Blumberg, B. Büchner, M. Dumm, P. Foury, M. Grüninger, C. Hess, V. Ilakovac, P. Lemmens, P. Littlewood, A. Maeda, M. Miljak, P. Monceau, A. Muramatsu, P. Pervan, J.P. Pouget, M. Prester, T. Rößm, E. Tutiš, S. Uchida and many other colleagues whom we all want to thank very much. We thank D. Jérôme for communicating his nuclear magnetic resonance results prior to publication and for useful discussions. We especially acknowledge a continuous scientific interaction and illuminating discussions with O. Milat, I. Mrkonjić and S. Barišić. P. Haas performed the optical experiments in the course of his Ph.D. Thesis. It is also a pleasure to acknowledge G. Untereiner for her skillful preparation of many dozens of samples. We thank the Deutsche Forschungsgemeinschaft (DFG) for the continuous financial support. This work has also enjoyed financial support by the Croatian Ministry of Science, Education and Sports, grant 0035015 and by the Russian Foundation for Basic Research, grant N 05-02-16490-a.

References

- [1] P. Fulde, *Electron Correlations in Molecules and Solids*, third ed., Springer, Berlin, 1995.
- [2] P.A. Cox, *Transition Metal Oxides*, Clarendon Press, Oxford, 1992.
- [3] C.N.R. Rao, B. Raveau, *Transition Metal Oxides: Structure, Properties and Synthesis of Ceramic Oxides*, second ed., Wiley-VCH, New York, 1998.
- [4] S. Maekawa, T. Tohyama, S.E. Barnes, S. Ishihara, W. Koshibae, G. Khaliullin, *Physics of Transition Metal Oxides*, Springer, Berlin, 2004.
- [5] M. Uehara, T. Nagata, J. Akimitsu, H. Takahashi, N. Môri, K. Kinoshita, *J. Phys. Soc. Jpn.* 65 (1996) 2764.
- [6] E. Dagotto, J. Rieira, D. Scalapino, *Phys. Rev. B* 45 (1992) 5744.
- [7] E. Dagotto, *Rep. Prog. Phys.* 62 (1999) 1525.
- [8] P. Lemmens, G. Güntherodt, C. Gros, *Phys. Rep.* 375 (2003) 1.
- [9] M. Grüninger, M. Windt, E. Benckiser, T.S. Nunner, K.P. Schmidt, G.S. Uhrig, T. Kopp, *Adv. Solid State Phys.* 43 (2003) 95.
- [10] A. Gozar, G. Blumberg, in: A.V. Narlikar (Ed.), *Frontiers in Magnetic Materials*, Springer, Berlin, 2005.

- [11] D. Baeriswyl, D.K. Campbell, J.M.P. Carmelo, F. Guinea, E. Louis, *The Hubbard Model: Its Physics and Mathematical Physics*, NATO ASI Series B, vol. 343, Plenum Press, New York, 1995.
- [12] F.H.L. Essler, H. Frahm, F. Göhmann, A. Klümper, V.E. Korepin, *The One-Dimensional Hubbard Model*, Cambridge University Press, Cambridge, 2005.
- [13] T. Giamarchi, *Quantum Physics in One Dimension*, Oxford University Press, Oxford, 2004.
- [14] D. Baeriswyl, L. Degiorgi, *Strong Interactions in Low Dimensions*, Kluwer Academic, Dordrecht, 2004.
- [15] J. Hubbard, *Proc. R. Soc. A* 276 (1963) 238.
- [16] J.R. Waldram, *Superconductivity of Metals and Cuprates*, IOP Publishing, Bristol & Philadelphia, 1996.
- [17] M. Rasetti (Ed.), *The Hubbard model*, World Scientific, Singapore, 1991.
- [18] M. Imada, A. Fujimori, Y. Tokura, *Rev. Mod. Phys.* 70 (1998) 1039.
- [19] V.J. Emery, *Phys. Rev. B* 14 (1976) 2989.
- [20] K.V. Efetov, K.I. Larkin, *Soviet Phys. JETP* 42 (1975) 390.
- [21] V.J. Emery, in: J. Devreese, R. Evrard, V. van Doren (Eds.), *Highly Conducting One-Dimensional Solids*, Plenum, New York, 1979, p. 247.
- [22] P.W. Anderson, *Phys. Rev.* 115 (1959) 2.
- [23] K.C. Ung, S. Mazumdar, D. Toussaint, *Phys. Rev. Lett.* 73 (1994) 2603.
- [24] S. Mazumdar, R.T. Clay, D.K. Campbell, *Phys. Rev. B* 62 (2000) 13400.
- [25] V.J. Emery, R. Bruinsma, S. Barišić, *Phys. Rev. Lett.* 48 (1982) 1039.
- [26] H.J. Schulz, *Phys. Rev. Lett.* 71 (1993) 1864.
- [27] J.P. Pouget, in: E.M. Conwell (Ed.), *Highly Conducting Quasi-One-Dimensional Organic Crystals, Semiconductors and Semimetal*, vol. 27, p. 87, Academic Press, New York, 1988.
- [28] J.P. Pouget, in: C. Schlenker, J. Dumas, M. Greenblatt, S. van Smaalen (Eds.), *Physics and Chemistry of Low Dimensional Inorganic Conductors*, NATO ASI Series B, vol. 354, Plenum Press, New York, 1996.
- [29] D.J. Scalapino, J.E. Hirsch, *J. Phys. Colloq.* 44 (1983) C3–1507.
- [30] J. Riera, D. Poilblanc, *Phys. Rev. B* 59 (1999) 2667.
- [31] J.P. Pouget, S. Ravy, *J. Phys. I France* 6 (1996) 1501.
- [32] J.P. Pouget, S. Ravy, *Synthetic Metals* 85 (1997) 1523.
- [33] P.W. Anderson, *Science* 235 (1987) 1196.
- [34] M.R. Norman, C. Pépin, *Rep. Prog. Phys.* 66 (2003) 1547.
- [35] S.-C. Zhang, T.M. Rice, *Phys. Rev. B* 37 (1988) R3759.
- [36] D. Vaknin, S.K. Sinha, D.E. Moncton, D.C. Johnson, J. Newsam, C.R. Safinya, H.E. King Jr., *Phys. Rev. Lett.* 58 (1987) 2802.
- [37] G. Shirane, Y. Endo, R.J. Birgeneau, M.A. Kastner, Y. Hidaka, M. Oda, M. Suzuki, T. Murakami, *Phys. Rev. Lett.* 59 (1987) 1613.
- [38] D. Adler, in: F. Seitz, D. Turnbull, H. Ehrenreich (Eds.), *Solid State Physics*, vol. 21, Academic Press, New York, 1968.
- [39] J. Zaanen, G.A. Sawatzky, J.W. Allen, *Phys. Rev. Lett.* 55 (1985) 418.
- [40] M.K. Kelly, P. Barboux, J.M. Tarascon, D.E. Aspnes, *Phys. Rev. B* 40 (1989) 6797.
- [41] Y. Tokura, S. Koshihara, T. Arima, H. Takagi, S. Ishibashi, T. Ido, S. Uchida, *Phys. Rev. B* 41 (1990) 11657.
- [42] E. Dagotto, T.M. Rice, *Science* 271 (1996) 618.
- [43] N. Motoyama, T. Osafune, T. Kakeshita, H. Eisaki, S. Uchida, *Phys. Rev. B* 55 (1997) R3386.
- [44] R.M. Noack, S.R. White, D.J. Scalapino, *Physica C* 270 (1996) 281.
- [45] R.S. Eccleston, M. Uehara, J. Akimitsu, H. Eisaki, N. Motoyama, S. Uchida, *Phys. Rev. Lett.* 81 (1998) 1702.
- [46] M. Arai, H. Tsunetsugu, *Phys. Rev. B* 56 (1997) R4305.
- [47] J. Sólyom, *Adv. Phys.* 28 (1979) 201.
- [48] T. Siegrist, L.F. Schneemeyer, S.A. Sunshine, J.V. Waszczak, R.S. Roth, *Mat. Res. Bull.* 23 (1988) 1429.
- [49] E.M. McCarron, M.A. Subramanian, J.C. Calabrese, R.L. Harlow, *Mat. Res. Bull.* 23 (1988) 1355.
- [50] K. Kato, E. Takayama-Muromachi, K. Kosuda, Y. Uchida, *Acta Crystallogr. C* 44 (1988) 1881.
- [51] O. Milat, G. Van Tendeloo, S. Amelinckx, M. Mehbod, R. Deltour, *Acta Crystallogr. B* 48 (1992) 618.
- [52] Z. Hiroi, S. Amelinckx, G. Van Tendeloo, N. Kobayashi, *Phys. Rev. B* 54 (1996) 15849.
- [53] T. Ohta, F. Izumi, M. Onoda, M. Isobe, E. Takayama-Muromachi, A.W. Hewat, *J. Phys. Soc. Jpn.* 66 (1997) 3107–3114.
- [54] J. Etrillard, M. Braden, A. Gukasov, U. Ammerahl, A. Revcolevschi, *Physica C* 403 (2004) 290–296.
- [55] M. Isobe, M. Onoda, T. Ohta, F. Izumi, K. Kimoto, E. Takayama-Muromachi, A.W. Hewat, K. Ohoyama, *Phys. Rev. B* 62 (2000) 11667.
- [56] J.B. Goodenough, *Phys. Rev.* 100 (1955) 564.
- [57] J. Kanamori, *J. Phys. Chem. Solids* 10 (1959) 87.
- [58] P.W. Anderson, *Solid State Phys.* 14 (1963) 99.
- [59] W. Geertsma, D.I. Khomskii, *Phys. Rev. B* 54 (1996) 3011.
- [60] N. Motoyama, H. Eisaki, S. Uchida, *Phys. Rev. Lett.* 76 (1996) 3212.
- [61] K.M. Kojima, Y. Fudamoto, M. Larkin, G.M. Luke, J. Merrin, B. Nachumi, Y.J. Uemura, N. Motoyama, H. Eisaki, S. Uchida, K. Yamada, Y. Endoh, S. Hosoya, B.J. Sternlieb, G. Shirane, *Phys. Rev. Lett.* 78 (1997) 1787.
- [62] H. Bethe, *Z. Phys.* 71 (1931) 205.
- [63] A. Sapiña, J. Rodriguez-Carvajal, M.J. Sanchis, R. Ibanez, A. Beltran, D. Beltran, *Solid State Commun.* 74 (1990) 779.
- [64] M.A. Kastner, R.J. Birgeneau, G. Shirane, Y. Endo, *Rev. Mod. Phys.* 70 (1998) 897.
- [65] M. Azuma, Z. Hiroi, M. Takano, K. Ishida, Y. Kitaoka, *Phys. Rev. Lett.* 73 (1994) 3463.
- [66] D.C. Johnston, *Phys. Rev. B* 54 (1996) 13009.
- [67] T. Imai, K.R. Thurber, K.M. Shen, A.W. Hunt, F.C. Chou, *Phys. Rev. Lett.* 81 (1998) 220.

- [68] S. Gopalan, T.M. Rice, M. Sigrist, *Phys. Rev. B* 49 (1994) 8901.
- [69] M. Matsuda, K.M. Kojima, Y.J. Uemura, J.L. Zarestsky, K. Nakajima, K. Kakurai, T. Yokoo, S.M. Shapiro, G. Shirane, *Phys. Rev. B* 57 (1998) 11467.
- [70] S.A. Carter, B. Batlogg, R.J. Cava, J.J. Krajewski, W.F. Peck Jr., T.M. Rice, *Phys. Rev. Lett.* 77 (1996) 1378.
- [71] L.P. Regnault, J.P. Boucher, H. Moudden, J.E. Lorenzo, A. Hiess, U. Ammerahl, G. Dhalenne, A. Revcolevschi, *Phys. Rev. B* 59 (1999) 1055.
- [72] M. Kato, K. Shiotani, Y. Koike, *Physica C* 258 (1996) 284.
- [73] T.F.A. Müller, V. Anisimov, T.M. Rice, I. Dasgupta, T. Saha-Dasgupta, *Phys. Rev. B* 57 (1998) R12655.
- [74] T. Takahashi, T. Yokoya, A. Ashihara, O. Akaki, H. Fujisawa, A. Chainani, M. Uehara, T. Nagata, J. Akimitsu, H. Tsunetsugu, *Phys. Rev. B* 56 (1997) 7870.
- [75] I. Mrkonjić, S. Barišić, *Eur. Phys. J. B* 34 (2003) 69.
- [76] N.M. Plakida, *High-Temperature Superconductivity*, Springer, Berlin, Heidelberg, 1995.
- [77] T. Osafune, N. Motoyama, H. Eisaki, S. Uchida, *Phys. Rev. Lett.* 78 (1997) 1980.
- [78] I. Mrkonjić, S. Barišić, *Eur. Phys. J. B* 34 (2003) 441.
- [79] A. Ino, C. Kim, M. Nakamura, T. Yoshida, T. Mizokawa, A. Fujimori, Z.-X. Shen, T. Kakeshita, H. Eisaki, S. Uchida, *Phys. Rev. B* 65 (2002) 094504.
- [80] Y. Mizuno, T. Tohyama, S. Maekawa, *J. Phys. Soc. Jpn.* 66 (1997) 937.
- [81] N. Nücker, M. Merz, C.A. Kuntscher, S. Gerhold, S. Schuppler, R. Neudert, M.S. Golden, J. Fink, D. Schild, S. Stadler, V. Chakarian, J. Freeland, Y.U. Idzerda, K. Conder, M. Uehara, T. Nagata, J. Goto, J. Akimitsu, N. Motoyama, H. Eisaki, S. Uchida, U. Ammerahl, A. Revcolevschi, *Phys. Rev. B* 62 (2000) 14384.
- [82] Y. Gotoh, I. Yamaguchi, Y. Takahashi, J. Akimoto, M. Goto, M. Onoda, H. Fujino, T. Nagata, J. Akimitsu, *Phys. Rev. B* 68 (2003) 224108.
- [83] S. Uchida, T. Ido, H. Takagi, T. Arima, Y. Tokura, S. Tajima, *Phys. Rev. B* 43 (1991) 7942.
- [84] V. Kataev, K.-Y. Choi, M. Grüninger, U. Ammerahl, B. Büchner, A. Freimuth, A. Revcolevschi, *Phys. Rev. Lett.* 86 (2001) 2882.
- [85] V. Kataev, K.-Y. Choi, M. Grüninger, U. Ammerahl, B. Büchner, A. Freimuth, A. Revcolevschi, *Phys. Rev. B* 64 (2001) 104422.
- [86] Y. Piskunov, D. Jérôme, P. Auban-Senzier, P. Wzietek, A. Yakubovskiy, *Phys. Rev. B* 72 (2005) 064512.
- [87] M. Matsuda, K. Katsumata, *Phys. Rev. B* 53 (1996) 12201.
- [88] M. Takigawa, N. Motoyama, H. Eisaki, S. Uchida, *Phys. Rev. B* 57 (1998) 1124.
- [89] M. Troyer, H. Tsunetsugu, D. Würtz, *Phys. Rev. B* 50 (1994) 13515.
- [90] M. Matsuda, K. Katsumata, H. Eisaki, N. Motoyama, S. Uchida, S.M. Shapiro, G. Shirane, *Phys. Rev. B* 54 (1996) 12199.
- [91] M. Matsuda, T. Yoshihara, K. Kakurai, G. Shirane, *Phys. Rev. B* 59 (1999) 1060.
- [92] A. Brooks Harris, *Phys. Rev. B* 7 (1973) 3166.
- [93] O. Milat, private communication.
- [94] T. Fukuda, J. Mizuki, M. Matsuda, *Phys. Rev. B* 66 (2002) 012104.
- [95] S. van Smaalen, *Phys. Rev. B* 67 (2003) 026101.
- [96] M. Braden, J. Etrillard, A. Gukasov, U. Ammerahl, A. Revcolevschi, *Phys. Rev. B* 69 (2004) 214426.
- [97] D.E. Cox, T. Iglesias, K. Hirota, G. Shirane, M. Matsuda, N. Motoyama, H. Eisaki, S. Uchida, *Phys. Rev. B* 57 (1998) 10750.
- [98] P. Abbamonte, L. Venema, A. Rusydi, G.A. Sawatzky, G. Logvenov, I. Božović, *Science* 297 (2002) 581.
- [99] P. Abbamonte, G. Blumberg, A. Rusydi, A. Gozar, P.G. Evans, T. Siegrist, L. Venema, H. Eisaki, E.D. Isaacs, G.A. Sawatzky, *Nature* 431 (2004) 1078.
- [100] A. Gellé, M.B. Lepetit, *Phys. Rev. Lett.* 92 (2004) 236402.
- [101] T. Nagata, H. Fujino, J. Akimitsu, M. Nishi, K. Kakurai, S. Katano, M. Hiroi, M. Sera, N. Kobayashi, *J. Phys. Soc. Jpn.* 68 (1999) 2206.
- [102] S. Tsuji, K. Kumagai, M. Kato, Y. Koike, *J. Phys. Soc. Jpn.* 65 (1996) 3474.
- [103] K. Kumagai, S. Tsuji, M. Kato, Y. Koike, *Phys. Rev. Lett.* 78 (1997) 1992.
- [104] M. Isobe, Y. Uchida, E. Takayama-Muromachi, *Phys. Rev. B* 59 (1999) 8703.
- [105] S. Ohsugi, K. Magishi, S. Matsumoto, Y. Kitaoka, T. Nagata, J. Akimitsu, *Phys. Rev. Lett.* 82 (1999) 4715.
- [106] M. Kato, T. Adachi, Y. Koike, *Physica C* 265 (1996) 107.
- [107] M. Matsuda, K. Katsumata, T. Yokoo, S.M. Shapiro, G. Shirane, *Phys. Rev. B* 54 (1996) 15626.
- [108] U. Ammerahl, A. Revcolevschi, *J. Cryst. Growth* 197 (1999) 825.
- [109] M. Matsuda, K. Katsumata, T. Osafune, N. Motoyama, H. Eisaki, S. Uchida, T. Yokoo, S.M. Shapiro, G. Shirane, J.L. Zarestsky, *Phys. Rev. B* 56 (1997) 14499.
- [110] T. Vuletić, B. Korin-Hamzić, S. Tomić, B. Gorshunov, P. Haas, M. Dressel, J. Akimitsu, T. Sasaki, T. Nagata, *Phys. Rev. B* 67 (2003) 184521.
- [111] N.F. Mott, E.A. Davis, *Electronic Processes in Non-crystalline Solids*, Oxford University, London, 1971.
- [112] Z.G. Yu, X. Song, *Phys. Rev. Lett.* 86 (2001) 6018.
- [113] P.A. Lee, *Phys. Rev. Lett.* 53 (1984) 2042.
- [114] T.V. Ramakrishnan, in: J. Souletie, J. Vannimenus, R. Stora (Eds.), *Les Houches, Session XLVI, 1986—Chance and Matter*, Elsevier Science Publishers B.V., Amsterdam, 1987, p. 213.
- [115] M. Matsuda, K. Katsumata, R.S. Eccleston, S. Brehmer, H.J. Mikeska, *Phys. Rev. B* 62 (2000) 8903.
- [116] T. Barnes, J. Riera, *Phys. Rev. B* 50 (1994) 6817.
- [117] K. Ishida, Y. Kitaoka, K. Asayama, M. Azuma, Z. Hiroi, M. Takano, *J. Phys. Soc. Jpn.* 63 (1994) 3222.
- [118] A.W. Sandvik, E. Dagotto, D.J. Scalapino, *Phys. Rev. B* 53 (1996) R2934.
- [119] D.A. Ivanov, P.A. Lee, *Phys. Rev. B* 59 (1999) 4803.
- [120] F. Naef, X. Wang, *Phys. Rev. Lett.* 84 (2000) 1320.
- [121] M. Windt, M. Grüninger, T. Nunner, C. Knetter, K.P. Schmidt, G.S. Uhrig, T. Kopp, A. Freimuth, A. Ummerahl, B. Büchner, A. Revcolevschi, *Phys. Rev. Lett.* 87 (2001) 127002.

- [122] C. Hess, C. Baumann, U. Ammerahl, B. Büchner, F. Heidrich-Meisner, W. Brenig, A. Revcolevschi, *Phys. Rev. B* 64 (2001) 184305.
- [123] K.R. Thurber, K.M. Shen, A.W. Hunt, T. Imai, F.C. Chou, *Phys. Rev. B* 67 (2003) 094512.
- [124] R.S. Eccleston, M. Azuma, M. Takano, *Phys. Rev. B* 53 (1996) R14721.
- [125] S. Katano, T. Nagata, J. Akimitsu, M. Nishi, K. Kakurai, *Phys. Rev. Lett.* 82 (1999) 636.
- [126] S. Sugai, M. Suzuki, *Phys. Stat. Sol.* 215 (1999) 653.
- [127] A. Gozar, G. Blumberg, B.S. Dennis, B.S. Shastry, N. Motoyama, H. Eisaki, S. Uchida, *Phys. Rev. Lett.* 87 (2001) 197202.
- [128] M. Sigrist, T.M. Rice, F.C. Zhang, *Phys. Rev. B* 49 (1994) 12058.
- [129] R.M. Noack, S.R. White, D.J. Scalapino, *Phys. Rev. Lett.* 73 (1994) 882.
- [130] D. Poilblanc, H. Tsunetsugu, T.M. Rice, *Phys. Rev. B* 50 (1994) R6511.
- [131] J. Akimitsu, M. Uehara, T. Nagata, S. Matsumoto, Y. Kitaoka, H. Takahashi, N. Môri, *Physica C* 263 (1996) 475.
- [132] K. Magishi, S. Matsumoto, Y. Kitaoka, K. Ishida, K. Asayama, M. Uehara, T. Nagata, J. Akimitsu, *Phys. Rev. B* 57 (1998) 11533.
- [133] Y. Piskunov, D. Jérôme, P. Auban-Senzier, P. Wzietek, C. Bourbonnais, U. Ammerahl, G. Dhalenne, A. Revcolevschi, *Eur. Phys. J. B* 24 (2001) 443.
- [134] Y. Piskunov, D. Jérôme, P. Auban-Senzier, P. Wzietek, A. Yakubovsky, *Phys. Rev. B* 69 (2004) 014510.
- [135] A.V. Sologubenko, K. Giannó, H.R. Ott, U. Ammerahl, A. Revcolevschi, *Phys. Rev. Lett.* 84 (2000) 2714.
- [136] K. Kudo, S. Ishikawa, T. Noji, T. Adachi, Y. Koike, K. Maki, S. Tsuji, K. Kumagai, *J. Phys. Soc. Jpn.* 70 (2001) 437.
- [137] T. Imai, C.P. Slichter, K. Yoshimura, K. Kosuge, *Phys. Rev. Lett.* 70 (1993) 1002.
- [138] M.W. McElfresh, J.M.D. Coey, P. Strobel, S. von Molnar, *Phys. Rev. B* 40 (1989) 825.
- [139] M. Kato, K. Shiota, Y. Koike, *Physica C* 258 (1996) 284.
- [140] T. Adachi, K. Shiota, M. Kato, T. Noji, Y. Koike, *Solid State Commun.* 105 (1998) 639.
- [141] H. Eisaki, N. Motoyama, K.M. Kojima, S. Uchida, N. Takeshita, N. Mori, *Physica C* 341 (2000) 363.
- [142] K.M. Kojima, N. Motoyama, H. Eisaki, S. Uchida, *J. Electron Spectrosc.* 117 (2001) 237.
- [143] N. Motoyama, H. Eisaki, S. Uchida, N. Takeshita, N. Môri, T. Nakanishi, H. Takahashi, *Europhys. Lett.* 58 (2002) 758.
- [144] T. Vuletić, B. Korin-Hamzić, S. Tomić, B. Gorshunov, P. Haas, T. Rößm, M. Dressel, J. Akimitsu, T. Sasaki, T. Nagata, *Phys. Rev. Lett.* 90 (2003) 257002.
- [145] T. Vuletić, T. Ivek, B. Korin-Hamzić, S. Tomić, B. Gorshunov, P. Haas, M. Dressel, J. Akimitsu, T. Sasaki, T. Nagata, *Phys. Rev. B* 71 (2005) 012508.
- [146] T. Nagata, M. Uehara, J. Goto, J. Akimitsu, N. Motoyama, H. Eisaki, S. Uchida, H. Takahashi, T. Nakanishi, N. Môri, *Phys. Rev. Lett.* 81 (1998) 1090.
- [147] T. Nagata, M. Uehara, J. Goto, N. Komiya, J. Akimitsu, N. Motoyama, H. Eisaki, S. Uchida, H. Takahashi, T. Nakanishi, N. Môri, *Physica C* 282–287 (1997) 153.
- [148] M. Isobe, T. Ohta, M. Onoda, F. Izumi, S. Nakano, J.Q. Li, Y. Matsui, E. Takyama-Muromachi, T. Matsumoto, H. Hayakawa, *Phys. Rev. B* 57 (1998) 613.
- [149] T. Pang, *Phys. Rev. Lett.* 62 (1989) 2176.
- [150] S. Pachot, P. Bordet, R.J. Cava, C. Chaillout, C. Darie, M. Hanfland, M. Marezio, H. Takagi, *Phys. Rev. B* 59 (1999) 12048.
- [151] N. Fujiwara, N. Mori, Y. Uwatoko, T. Matsumoto, N. Motoyama, S. Uchida, *Phys. Rev. Lett.* 90 (2003) 137001.
- [152] H. Tsunetsugu, M. Troyer, T.M. Rice, *Phys. Rev. B* 49 (1994) 16078.
- [153] T. Ito, H. Takagi, S. Ishibashi, T. Ido, S. Uchida, *Nature* 350 (1991) 596.
- [154] S. Tomić, J.R. Cooper, W. Kang, D. Jérôme, K. Maki, *J. Phys. I France* 1 (1991) 1603.
- [155] G. Grüner, *Rev. Mod. Phys.* 60 (1988) 1129.
- [156] P. Monceau (Ed.), *Electronic Properties of Inorganic Quasi-One-Dimensional Compounds*, D. Reidel Publishing Co., Dordrecht, Holland, 1985.
- [157] X. Huang, K. Maki, *Phys. Rev. B* 42 (1990) 6498.
- [158] T. Osafune, N. Motoyama, H. Eisaki, S. Uchida, S. Tajima, *Phys. Rev. Lett.* 82 (1999) 1313.
- [159] G. Grüner, *Density Waves in Solids*, Addison-Wesley, Reading, MA, 1994.
- [160] C. Hess, H. ElHaes, B. Büchner, U. Ammerahl, M. Hückler, A. Revcolevschi, *Phys. Rev. Lett.* 93 (2004) 027005.
- [161] B. Gorshunov, P. Haas, T. Rößm, M. Dressel, T. Vuletić, B. Korin-Hamzić, S. Tomić, J. Akimitsu, T. Nagata, *Phys. Rev. B* 66 (2002) 060508(R).
- [162] G. Blumberg, P. Littlewood, A. Gozar, B.S. Dennis, N. Motoyama, H. Eisaki, S. Uchida, *Science* 297 (2002) 584.
- [163] P.B. Littlewood, *Phys. Rev. B* 36 (1987) 3108.
- [164] K. Petukhov, M. Dressel, *Phys. Rev. B* 71 (2005) 073101.
- [165] A. Gozar, G. Blumberg, P. Littlewood, B.S. Dennis, N. Motoyama, H. Eisaki, S. Uchida, *Phys. Rev. Lett.* 91 (2003) 087401.
- [166] H. Kitano, R. Isobe, T. Hanaguri, A. Maeda, N. Motoyama, M. Takaba, K. Kojima, H. Eisaki, S. Uchida, *Europhys. Lett.* 56 (2001) 434.
- [167] H. Kitano, R. Inoue, A. Maeda, N. Motoyama, K. Kojima, H. Eisaki, S. Uchida, *Physica C* 341–348 (2000) 463.
- [168] P.A. Lee, T.M. Rice, P.W. Anderson, *Phys. Rev. B* 14 (1974) 703.
- [169] D. Jérôme, H.J. Schulz, *Adv. Phys.* 31 (1982) 299–490.
- [170] T.W. Kim, D. Reagor, G. Grüner, K. Maki, A. Virosztek, *Phys. Rev. B* 40 (1989) 5372.
- [171] B. Ruzicka, L. Degiorgi, U. Ammerahl, G. Dhalenne, A. Revcolevschi, *Eur. Phys. J. B* 6 (1998) 301;
B. Ruzicka, L. Degiorgi, U. Ammerahl, G. Dhalenne, A. Revcolevschi, *Physica B* 259–261 (1999) 1036;
B. Ruzicka, L. Degiorgi, U. Ammerahl, G. Dhalenne, A. Revcolevschi, *Physica C* 317–318 (1999) 282;
B. Ruzicka, L. Degiorgi, U. Ammerahl, G. Dhalenne, A. Revcolevschi, *Physica C* 341–348 (2000) 359.
- [172] H. Fröhlich, *Proc. R. Soc. A* 223 (1954) 296.
- [173] D. Jérôme, L. G. Caron (Eds.), *Low-Dimensional Conductors and Superconductors*, NATO ASI Series B, Plenum Press, New York, 1987.

- [174] A. Maeda, R. Inoue, H. Kitano, N. Motoyama, H. Eisaki, S. Uchida, *Phys. Rev. B* 67 (2003) 115115.
- [175] H. Kitano, R. Inoue, A. Maeda, N. Motoyama, K.M. Kojima, S. Uchida, *Physica C* 388–389 (2003) 231.
- [176] T. Vuletić, Ph.D. Thesis, University of Zagreb, unpublished, 2004; browse <http://real-science.ifs.hr/>.
- [177] Wei-yu Wu, L. Mihály, G. Grüner, *Solid State Commun.* 55 (1985) 663.
- [178] L. Mihaly, G.X. Tessema, *Phys. Rev. B* 33 (1986) 5858.
- [179] M.V. Klein, in: M. Cardona (Ed.), *Light Scattering in Solids*, vol. I, Springer, Berlin, Heidelberg, New York, 1983 (Chapter 4).
- [180] S. Tomić, N. Biškup, M. Pinterić, J.U. von Schütz, H. Schmitt, R. Moret, *Europhys. Lett.* 38 (1997) 219.
- [181] T. Sambongi, K. Tsutsumi, Y. Shiozaki, M. Yamamoto, K. Yamaya, Y. Abe, *Solid State Commun.* 22 (1977) 729.
- [182] D. Starešinić, Ph.D. Thesis, University of Zagreb, unpublished, 2000.
- [183] D. Starešinić, K. Biljaković, W. Brütting, K. Hosseini, P. Monceau, H. Berger, F. Levy, *Phys. Rev. B* 65 (2002) 165109.
- [184] S.R. White, I. Affleck, D.J. Scalapino, *Phys. Rev. B* 65 (2002) 165122.
- [185] A.F. Ioffe, A.R. Regel, *Prog. Semicond.* 4 (1960) 237.
- [186] E. Orignac, T. Giamarchi, *Phys. Rev. B* 56 (1997) 7167.
- [187] E.H. Kim, *Phys. Rev. Lett.* 86 (2001) 1315.
- [188] S.T. Carr, A.M. Tsvelik, *Phys. Rev. B* 65 (2002) 195121.
- [189] M. Tsuchiizu, Y. Suzumura, *J. Phys. Soc. Jpn.* 73 (2004) 804.
- [190] M. Tsuchiizu, Y. Suzumura, *Phys. Rev. B* 72 (2005) 075121.
- [191] C. Nayak, *Phys. Rev. B* 62 (2000) 4880.
- [192] C. Wu, W.V. Liu, E. Fradkin, *Phys. Rev. B* 68 (2003) 115104.
- [193] U. Schollwöck, S. Chakravarty, J.O. Fjærestad, J.B. Marston, M. Troyer, *Phys. Rev. Lett.* 90 (2003) 186401.
- [194] H.J. Schulz, *Phys. Rev. B* 53 (1996) R2959.
- [195] G.S. Boebinger, Y. Ando, A. Passner, T. Kimura, M. Okuya, J. Shimoyama, K. Kishio, K. Tamasaku, N. Ichikawa, S. Uchida, *Phys. Rev. Lett.* 77 (1996) 5417.